UNIVERSITY OF CALIFORNIA,
IRVINE

Controlling Structural and Electronic Molecular Architecture of Electrocatalysts and Dynamic Polymers using Intramolecular Hydrogen Bonds

DISSERTATION

submitted in partial satisfaction of the requirements
for the degree of

DOCTOR OF PHILOSOPHY

in Chemistry

by

Juliet Fariba Khosrowabadi

Dissertation Committee:
Assistant Professor Jenny Y. Yang, Chair
Associate Professor Andrew S. Borovik
Associate Professor Elizabeth R. Jarvo

2016

DEDICATION

For my family: Chris, Baba, Mom, and Sissy

TABLE OF CONTENTS

LIST OF FIGURES

LIST OF TABLES

LIST OF SCHEMES

LIST OF CHARTS

ACKNOWLEDGMENTS

Graduate school is definitely not the easiest place to be but being around good people made it an enjoyable and interesting place to learn and live.

I express sincere gratitude for my PI Professor Jenny Y. Yang for taking a chance on me and really allowing me to grow as a scientist. I hope I can make you proud as your first student.

I would like to thank my committee members Professor Andy Borovik and Professor Elizabeth Jarvo for helpful life and scientific discussion.

To my group members, past and present, thank you for making every day fun to do science. I can say I was very lucky to be able to call my labmates friends and colleagues. To past members (Dr. Dave Shaffer and Steve Poteet) and current members (Dr. Annie Chantarojsiri, Dr. Charlene Tsay, Brian Lydon, Zach Thammavongsy, Bianca Ceballos, Drew Cunningham, Alex Reath, Caitlin Hanna) thank you for the support, yelling, and laughing that took place on Electric Avenue.

Thank you Friend Group™ for being wonderful people to spend five years with. The many days and nights of studying, late nights and new experiences can never ever be replaced. To: Dr. Oliva Cromwell, Dr. Mary Beth Daub, Dr. Ethan Hill, Dr. Aaron Hollas, Future Dr. Krysten Jones, Future Dr. Domarin Khago, Dr. Chris Kotyk, Dr. Greg Lackner, Dr. Dave McCutcheon, Future Dr. Greg Suryn, and Future Dr. Nick Tallarida I look forward to our continuing friendships and biannual vacations.

Thank you to my family (biological and by law) for helping me through everything in life. To Reza, April, Farzaneh, Will, Bruce, Priscilla, John, and Nick. I love you all.

Lastly, thank you to my husband Dr. Chris Kotyk for being smart, funny, weird and the most supportive person I have ever met. I am thankful for gaining something so positive out a such a difficult place in life. I love you and cannot wait to experience the world with you.

CURRICULUM VITAE

JULIET F. KHOSROWABADI KOTYK

EDUCATION

2016 — University of California, Irvine
Doctor of Philosophy, Chemistry

2010 — University of California, Los Angeles
Bachelor of Science, Chemistry

RESEARCH EXPERIENCE

2013 – 2016 — **Graduate Student Researcher**, University of California, Irvine
Advisor: Prof. Jenny Yang

Inorganic Homogenous Electrocatalysis
Designed transition metals catalysts for fuel cell electrode applications that employ secondary coordination sphere effects to direct small molecule (H_2, CO_2, O_2) reduction reactivity.

2011 – 2013 — **Graduate Student Researcher**, University of California, Irvine
Advisor: Prof. Zhibin Guan

Single Molecule Studies of Dynamic Polymers
Studied single molecule bond rupture of electronically modified series of hydrogen bonding
biomimetic oligomers via Single Molecule Force Spectroscopy-Atomic Force Microscopy.

2010 – 2011 — **Research Technician**, University of California, Los Angeles
Advisor: Prof. Yves Rubin

Crystal Engineering of Carbon Nanotube Supramolecular Scaffolds
Synthesized and crystalized conjugated alkyne supramolecular macrocycles for discrete diameter nanotubes via topochemical polymerization for advanced electronic materials.

2008 – 2010 — **Undergraduate Student Researcher**, University of California, Los Angeles
Advisor: Prof. Yves Rubin

Bioactive Fullerene Derivatives
Synthesized and examined amino acid modified fullerenes (C_{60}) for competitive inhibition against amyloid-beta peptide aggregation for use as Alzheimer's disease treatment.

SELECTED PRESENTATIONS OF WORK

1. Suzuki, M.; **Khosrowabadi Kotyk, J. F.**; Khan, S.; Rubin, Y. "Directing the Crystallization of Dehydro[24]annulenes into Supramolecular Nanotubular Scaffolds" *J. Am. Chem. Soc.*, **2016**, *138*, 5939–5956.
2. Suzuki, M.; Guo, Z.; Tahara, K.; **Khosrowabadi Kotyk, J. F.**; Nguyen, H.; Gotoda, J.; Rubin, Y.; Tobe, Y. "Self-Assembled Dehydro[24]annulene Monolayers at the

Liquid/Solid Interface: Towards On-Surface Synthesis of Tubular π-Conjugated Nanowires" *Langmuir*, **2016**, *32*, 5532–5541

3. **Khosrowabadi Kotyk, J. F.**; Yang, J. Y. "Copper Tetradentate N_2Py_2 Complexes with Pendant Bases in the Secondary Coordination Sphere: Improved Ligand Synthesis and Protonation Studies" *J. Coord. Chem.* DOI: 10.1080/00958972.2015.1130223
4. Thammavongsy, Z.; **Khosrowabadi Kotyk, J. F.**; Tsay, C.; Yang, J. Y. "Flexibility is Key: Synthesis of a Tripyridylamine (TPA) Congener with a Phosphorus Apical Donor and Coordination to Cobalt(II)" *Inorg. Chem.* **2015**, *54*, 11505–11510.
5. **Khosrowabadi Kotyk, J. F.**; "Incorporation of Second Coordination Sphere Pendant Bases for Use in Electrocatalysis" [poster] Southern California Organometallics Conference, Pasadena, CA, February 2015
6. **Khosrowabadi Kotyk, J. F.**; "Copper, Cobalt and Nickel Molecular Complexes Toward Electrochemical Small Molecule Activation" [presentation] ACS Spring 2015 Conference (Inorganic Catalysts), Denver, CO, March 2015
7. **Khosrowabadi Kotyk, J. F.**; "Molecular Complexes for Use as Electrocatalysts in Fuel Cells" [poster] Southern California Organometallics Conference, Riverside, CA, December 2015
8. **Khosrowabadi Kotyk, J. F.**; "Intramolecular C-H Activation by a Rhodium Complex" [presentation] Southern California Organometallics Conference, Irvine, CA, April 2016

LEADERSHIP AND PROFESSIONAL DEVELOPMENT

Leadership

- Trained and mentored three undergraduate students to safely and successfully perform scientific research with oxygen sensitive, and pyrophoric materials. — 2013 – 2016
- Instructed and oversaw 35 graduate student teaching assistants to effectively train >1000 undergraduate students in organic chemistry laboratory. — 2013 – 2014

Professional Development and Awards

- **[Award]** Dissertation Fellowship, University of California, Irvine — Fall 2016
- **[Award]** UC Irvine Department of Chemistry Upper Division Teaching — June 2016
- **[Award]** CENTC, Seattle, WA — July 2015
  Center for Enabling New Technologies Through Catalysis, National Science Foundation Phase II Center for Chemical Innovation, "Bringing New Technologies to the Marketplace" Summer School
- **[Award]** UC Irvine Department of Physical Sciences Travel Award — March 2015
- One-on-One SMFS-AFM training at Asylum Research, Santa Barbara, CA — June 2013
- **[Award]** Dean's Honor List, University of California, Los Angeles — 2008 – 2010

TEACHING EXPERIENCE

Lecture Teaching Assistant, University of California, Irvine — 2014 – 2016
General, Organic, and Upper Division Inorganic Chemistry

Head Laboratory Teaching Assistant, University of California, Irvine — 2013 – 2014
Organic Chemistry

Laboratory Teaching Assistant, University of California, Irvine — 2011 – 2013
General and Organic Chemistry

Laboratory Teaching Assistant, University of California, Los Angeles — 2010 – 2011
Advanced Spectroscopy

ABSTRACT OF THE DISSERTATION

Controlling Structural and Electronic Molecular Architecture of Electrocatalysts and Dynamic Polymers using Intramolecular Hydrogen Bonds

by

Juliet Fariba Khosrowabadi

Doctor of Philosophy in Chemistry

University of California, Irvine, 2016

Professor Jenny Y. Yang, Chair

The development of cost effective renewable energy sources is necessary to meet increasing demand and transition from fossil fuels as a primary energy source. Catalysis by transition metal molecular complexes for fuel forming and utilization reactions show promise due to their abundance and low cost. Additionally, molecular systems can be studied using common techniques. Systematic ligand design and structure-function relationships can be utilized to learn fundamental properties of these important fuel storage and generation transformations, which in turn is essential to the design of new electrocatalysts.

This dissertation describes the design of transition metal complexes that incorporate pendant bases in the secondary coordination sphere to mimic the functionally of proton relays in biological systems. The complexes were investigated for their reactivity towards the efficient transformation of small molecules to chemical fuels or use in fuel cells. Investigating these complexes electrocatalytically allows for the elucidation of bond strengths, mechanistic information, thermochemical cycles and free energy of the overall target reactions. A multidisciplinary approach is invoked, founded on the design and synthesis of organic compounds,

development of metal complexes, and characterization by organic, inorganic and analytical methods to determine structure-activity relationships of rationally designed ligand frameworks.

Chapter 1 describes the design, synthesis and characterization of neutral tetradentate diamino–dipyridal ligands (N_2Py_2) containing hydrogen bond donor (L^{MMA}) and hydrogen bond acceptor (L^{DMA}) functionalities.

Chapter 2 describes the synthesis and characterization of divalent copper complexes utilizing L^{MMA} and L^{DMA}. The structural, electronic, and electrochemical properties of these complexes are described. The protonation of the monovalent complexes exhibited the unexpected site of protonation on the ethylenediamine backbone. The reactivity of the copper complexes with dioxygen was also investigated.

Chapter 3 describes the synthesis, characterization, structural, electronic, and electrochemical properties of cobalt complexes containing the L^{MMA} and L^{DMA} ligands. The reactivity of the divalent cobalt complexes with protons, water, dioxygen, and carbon dioxide is presented. The most interesting finding with these complexes is the improved water oxidation reactivity of $[CoL^{DMA}(CH_3CN)_2][BF_4]_2$ compared to the analogous complex with no pendant base present. Additionally, solid state structures of stable aquo complexes were obtained that demonstrated intramolecular hydrogen-bonding between water and pendant bases.

INTRODUCTION

0.1. Renewable Energy

There is growing need for alternative energy resources to reduce reliance on fossil fuels, which are exacerbating global climate change and producing harmful greenhouse gases. Current renewable energy resources such as solar and wind produce energy intermittently, requiring improved methods of energy storage to match supply with demand.[1,2] Development of new energy sources that can be stored, transported and used during peak demand specifically using abundant small molecule feedstocks such as CO_2, O_2, H_2, and H_2O is highly desired to create a sustainable energy cycle. However, these small molecules are inert and the conversion to useful products is complex and energetically demanding.

Conversion of small molecules into transportable chemical fuels (fuel generation) using an electrochemical potential is favorable due to their availability, overall environmentally benign byproducts, and low thermal input.[3-6] Fundamental research for the efficient and selective conversion of small molecules is critical to utilization of non-noble metal catalysts in electrocatalytic energy production and storage for scalable usage. Some industrially relevant reactions important for fuel generation or usage as energy in fuel cells are shown in Equations 1–7.

Fuel Forming Reactions

$$CO_2 + 2\,H^+ + 2\,e^- \longrightarrow CO + H_2O \qquad \textbf{eq 1}$$

$$CO_2 + 6\,H^+ + 6\,e^- \longrightarrow CH_3OH + H_2O \qquad \textbf{eq 2}$$

Development of methods to produce carbon-based fuels through greener methods such as conversion of excess carbon dioxide, a greenhouse gas, from the atmosphere is highly sought

after.[7] Carbon dioxide can be converted to a variety of carbon-based fuels. The two electron reduction to carbon monoxide (Equation 1) can be combined with hydrogen from renewable generation methods[8] to produce value hydrocarbons through Fischer-Tropsch processes. Direct fuel forming reactions such as the six electron six proton reduction of carbon dioxide to methanol (Equation 2), a transportable fuel, are more difficult. However, this important technology needs development to convert abundant small molecule feedstocks to non-fossil fuel renewable energy resources.[9]

$$2\,H^+ + 2\,e^- \longrightarrow H_2 \qquad \textbf{eq 3}$$

Utilization of a small molecule such as hydrogen as a simple chemical fuel is desirable to transition away from solely carbon-based fuels. Hydrogen can be produced from the two electron reduction of protons, or the hydrogen evolution reaction (HER) (Equation 3).

Fuel Using Reactions

$$H_2 \longrightarrow 2\,H^+ + 2\,e^- \qquad \textbf{eq 4}$$

Carbon neutral small molecule transformations for fuel utilization in alternative fuel technologies such as fuel cells are a highly valuable practical application for the switch to a sustainable energy economy. Fuel cells convert chemical energy into electrical energy through small molecule electrochemical oxidation at the anode or reduction at the cathode. Equation 4 shows the microscopic reverse of the HER, hydrogen oxidation, where hydrogen gas is a proton source at the anode in proton exchange membrane (PEM) fuel cells for electrical energy generation in a fuel utilization reaction.

$$O_2 + 4\,H^+ + 4\,e^- \longrightarrow 2\,H_2O \qquad \textbf{eq 5}$$

While fuel oxidation occurs at the anode in PEM fuel cells, the four electron reduction of dioxygen, or the oxygen reduction reaction (ORR, Equation 5), occurs as a proton and electron acceptor at the cathode to generate water.

$$2\,H_2O \longrightarrow O_2 + 4\,H^+ + 4\,e^- \qquad \textbf{eq 6}$$

$$\underline{4\,H^+ + 4\,e^- \longrightarrow 2\,H_2}$$

$$2\,H_2O \longrightarrow O_2 + 2\,H_2 \qquad \textbf{eq 7}$$

Water splitting (Equation 7) involves two half reactions requiring a total of four protons and electrons. The first reaction is water oxidation to dioxygen or the oxygen evolution reaction (OER) in Equation 6 and the second reaction is the HER from reduction of protons from water. PEM fuels cells utilize two abundant gases, H_2 and O_2, to generate electricity and the water produced by the ORR at the cathode can potentially be recycled to feed back into the process. Ideally, the water can be reincorporated into the system using water splitting to generate both H_2 and O_2 to create a fully carbon neutral cycle.

There are several benefits to promoting small molecule reactivity using fuel cells and electrocatalysis. Development of earth abundant and cost effective transition metal electrocatalysts for the production and usage of energy dense chemical fuels is highly sought after because current technology uses expensive noble metal catalysts prohibiting large scale accessibility. Electrochemistry removes the need for a chemical redox partner for atom efficient conversion and less byproduct formation. Additionally, it allows for determination of thermodynamic and kinetic parameters to learn from and adjust catalyst design to better understand how to effectively use abundant transition metal electrocatalysts.[10]

Biological systems interconvert energy from a variety of these small molecule transformations that require many proton and electron transfer steps. Nature has evolved to

perform these complex reactions precisely and efficiently. As a route to develop earth abundant catalysts for energy storage applications, enzyme active sites can act as inspiration.

0.2. Small Molecule Activation in Nature

There are known metabolic pathways in which biological systems produce energy through small molecule catalysis that include production and use of H_2, reduction of O_2 and oxidation of water, and fixation of CO_2 into organic carbon.[11,12] These pathways store and utilize energy from chemical bonds and carry out these complex transformations in a simple and controlled manner using specialized microenvironments.

Bioinorganic complexes are affected both by their primary coordination sphere as well as the surrounding proximal amino acid domain. The primary coordination sphere includes ligands that are covalently bound to the metal center and influence the coordination geometry, electronics, and chemical reactivity. The secondary coordination sphere typically involves non-covalent interactions such as hydrogen-bonding that impact selectivity and kinetics. Many enzyme active sites utilize abundant transition metal centers and through the incorporation of weak forces such as hydrogen-bonding have exquisite reactivity for specific reactions.

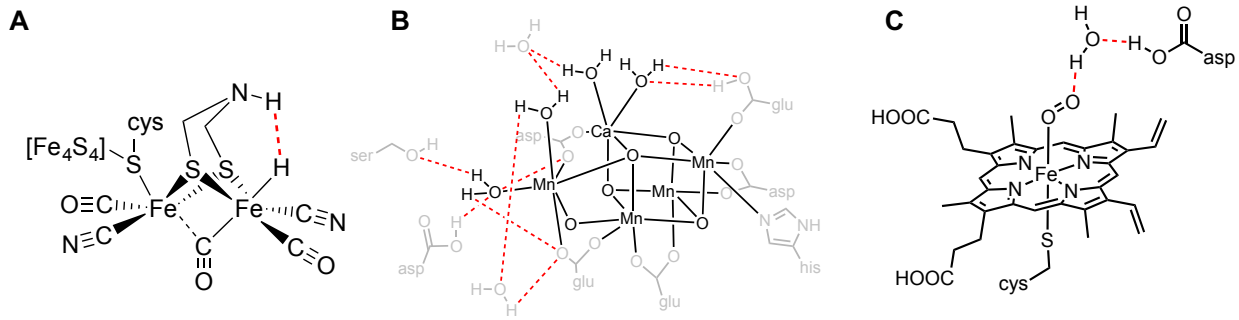

Figure 0.1. Representation of active sites A) [FeFe]-hydrogenase, B) Oxygen Evolving Complex in Photosystem II, and C) cytochrome P450 highlighting hydrogen-bonding interactions in red.

Proton relays are employed in natural enzymatic systems for multi-proton and multi-electron processes. Many enzymes have evolved to feature hydrogen bond donor or acceptor units in the outer sphere environment of the active metal site to shuttle protons to and from substrates or to stabilize highly energetic intermediates (Figure 0.1).[13-15]

The [FeFe]-hydrogenase consists of a di-iron cluster with a flexible pendant amine, Figure 0.1A. This proximal base in the secondary sphere aids in efficient H_2 production.[15,16] The active site of the Oxygen Evolving Complex (OEC) in Photosystem II contains a Mn_4O_5Ca cluster with an extensive hydrogen-bonding network involving the bound water molecules to a dangling manganese atom and the calcium ion.[17,18] The complex secondary sphere channel helps shuttle water or oxygen molecules to and from the active site for the OER, Figure 0.1B. The ORR occurs at the iron porphyrin (heme) active site in monooxygenase cytochrome P450 containing a stabilizing hydrogen-bonding network amongst adjacent amino acids and the activated oxygen bound metal center, Figure 0.1C.[19-21]

Effective proton transport is crucial to biological natural processes as well as chemical transformations to useful energy products. Efficient small molecule transformations occur through multiple proton and electron transfer steps that combine into a concerted mechanism. Such a process readily occurs in nature as proton-coupled electron transfer (PCET) to reduce the energetic barriers and improve selectivity of chemical reactions.[22,23]

Natural metalloenzymes can perform various controlled multi-electron redox transformations and analysis of the active site and its properties may aid in development of synthetic functional model systems. However, a current limitation in the catalytic response of homogenous catalysts is the high energetic barriers and slow kinetics associated with proton

movement.[24] Therefore the biomimetic approach of incorporating of pendant bases into the secondary coordination sphere of molecular catalysts is promising.

0.3. Molecular Design in Synthetic Catalysts

Molecular catalysts are well-defined and synthetically accessible complexes. Homogenous molecular catalysts have benefits over more commonly used industrial heterogeneous catalysts due to their ease in determining mechanism and greater control over tuning catalytic activity through synthetic modification. The rational design of ligand scaffolds that contain a combination of specific primary and secondary coordination sphere properties would allow for fundamental structure-function relationships to be gained by systematic chemical design of ligands.

In order to mimic biological environments in transition metal complexes, many new ligands have been developed that incorporate functionalities to manage proton inventory in the secondary coordination sphere.[25-46] The resulting complexes often display more selective, efficient, or rapid catalysis than analogs that lack proton relays.[8,47-69] These biomimetic secondary coordination sphere interactions have been exploited in many synthetic systems. Homogenous molecular catalysts containing pendant bases such as carboxylic acid, hydroxyl, amine, pyridyl, and urea units have been shown to facilitate small molecule activation through a PCET mechanistic pathway.[22,70]

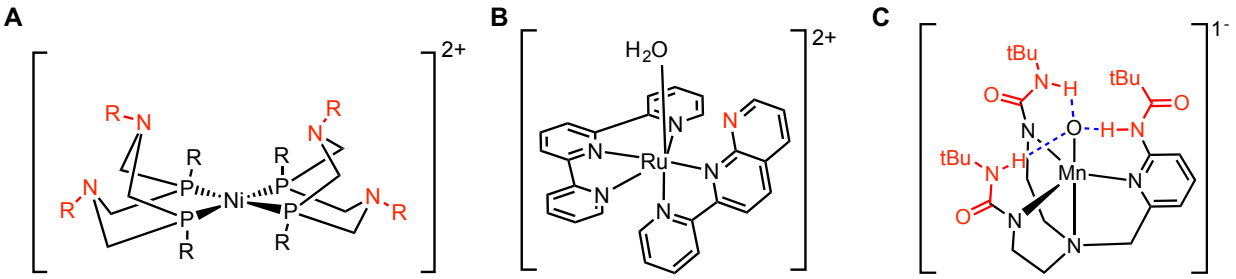

Figure 0.2. Representation of complexes with pendant bases in secondary coordination sphere A) generic nickel complex by Dubois,[8,68] B) ruthenium complex by Thummel and Fujita,[28] and C) manganese complex by Borovik,[62] highlighting pendant bases in red and hydrogen-bonding interactions in blue.

Some examples of biomimetic systems relevant to the enzymes shown in Figure 0.1 are represented in Figure 0.2. Dubois and coworkers have reported a variety of nickel diphosphine (P_2N_2) complexes that are highly active toward the HER or oxidation of hydrogen as a mimic of the pendant amine present in [FeFe]-hydrogenase.[8,68] The mimicry of OER behavior of the OEC active site has been shown with a ruthenium polypyridyl catalyst with a proximal naphthalene unit.[28] Borovik and coworkers have shown ORR activity, similar to cytochrome P450, with manganese complexes incorporating a tripodal ligand containing urea and carboxyamidopyridyl units as hydrogen bond donors.[62]

Incorporation of non-covalent interactions such as intramolecular hydrogen bonds invokes metal ligand cooperativity that typically improves small molecule activation compared to unfunctionalized analogs. Pendant base moieties modulate reactivity by stabilization of transition states in highly energetic intermediates.

0.4. Research Goals

The research presented in this dissertation is a synthetic inorganic chemical approach to energy conversion challenges based on biological design principles. Development of molecular homogenous non-precious metal electrocatalysts for small molecule activation for use in fuel

generation reactions or fuel cells is discussed. Additionally, attempts to expand the scope of reactivity and understand the effect of ligand environment on molecular metal complexes is shown.

Facile ligand modification can provide various molecular complexes with proton relays in the secondary coordination sphere to study simple and efficient proton movement to and from the metal center. Incorporation of proton relays can be utilized to investigate enhanced rates, decrease activation energy, and promote selectivity on a molecular level. Secondary coordination sphere interactions can affect function by promoting more efficient and selective reactions by stabilization of the transition state. Bound substrates can be influenced by intramolecular hydrogen bonding from vicinal hydrogen bond acceptors or donors to dictate function or reactivity.

Chart 0.1. Possible modifications of N_2Py_2 ligand scaffold.

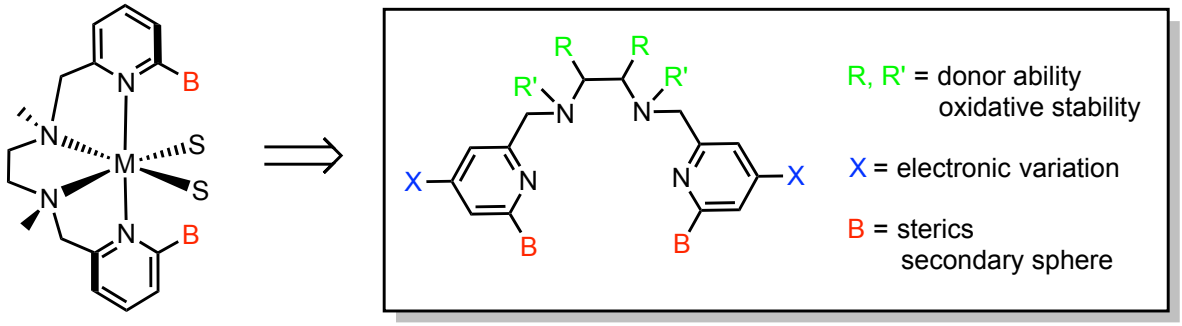

A synthetically tunable neutral multidentate electron rich sigma donor N_2Py_2 ligand scaffold was used to position the pendant base over an open coordination site of a metal complex in an octahedral geometry (Chart 0.1).

Chart 0.2. Series of N_2Py_2 ligands.

No Hydogen Bonding **Hydrogen Bond Donor** **Hydrogen Bond Acceptor**

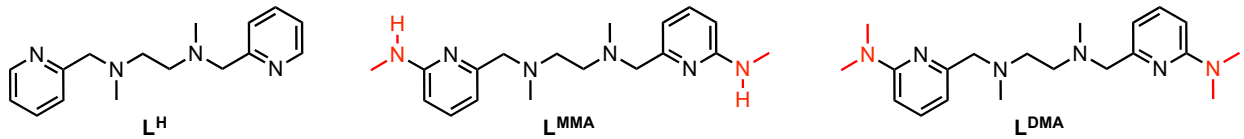

The previously studied L^H ligand (BPMEN = *N*,*N*′-dimethyl-*N*,*N*′-bis(2-pyridylmethyl)ethane-1,2-diamine) has been modified at the 6- and 6′- positions to incorporate a methylamine hydrogen bond donor (L^{MMA}) and dimethylamine hydrogen bond acceptor (L^{DMA}), Chart 0.2. This series was designed to investigate the structure-function effect of incorporating a tethered basic group on the electrocatalytic small molecule activity of copper, cobalt and rhodium complexes.

Characterization of complexes was performed using NMR, UV-Vis, IR, and EPR spectroscopy, MS spectrometry, EA and X-ray diffraction. Electrochemical techniques are used to test for catalytic activity of new catalysts.

0.5. References

(1) Dresselhaus, M. S.; Thomas, I. L. *Nature* **2001**, *414*, 332-337.

(2) Boudghene Stambouli, A.; Traversa, E. *Renew. Sust. Energ. Rev.* **2002**, *6*, 295-304.

(3) Chen, Z.; Higgins, D.; Yu, A.; Zhang, L.; Zhang, J. *Energy Environ. Sci.* **2011**, *4*, 3167-3192.

(4) Faber, M. S.; Jin, S. *Energy Environ. Sci.* **2014**, *7*, 3519-3542.

(5) Jaouen, F.; Proietti, E.; Lefevre, M.; Chenitz, R.; Dodelet, J.-P.; Wu, G.; Chung, H. T.; Johnston, C. M.; Zelenay, P. *Energy Environ. Sci.* **2011**, *4*, 114-130.

(6) Wang, M.; Chen, L.; Sun, L. *Energy Environ. Sci.* **2012**, *5*, 6763-6778.

(7) Arakawa, H.; Aresta, M.; Armor, J. N.; Barteau, M. A.; Beckman, E. J.; Bell, A. T.; Bercaw, J. E.; Creutz, C.; Dinjus, E.; Dixon, D. A.; Domen, K.; DuBois, D. L.; Eckert, J.; Fujita, E.; Gibson, D. H.; Goddard, W. A.; Goodman, D. W.; Keller, J.; Kubas, G. J.; Kung, H. H.; Lyons, J. E.; Manzer, L. E.; Marks, T. J.; Morokuma, K.; Nicholas, K. M.; Periana, R.; Que, L.; Rostrup-Nielson, J.; Sachtler, W. M. H.; Schmidt, L. D.; Sen, A.; Somorjai, G. A.; Stair, P. C.; Stults, B. R.; Tumas, W. *Chem. Rev.* **2001**, *101*, 953-996.

(8) Rakowski Dubois, M.; Dubois, D. L. *Acc. Chem. Res.* **2009**, *42*, 1974-1982.

(9) Appel, A. M.; Bercaw, J. E.; Bocarsly, A. B.; Dobbek, H.; DuBois, D. L.; Dupuis, M.; Ferry, J. G.; Fujita, E.; Hille, R.; Kenis, P. J. A.; Kerfeld, C. A.; Morris, R. H.; Peden, C. H. F.; Portis, A. R.; Ragsdale, S. W.; Rauchfuss, T. B.; Reek, J. N. H.; Seefeldt, L. C.; Thauer, R. K.; Waldrop, G. L. *Chem. Rev.* **2013**, *113*, 6621-6658.

(10) Rountree, E. S.; McCarthy, B. D.; Eisenhart, T. T.; Dempsey, J. L. *Inorg. Chem.* **2014**, *53*, 9983-10002.

(11) Fontecilla-Camps, J. C.; Amara, P.; Cavazza, C.; Nicolet, Y.; Volbeda, A. *Nature* **2009**, *460*, 814-822.

(12) Solomon, E. I.; Chen, P.; Metz, M.; Lee, S.-K.; Palmer, A. E. *Angew. Chem. Int. Ed.* **2001**, *40*, 4570-4590.

(13) Karlin, K. D. *Science* **1993**, *261*, 701-708.

(14) Denisov, I. G.; Makris, T. M.; Sligar, S. G.; Schlichting, I. *Chem. Rev.* **2005**, *105*, 2253-2278.

(15) Fontecilla-Camps, J. C.; Volbeda, A.; Cavazza, C.; Nicolet, Y. *Chem. Rev.* **2007**, *107*, 4273-4303.

(16) Lubitz, W.; Ogata, H.; Rüdiger, O.; Reijerse, E. *Chem. Rev.* **2014**, *114*, 4081-4148.

(17) Cady, C. W.; Crabtree, R. H.; Brudvig, G. W. *Coord. Chem. Rev.* **2008**, *252*, 444-455.

(18) Yocum, C. F. *Coord. Chem. Rev.* **2008**, *252*, 296-305.

(19) Schlichting, I.; Berendzen, J.; Chu, K.; Stock, A. M.; Maves, S. A.; Benson, D. E.; Sweet, R. M.; Ringe, D.; Petsko, G. A.; Sligar, S. G. *Science* **2000**, *287*, 1615-1622.

(20) Martinis, S. A.; Atkins, W. M.; Stayton, P. S.; Sligar, S. G. *J. Am. Chem. Soc.* **1989**, *111*, 9252-9253.

(21) Gerber, N. C.; Sligar, S. G. *J. Am. Chem. Soc.* **1992**, *114*, 8742-8743.

(22) Weinberg, D. R.; Gagliardi, C. J.; Hull, J. F.; Murphy, C. F.; Kent, C. A.; Westlake, B. C.; Paul, A.; Ess, D. H.; McCafferty, D. G.; Meyer, T. J. *Chem. Rev.* **2012**, *112*, 4016-4093.

(23) Dempsey, J. L.; Winkler, J. R.; Gray, H. B. *Chem. Rev.* **2010**, *110*, 7024-7039.

(24) Kramarz, K. W.; Norton, J. R. In *Progress in Inorganic Chemistry*; John Wiley & Sons, Inc.: 2007, p 1-65.

(25) Adelhardt, M.; Chalkley, M. J.; Heinemann, F. W.; Sutter, J.; Scheurer, A.; Meyer, K. *Inorg. Chem.* **2014**, *53*, 2763-2765.

(26) Borovik, A. S. *Acc. Chem. Res.* **2005**, *38*, 54-61.

(27) Bosch, S.; Comba, P.; Gahan, L. R.; Schenk, G. *Inorg. Chem.* **2014**, *53*, 9036-9051.

(28) Boyer, J. L.; Polyansky, D. E.; Szalda, D. J.; Zong, R.; Thummel, R. P.; Fujita, E. *Angew. Chem. Int. Ed.* **2011**, *50*, 12600-12604.

(29) Cheruzel, L. E.; Cui, J.; Mashuta, M. S.; Grapperhaus, C. A.; Buchanan, R. M. *Tetrahedron Lett.* **2011**, *52*, 4771-4774.

(30) Coucouvanis, D. *Inorganic Syntheses*; John Wiley & Sons, Inc.: New York, 2002; Vol. 33.

(31) Gavette, J. V.; Klug, C. M.; Zakharov, L. N.; Shores, M. P.; Haley, M. M.; Johnson, D. W. *Chem. Comm.* **2014**, *50*, 7173-7175.

(32) Hammes, B. S.; Young, J. V. G.; Borovik, A. S. *Angew. Chem. Int. Ed.* **1999**, *38*, 666-669.

(33) Hart, J. S.; Nichol, G. S.; Love, J. B. *Dalton Trans.* **2012**, *41*, 5785-5788.

(34) Kendall, A. J.; Zakharov, L. N.; Gilbertson, J. D. *Inorg. Chem.* **2010**, *49*, 8656-8658.

(35) MacBeth, C. E.; Larsen, P. L.; Sorrell, T. N.; Powell, D.; Borovik, A. S. *Inorg. Chim. Acta* **2002**, *341*, 77-84.

(36) Matson, E. M.; Bertke, J. A.; Fout, A. R. *Inorg. Chem.* **2014**, *53*, 4450-4458.

(37) Moore, C. M.; Szymczak, N. K. *Dalton Trans.* **2012**, *41*, 7886-7889.

(38) Moore, C. M.; Szymczak, N. K. *Chem. Comm.* **2013**, *49*, 400-402.

(39) Shirin, Z.; Hammes, B. S.; Young, V. G.; Borovik, A. S. *J. Am. Chem. Soc.* **2000**, *122*, 1836-1837.

(40) Teets, T. S.; Labinger, J. A.; Bercaw, J. E. *Organometallics* **2013**, *32*, 5530-5545.

(41) Tutusaus, O.; Ni, C.; Szymczak, N. K. *J. Am. Chem. Soc.* **2013**, *135*, 3403-3406.

(42) Yang, J. Y.; Bachmann, J.; Nocera, D. G. *J. Org. Chem.* **2006**, *71*, 8706-8714.

(43) Yang, J. Y.; Liu, S.-Y.; Korendovych, I. V.; Rybak-Akimova, E. V.; Nocera, D. G. *ChemSusChem* **2008**, *1*, 941-949.

(44) Yang, J. Y.; Nocera, D. G. *Tetrahedron Lett.* **2008**, *49*, 4796-4798.

(45) Yeh, C.-Y.; Chang, C. J.; Nocera, D. G. *J. Am. Chem. Soc.* **2001**, *123*, 1513-1514.

(46) Zinn, P. J.; Powell, D. R.; Day, V. W.; Hendrich, M. P.; Sorrell, T. N.; Borovik, A. S. *Inorg. Chem.* **2006**, *45*, 3484-3486.

(47) Ahn, S. T.; Bielinski, E. A.; Lane, E. M.; Chen, Y.; Bernskoetter, W. H.; Hazari, N.; Palmore, G. T. R. *Chem. Comm.* **2015**, *51*, 5947-5950.

(48) Bullock, R. M.; Appel, A. M.; Helm, M. L. *Chem. Comm.* **2014**, *50*, 3125-3143.

(49) Carver, C. T.; Matson, B. D.; Mayer, J. M. *J. Am. Chem. Soc.* **2012**, *134*, 5444-5447.

(50) Costentin, C.; Drouet, S.; Robert, M.; Savéant, J.-M. *Science* **2012**, *338*, 90.

(51) Costentin, C.; Passard, G.; Robert, M.; Savéant, J.-M. *J. Am. Chem. Soc.* **2014**, *136*, 11821-11829.

(52) Das, P.; Ho, M.-H.; O'Hagan, M.; Shaw, W. J.; Morris Bullock, R.; Raugei, S.; Helm, M. L. *Dalton Trans.* **2014**, *43*, 2744-2754.

(53) Dogutan, D. K.; McGuire, R.; Nocera, D. G. *J. Am. Chem. Soc.* **2011**, *133*, 9178-9180.

(54) Dogutan, D. K.; Stoian, S. A.; McGuire, R.; Schwalbe, M.; Teets, T. S.; Nocera, D. G. *J. Am. Chem. Soc.* **2011**, *133*, 131-140.

(55) Galan, B. R.; Schöffel, J.; Linehan, J. C.; Seu, C.; Appel, A. M.; Roberts, J. A. S.; Helm, M. L.; Kilgore, U. J.; Yang, J. Y.; DuBois, D. L.; Kubiak, C. P. *J. Am. Chem. Soc.* **2011**, *133*, 12767-12779.

(56) Jacobsen, G. M.; Yang, J. Y.; Twamley, B.; Wilson, A. D.; Bullock, R. M.; Rakowski DuBois, M.; DuBois, D. L. *Energy Environ. Sci.* **2008**, *1*, 167-174.

(57) Matson, B. D.; Carver, C. T.; Von Ruden, A.; Yang, J. Y.; Raugei, S.; Mayer, J. M. *Chem. Comm.* **2012**, *48*, 11100-11102.

(58) Matson, E. M.; Park, Y. J.; Fout, A. R. *J. Am. Chem. Soc.* **2014**, *136*, 17398-17401.

(59) McGuire Jr, R.; Dogutan, D. K.; Teets, T. S.; Suntivich, J.; Shao-Horn, Y.; Nocera, D. G. *Chem. Sci.* **2010**, *1*, 411-414.

(60) Moore, C. M.; Szymczak, N. K. *Chem. Sci.* **2015**, *6*, 3373-3377.

(61) Seu, C. S.; Appel, A. M.; Doud, M. D.; DuBois, D. L.; Kubiak, C. P. *Energy Environ. Sci.* **2012**, *5*, 6480-6490.

(62) Shook, R. L.; Peterson, S. M.; Greaves, J.; Moore, C.; Rheingold, A. L.; Borovik, A. S. *J. Am. Chem. Soc.* **2011**, *133*, 5810-5817.

(63) Solis, B. H.; Hammes-Schiffer, S. *Inorg. Chem.* **2014**, *53*, 6427-6443.

(64) Warren, J. J.; Mayer, J. M. *Biochemistry* **2015**, *54*, 1863-1878.

(65) Weiss, C. J.; Das, P.; Miller, D. L.; Helm, M. L.; Appel, A. M. *ACS Catal.* **2014**, *4*, 2951-2958.

(66) Weiss, C. J.; Wiedner, E. S.; Roberts, J. A. S.; Appel, A. M. *Chem. Comm.* **2015**, *51*, 6172-6174.

(67) Yang, J. Y.; Bullock, R. M.; Dougherty, W. G.; Kassel, W. S.; Twamley, B.; DuBois, D. L.; Rakowski DuBois, M. *Dalton Trans.* **2010**, *39*, 3001-3010.

(68) Yang, J. Y.; Bullock, R. M.; DuBois, M. R.; DuBois, D. L. *MRS Bulletin* **2011**, *36*, 39-47.

(69) Yang, J. Y.; Nocera, D. G. *J. Am. Chem. Soc.* **2007**, *129*, 8192-8198.

(70) Zhao, M.; Wang, H.-B.; Ji, L.-N.; Mao, Z.-W. *Chem. Soc. Rev.* **2013**, *42*, 8360-8375.

CHAPTER 1

N_2Py_2 Ligands with Hydrogen-Bonding Pendant Bases in the Secondary Coordination Sphere: Design, Synthesis and Characterization

Portions of this chapter have been published:
Khosrowabadi Kotyk, J. F.; Ziller, J. W.; Yang, J. Y. *J. Coord. Chem.*, 2016, *69*, 1990-2002.

1.1. Motivation and Specific Aims

The previously studied L^H ligand (BPMEN = *N*,*N*′-dimethyl-*N*,*N*′-bis(2-pyridylmethyl)ethane-1,2-diamine) has been modified at the 6- and 6′- positions to incorporate a hydrogen bond donor (L^{MMA}) and hydrogen bond acceptor (L^{DMA}). Neutral tetradentate diamino–dipyridal ligands (N_2Py_2) containing moieties capable of hydrogen-bonding have been synthesized to improve understanding of the structure-function relationship of secondary sphere interactions in transition metal complexes. Ligand design using pre-positioned basic functionalities has been shown to facilitate multi-proton redox reactivity. The multifunctional ligand framework attempts to impart diverse reactivity depending on the nature of the ligand to mimic enzyme active sites.

1.2. Background

Neutral tetradentate diamino–dipyridal ligands (N_2Py_2) have commonly been used as a scaffold for transition metal-mediated catalysis in a variety of different reactions, including olefin epoxidation[1-6] and alkane,[7-15] alkyne,[16] sp^2 C–H bond,[17] alcohol,[18] and water oxidation.[19-21] Although the N_2Py_2 ligand scaffold has primarily been studied on iron systems[1,3-17,19-27] examples of the L^H ligand (BPMEN = *N*,*N*′-dimethyl-*N*,*N*′-bis(2-pyridylmethyl)ethane-1,2-diamine) and modified derivatives have been used on vanadium,[28] chromium,[29] manganese,[2,23,26,30-34] nickel,[23,35] cobalt,[23,36,37] copper,[23,38-42] zinc,[23,43] gallium,[36] and ruthenium[18,44] for an assortment of reactivity ranging from molecular machines to drug release agents. The strong σ-donating ability of nitrogens in the ligand scaffold is desirable because they can support high-valent oxidation states.

The design of functional mimics of natural systems through the incorporation of pendant bases in the secondary coordination sphere of transition metal complexes has been shown to improve reactivity for small molecule activation. When the pendant base is poised over the open

coordination center the activity or selectivity is improved compared to their unfunctionalized parent ligands or if pendant base is distant from the metal center.[45-49] The presence of pendant bases can act as proton reservoirs or stabilize highly energetic intermediates through hydrogen-bonding interactions.

Chart 1.1. Series of N_2Py_2 Ligands.

No Hydogen Bonding **Hydrogen Bond Donor** **Hydrogen Bond Acceptor**

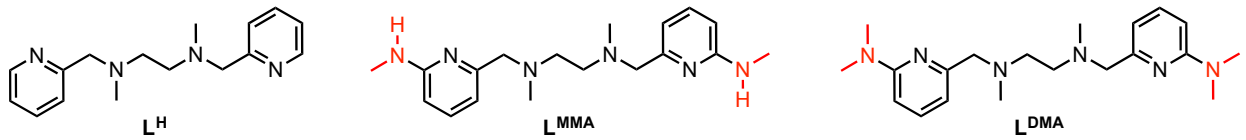

The utility and oxidative stability of the N_2Py_2 ligand scaffold and possibility of modification of the pyridine rings made them desirable candidates to incorporate cooperative groups poised over the open coordination site in an octahedral complex. A series of ligands was developed to study changes in reactivity using a basic functional group capable of hydrogen-bonding. These ligands employ hydrogen-bonding interactions to direct substrate coordination or stabilize intermediates on the path to desired products. The L^H ligand has been modified to incorporate methylamine and dimethylamine groups at the 6- and 6′- positions of the pyridine rings (Chart 1.1). The ligand with pendant methylamines (L^{MMA}) is designed to behave as a hydrogen bond donor and would ideally be useful for reduction reactions. The hydrogen bond acceptor dimethylamine ligand (L^{DMA}) is best suited for oxidation reactions. Additionally, although amines are generally used as Brönsted bases, protonated pendant bases can also serve as effective proton donors to coordinated substrates.[48,50-52] In order to investigate the effect of the pendant bases, the congener without pendant bases (L^H) was also synthesized.

The synthesis L^{DMA} has been previously reported.[53] The prior ligand preparation required multiple steps and the use of an expensive starting material. To facilitate additional studies with this ligand, an improved two-step preparation was developed using cheaper and more accessible precursors to furnish the ligand in higher yield.[54]

1.3. Results and Discussion

1.3.1. Synthesis of Pendant Base Ligands

Formulation and purity of the ligands were confirmed by HR-MS and ^{1}H and ^{13}C NMR spectroscopy, respectively.

Scheme 1.1. Synthesis of L^{H} ligand using 2-(chloromethyl)pyridine.

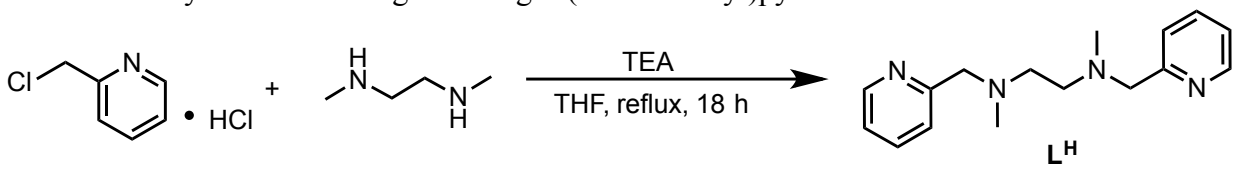

The synthesis of L^{H}, which contains no pendant base functionalities, has been previously reported.[42] As shown in Scheme 1.1, nucleophilic substitution under basic conditions using N,N′-dimethylethylenediamine and 2-(chloromethyl)pyridine provides L^{H} in 91% yield.

Scheme 1.2. Synthesis of L^{MMA} ligand using precursor *tert*-butyl (6-formylpyridin-2-yl)(methyl)carbamate[55].

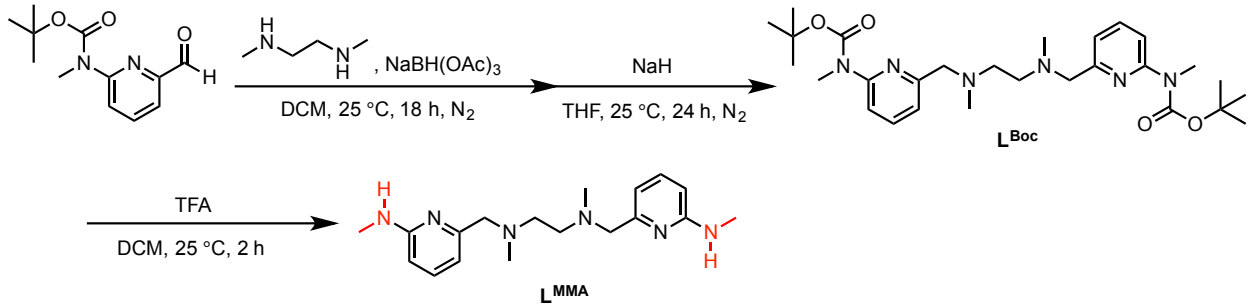

Preparation of L^{MMA} through one-pot reductive amination with N,N′-dimethylethylenediamine and precursor *tert*-butyl (6-formylpyridin-2-yl)(methyl)carbamate[55] afforded the Boc-protected ligand L^{Boc}. Deprotection of L^{Boc} with trifluoroacetic acid and purification using automated reversed phase column chromatography gave the ligand L^{MMA} in 33% yield over three steps from 6-bromo-2-pyridinecarboxaldehyde, Scheme 1.2.

Scheme 1.3. Synthesis of L^{DMA} ligand using 6-bromo-2-pyridinecarboxaldehyde.[54]

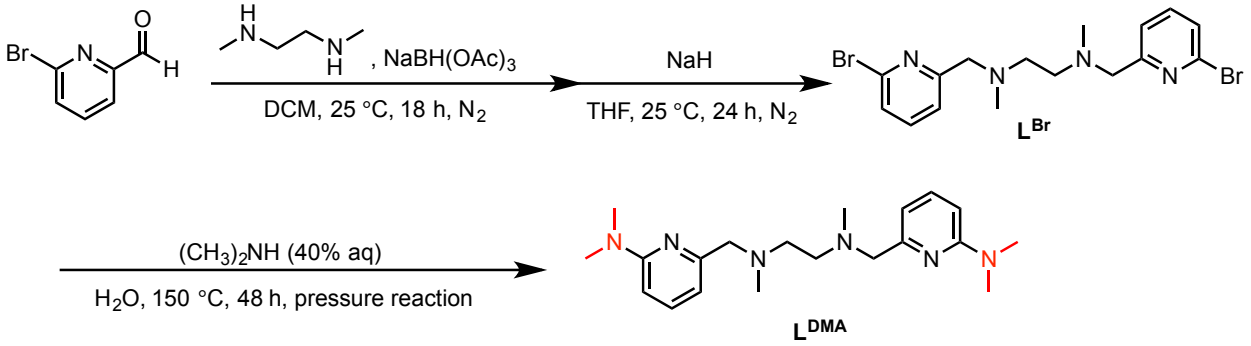

The synthesis of L^{DMA} has been previously reported.[53] However, the prior procedure required the expensive and not readily available precursor 6-(dimethylamino)picolinaldehyde. Independent preparation of the precursor in three steps using a published procedure[57] (64% yield) gave the ligand in 33% yield overall.

In order to facilitate ligand preparation, an improved route to L^{DMA} was developed (Scheme 1.3).[54] One-pot reductive amination using N,N′-dimethylethylenediamine and 6-bromo-2-formylpyridine followed by deprotonation yields L^{Br} containing bromo- functionalities in the 6- and 6′- positions. Nucleophilic aromatic substitution using aqueous dimethylamine under pressure affords L^{DMA}. This preparation uses inexpensive and more readily available reagents. The yield is increased to 85%, offering significant improvements over the previously published synthesis.

1.3.2. Physical Characterization of Ligands

Cyclic Voltammetry

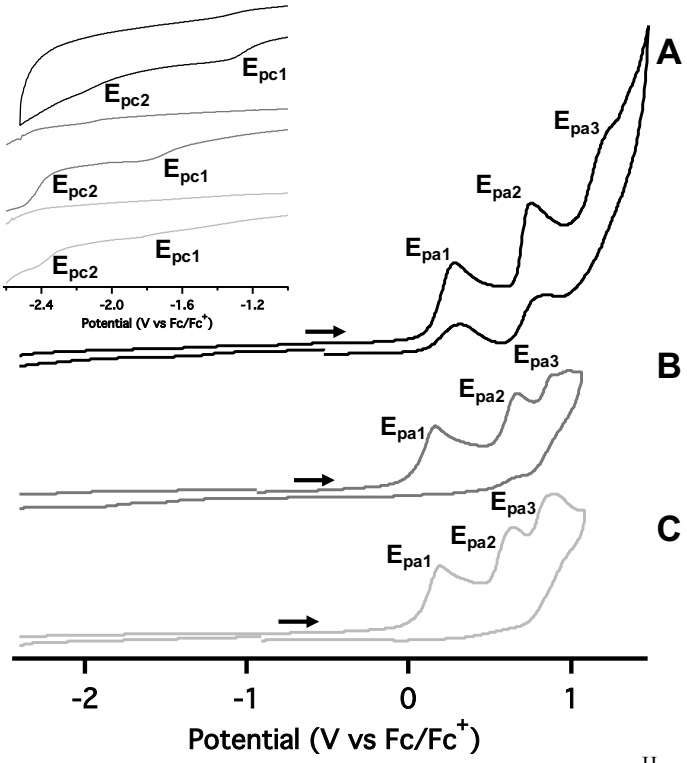

Figure 1.1. Full scan cyclic voltammograms of 1 mM solutions of A) L^{H}, B) L^{MMA}, and C) L^{DMA} in 0.10 M Bu_4NBF_4 in CH_3CN at 100 mV/s. Inset: Zoomed in reductive region.

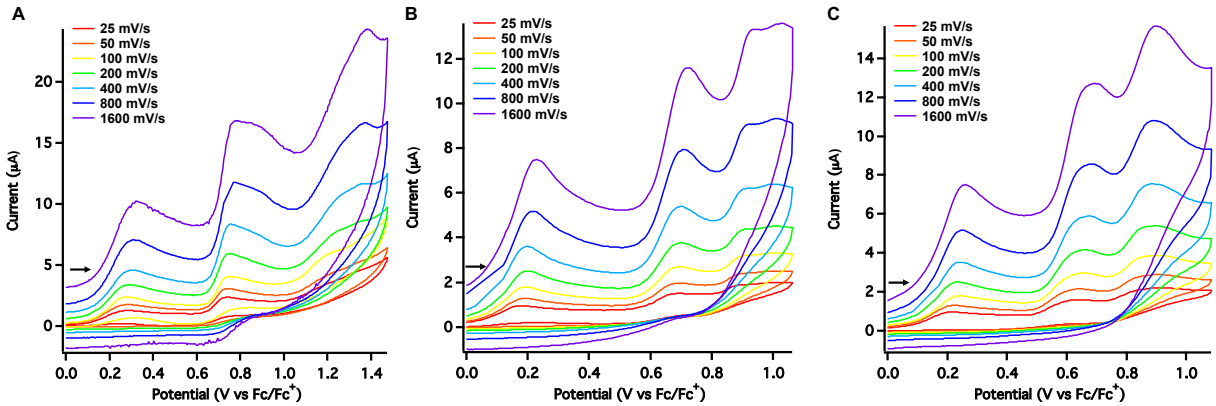

Figure 1.2. Scan rate dependent cyclic voltammograms of oxidative events of 1.0 mM solutions of A) L^{H}, B) L^{MMA}, and C) L^{DMA} in 0.10 M Bu_4NBF_4 in CH_3CN at scan rates 25–1600 mV/s.

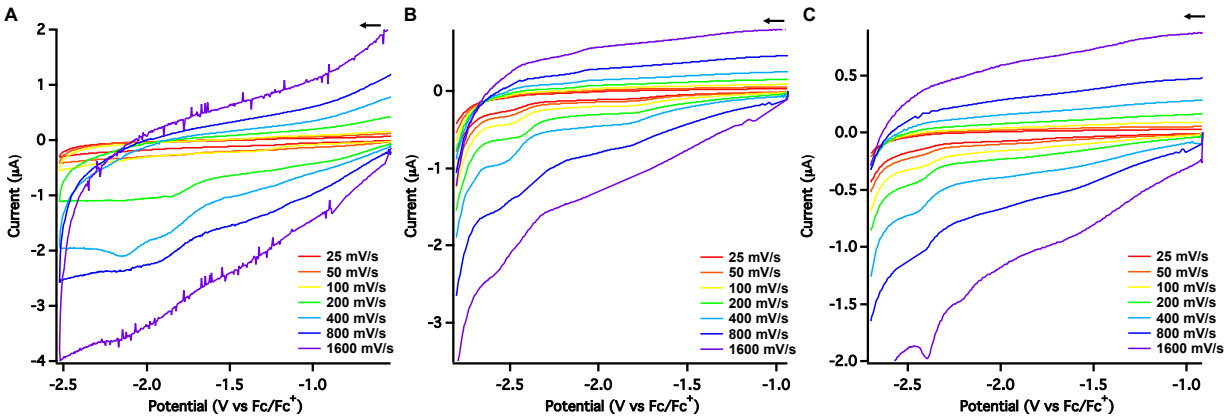

Figure 1.3. Scan rate dependent cyclic voltammograms of reductive events of 1.0 mM solutions of A) L^{H}, B) L^{MMA}, and C) L^{DMA} in 0.10 M Bu_4NBF_4 in CH_3CN at scan rates 25–1600 mV/s.

The full scan cyclic voltammograms for all three ligands are shown in Figure 1.1. All tabulated data for oxidation and reduction events (E_{pa} and E_{pc}, respectively) is shown in Table 1.1.

Cyclic voltammetry of L^{H} is consistent with previously published data;[40] however, the reported values are not corrected for the ferrocene/ferrocenium couple. Therefore, the comparison between the data presented here is an estimate. Additionally, they attribute the solvent reduction peaks incorrectly to the ligand. There are three irreversible oxidative peaks (E_{pa} = 0.28, 0.66, and 1.22 V) and two irreversible reductive peaks (E_{pc} = −1.34 and −2.19 V). All five features remain irreversible at all scan rates tested, 25–1600 mV/s (Figure 1.2A and 1.3A).

The L^{MMA} ligand also exhibits three oxidative peaks (E_{pa} = 0.16, 0.67, and 0.87 V) which are irreversible at all scan rates tested (25–1600 mV/s) (Figure 1.2B). The reduction peaks are E_{pc} = −1.83 and −2.51 V and remain irreversible at all scan rates tested, 25–1600 mV/s (Figure 1.3B).

Three irreversible oxidative events and two irreversible reductions are present for the L^{DMA} ligand, all of which are irreversible at all scan rates tested, 25–1600 mV/s (Figure 1.2C and 1.3C). The oxidative events are at E_{pa} = 0.27, 0.65, and 0.85 V while the reduction events are E_{pc} = −1.85 and −2.43 V.

Table 1.1. Electrochemical values for the oxidation events (E_{pa}) and reduction events (E_{pc}) of L^{H}, L^{MMA}, and L^{DMA} in CH_3CN at 100 mV/s.

	Potential (V vs Fc)		
	L^{H}	**L^{MMA}**	**L^{DMA}**
E_{pa1}	0.28	0.16	0.27
E_{pa2}	0.66	0.67	0.65
E_{pa3}	1.22	0.87	0.85
E_{pc1}	-1.34	-1.83	-1.85
E_{pc2}	-2.19	-2.51	-2.43

When comparing the oxidations of all three ligands, the first two events (E_{pa1} and E_{pa2}) occur at similar potentials. The E_{pa1} and E_{pa2} may be related to the oxidation of the ethylenediamine backbone of the ligand which should be around the same potential for all three ligands due to the similarity in structure.[58-60] E_{pa3} may be linked to the electron rich nature of the ring because it is more variable across the series and occurs at lower potentials for the ligands with electron donating amines present (L^{MMA} and L^{DMA}). On a related note, the more electron donating nature of these methylamine and dimethylamine groups makes the ligands more difficult to reduce, the E_{pc1} and E_{pc2} occur at more negative potentials for L^{MMA} and L^{DMA} compared to L^{H}.

Ultraviolet-Visible Spectroscopy

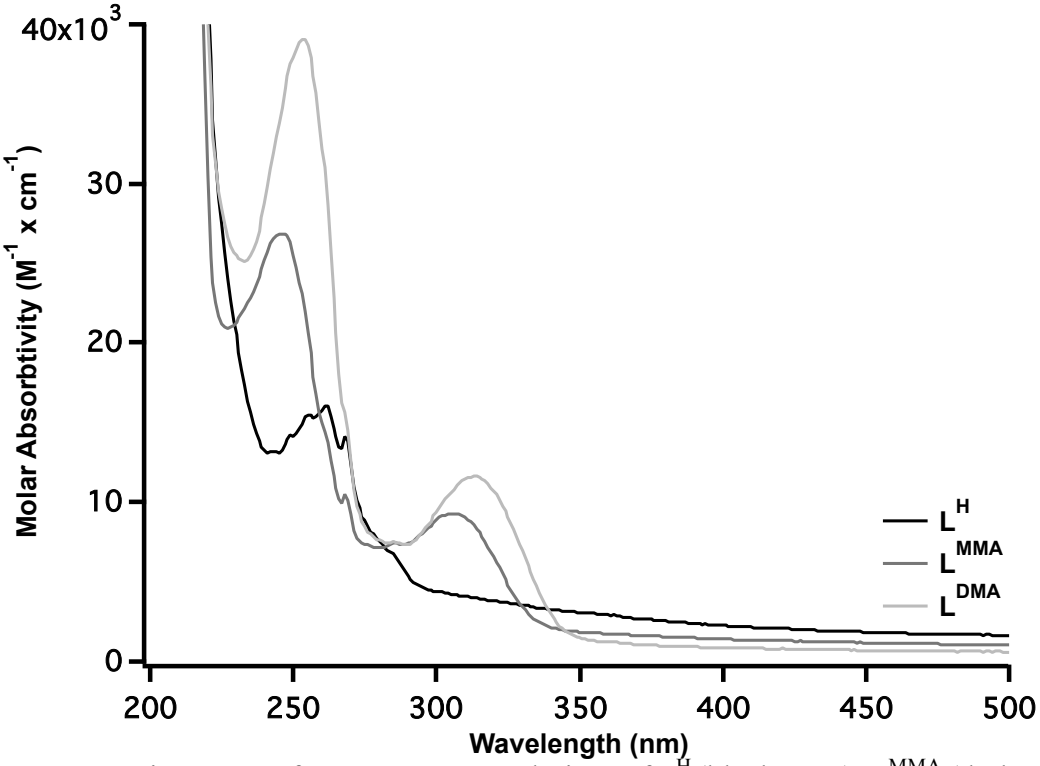

Figure 1.4. UV-Vis spectra of 20 μM CH_3CN solutions of L^H (black trace), L^{MMA} (dark gray trace), and L^{DMA} (light gray trace).

Table 1.2. Maximum wavelength (λ_{max}) and molar absorptivity (ε) values for L^H, L^{MMA}, and L^{DMA} determined by UV-Vis.

	π–π*		**π–π***	
	λ_{max}(nm)	**ε ($M^{-1} \times cm^{-1}$)**	**λ_{max}(nm)**	**ε ($M^{-1} \times cm^{-1}$)**
L^H	262	6,600	-	-
L^{MMA}	246	6,800	306	170,000
L^{DMA}	254	30,000	313	9,900

UV–Vis spectra of all ligands were taken in CH_3CN solutions and are shown in Figure 1.4. The primary absorption band, observed for all three ligands, has a maximum wavelength (λ_{max}) range from 246–262 nm and is attributed to the pyridyl *π*–*π** transitions. The secondary absorption band (λ_{max} around 306–313 nm) occurs only for the amine substituted ligands L^{MMA} and L^{DMA} and is due the tautomeric 2-iminopyridine structure possible for heteroatom substituted pyridines.[61,62]

The primary absorption band for L^{MMA} and L^{DMA} display a hypsochromic shift to shorter wavelengths compared to L^{H}. The methylamine and dimethylamine groups of L^{MMA} and L^{DMA} likely promote electron donation into the pyridine ring therefore changing the HOMO-LUMO gap (π–π*) and shifts the absorption maxima. L^{DMA} has the longest λ_{max}, of the amine substituted ligands, for both the primary and secondary absorption bands. Thus, it has the smallest energy gap and requires the least energy for electronic excitation, Table 1.2.

Infrared Spectroscopy

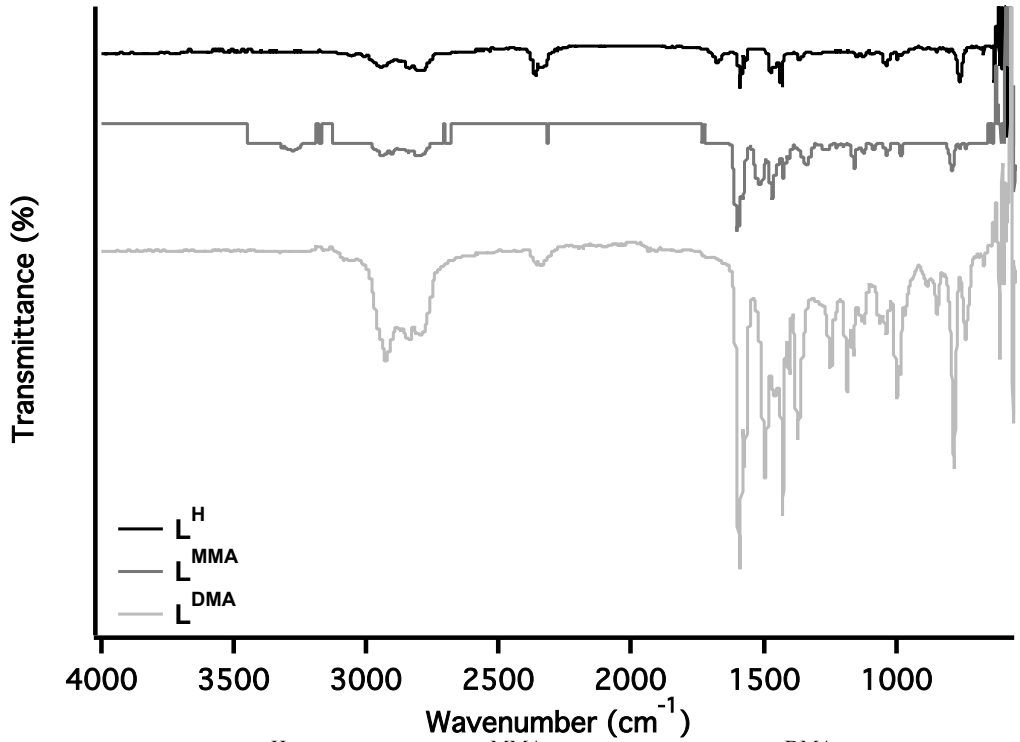

Figure 1.5. IR spectra of L^{H} (black trace), L^{MMA} (dark gray), and L^{DMA} (light gray).

Solid state infrared spectra of the ligands L^{H}, L^{MMA}, and L^{DMA} are shown in Figure 1.5. The features common among all three ligands are the C–H stretching frequencies around the 3000 cm^{-1} region for both sp^2 and sp^3 hybridized carbons indicative of the alkane and aromatic functionalities. A major difference between the ligand structures can be seen via the N–H

stretching frequency of the L^{MMA} ligand, which contains a secondary amine and exhibits a stretching frequency at 3270 cm^{-1} which is within normal range for amines.

1.4. Conclusion

A series of tetradentate N_2Py_2 ligands have been synthesized and fully characterized. The synthesis of L^{MMA} has been shown for the first time in three steps from 6-bromo-2-pyridinecarboxaldehyde. An improved preparation for L^{DMA} was developed.[54] This synthetic route uses cheaper and more readily available precursors with fewer steps and greater overall yield.

Incorporation of methylamine and dimethylamine moieties allows for hydrogen-bonding interactions and protonation/deprotonation of substrates within close range to the coordination environment of the metal center. The roles of a hydrogen bond donor (L^{MMA}) and hydrogen bond acceptor (L^{DMA}) and their respective proton transfer behavior in reduction and oxidation reactions will be investigated in Chapter 2 and 3.

1.5. Experimental Details

General Experiment Considerations

All reagents were purchased from commercial suppliers and used without further purification. The precursor *tert*-butyl (6-formylpyridin-2-yl)(methyl)carbamate was synthesized according to literature procedures.[55] Unless otherwise noted, all organic chemical manipulations were performed in air. Compounds were purified via flash column chromatography using Sorbent Technologies 60 Å, 230–400 mesh silica gel, unless otherwise stated. Anhydrous solvents were sparged with UHP argon (Praxair) and passed through columns containing Q-5 and molecular sieves before use.

Reversed Phase Column Chromatography: In the case of automated reversed phase column chromatography, a Teledyne Isco CombiFlash® Rf+ PurIon purification system controlled by PeakTrak® Software was used. The stationary phase was an octadecyl (C18) derivatized silica gel (60 Å) column while the eluent was H_2O/CH_3CN (90:10 to 0:100) containing 0.1 % trifluoroacetic acid (TFA). The eluent was monitored with a single channel UV detector at a wavelength of 254 nm and 280 nm. The desired fractions were basified with saturated $NaHCO_3$ solution (aq) and extracted with DCM. Thin-layer chromatography (TLC) was conducted with E. Merck silica gel 60 F 254 pre-coated plates, (0.25 mm) and visualized by exposure to UV light (254 nm).

Physical Methods

Nuclear Magnetic Resonance (NMR) Spectroscopy: ^{1}H NMR spectra were recorded on 500 MHz on Bruker instruments. ^{1}H NMR spectra chemical shifts are reported as δ values in ppm relative to residual protio solvent: $CDCl_3$ (7.26 ppm), CD_3CN (1.94 ppm). Proton NMR data are reported as follows: chemical shift (δ ppm), multiplicity (s = singlet, d = doublet, t = triplet, q = quartet), coupling constants (J) in Hertz (Hz), and integration. Multiplets (m) are reported over the range (ppm). Data for ^{13}C NMR spectra are decoupled proton spectra and are reported in terms of chemical shift (δ ppm).

Mass Spectrometry (MS): High resolution mass spectra (HR-MS) and electrospray ionization mass spectra (ESI-MS) were obtained on a Micromass LCT and collected at the University of California-Irvine Mass Spectrometry Facility.

Ultraviolet-Visible (UV-Vis) Spectroscopy: Ultraviolet-Visible spectra were collected as 10 μM solutions in 3 mL CH_3CN in a 1 cm quartz cuvette or as 1mM solutions in 0.3 mL CH_3CN in a

1 mm quartz cuvette using an Agilent Technologies Cary 60 UV–vis spectrometer. A Bruker SMART APEX II diffractometer was used to collect all the data.

Infrared (IR) Spectroscopy: Infrared spectra were collected using a Thermo Scientific Nicolet iS5 spectrometer with an iD5 ATR attachment in a nitrogen filled glovebox. The sample was prepared by evaporating an acetonitrile solution of the compound onto an ATR crystal, unless otherwise noted.

Cyclic Voltammetry (CV): Electrochemical experiments were performed under an atmosphere of nitrogen in a solution containing 0.1 M Bu_4NBF_4 or Bu_4NPF_6 in acetonitrile. Glassy carbon was used as the working and auxiliary electrode and a silver wire was used as a pseudoreference electrode. Ferrocene was used as an internal standard, and all potentials are referenced to the ferrocenium/ferrocene couple. Cyclic voltammetry experiments were performed with a Pine Wavedriver 10 or 20 potentiostat and Pine Aftermath software version 1.4.7881.

Synthesis of Ligands

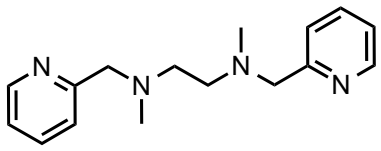

N^1,N^2-dimethyl-N^1,N^2-bis(pyridin-2-ylmethyl)ethane-1,2-diamine (L^H). 2-(chloromethyl)pyridine hydrochloride (1.5 g, 9.1 mmol) was added to a solution of *N,N'*-dimethylethylenediamine (0.49 mL, 0.40 g, 4.6 mmol) in 15 mL dry THF. Triethylamine (2.6 mL, 1.8 g, 18 mmol) was added and the reaction solution was stirred at reflux for 18 h. The mixture was cooled to room temperature, then in an ice bath, and filtered. The light pink filtrate was diluted with CH_2Cl_2 and washed with 1M KOH. The aqueous layer was extracted with 3 X 5 mL portions of DCM, and the organics were combined, dried over $MgSO_4$, and filtered. Removal of the solvent afforded L^H as a dark brown oil (1.1 g, 4.6 mmol, 91% yield). ^{1}H NMR ($CDCl_3$) δ

= 8.51 (m, 2H, Py-H), 7.61 (m, 2H, Py-H), 7.39 (d, J = 10 Hz, 2H, Py-H), 7.12 (m, 2H, Py-H), 3.66 (s, 4H, -CH_2), 2.62 (s, 4H, -C_2H_4), 2.25 (s, 6H, N-CH_3). Spectral data consistent with previously reported literature values.[42] ^{1}H NMR spectrum of L^H in CD_3CN shown below for comparison to diamagnetic metal complexes.

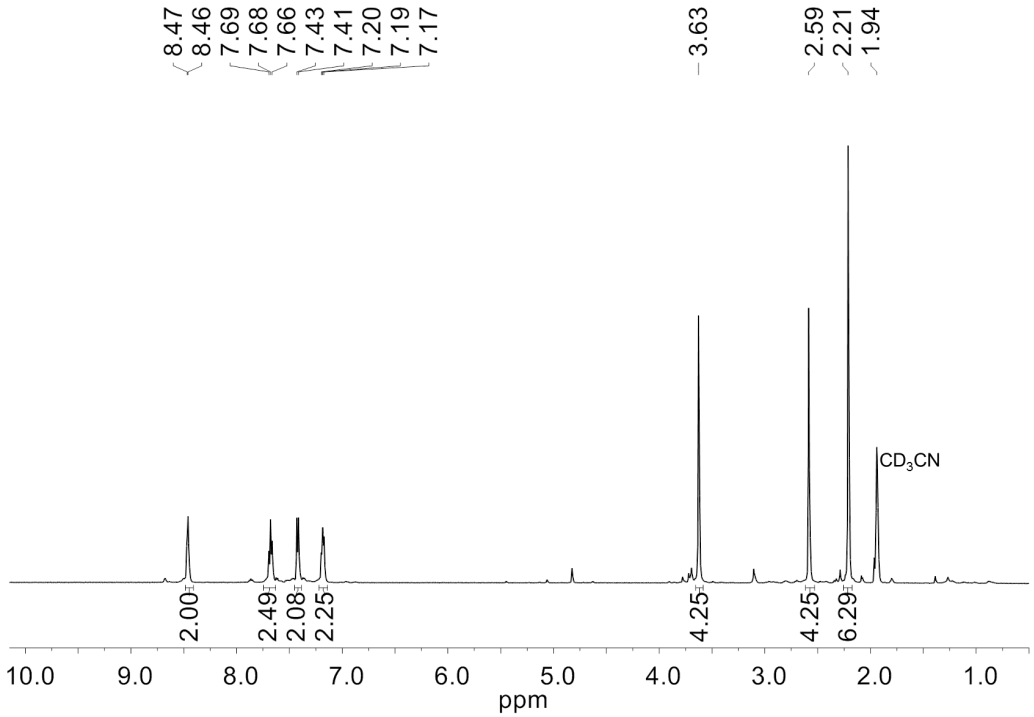

Figure 1.6. ^{1}H NMR of L^H in CD_3CN.

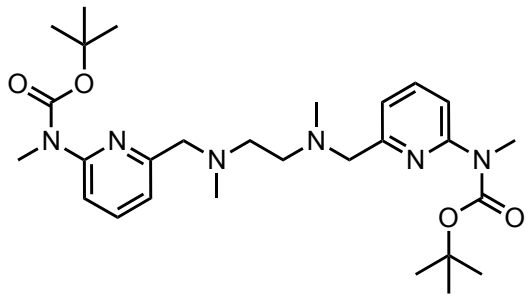

di-*tert*-butyl (((ethane-1,2-diylbis(methylazanediyl))bis(methylene))bis(pyridine-6,2-diyl))bis(methylcarbamate) (L^{Boc}). A solution of sodium triacetoxyborohydride (4.5 g, 21 mmol) and *tert*-butyl (6-formylpyridin-2-yl)(methyl)carbamate[55] (1.9 g, 8.0 mmol) in dry dichloromethane (20 mL) was

treated with *N*,*N*′-dimethylethylenediamine (0.57 mL, 0.47 g, 5.3 mmol) and the mixture was stirred at 25 °C under nitrogen for 18 h. The resulting mixture was quenched with 20 mL sat. aqueous sodium bicarbonate. The organic layer was removed and the aqueous layer was extracted 3 × 20 mL portions of dichloromethane. The organic layers were combined, dried over $MgSO_4$, filtered and concentrated to afford a brown oil (2.5 g, 4.7 mmol). The protonated di-*tert*-butyl (((ethane-1,2-diylbis(methylazanediyl))bis(methylene))bis(pyridine-6,2-diyl))bis(methylcarbamate) obtained above was dissolved in 20 mL dry tetrahydrofuran. Sodium hydride (60% dispersion in mineral oil, 0.42 g, 10.0 mmol) was added and the resulting solution was stirred at 25 °C under nitrogen for 24 h. The solution was concentrated to give a crude brown oil. The crude oil was purified by flash column chromatography (ethyl acetate/methanol, 90:10) to obtain $\mathbf{L^{Boc}}$ as a yellow oil (1.4 g, 2.7 mmol, 67% yield). ^{1}H NMR ($CDCl_3$): δ = 7.57 (t, $^3J_{HH}$ = 10.0 Hz, 2H, Ar–*H*), 7.47 (d, $^3J_{HH}$ = 10.0 Hz, 2H, Ar–*H*), 7.11 (d, $^3J_{HH}$ = 10.0 Hz, 2H, Ar–*H*), 3.68 (s, 4H, Ar–C*H*$_2$–N–), 3.37 (s, 6H, BOC–N–C*H*$_3$), 2.67 (s, 4H, –C*H*$_2$–C*H*$_2$–), 2.33 (s, 6H, –N–C*H*$_3$), 1.50 (s, 18H, –O–C–(C*H*$_3$)$_3$); ^{13}C NMR ($CDCl_3$): δ = 154.67, 154.60, 137.40, 118.66, 117.63, 81.11, 63.59, 55.10, 42.90, 34.45, 28.47; HR-MS (ESI) *m/z* calcd for $C_{28}H_{44}N_6O_4Na$ ($[M+Na]^+$) 551.3322, found 551.3344.

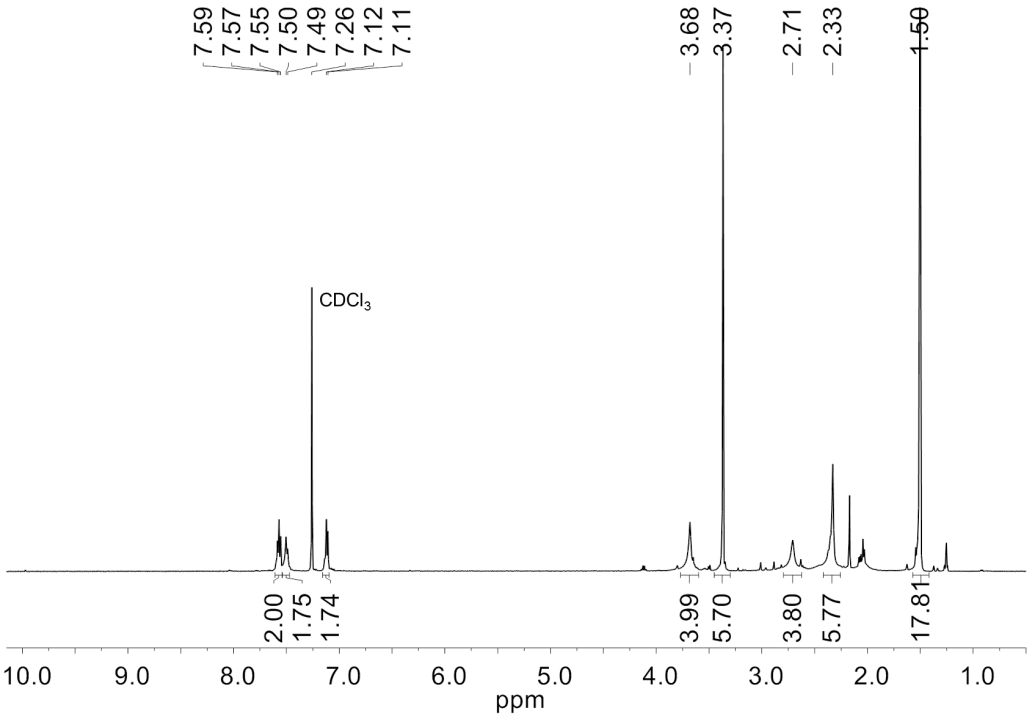

Figure 1.7. ^{1}H NMR of L^{Boc} in $CDCl_3$.

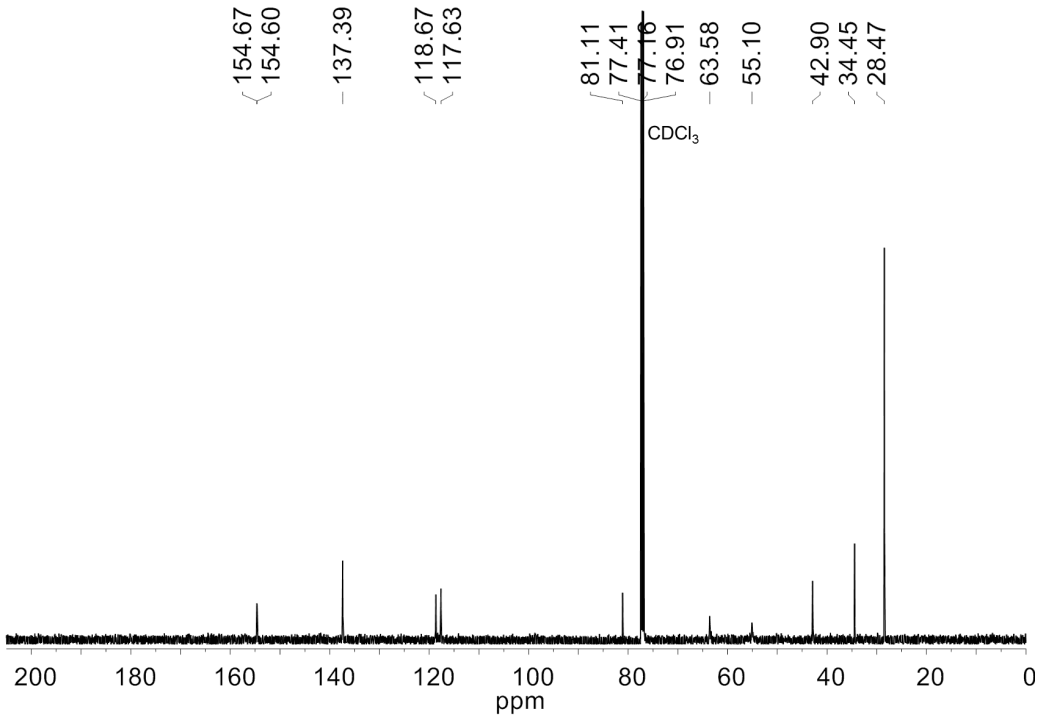

Figure 1.8. $^{13}C\{^{1}H\}$ NMR of L^{Boc} in $CDCl_3$.

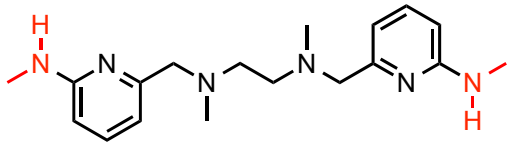

N^1,N^2-dimethyl-N^1,N^2-bis((6-(methylamino)pyridin-2-yl)methyl)ethane-1,2-diamine ($\mathbf{L}^{\mathbf{MMA}}$). Trifluoroacetic acid (TFA) (7.9 mL, 6.1 g, 53 mmol) was added to a solution of $\mathbf{L}^{\mathbf{Boc}}$ (1.4 g, 2.6 mmol) in DCM (10 mL) at 0 °C, then stirred at 25 °C for 6 h. The resulting mixture was quenched with 20 mL sat. aqueous sodium bicarbonate. The organic layer was removed and the aqueous layer was extracted 3 × 20 mL portions of dichloromethane. The organic layers were combined, dried over $MgSO_4$, filtered and concentrated to afford a crude brown oil. The crude oil was purified using automated reversed phase column to obtain $\mathbf{L}^{\mathbf{MMA}}$ as an orange oil (0.67 g, 49% yield). ^{1}H NMR ($CDCl_3$): δ = 7.40 (t, $^3J_{HH}$ = 10.0 Hz, 2H, Ar-*H*), 6.66 (d, $^3J_{HH}$ = 10.0 Hz, 2H, Ar–*H*), 6.24 (d, $^3J_{HH}$ = 10.0 Hz, 2H, Ar–*H*), 3.51 (s, 4H, Ar-CH_2–N–), 2.87 (s, 6H, –NH–CH_3), 2.65 (s, 4H, –CH_2–CH_2–), 2.28 (s, 6H, –N–CH_3); ^{13}C{^{1}H} NMR ($CDCl_3$): δ = 159.53, 155.76, 138.31, 112.42, 104.12, 63.22, 54.42, 42.60, 29.31; HR-MS (ESI) *m/z* calcd for $C_{18}H_{28}N_6Na$ ($[M+Na]^+$) 351.2273, found 351.2261.

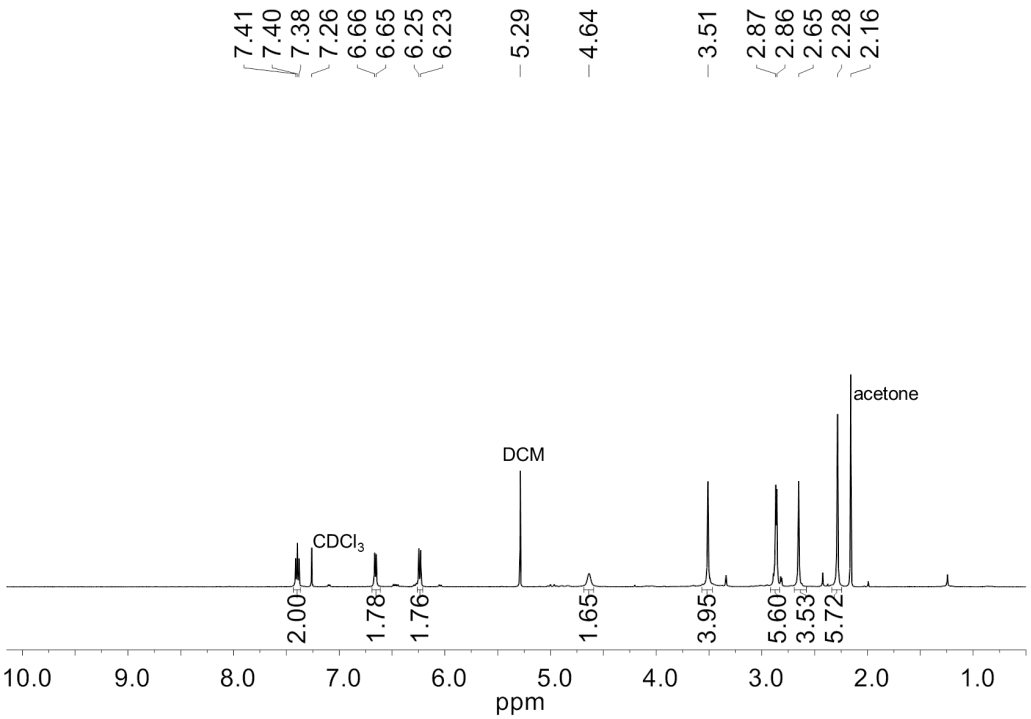

Figure 1.9. ^{1}H NMR of L^{MMA} in $CDCl_3$.

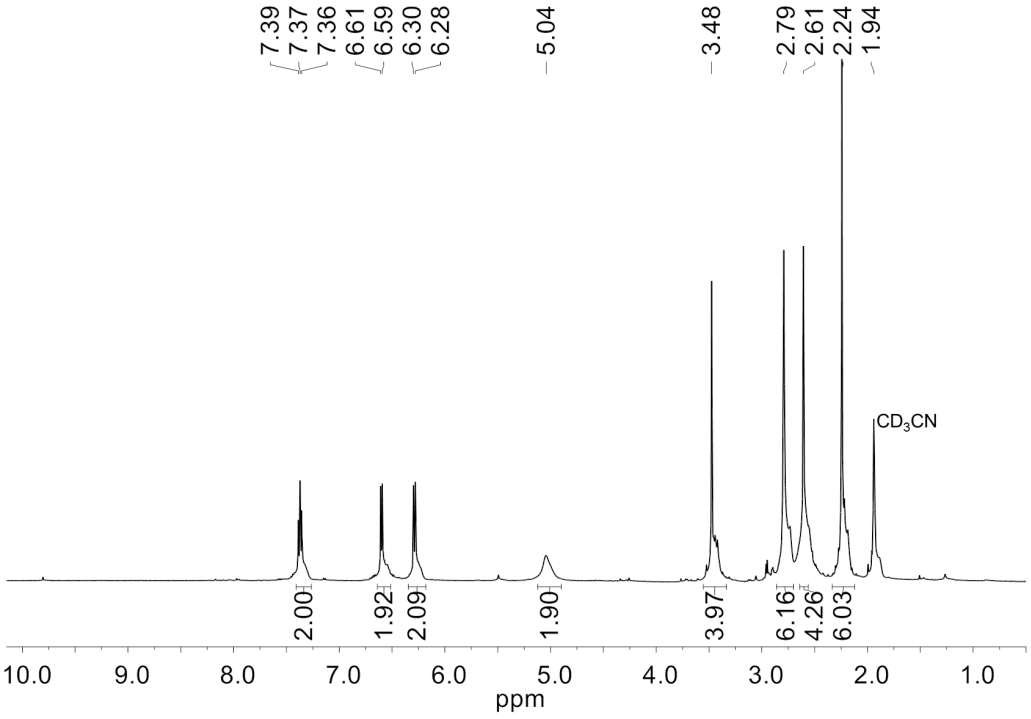

Figure 1.10. ^{1}H NMR of L^{MMA} in CD_3CN.

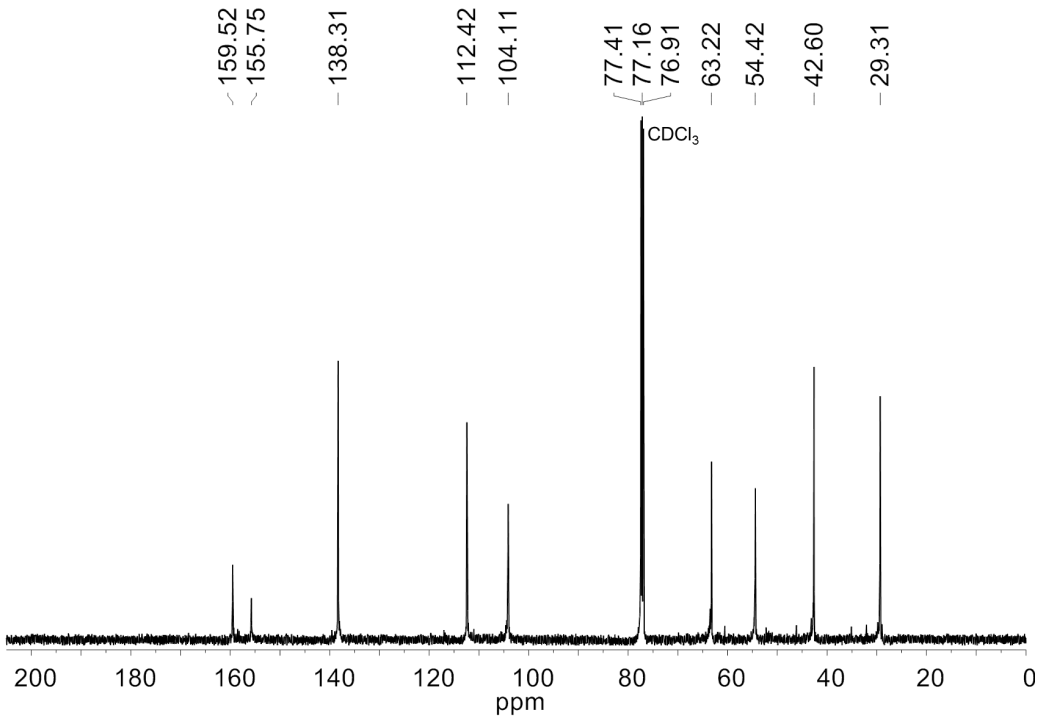

Figure 1.11. $^{13}C\{^{1}H\}$ NMR of L^{MMA} in $CDCl_3$.

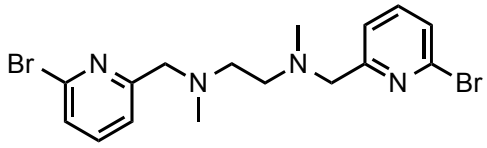

***N*^{1},*N*^{2}-bis((6-bromopyridin-2-yl)methyl)-*N*^{1},*N*^{2}-dimethylethane-1,2-diamine** (**L^{Br}**)**.** A solution of sodium triacetoxyborohydride (1.5 g, 7.2 mmol) and 6-bromo-2-formylpyridine (1.1 g, 5.4 mmol) in dry dichloromethane (20 mL) was treated with *N*,*N*′-dimethylethylenediamine (0.19 mL, 0.15 g, 1.8 mmol) and the mixture was stirred at 25 °C under nitrogen for 18 h. The resulting mixture was quenched with 20 mL sat. aqueous sodium bicarbonate. The organic layer was removed and the aqueous layer was extracted 3 × 20 mL portions of ethyl acetate. The organic layers were combined, dried over $MgSO_4$, filtered and concentrated to afford a brown oil (1.2 g, 2.8 mmol). The protonated *N*^{1},*N*^{2}-bis((6-bromopyridin-2-yl)methyl)-*N*^{1},*N*^{2}-dimethylethane-1,2-diamine obtained above was dissolved in 20 mL dry tetrahydrofuran. Sodium hydride (60% dispersion in mineral oil, 0.24 g, 6.1 mmol) was

added and the resulting solution was stirred at 25 °C under nitrogen for 24 h. The solution was concentrated to give a brown solid that was dissolved in large portions of hexane and filtered three times. Resulting filtrate was concentrated to give $\mathbf{L^{Br}}$ as a light yellow oil (0.68 g, 89% yield). ^{1}H NMR ($CDCl_3$): δ = 7.50 (t, $^3J_{HH}$ = 10.0 Hz, 2H, Ar–*H*), 7.44 (d, $^3J_{HH}$ = 10.0 Hz, 2H, Ar–*H*), 7.34 (d, $^3J_{HH}$ = 10.0 Hz, 2H, Ar–*H*), 3.67 (s, 4H, Ar–C*H*$_2$–N–), 2.61 (s, 4H, –C*H*$_2$–C*H*$_2$–), 2.27 (s, 6H, –N–C*H*$_3$); ^{13}C{^{1}H} NMR ($CDCl_3$): δ = 161.66, 141.34, 138.90, 126.31, 121.72, 63.61, 55.63, 43.11, 29.85; HR-MS (ESI) *m/z* calcd for $C_{16}H_{20}N_4Br_2Na$ ([M+Na]$^+$) 448.9952, found 448.9930.

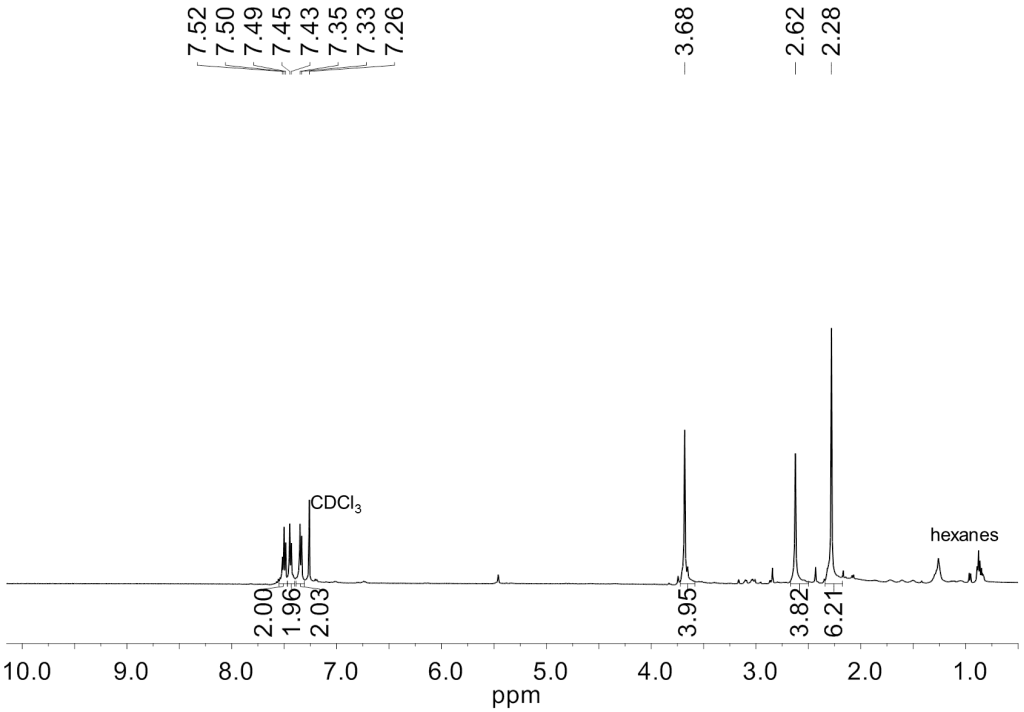

Figure 1.12. ^{1}H NMR of L^{Br} in $CDCl_3$.

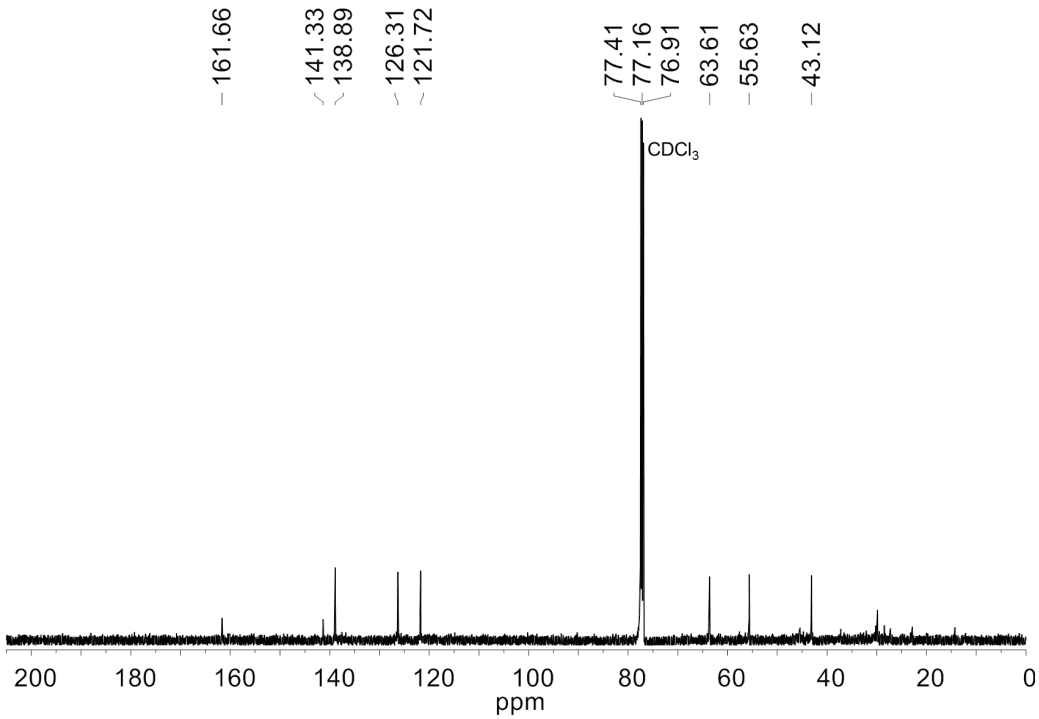

Figure 1.13. $^{13}C\{^{1}H\}$ NMR of L^{Br} in $CDCl_3$.

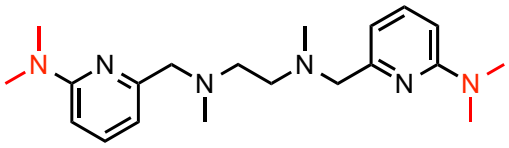

N,N'-bis((6-(dimethylamino)pyridin-2-yl)methyl)-N,N'-dimethylethane-1,2-diamine (L^{DMA}). In a Schlenk flask, aqueous DMA (40% w/w, 2.0 mL, 1.8 g, 16 mmol) was added to a solution of $\mathbf{L^{Br}}$ (0.68 g, 1.6 mmol) in water (5 mL). The resulting mixture was sealed under pressure, stirred and heated to 50 °C for 48 h and then cooled to room temperature. The resulting mixture was extracted with dichloromethane several times and the organic layers were combined, dried over $MgSO_4$, filtered and concentrated to give $\mathbf{L^{DMA}}$ as a dark brown oil (0.54 g, 95% yield). The ligand can be observed by thin-layer chromatography on a silica plate using an eluent solution of ethyl acetate/methanol/triethylamine (89:10:1). ^{1}H NMR ($CDCl_3$): δ = 7.39 (t, $^{3}J_{HH}$ = 10.0 Hz, 2H, Ar-*H*), 6.64 (d, $^{3}J_{HH}$ = 10.0 Hz, 2H, Ar–*H*), 6.38 (d, $^{3}J_{HH}$ = 10.0 Hz, 2H, Ar–*H*), 3.50 (s, 4H, Ar-CH_2–N–), 3.03 (s, 12H, –N–(CH_3)$_2$), 2.60 (s, 4H,

–CH_2–CH_2–), 2.26 (s, 6H, –N–CH_3); $^{13}C\{^1H\}$ NMR ($CDCl_3$): δ = 159.11, 137.55,110.79, 103.90, 64.13, 55.22, 43.09, 38.07; HR-MS (ESI) *m/z* calcd for $C_{20}H_{32}N_6Na$ ($[M+Na]^+$) 379.2586, found 379.2574.

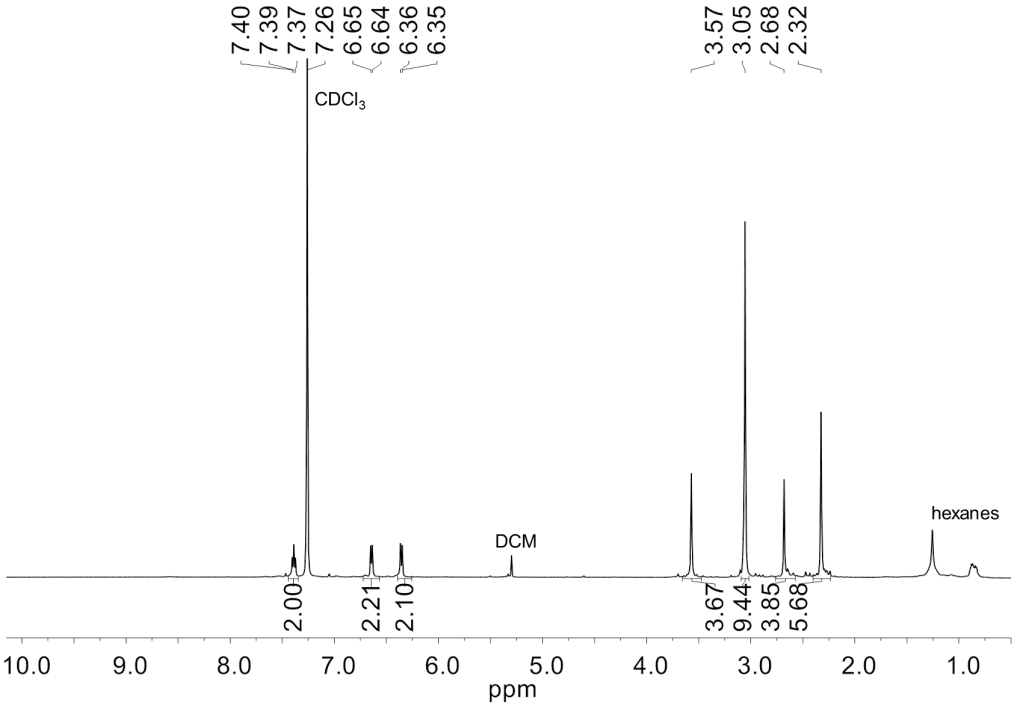

Figure 1.14. ^1H NMR of L^{DMA} in $CDCl_3$.

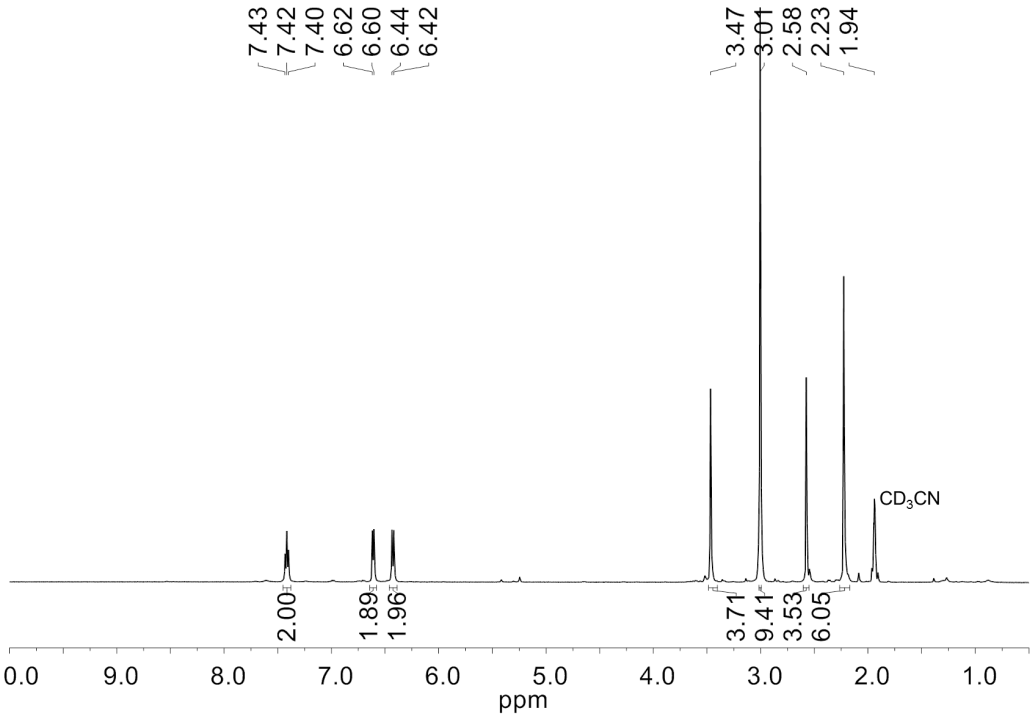

Figure 1.15. ^{1}H NMR of L^{DMA} in CD_3CN.

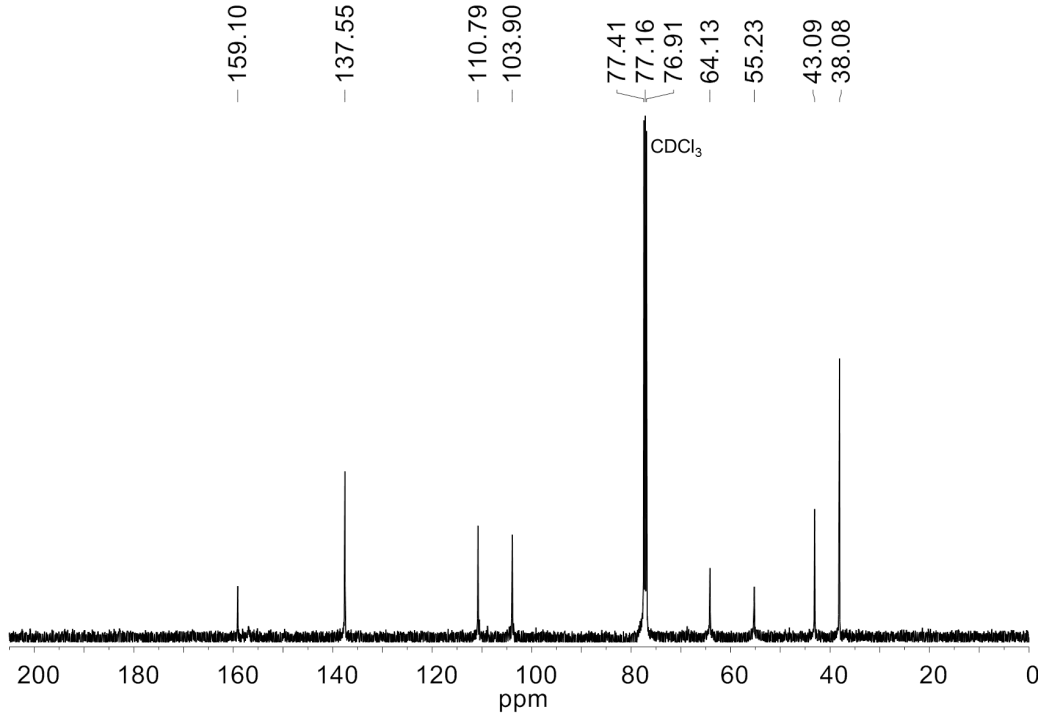

Figure 1.16. $^{13}C\{^{1}H\}$ NMR of L^{DMA} in $CDCl_3$.

1.6. References

(1) White, M. C.; Doyle, A. G.; Jacobsen, E. N. *J. Am. Chem. Soc.* **2001**, *123*, 7194-7195.

(2) Murphy, A.; Pace, A.; Stack, T. D. P. *Org. Lett.* **2004**, *6*, 3119-3122.

(3) Taktak, S.; Kryatov, S. V.; Haas, T. E.; Rybak-Akimova, E. V. *J. Mol. Catal. A: Chem.* **2006**, *259*, 24-34.

(4) Lyakin, O. Y.; Bryliakov, K. P.; Talsi, E. P. *Inorg. Chem.* **2011**, *50*, 5526-5538.

(5) Morris, L. S.; Girouard, M. P.; Everhart, M. H.; McClain, W. E.; van Paridon, J. A.; Pike, R. D.; Goh, C. *Inorg. Chim. Acta* **2014**, *413*, 149-159.

(6) McArthur, S.; Baird, M. C. *Euro. Polym. J.* **2014**, *55*, 170-178.

(7) Tetard, D.; Verlhac, J.-B. *J. Mol. Catal. A: Chem.* **1996**, *113*, 223-230.

(8) Britovsek, G. J. P.; England, J.; White, A. J. P. *Inorg. Chem.* **2005**, *44*, 8125-8134.

(9) Turitsyna, E. A.; Gritsenko, O. N.; Shteinman, A. A. *Kinetics and Catalysis* **2007**, *48*, 53-59.

(10) Makhlynets, O. V.; Rybak-Akimova, E. V. *Chem. Eur. J.* **2010**, *16*, 13995-14006.

(11) He, Y.; Gorden, J. D.; Goldsmith, C. R. *Inorg. Chem.* **2011**, *50*, 12651-12660.

(12) Zhang, Q.; Gorden, J. D.; Goldsmith, C. R. *Inorg. Chem.* **2013**, *52*, 13546-13554.

(13) Kejriwal, A.; Biswas, A. N.; Choudhury, A.; Bandyopadhyay, P. *Transition Met. Chem.* **2014**, *39*, 909-915.

(14) Okuno, T.; Ito, S.; Ohba, S.; Nishida, Y. *J. Chem. Soc., Dalton Trans.* **1997**, 3547-3551.

(15) Chen, K.; Que Jr, L. *Chem. Comm.* **1999**, 1375-1376.

(16) Yeon Ryu, J.; Heo, S.; Park, P.; Nam, W.; Kim, J. *Inorg. Chem. Comm.* **2004**, *7*, 534-537.

(17) Taktak, S.; Flook, M.; Foxman, B. M.; Que, J. L.; Rybak-Akimova, E. V. *Chem. Comm.* **2005**, 5301-5303.

(18) Li, C.-K.; Tang, W.-T.; Che, C.-M.; Wong, K.-Y.; Wang, R.-J.; Mak, T. C. W. *J. Chem. Soc., Dalton Trans.* **1991**, 1909-1914.

(19) Fillol, J. L.; Codolà, Z.; Garcia-Bosch, I.; Gómez, L.; Pla, J. J.; Costas, M. *Nat. Chem.* **2011**, *3*, 807-813.

(20) Klepser, B. M.; Bartlett, B. M. *J. Am. Chem. Soc.* **2014**, *136*, 1694-1697.

(21) Panchbhai, G.; Singh, W. M.; Das, B.; Jane, R. T.; Thapper, A. *Eur. J. Inorg. Chem.* **2016**, *2016*, 3262-3268.

(22) Roux, Y.; Ghattas, W.; Avenier, F.; Guillot, R.; Simaan, A. J.; Mahy, J. P. *Dalton Trans.* **2015**, *44*, 5966-5968.

(23) Glerup, J.; Goodson, P. A.; Hodgson, D. J.; Michelsen, K. *Inorg. Chem.* **1995**, *34*, 6255-6264.

(24) Poussereau, S.; Blondin, G.; Cesario, M.; Guilhem, J.; Chottard, G.; Gonnet, F.; Girerd, J.-J. *Inorg. Chem.* **1998**, *37*, 3127-3132.

(25) Taktak, S.; Kryatov, S. V.; Rybak-Akimova, E. V. *Inorg. Chem.* **2004**, *43*, 7196-7209.

(26) Coates, C. M.; Hagan, K.; Mitchell, C. A.; Gorden, J. D.; Goldsmith, C. R. *Dalton Trans.* **2011**, *40*, 4048-4058.

(27) Luan, J.; Zhou, J.; Liu, Z.; Zhu, B.; Wang, H.; Bao, X.; Liu, W.; Tong, M.-L.; Peng, G.; Peng, H.; Salmon, L.; Bousseksou, A. *Inorg. Chem.* **2015**, *54*, 5145-5147.

(28) Egdal, R. K.; Bond, A. D.; McKenzie, C. J. *Acta Crystallogr. Sect. E* **2005**, *61*, m412-m413.

(29) Goodson, P. A.; Glerup, J.; Hodgson, D. J.; Michelsen, K.; Rychlewska, U. *Inorg. Chem.* **1994**, *33*, 359-366.

(30) Hureau, C.; Blondin, G.; Cesario, M.; Un, S. *J. Am. Chem. Soc.* **2003**, *125*, 11637-11645.

(31) Murphy, A.; Dubois, G.; Stack, T. D. P. *J. Am. Chem. Soc.* **2003**, *125*, 5250-5251.

(32) Glerup, J.; Goodson, P. A.; Hazell, A.; Hazell, R.; Hodgson, D. J.; McKenzie, C. J.; Michelsen, K.; Rychlewska, U.; Toftlund, H. *Inorg. Chem.* **1994**, *33*, 4105-4111.

(33) Arulsamy, N.; Glerup, J.; Hazell, A.; Hodgson, D. J.; McKenzie, C. J.; Toftlund, H. *Inorg. Chem.* **1994**, *33*, 3023-3025.

(34) Hureau, C.; Blondin, G.; Charlot, M.-F.; Philouze, C.; Nierlich, M.; Césario, M.; Anxolabéhère-Mallart, E. *Inorg. Chem.* **2005**, *44*, 3669-3683.

(35) Kryatova, M. S.; Makhlynets, O. V.; Nazarenko, A. Y.; Rybak-Akimova, E. V. *Inorg. Chim. Acta* **2012**, *387*, 74-80.

(36) Bustamante, F. L. S.; Miranda, F. S.; Castro, F. A. V.; Resende, J. A. L. C.; Pereira, M. D.; Lanznaster, M. *J. Inorg. Biochem.* **2014**, *132*, 37-44.

(37) Wang, J.-W.; Sahoo, P.; Lu, T.-B. *ACS Catal.* **2016**, *6*, 5062-5068.

(38) Company, A.; Güell, M.; Popa, D.; Benet-Buchholz, J.; Parella, T.; Fontrodona, X.; Llobet, A.; Solà, M.; Ribas, X.; Luis, J. M.; Costas, M. *Inorg. Chem.* **2006**, *45*, 9643-9645.

(39) Mautner, F. A.; Soileau, J. B.; Bankole, P. K.; Gallo, A. A.; Massoud, S. S. *J. Mol. Struct.* **2008**, *889*, 271-278.

(40) Pandiyan, T.; Guadalupe, H. J.; Cruz, J.; Bernès, S.; Ugalde-Salvdivar, V. M.; González, I. *Eur. J. Inorg. Chem.* **2008**, *2008*, 3274-3285.

(41) Mautner, F. A.; Mikuriya, M.; Ishida, H.; Sakiyama, H.; Louka, F. R.; Humphrey, J. W.; Massoud, S. S. *Inorg. Chim. Acta* **2009**, *362*, 4073-4080.

(42) Mautner, F. A.; Koikawa, M.; Mikuriya, M.; Harrelson, E. V.; Massoud, S. S. *Polyhedron* **2013**, *59*, 17-22.

(43) Bandara, H. M. D.; Kennedy, D. P.; Akin, E.; Incarvito, C. D.; Burdette, S. C. *Inorg. Chem.* **2009**, *48*, 8445-8455.

(44) Weickmann, D.; Frey, W.; Plietker, B. *Chem. Eur. J.* **2013**, *19*, 2741-2748.

(45) Rakowski DuBois, M.; DuBois, D. L. *Chem. Soc. Rev.* **2009**, *38*, 62-72.

(46) DuBois, D. L.; Bullock, R. M. *Eur. J. Inorg. Chem.* **2011**, *2011*, 1017-1027.

(47) Carver, C. T.; Matson, B. D.; Mayer, J. M. *J. Am. Chem. Soc.* **2012**, *134*, 5444-5447.

(48) Matson, B. D.; Carver, C. T.; Von Ruden, A.; Yang, J. Y.; Raugei, S.; Mayer, J. M. *Chem. Comm.* **2012**, *48*, 11100-11102.

(49) Boyer, J. L.; Polyansky, D. E.; Szalda, D. J.; Zong, R.; Thummel, R. P.; Fujita, E. *Angew. Chem. Int. Ed.* **2011**, *50*, 12600-12604.

(50) Henry, R. M.; Shoemaker, R. K.; DuBois, D. L.; DuBois, M. R. *J. Am. Chem. Soc.* **2006**, *128*, 3002-3010.

(51) Jacobsen, G. M.; Shoemaker, R. K.; Rakowski DuBois, M.; DuBois, D. L. *Organometallics* **2007**, *26*, 4964-4971.

(52) Delgado, M.; Sommer, S. K.; Swanson, S. P.; Berger, R. F.; Seda, T.; Zakharov, L. N.; Gilbertson, J. D. *Inorg. Chem.* **2015**, *54*, 7239-7248.

(53) Hoffert, W. A.; Mock, M. T.; Appel, A. M.; Yang, J. Y. *Eur. J. Inorg. Chem.* **2013**, *2013*, 3846-3857.

(54) Khosrowabadi Kotyk, J. F.; Ziller, J. W.; Yang, J. Y. *J. Coord. Chem.* **2016**, *69*, 1990-2002.

(55) Conway, J. H.; Fiedler, D. *Angew. Chem. Int. Ed.* **2015**, *54*, 3941-3945.

(56) Kobayashi, Y.; Kuroda, M.; Toba, N.; Okada, M.; Tanaka, R.; Kimachi, T. *Org. Lett.* **2011**, *13*, 6280-6283.

(57) Tsukamoto, I.; Koshio, H.; Kuramochi, T.; Saitoh, C.; Yanai-Inamura, H.; Kitada-Nozawa, C.; Yamamoto, E.; Yatsu, T.; Shimada, Y.; Sakamoto, S.; Tsukamoto, S.-i. *Bioorg. Med. Chem.* **2009**, *17*, 3130-3141.

(58) Antoniadou, S.; Jannakoudakis, A. D.; Jannakoudakis, P. D.; Theodoridou, E. *J. Appl. Electrochem.* **1992**, *22*, 1060-1064.

(59) Herlem, G.; Reybier, K.; Trokourey, A.; Fahys, B. *J. Electrochem. Soc.* **2000**, *147*, 597-601.

(60) Kumar, A.; Vaishali; Ramamurthy, P. *Int. J. Chem. Kinet.* **2000**, *32*, 286-293.

(61) Anderson, L. C.; Seeger, N. V. *J. Am. Chem. Soc.* **1949**, *71*, 340-342.

(62) Kereselidze, J. A.; Zarkua, T. S. *Chemistry of Heterocyclic Compounds* **2000**, *36*, 1161-1163.

CHAPTER 2

Copper Tetradentate N_2Py_2 Complexes with Pendant Bases in the Secondary Coordination Sphere: Protonation Studies and Oxygen Activation

Portions of this chapter have been published:
Khosrowabadi Kotyk, J. F.; Ziller, J. W.; Yang, J. Y. *J. Coord. Chem.*, **2016**, *69*, 1990-2002.

2.1. Motivation and Specific Aims

The Cu(II) and Cu(I) complexes of a family of hydrogen-boding ligands (L^{H}, L^{MMA}, L^{DMA}) were synthesized and characterized in order to explore the oxygen activation chemistry of copper complexes with ligands bearing pendant amines. Additionally, protonation studies of the diamagnetic Cu(I) complexes were performed via ^{1}H NMR spectroscopy to determine the pK_a of the pendant bases. These pendant bases attempt to mimic biology as hydrogen bond donors and acceptors to metal-bound substrates. These features may lower activation barriers for small molecule activation, specifically toward oxygen reduction reaction (ORR) intermediates. The development of improved catalysts for activation of dioxygen may provide insight into the mechanism of dioxygen activation and lead to improved catalyst design.

2.2. Background

$$O_2 + 4\,H^+ + 4\,e^- \rightleftharpoons 2\,H_2O \qquad \textbf{eq 1}$$

Oxygen activation is an important process in biological metabolism and renewable energy related technology (i.e. Proton Exchange Membrane (PEM) fuel cells). The oxygen reduction reaction (ORR) can occur through two main pathways: a four-electron route that directly converts O_2 to H_2O (Equation 1), or the two-electron route through a hydrogen peroxide (H_2O_2) intermediate.[1] The reduction of oxygen in fuel cells is kinetically slow despite high platinum catalyst loading, which also increases their cost. The efficiency and stability of PEM fuel cells can also be degraded by hydrogen peroxide based radicals produced through the two-electron reduction process; therefore it is important to find earth abundant transition metal catalysts that can perform the direct selective four-electron reduction of oxygen.[2]

In biology, iron and copper metalloenzymes activate dioxygen. The presence of iron and copper is likely due to their abundance in the earth's crust and the accessibility of multiple redox states, which permits multi-electron transformations.[3-8]

Secondary coordination sphere proton relays play an essential role in mediating redox reactivity in biological and synthetic systems. Enzymes incorporate distal hydrogen bond donors and acceptors to organize substrates in metalloenzyme active sites for catalysis and facilitate proton-coupled electron transfer (PCET).[9-13] Stabilization of O_2 bound adducts using distal amino acids through hydrogen-bonding networks lowers activation barriers for more efficient conversion of dioxygen.[14]

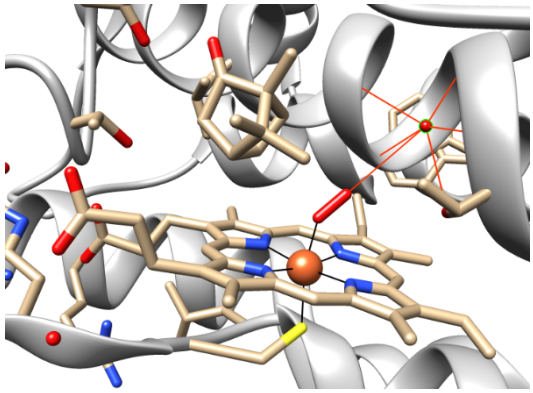

Figure 2.1. Structure of the monooxygenase cytochrome P450 (PDB 1DZ8). Red = O, orange = Fe, blue = N. Red lines represent H-bonding interactions.

For example, iron porphyrin (heme) systems are prevalent in biology and play an important role in oxygen chemistry. The active site of human hemoglobin incorporates an iron heme and when bound to oxygen, features a hydrogen bond formed through an intermolecular imidazole histidine residue.[15] When the histidine position is altered, oxygen binding affinity is lowered compared to wild type enzyme.[16] The active site of another iron heme system in monooxygenase cytochrome P450 contains a charge transfer and hydrogen-bonding network amongst many amino acids and the activated oxygen bound metal center (Figure 2.1).[17-19]

Additionally, copper systems such as the hemocyanin serve a similar function to hemoglobin as an oxygen transport protein in mollusks using a dinuclear activation site.[5,20] Mononuclear copper oxidases such as amine oxidase and galactose oxidase couple the reductive activation of dioxygen to peroxide with the oxidation of another substrate, a topa-quinone in amine oxidase and a tyrosine in galactose oxidase.[5] The four-electron reduction of oxygen directly to water requires a multi-copper site as well as a redox active heme ligand such as in heme-copper oxidase (also referred to as heme-copper oxygen reductase).[21] Cytochrome c oxidase, a cooperative copper and iron heme oxidase protein, contains both a copper and iron atom at the active site. A distal tyrosine is responsible for proton transfer to the iron bound oxygen.[22]

Several synthetic biomimetic first row transition metal complexes can catalytically reduce oxygen.[23-28] Many researchers have developed a variety of porphyrin and corrole based systems to mimic the structural aspects of heme oxidases.[29-33] Although, few synthetic copper complexes have been successful at oxygen activation, enzymatic mononuclear copper active sites have inspired synthetic mononuclear copper catalysts for the oxygen reduction reaction.[34-37]

Mayer and coworkers utilized pendant bases benzoic acid or pyridine modified iron porphyrins to reduce oxygen to water.[38,39] Dubois and coworkers utilized nickel diphosphine with pendant amines to reduce oxygen electrocatalytically.[40] A tripodal ligand containing urea and carboxyamidopyridyl units as hydrogen bond donors was utilized by Borovik and coworkers to reduce oxygen to water.[41]

Therefore, copper complexes bearing pendant bases were explored to elucidate structure-activity relationships with hydrogen-bonding ligands and attempt to expand the reactivity of the multi-electron reduction of oxygen to water.

2.3. Results and Discussion

2.3.1. Synthesis of Divalent and Monovalent Copper Complexes

Preparation of Divalent Cu(II) Complexes

Scheme 2.1. Preparation of divalent copper complexes $[CuL^{H}(CH_3CN)][BF_4]_2$, $[CuL^{MMA}(CH_3CN)][BF_4]_2$, and $[CuL^{DMA}][BF_4]_2$ via metalation with $[Cu(CH_3CN)_4][BF_4]_2$.

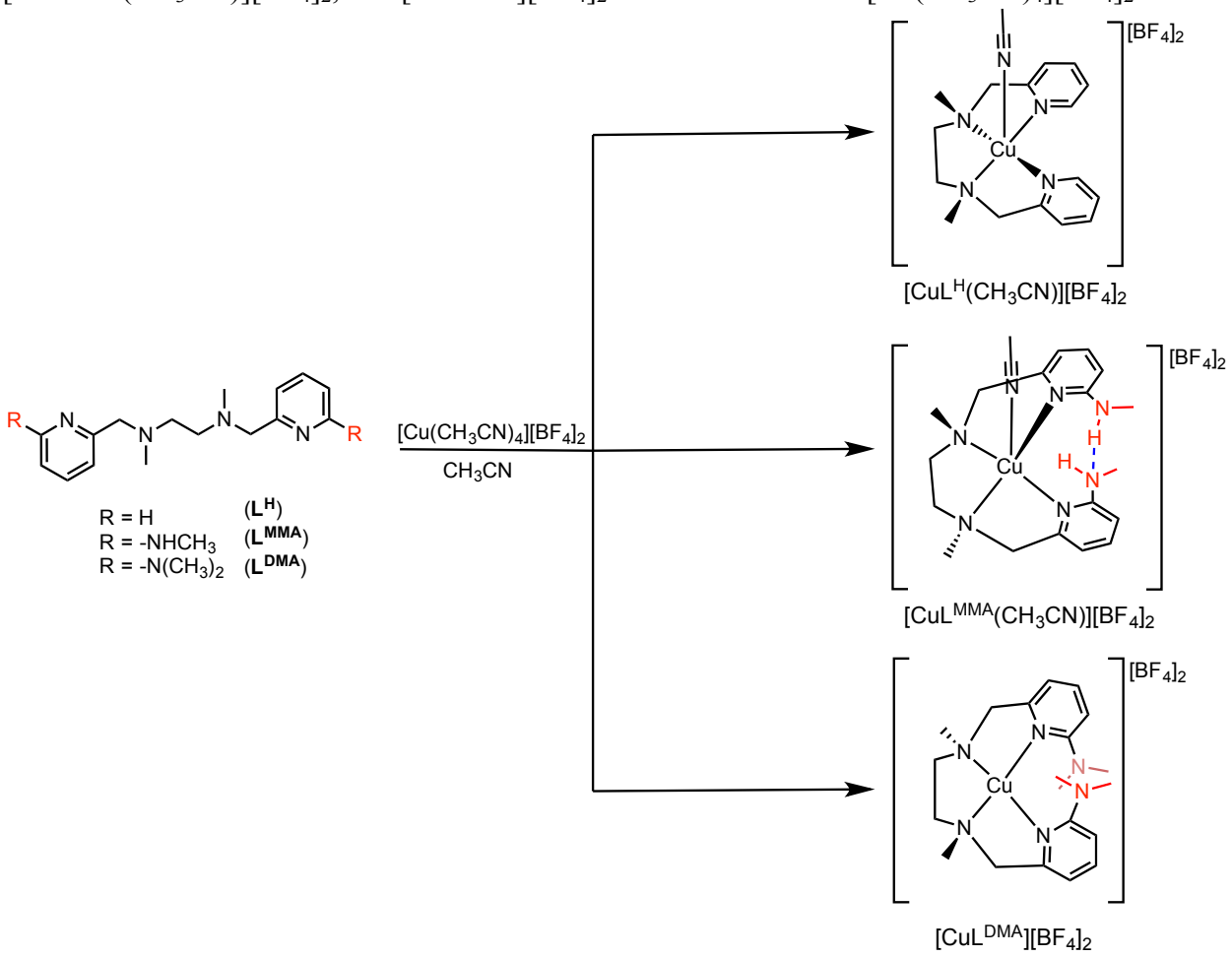

The divalent copper complexes $[CuL^{H}(CH_3CN)][BF_4]_2$, $[CuL^{MMA}(CH_3CN)][BF_4]_2$, and $[CuL^{DMA}][BF_4]_2$ were synthesized by metalation using $[Cu(CH_3CN)_4][BF_4]_2$[42] in 82–99% yield (Scheme 2.1). The $[CuL^{H}(CH_3CN)][BF_4]_2$, $[CuL^{MMA}(CH_3CN)][BF_4]_2$, and $[CuL^{DMA}][BF_4]_2$ complexes are dark blue, teal and dark purple as pure solids, respectively. Formulation and purity, respectively, were confirmed by ESI-MS and elemental analysis.

Preparation of Monovalent Cu(I) Complexes

Scheme 2.2. Preparation of monovalent copper complexes $[CuL^{H}][BF_4]$, $[CuL^{MMA}][BF_4]$, and $[CuL^{DMA}][BF_4]$ via reduction of divalent complexes.

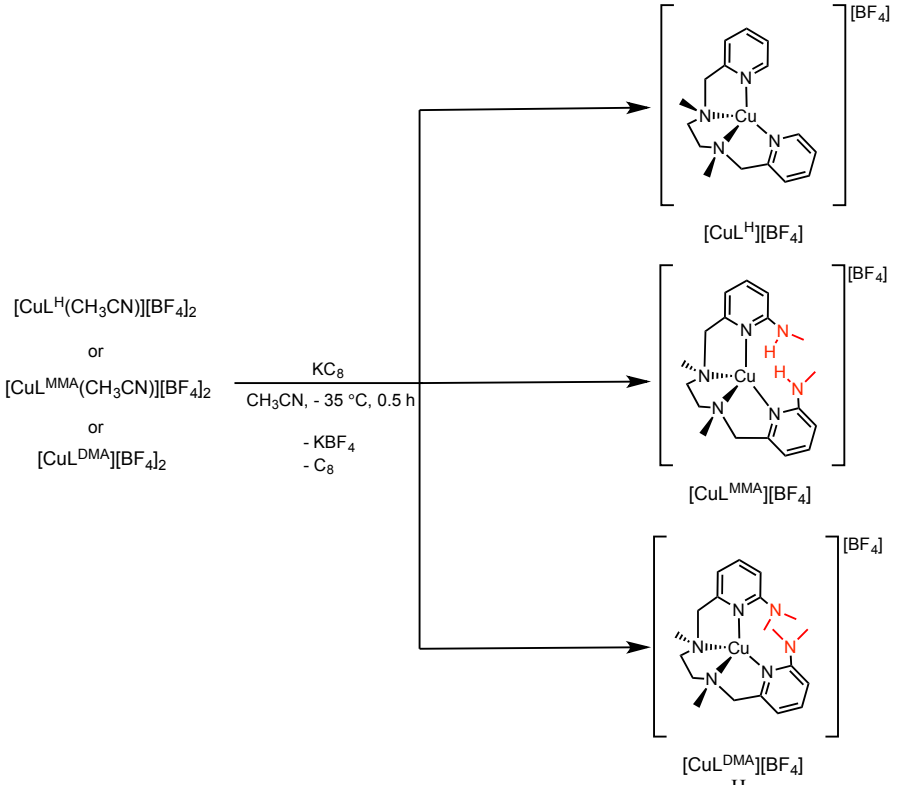

Scheme 2.3. Preparation of monovalent copper complexes $[CuL^{H}][BF_4]$, $[CuL^{MMA}][BF_4]$, and $[CuL^{DMA}][BF_4]$ via metalation with $[Cu(CH_3CN)_4][BF_4]$.

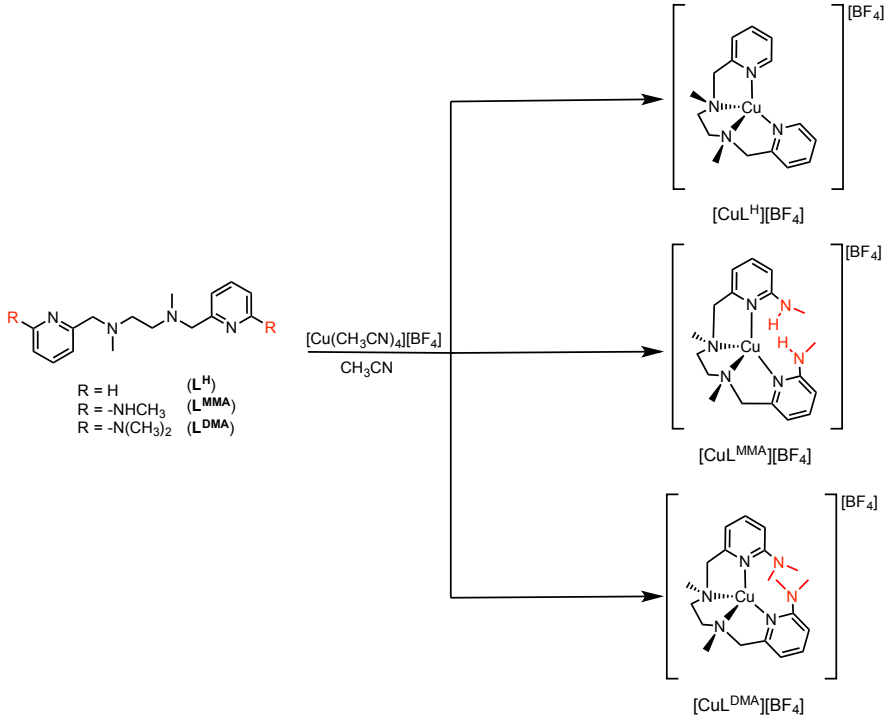

The Cu(I) species $[CuL^{H}][BF_4]$, $[CuL^{MMA}][BF_4]$, and $[CuL^{DMA}][BF_4]$ were synthesized by chemical reduction with one equivalent of potassium graphite (Scheme 2.2) or metalation with the monovalent copper starting material $[Cu(CH_3CN)_4][BF_4]$[43] to give yellow solids (Scheme 2.3). The resulting diamagnetic complexes were characterized for formulation and purity by ESI-MS and ^{1}H NMR spectroscopy, respectively. It should be noted the Cu(I) complexes are very sensitive to residual dichloromethane and will abstract chloride to form Cu(II) complexes (see Appendix A).

2.3.2. Physical Characterization of Divalent and Monovalent Copper Complexes

Solid State Structures of Divalent Cu(II) Complexes

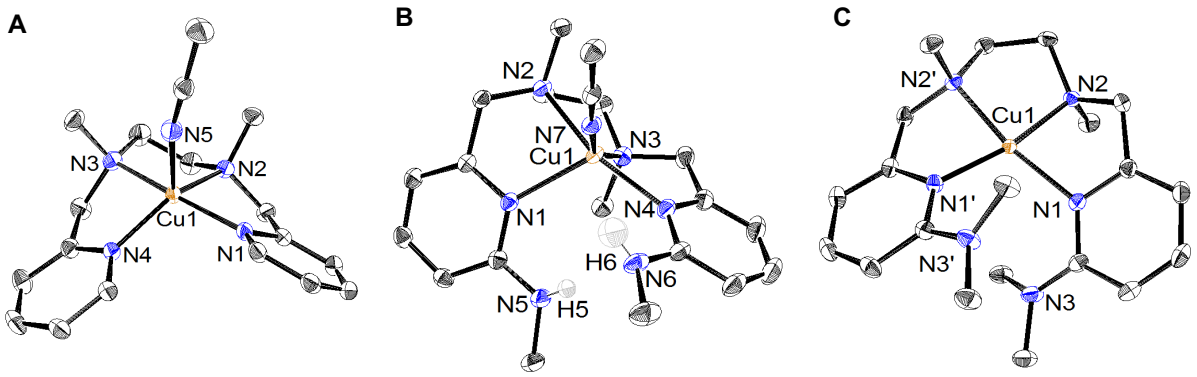

Figure 2.2. ORTEP of the divalent copper complexes A) $[CuL^{H}(CH_3CN)][BF_4]_2$, B) $[CuL^{MMA}(CH_3CN)][BF_4]_2$ and C) $[CuL^{DMA}][BF_4]_2$. Thermal ellipsoids are drawn at the 50% probability level. The BF_4^- counter anions, solvent molecules and hydrogen atoms other than the protons on L^{MMA} have been removed for clarity

Table 2.1. Values for τ_4 and τ_5 of the divalent copper complexes $[CuL^{H}(CH_3CN)][BF_4]_2$, $[CuL^{MMA}(CH_3CN)][BF_4]_2$, and $[CuL^{DMA}][BF_4]_2$ determined by X-ray crystallography.

	τ_4			τ_5		
	Ideal Square Planar	**Ideal Tetrahedral**	**Compound**	**Ideal Square Pyramidal**	**Ideal Trigonal Bipyramidal**	**Compound**
$[CuL^{H}(CH_3CN)][BF_4]_2$	-	-	-	0	1	0.36
$[CuL^{MMA}(CH_3CN)][BF_4]_2$	-	-	-	0	1	0.10
$[CuL^{DMA}][BF_4]_2$	0	1	0	-	-	-

Comparison of the solid state structures determined by single crystal X-ray crystallography indicates all three divalent copper centers are coordinated by the tetradentate N_2Py_2 ligands (Figure 2.2). Hydrogen atoms shown in $[CuL^{MMA}(CH_3CN)][BF_4]_2$ structure were found in the difference map.

The complexes $[CuL^{H}(CH_3CN)][BF_4]_2$ and $[CuL^{MMA}(CH_3CN)][BF_4]_2$ have an acetonitrile bound to give a five-coordinate coordination environment. Interestingly, only the methyl groups on the amine backbone of $[CuL^{H}(CH_3CN)][BF_4]_2$ are *cis* to one another. However, DFT calculations have shown that the *cis* and *trans* geometric isomers of BPMEN-like ligands are both energetically favorable and exist in equilibrium.[44] The coordination geometry is pseudo square pyramidal with a τ_5 value of 0.36, where $\tau_5 = 1$ is an ideal trigonal bipyramidal and $\tau_5 = 0$ is an ideal square pyramidal geometry.[45]

$[CuL^{MMA}(CH_3CN)][BF_4]_2$ has a τ_5 value of 0.10 indicating a distorted square pyramidal geometry where the bound acetonitrile, N2, N3, and N4 form the basal plane. All τ_4 and τ_5 values are tabulated in Table 2.1. The hydrogen atoms on the methylamine moieties of the L^{MMA} ligand exhibit hydrogen bonds as intended. The hydrogen atom, H5, of one methylamine arm acts as a hydrogen bond donor to the nitrogen, N6, from the other methylamine with a distance of 2.204 Å. Hydrogen atom, H6, of the second methylamine faces toward the bound acetonitrile with a distance

of 2.376 Å. Additionally, the methyl groups on the ethylenediamine backbone are *trans* to one another.

In contrast, $[CuL^{DMA}][BF_4]_2$ has an ideal four coordinate square planar coordination geometry (τ_4 value of 0.00); there is a two-fold symmetric C_2 axis in the solid state crystal structure. The two methyl groups on the amine backbone are *trans* to one another while the dimethylamine functionalities are stacked directly above one another likely blocking the fifth coordination site.

Solid State Structures of Monovalent Cu(I) Complexes

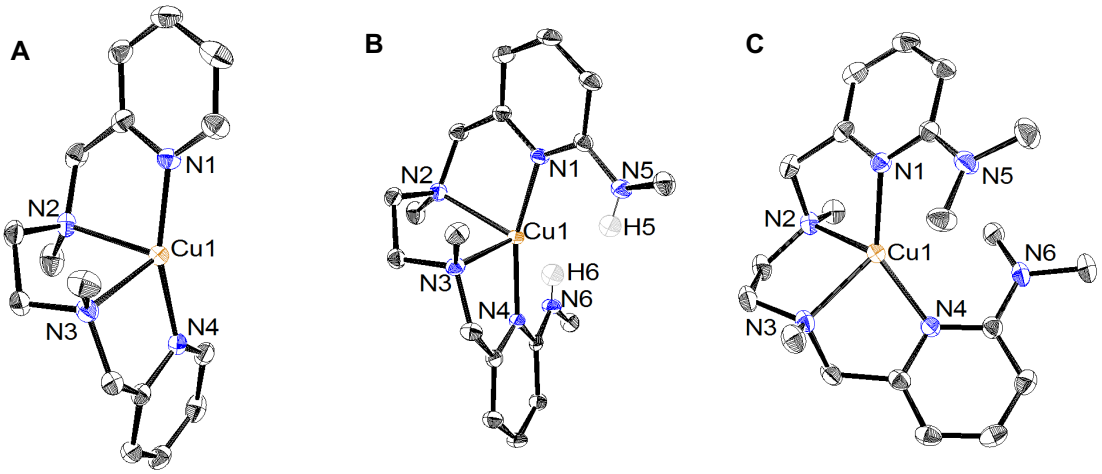

Figure 2.3. ORTEP of the monovalent copper complexes A) $[CuL^{H}][BF_4]$, B) $[CuL^{MMA}][BF_4]$ and C) $[CuL^{DMA}][BF_4]$. Thermal ellipsoids are drawn at the 50% probability level. The BF_4^- counter anions, solvent molecules and hydrogen atoms other than the protons on L^{MMA} have been removed for clarity.

Table 2.2. Values for τ_4 and τ_4' of the monovalent copper complexes $[CuL^{H}][BF_4]$, $[CuL^{MMA}][BF_4]$, and $[CuL^{DMA}][BF_4]$ determined by X-ray crystallography.

	Ideal Square Planar	**$[CuL^{H}][BF_4]$**	**$[CuL^{MMA}][BF_4]$**	**$[CuL^{DMA}][BF_4]$**	**Ideal Tetrahedral**
τ_4	0.00	0.60	0.59	0.64	1.00
τ_4'	0.00	0.46	0.44	0.61	1.00

The X-ray crystal structures of all three complexes are shown in Figure 2.3. Hydrogen atoms shown in $[CuL^{MMA}][BF_4]$ structure were found in the difference map. All three monovalent copper solid state structures are four coordinate, the methyl groups in the amine backbone are *trans* to each other in all compounds. Four coordinate geometries can be described by a parameter known as τ_4, where $\tau_4 = 1$ is an ideal tetrahedral and $\tau_4 = 0$ is an ideal square planar geometry.[46] Recently, a new τ_4' parameter has been established to more accurately describe geometries that may seem deceptively similar with the τ_4 value.[47] Upon inspection of the τ_4 parameters all the complexes have values close to 0.60; $[CuL^{H}][BF_4]$ ($\tau_4 = 0.60$), $[CuL^{MMA}][BF_4]$ ($\tau_4 = 0.59$), and $[CuL^{DMA}][BF_4]$ ($\tau_4 = 0.64$). This similarity in τ_4 value implies all three structures exhibit distorted tetrahedral or see-saw like geometries consistent with a Cu(I) d^{10} metal ions. However, analyzing the τ_4' parameter, $[CuL^{H}][BF_4]$ ($\tau_4' = 0.46$), $[CuL^{MMA}][BF_4]$ ($\tau_4' = 0.44$), and $[CuL^{DMA}][BF_4]$ ($\tau_4' = 0.61$), the $[CuL^{DMA}][BF_4]$ complex is more tetrahedral-like with a value closer to 1.00 than the other two complexes. This geometric difference is likely due to the steric crowding of the dimethylamine moieties. All τ_4 and τ_4' are tabulated in Table 2.2.

Cyclic Voltammetry

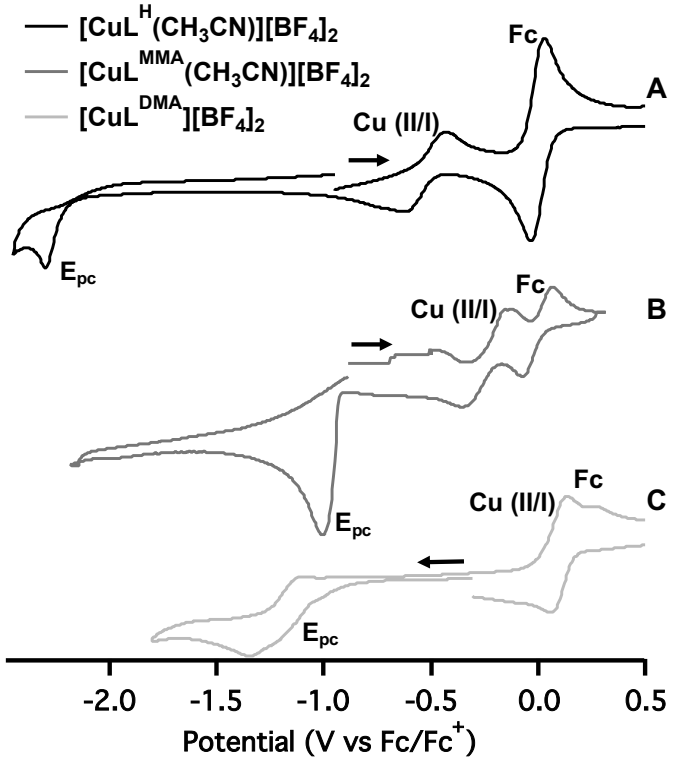

Figure 2.4. Full scan cyclic voltammograms of 1 mM solutions of A) $[CuL^{H}(CH_3CN)][BF_4]_2$, B) $[CuL^{MMA}(CH_3CN)][BF_4]_2$, and C) $[CuL^{DMA}][BF_4]_2$ in 0.10 M Bu_4NBF_4 in CH_3CN at 100 mV/s.

Table 2.3. Electrochemical values for the Cu(II/I) couple (E°′) and the Cu(I/0) reduction event (E_{pc}) of $[CuL^{H}(CH_3CN)][BF_4]_2$, $[CuL^{MMA}(CH_3CN)][BF_4]_2$, and $[CuL^{DMA}][BF_4]_2$ in CH_3CN at 100 mV/s.

	Potential (V vs Fc)		
	$[CuL^{H}(CH_3CN)][BF_4]_2$	**$[CuL^{MMA}(CH_3CN)][BF_4]_2$**	**$[CuL^{DMA}][BF_4]_2$**
Cu(II/I), E°′	-0.48	-0.23	-0.16
Cu(I/0), E_{pc}	-2.26	-0.96	-1.35

The cyclic voltammograms of $[CuL^{H}(CH_3CN)][BF_4]_2$, $[CuL^{MMA}(CH_3CN)][BF_4]_2$ and $[CuL^{DMA}][BF_4]_2$ are shown in Figure 2.4. Tabulated data for $E°'$ for the Cu(II/I) couples and E_{pc} for the Cu(I/0) reduction events are shown in Table 2.3.

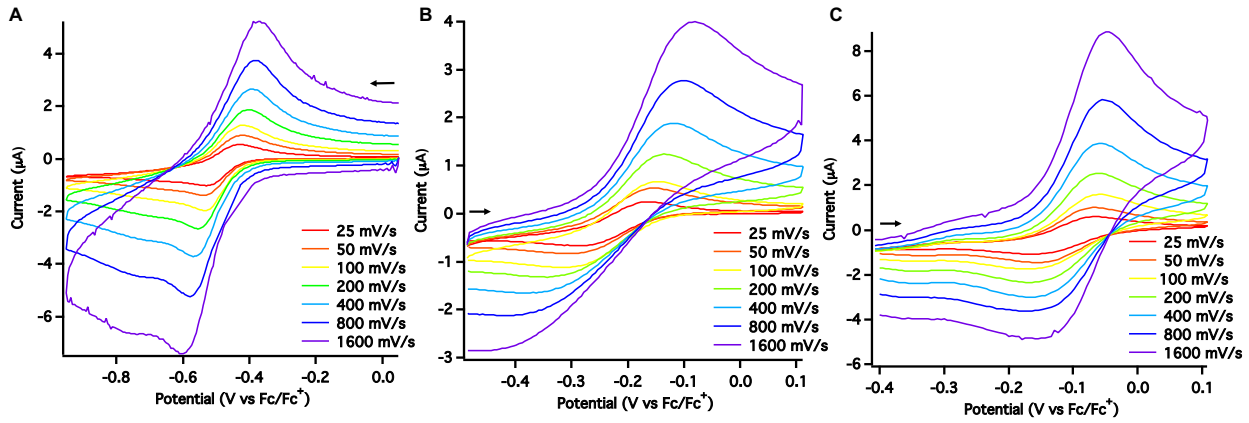

Figure 2.5. Scan rate dependent cyclic voltammograms of Cu(II/I) couple of 1.0 mM solutions of A) $[CuL^{H}(CH_3CN)][BF_4]_2$, B) $[CuL^{MMA}(CH_3CN)][BF_4]_2$, and C) $[CuL^{DMA}][BF_4]_2$ in 0.10 M Bu_4NBF_4 in CH_3CN at scan rates 25–1600 mV/s.

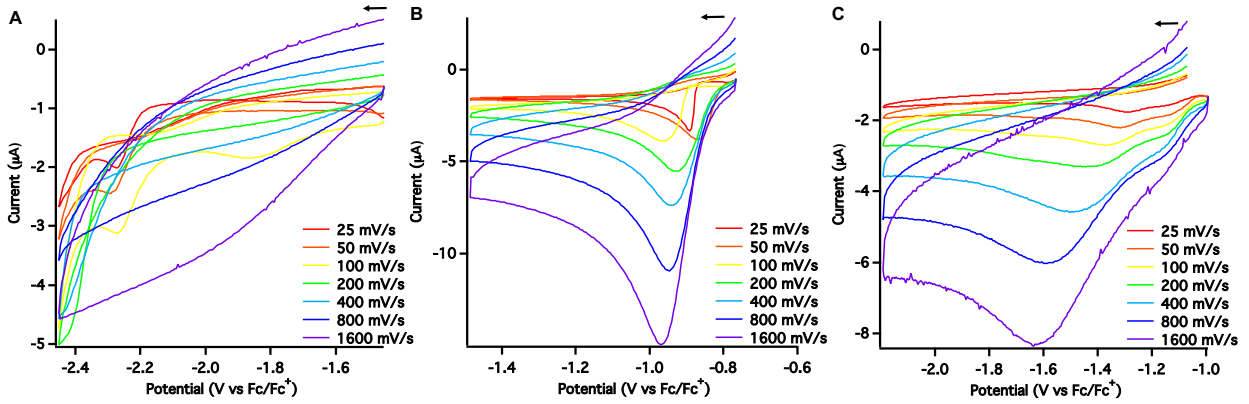

Figure 2.6. Scan rate dependent cyclic voltammograms of Cu(I/0) reduction event of 1.0 mM solutions of A) $[CuL^{H}(CH_3CN)][BF_4]_2$, B) $[CuL^{MMA}(CH_3CN)][BF_4]_2$, and C) $[CuL^{DMA}][BF_4]_2$ in 0.10 M Bu_4NBF_4 in CH_3CN at scan rates 25–1600 mV/s.

Table 2.4. Electrochemical values for Cu(II/I) couple of $[CuL^{H}(CH_3CN)][BF_4]_2$ at scan rates 25–1600 mV/s.

Scan Rate (mV/s)	i_a (µA)	i_c (µA)	i_a/i_c	E_{pa} (V)	E_{pc} (V)	ΔE_p (mV)	$E°'$ (V)
25	0.54	-1.02	0.53	-0.43	-0.53	101.05	-0.48
50	0.90	-1.39	0.64	-0.42	-0.54	121.32	-0.48
100	1.28	-1.97	0.65	-0.42	-0.53	121.32	-0.48
200	1.87	-2.66	0.70	-0.40	-0.55	151.62	-0.48
400	2.65	-3.72	0.71	-0.39	-0.57	176.74	-0.48
800	3.74	-5.24	0.71	-0.38	-0.58	196.70	-0.48
1600	5.23	-7.42	0.71	-0.37	-0.61	242.72	-0.49

Table 2.5. Electrochemical values for Cu(II/I) couple of $[CuL^{MMA}(CH_3CN)][BF_4]_2$ at scan rates 25–1600 mV/s.

Scan Rate (mV/s)	i_a (µA)	i_c (µA)	i_a/i_c	E_{pa} (V)	E_{pc} (V)	ΔE_p (mV)	$E°'$ (V)
25	0.56	-0.58	0.97	-0.16	-0.29	127.59	-0.22
50	0.76	-0.79	0.96	-0.16	-0.29	132.91	-0.22
100	1.16	-1.10	1.06	-0.14	-0.31	168.13	-0.22
200	1.49	-1.44	1.04	-0.12	-0.33	213.22	-0.23
400	2.00	-1.81	1.11	-0.11	-0.36	253.68	-0.24
800	2.74	-2.59	1.06	-0.10	-0.40	298.62	-0.25
1600	3.77	-3.42	1.10	-0.08	-0.40	318.10	-0.24

Table 2.6. Electrochemical values for Cu(II/I) couple of $[CuL^{DMA}][BF_4]_2$ at scan rates 25–1600 mV/s.

Scan Rate (mV/s)	i_a (µA)	i_c (µA)	i_a/i_c	E_{pa} (V)	E_{pc} (V)	ΔE_p (mV)	$E°'$ (V)
25	0.59	-1.08	0.55	-0.06	-0.16	98.70	-0.11
50	1.00	-1.14	0.88	-0.06	-0.33	60.92	-0.20
100	1.59	-1.75	0.91	-0.06	-0.17	113.65	-0.12
200	2.53	-2.34	1.08	-0.06	-0.16	106.12	-0.11
400	3.87	-3.01	1.29	-0.06	-0.16	106.10	-0.11
800	5.82	-3.63	1.60	-0.05	-0.17	107.32	-0.11
1600	8.86	-4.90	1.81	-0.05	-0.18	109.96	-0.11

The cyclic voltammograms of $[CuL^{H}(CH_3CN)][BF_4]_2$ exhibit a quasi-reversible event at $E°' = -0.48$ V (at 100 mV/s, $i_a/i_c = 0.65$, $\Delta E_p = 121$ mV compared to $\Delta E_p = 59$ mV for $FeCp_2^{0/+}$), attributed to the Cu(II/I) couple. The scan rate dependence is shown in Figure 2.5A and the

parameters are listed in Table 2.4. ΔE_p increases with scan rate as expected for a quasi-reversible redox event, indicating that the rate of electron transfer is slow and on the same order of magnitude as mass transport. The five-coordinate complex likely dissociates the acetonitrile ligand upon reduction to Cu(I), which may also contribute to the quasi-reversible nature of this couple. An irreversible reduction event attributed to the Cu(I/0) event (Figure 2.6A) was observed at E_{pc} = −2.26 V, which remained completely irreversible at the scan rates examined (25–1600 mV/s).

Cyclic voltammograms of $[CuL^{MMA}(CH_3CN)][BF_4]_2$ exhibited a quasi-reversible event at $E°' = -0.23$ V (at 100 mV/s, $i_a/i_c = 1.06$, $\Delta E_p = 168$ mV compared to $\Delta E_p = 152$ mV for $FeCp_2^{0/+}$) attributed to the Cu(II/I) couple. The scan rate dependence is shown in Figure 2.5B and the parameters are listed in Table 2.5. ΔE_p increases with scan rate as expected for a quasi-reversible redox event, and there is a loss in current for the return oxidation indicating that the rate of electron transfer is slow. The five-coordinate complex likely dissociates the acetonitrile ligand upon reduction to Cu(I), however the release of some steric strain may contribute to the more "reversible" nature of this couple compared to that of $[CuL^{H}(CH_3CN)][BF_4]_2$. The Cu(I/0) reduction event (Figure 2.6B) was observed at E_{pc} = −0.96 V, which remained completely irreversible at all scan rates (25–1600 mV/s).

Cyclic voltammetry of $[CuL^{DMA}][BF_4]_2$ at 100 mV/s also displayed two reduction events. $[CuL^{DMA}][BF_4]_2$ has a quasi-reversible event at $E°' = -0.12$ V (at 100 mV/s, $i_a/i_c = 0.91$, $\Delta E_p = 114$ mV compared to $\Delta E_p = 106$ mV for $FeCp_2^{0/+}$) attributed to the Cu(II/I) couple, shown in Figure 2.5C. The changes in anodic and cathodic currents by scan rate indicate slow kinetics (Table 2.6). The reduction of Cu(I) was observed at $E_{pc} = -1.35$ V and remained irreversible at the scan rates examined (25–1600 mV/s).

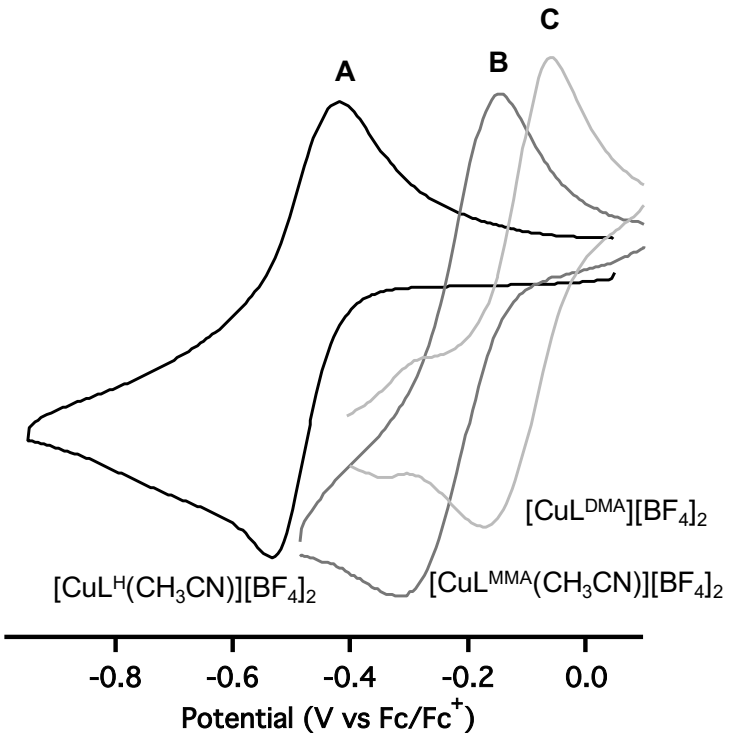

Figure 2.7. Cyclic voltammograms of Cu(II/I) couple of 1 mM solutions of A) $[CuL^{H}(CH_3CN)][BF_4]_2$, B) $[CuL^{MMA}(CH_3CN)][BF_4]_2$, and C) $[CuL^{DMA}][BF_4]_2$ in 0.10 M Bu_4NBF_4 in CH_3CN at 100 mV/s.

The Cu(II/I) couples are observed at significantly more positive potentials for the compounds with amine substituted ligands, which act as electron donating groups, ($[CuL^{MMA}(CH_3CN)][BF_4]_2$ and $[CuL^{DMA}][BF_4]_2$ versus $[CuL^{H}(CH_3CN)][BF_4]_2$) (Figure 2.7). The one electron reduction of d^9-Cu(II) to d^{10}-Cu(I) is accompanied by a geometric rearrangement to see-saw or tetrahedral from a pseudo square pyramidal in $[CuL^{H}(CH_3CN)]^{2+}$ and $[CuL^{MMA}(CH_3CN)]^{2+}$ or square planar geometry in $[CuL^{DMA}]^{2+}$. It is likely that releasing the steric strain from the nearly coplanar dimethylamine functionalities in $[CuL^{DMA}]^{2+}$ by reduction to the corresponding tetrahedral complex contributes to the positive reduction potential compared to $[CuL^{H}(CH_3CN)]^{2+}$ and $[CuL^{MMA}(CH_3CN)]^{2+}$ which are not sterically strained. This steric effect on the Cu(II/I) redox potential has been observed in other tetradentate copper complexes.[48] The positive potential for the Cu(II/I) couple and the smallest potential peak to peak separation (ΔE_p at

100 mV/s) for the $[CuL^{DMA}][BF_4]_2$ divalent complex is consistent with the observation that when left in solution, $[CuL^{DMA}]^{2+}$ reduces to $[CuL^{DMA}]^{1+}$ over time.

Ultraviolet-Visible Spectroscopy

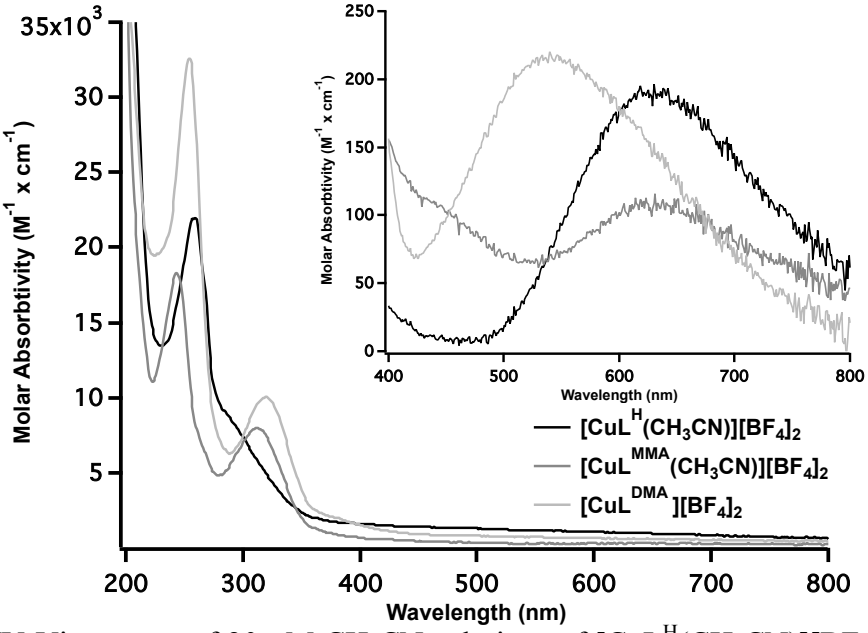

Figure 2.8. UV-Vis spectra of 20 μM CH_3CN solutions of $[CuL^{H}(CH_3CN)][BF_4]_2$ (black trace), $[CuL^{MMA}(CH_3CN)][BF_4]_2$ (dark gray trace), and $[CuL^{DMA}][BF_4]_2$ (light gray trace). Inset: UV-Vis spectra of 1 mM CH_3CN solutions, *d-d* transitions.

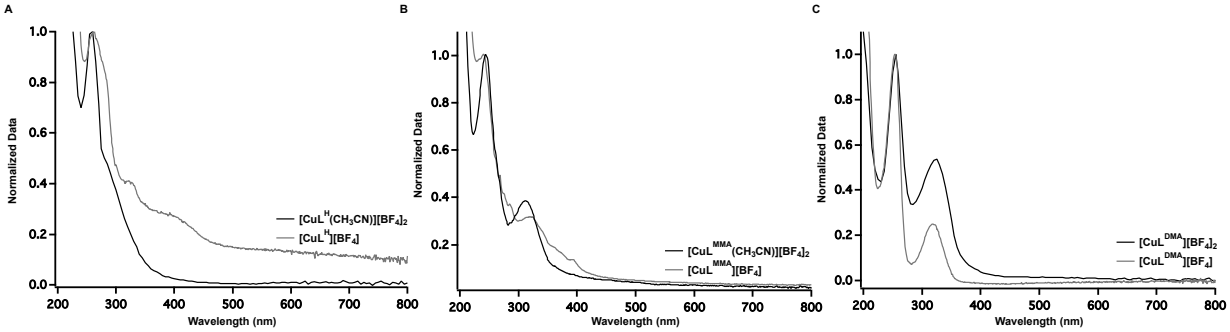

Figure 2.9. Normalized UV-Vis spectra of 10 μM CH_3CN solutions of divalent (black trace) and monovalent (gray trace) copper complexes A) $[CuL^{H}(CH_3CN)][BF_4]_2$ and $[CuL^{H}][BF_4]$, B) $[CuL^{MMA}(CH_3CN)][BF_4]_2$ and $[CuL^{MMA}][BF_4]$, C) $[CuL^{DMA}][BF_4]_2$ and $[CuL^{DMA}][BF_4]$.

UV–Vis spectra of all the divalent complexes were taken in CH_3CN solutions and are shown in Figure 2.8. The UV-Vis profile of $[CuL^{H}(CH_3CN)][BF_4]_2$, $[CuL^{MMA}(CH_3CN)][BF_4]_2$, and $[CuL^{DMA}][BF_4]_2$ show minimal change in the two absorption bands between 200-400 nm upon

reduction of the metal center aside from changes in the molar absorptivity, shown in Figure 2.9. The weak dependence of the spectra on the metal oxidation state indicate the absorption bands are due to pyridyl π–π* transitions within the ligand. The *d*-*d* transitions associated with the divalent Cu(II) complexes are shown in Figure 2.8, inset.

Table 2.7. Maximum wavelength (λ_{max}) and molar absorptivity (ε) values for the divalent copper complexes $[CuL^{H}(CH_3CN)][BF_4]_2$, $[CuL^{MMA}(CH_3CN)][BF_4]_2$,and $[CuL^{DMA}][BF_4]_2$ determined by UV-Vis.

	π–π*		**π–π***		**d–d**	
	λ_{max}(nm)	**ε ($M^{-1} \times cm^{-1}$)**	**λ_{max}(nm)**	**ε ($M^{-1} \times cm^{-1}$)**	**λ_{max}(nm)**	**ε ($M^{-1} \times cm^{-1}$)**
$[CuL^{H}(CH_3CN)][BF_4]_2$	260	11,000	-	-	625	200
$[CuL^{MMA}(CH_3CN)][BF_4]_2$	244	12,000	312	6,700	630	21
$[CuL^{DMA}][BF_4]_2$	255	26,000	325	9,200	541	250

The primary absorption band has a maximum wavelength (λ_{max}) range from 244–260 nm and is observed for all complexes. The primary absorption band for $[CuL^{MMA}(CH_3CN)][BF_4]_2$ and $[CuL^{DMA}][BF_4]_2$ display a hypsochromic shift to shorter wavelengths compared to $[CuL^{H}(CH_3CN)][BF_4]_2$, due to the electron donating nature of the amine substituents on the L^{MMA} and L^{DMA} ligands. $[CuL^{DMA}][BF_4]_2$ containing is shifted to the longest wavelength indicating L^{DMA} is the most electron donating ligand of the series. The secondary absorption band, seen only in $[CuL^{MMA}(CH_3CN)][BF_4]_2$ and $[CuL^{DMA}][BF_4]_2$, have a λ_{max} around 312–325 nm indicative of the tautomeric structure possible for heteroatom substituted pyridines from the ligand.[49] $[CuL^{DMA}][BF_4]_2$ is shifted to the longest wavelength, as shown in Table 2.7.

The UV-Vis spectra of the divalent complexes exhibit a broad *d*–*d* absorption band in the range of 541–630 nm with low molar absorptivity values. This feature is characteristic for five-

coordinate Cu(II) polypyridyl complexes with a square pyramidal or square planar geometry.[44,50-54]

Direct correlations cannot be made across all three divalent compounds due to the square planar geometry of $[CuL^{DMA}][BF_4]_2$ versus the pentacoordinate geometry of $[CuL^{H}(CH_3CN)][BF_4]_2$ and $[CuL^{MMA}(CH_3CN)][BF_4]_2$. However, it is apparent that the *d-d* transition for $[CuL^{DMA}][BF_4]_2$ is the most energetically intensive due to the short wavelength of the absorption band.

Infrared Spectroscopy

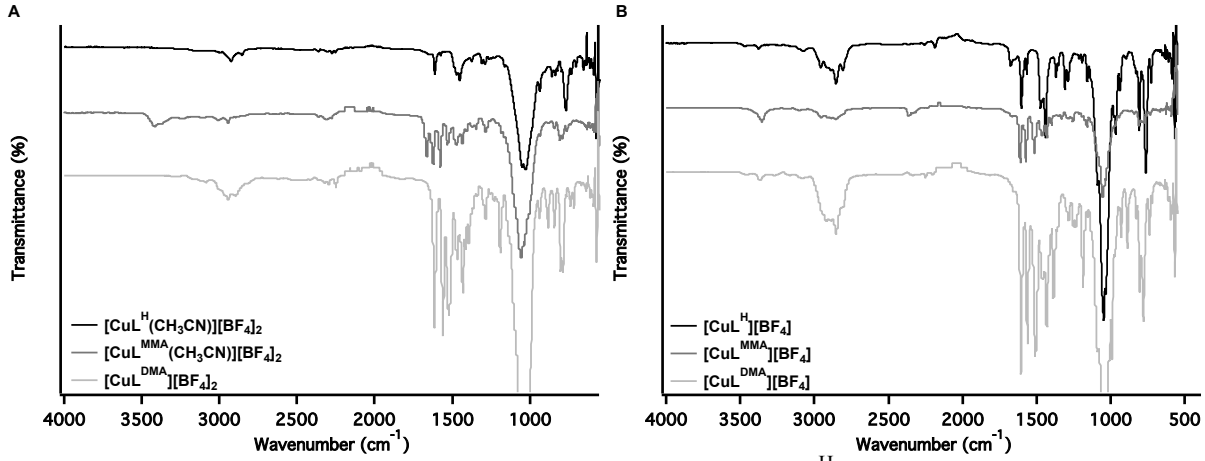

Figure 2.10. IR spectra of A) divalent complexes; $[CuL^{H}(CH_3CN)][BF_4]_2$ (black trace), $[CuL^{MMA}(CH_3CN)][BF_4]_2$ (dark gray), and $[CuL^{DMA}][BF_4]_2$ (light gray) and B) monovalent; complexes $[CuL^{H}][BF_4]$ (black trace), $[CuL^{MMA}][BF_4]$ (dark gray), and $[CuL^{DMA}][BF_4]$ (light gray).

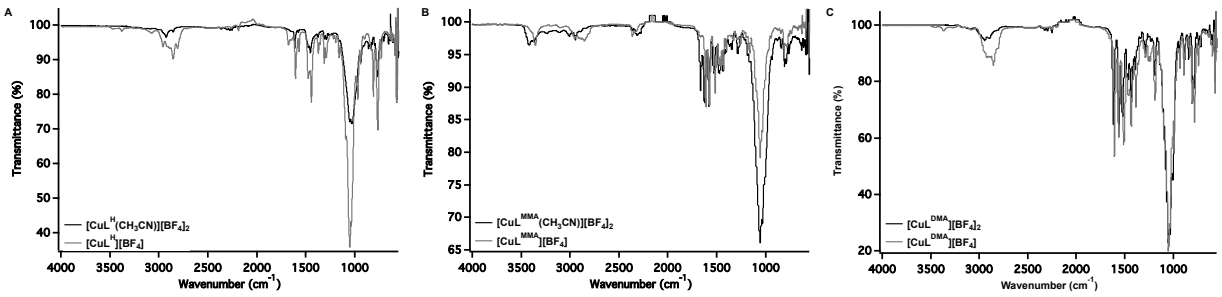

Figure 2.11. IR spectra of divalent (black trace) and monovalent complexes (gray trace) A) $[CuL^{H}(CH_3CN)][BF_4]_2$ and $[CuL^{H}][BF_4]$, B) $[CuL^{MMA}(CH_3CN)][BF_4]_2$ and $[CuL^{MMA}][BF_4]$, C) $[CuL^{DMA}][BF_4]_2$ and $[CuL^{DMA}][BF_4]$.

Solid state infrared spectra of the divalent complexes $[CuL^{H}(CH_3CN)][BF_4]_2$, $[CuL^{MMA}(CH_3CN)][BF_4]_2$, and $[CuL^{DMA}][BF_4]_2$ were taken and are shown in Figure 2.10A while the monovalent complexes are shown in Figure 2.10B. There are features that common to all six complexes in the IR spectra. All complexes exhibit a strong absorption band at 1048 cm^{-1} which belongs to the B–F stretching frequency of the BF_4^- anions (Figure 2.10). In the 3000 cm^{-1} region, all six complexes contain C-H stretching frequencies of both sp^2 and sp^3 hybridized carbons indicative of the alkane and aromatic functionalities of the ligand. However, a major difference between the ligand structures can be seen via the N–H stretching frequency of the L^{MMA} ligand, which contains a secondary amine. The divalent complex $[CuL^{MMA}(CH_3CN)][BF_4]_2$ exhibits a stretching frequency at 3410 cm^{-1} which is typical for amines and is notably higher than the N–H stretching frequency for the reduced monovalent complex, $[CuL^{MMA}][BF_4]$ (ν_{N-H} = 3355 cm^{-1}). $[CuL^{MMA}(CH_3CN)][BF_4]_2$ contains hydrogen-bonding interactions that are not possible in the reduced complex due to the geometry. The hydrogen-bonding interaction likely shifts the N–H stretching to a higher frequency because it requires more energy to vibrate. Otherwise, there are no major features of interest that change between the divalent oxidation state of the copper complexes in comparison to the monovalent complexes (Figure 2.11).

Electron Paramagnetic Resonance Spectroscopy

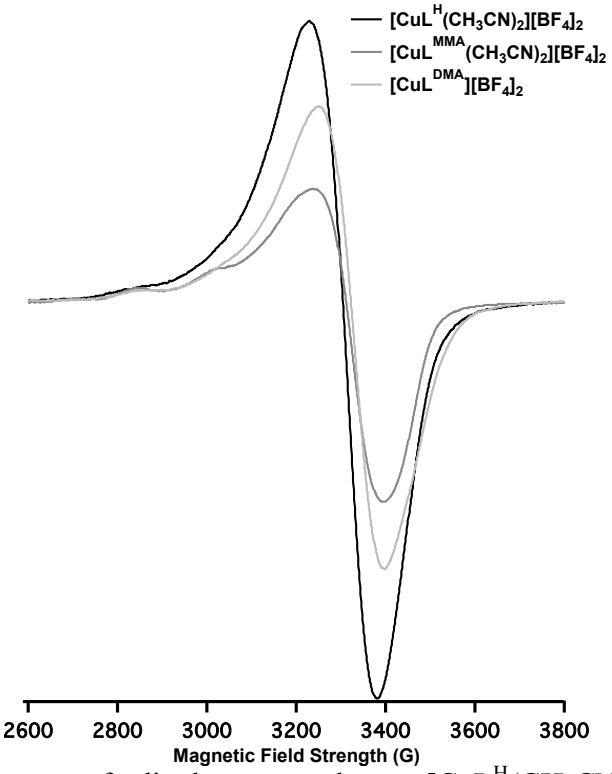

Figure 2.12. EPR spectra of divalent complexes $[CuL^{H}(CH_3CN)][BF_4]_2$ (black trace), $[CuL^{MMA}(CH_3CN)][BF_4]_2$ (dark gray trace) and $[CuL^{DMA}][BF_4]_2$ (light gray trace). All samples taken as 10 mM frozen CH_3CN solutions at 10 K.

Table 2.8. EPR g values of $[CuL^{H}(CH_3CN)][BF_4]_2$, $[CuL^{MMA}(CH_3CN)][BF_4]_2$, and $[CuL^{DMA}][BF_4]_2$ at 10 and 77 K.

	10 K		**77 K**	
	$g_\perp$	**$g_{//}$(A, mHZ)**	**$g_\perp$**	**$g_{//}$(A, mHZ)**
$[CuL^{H}(CH_3CN)][BF_4]_2$	2.09	-	2.09	-
$[CuL^{MMA}(CH_3CN)][BF_4]_2$	2.08	2.35 (511)	2.08	2.25 (528)
$[CuL^{DMA}][BF_4]_2$	2.07	2.22 (513)	2.07	2.42

All three divalent copper complexes at 10 K exhibit a signal with $g_\perp$ value of 2.1 which is consistent with a S=1/2 Cu(II) center (Figure 2.12). All g values and A values are tabulated in Table 2.8. The $[CuL^{MMA}(CH_3CN)][BF_4]_2$ shows hyperfine with a $g_{//}$ value of 2.35 and a splitting

of 511 mHz while the $[CuL^{DMA}][BF_4]_2$ complex shows a $g_{//}$ value of 2.22 with 513 mHz which is consistent with geometries with four-fold symmetry such as square pyramidal and square planar.[55]

2.3.3. Protonation Studies of Monovalent Copper Complexes

^{1}H NMR Spectroscopy

In an effort to estimate the pK_a of the pendant bases, protonation studies of the diamagnetic $[CuL^{DMA}][BF_4]$ were investigated using ^{1}H NMR spectroscopy, shown in Figure 2.13. Addition of one equivalent of $[PhNH_3][BF_4]$ (pK_a = 10.62 in CH_3CN)[56] to $[CuL^{DMA}][BF_4]$ in CD_3CN resulted in new resonances that correspond with aniline and no resonances that correspond with anilinium, indicating complete proton transfer. No resonances consistent with free ligand were observed. The protonation is cleanly reversible; addition of one equivalent of the strong base DBU (1,8-diazabicyclo[5.4.0] undec-7-ene, pK_a = 24.34 in CH_3CN)[56] regenerated the initial copper complex as well as protonated DBU.

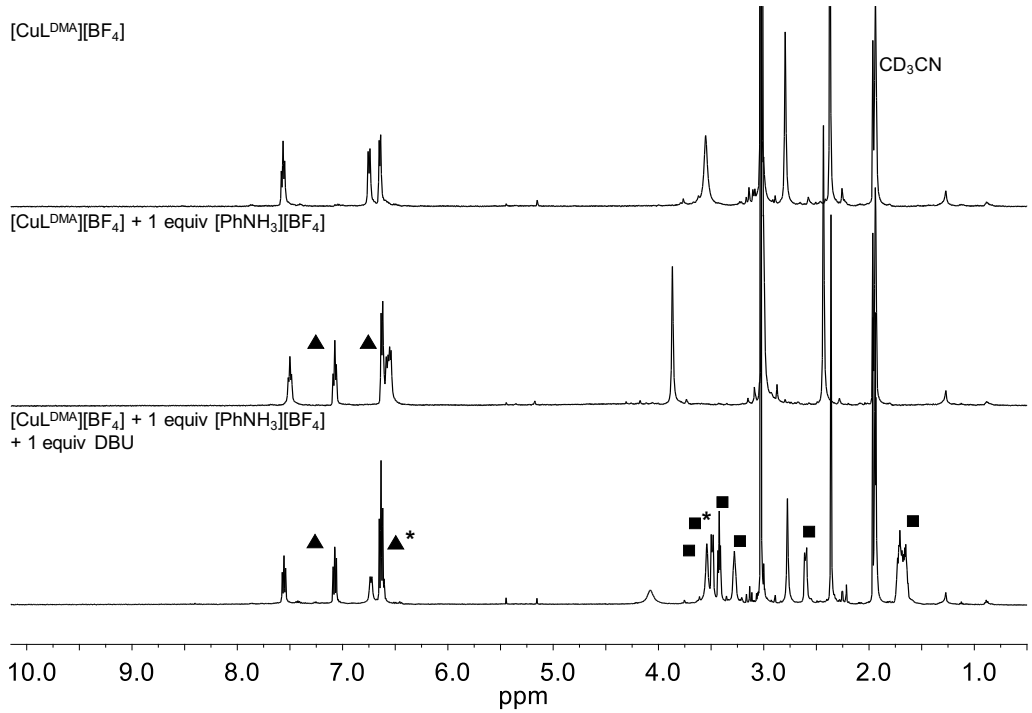

Figure 2.13. ^{1}H NMR spectra of [CuL^{DMA}][BF$_4$] in the presence of acid and base. Top: complex with no acid or base present. Middle: 1 equiv [PhNH$_3$][BF$_4$] added, triangle symbol (▲) indicates aniline resonances. Bottom: 1 equiv DBU added, square symbol (■) indicates [HDBU][BF$_4$] resonances. Asterisks (*) indicate an overlap with a resonance from the complex.

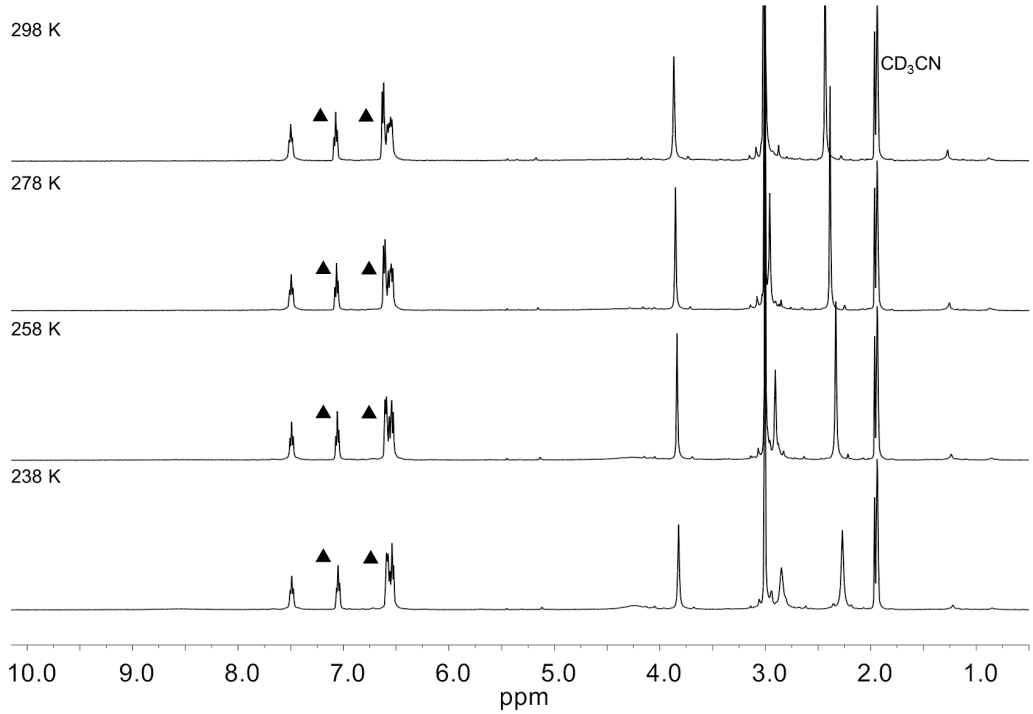

Figure 2.14. Variable temperature ^{1}H NMR of protonated [CuL^{DMA}][BF$_4$] complex in CD$_3$CN. Temperatures range from 238 K to 298 K. Triangle symbol (▲) indicates aniline resonances.

Table 2.9. Tabulated chemical shifts (ppm) in ^{1}H NMR spectra of protonated [CuL^{DMA}][BF_4] complex in CD_3CN.

	ppm	
	Complex	**Complex + [$PhNH_3$][BF_4]**
Ar-*H*	7.57	7.5
Ar-*H*	6.75	6.57
Ar-*H*	6.64	6.55
Ar-C*H*$_2$-N	3.55	3.87
N(C*H*$_3$)$_2$	3.03	3.02
C*H*$_2$CH$_2$	2.8	3.02
R$_2$NC*H*$_3$	2.37	2.43
N-*H* (298-238 K)	-	4.24

In the ^{1}H NMR spectrum of the singly protonated [CuL^{DMA}][BF_4], a broad peak at 4.25 ppm resolved when the temperature was lowered to 238 K, which is assigned to the proton transferred from anilinium. The ethylenediamine resonances on the complex were shifted downfield, with the methylene protons adjacent to the pyridine shifting downfield by the largest amount (0.32 ppm), followed by the methylene protons in the ethyl backbone shifting downfield (0.20 ppm) and the methyl resonances on the nitrogen of the amine backbone shifting downfield (0.06 ppm). In contrast, the methyl resonances corresponding to the pendant bases only shift upfield by 0.01 ppm (Table 2.9). This trend in change of chemical shifts indicated protonation occurred on the tertiary amine in the ethylenediamine backbone instead of the pendant base. Variable temperature ^{1}H NMR spectroscopy experiments on the protonated complex (Figure 2.14) indicated the methylene protons in the ethyl backbone and methyl resonances on the nitrogen of the amine backbone shift upfield as the temperature is lowered. These experiments suggested protonation occurs on the ethylenediamine ligand backbone, as opposed to the pendant bases.

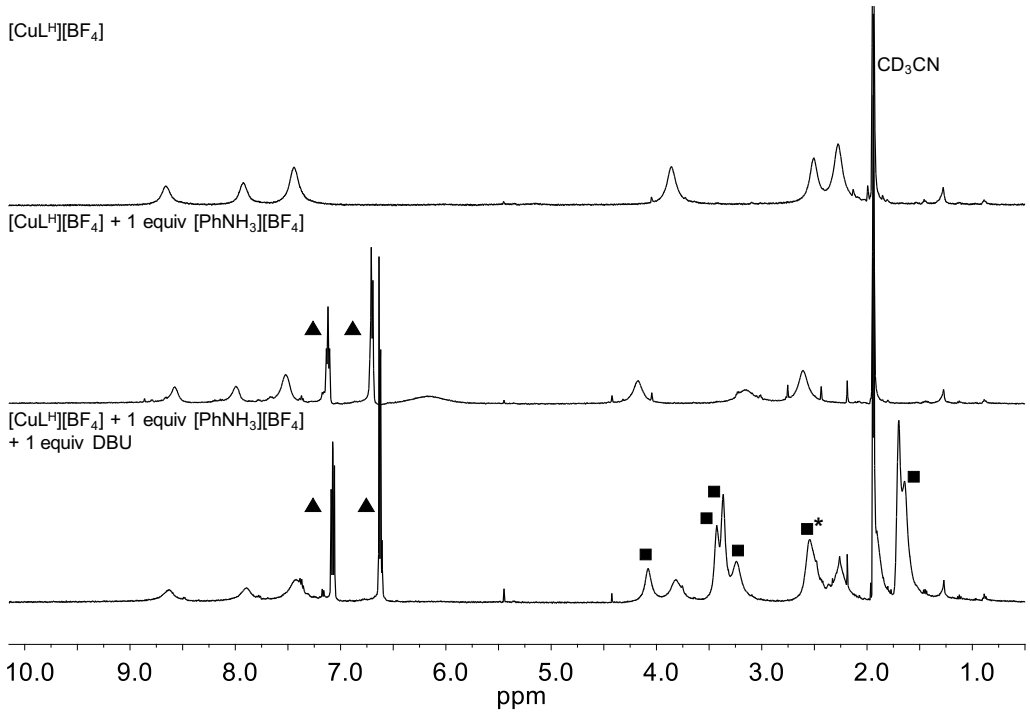

Figure 2.15. ^{1}H NMR spectra of [CuL^{H}][BF$_4$] in the presence of acid and base. Top: complex with no acid or base present. Middle: 1 equiv [PhNH$_3$][BF$_4$] added, triangle symbol (▲) indicates aniline resonances. Bottom: 1 equiv DBU added, square symbol (■) indicates [HDBU][BF$_4$] resonances. Asterisks (*) indicate an overlap with a resonance from the complex.

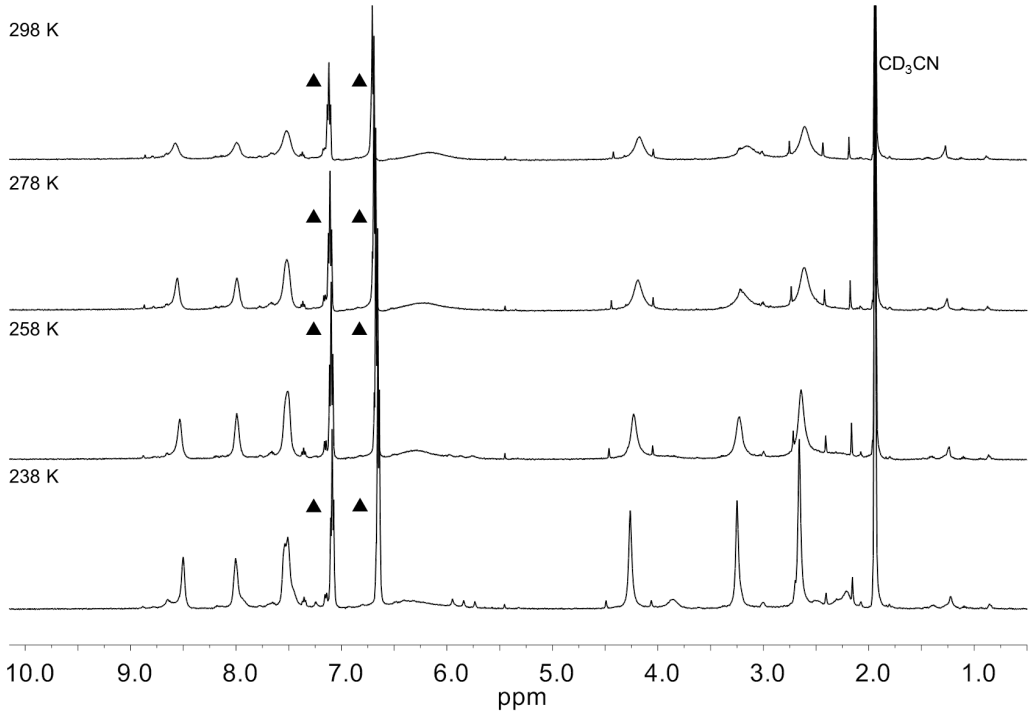

Figure 2.16. Variable temperature ^{1}H NMR of protonated [CuL^{H}][BF$_4$] complex in CD$_3$CN. Temperatures range from 238 K to 298 K. Triangle symbol (▲) indicates aniline resonances.

Table 2.10. Tabulated chemical shifts (ppm) in ^{1}H NMR spectra of protonated [CuL^H][BF_4] complex in CD_3CN.

	ppm	
	Complex	**Complex + [$PhNH_3$][BF_4]**
Ar-*H*	8.65	8.57
Ar-*H*	7.92	7.99
Ar-*H*	7.44	7.52
Ar-*H*		
Ar-C*H*$_2$-N	3.86	4.17
C*H*$_2$CH$_2$	2.5	3.16
R$_2$NC*H*$_3$	2.27	2.61
N-*H* (298-238 K)	-	6.17

In order to confirm the protonation location, the same ^{1}H NMR spectroscopic study was performed on [CuL^H][BF_4], shown in Figure 2.15. Addition of one equivalent of [$PhNH_3$][BF_4] in CD_3CN resulted in a similar downfield shift of the ethylenediamine resonances, with the methylene protons in the ethyl backbone shifting downfield by the largest amount (0.66 ppm), followed by the methyl resonances on the nitrogen of the amine backbone (0.34 ppm) and the methylene protons adjacent to the pyridine shifting downfield (0.31 ppm) (Table 2.10). After variable temperature ^{1}H NMR spectroscopy experiments on the protonated complex (Figure 2.16), the broad resonance at 6.21 ppm was assigned to the protonated amine on the complex. These changes are consistent with those observed with [CuL^{DMA}][BF_4], confirming the assignment of the site of protonation.

A variety of two-dimensional NMR experiments were performed to attempt to correlate the N-H proton to adjacent protons to corroborate the site of protonation. Homonuclear correlation spectroscopy (COSY) was attempted on the protonated [CuL^{DMA}][BF_4] at low temp (238K) and long range but no resonances corresponding to a correlation with the acidic proton were seen.

Heteronuclear NMR experiments $^{1}H–^{15}N$ heteronuclear single-quantum correlation spectroscopy (HSQC) and heteronuclear multiple-quantum correlation (HMQC) were also attempted, but due to the low abundance of natural ^{15}N in the samples, no signals were seen and thus none of the correlation techniques attempted were successful at revealing more useful information.

Infrared Spectroscopy

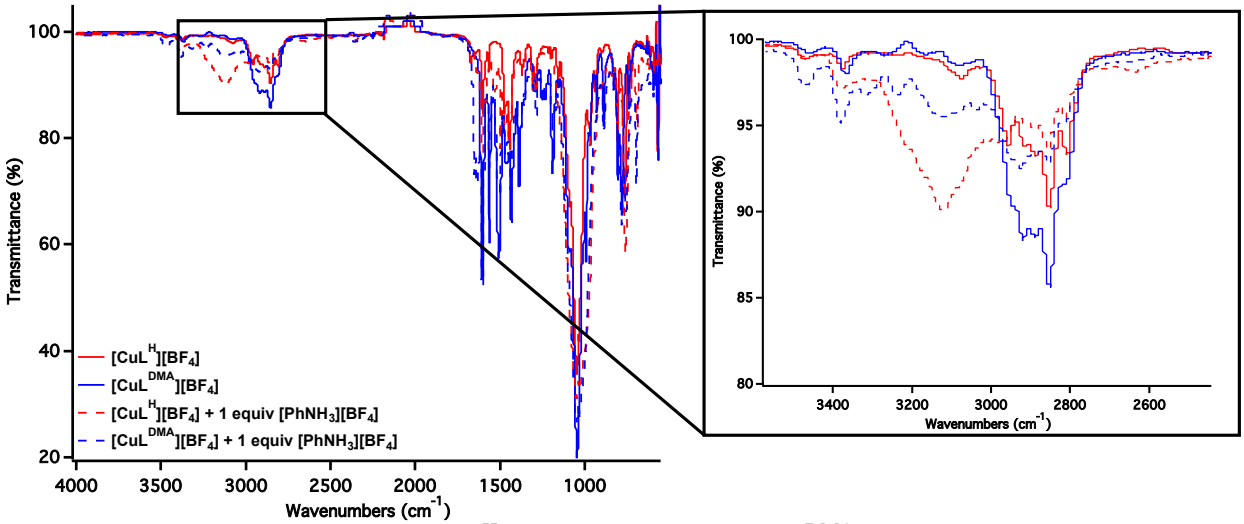

Figure 2.17. Infrared spectra of $[CuL^{H}][BF_4]$ (red trace), $[CuL^{DMA}][BF_4]$ (blue trace), protonated $[CuL^{H}][BF_4]$ (red dotted trace) and protonated $[CuL^{DMA}][BF_4]$ (blue dotted trace).

Infrared spectra of the protonated compounds of $[CuL^{H}][BF_4]$ and $[CuL^{DMA}][BF_4]$ were performed to confirm the site of protonation. Both protonated complexes exhibited a broad absorbance at $\nu_{N–H}$ = 3120 cm^{-1}, which is assigned to the N–H vibration, shown in Figure 2.17. This observation also denotes that protonation on both compounds occurs at the same location on the ligand backbone; thus the dimethylamine is not the site of protonation.

A ^{13}C NMR spectroscopy study of the ligand L^{H} at various pH values also suggests the tertiary backbone amine is protonated first.[44] It is unexpected that once the ligand is metal bound that the amines on the ligand backbone are more basic than the pendant amines. However, it is worth noting that the pK_a of protonated dimethylaniline in acetonitrile is 11.43[57] while the pK_a of

protonated trialkylated amines range from 18 to 20 (protonated triethylamine is 18.82,[57] and singly protonated N,N′-dimethylethylenediamine is 19.63).[58] From these examples, the protonated amines in the ligand backbone are estimated to be ~7 pK_a units higher than the protonated pendant bases in the free ligand. Although ligation to copper will reduce the basicity of the bound amine, protonation likely results in loss of coordination of the ethylenediamine nitrogens. The reversibility of the protonation event indicates that the amines re-coordinate upon deprotonation.

2.3.4. Reactivity with Dioxygen

Cyclic Voltammetry

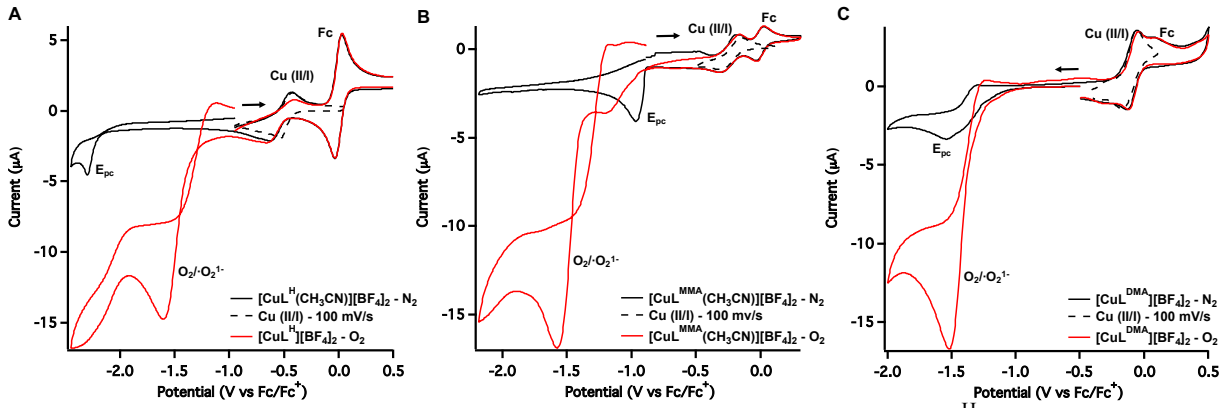

Figure 2.18. Cyclic voltammograms of 1.0 mM solutions of A) $[CuL^{H}(CH_3CN)][BF_4]_2$, B) $[CuL^{MMA}(CH_3CN)][BF_4]_2$, and C) $[CuL^{DMA}][BF_4]_2$ under N_2 (black trace) and O_2 (red trace), in 0.10 M Bu_4NBF_4 in CH_3CN at 100 mv/s. Dotted black trace is the isolated Cu(II/I) couple at 100 mV/s.

Cyclic voltammetry studies of all the divalent copper complexes in the presence of 1 atm O_2 (as air), show irreversible waves with large currents at E_{pc} = −1.60 V which is reduction of oxygen by the electrode (Figure 2.18). However, there are interesting features to note about the Cu(II/I) couples for the complexes.

The complex containing the non-pendant base ligand L^H $[CuL^{H}(CH_3CN)][BF_4]_2$ loses quasi-reversibility at the Cu(II/I) event ($E°'$ = −0.48 V) during the return oxidation after dioxygen is added indicating some interaction with oxygen as the Cu(I) oxidation state. After addition of

dioxygen, the return oxidation Cu(II/I) event ($E°'$ = −0.23 V) of $[CuL^{MMA}(CH_3CN)][BF_4]_2$ maintains quasi-reversibility with a slight positive shift of the oxidation event. Unlike $[CuL^{H}(CH_3CN)][BF_4]_2$ and $[CuL^{MMA}(CH_3CN)][BF_4]_2$ the Cu(II/I) event ($E°'$ = −0.12 V) of complex $[CuL^{DMA}][BF_4]_2$ remains the same under an oxygen atmosphere, indicating no reactivity with dioxygen. It is possible the metal center cannot be accessed by the substrate.

^{1}H NMR Spectroscopy

The diamagnetic monovalent species were exposed to 1 atm pure oxygen and the reaction was followed by ^{1}H NMR spectroscopy to determine if paramagnetic Cu(II) compounds were formed.

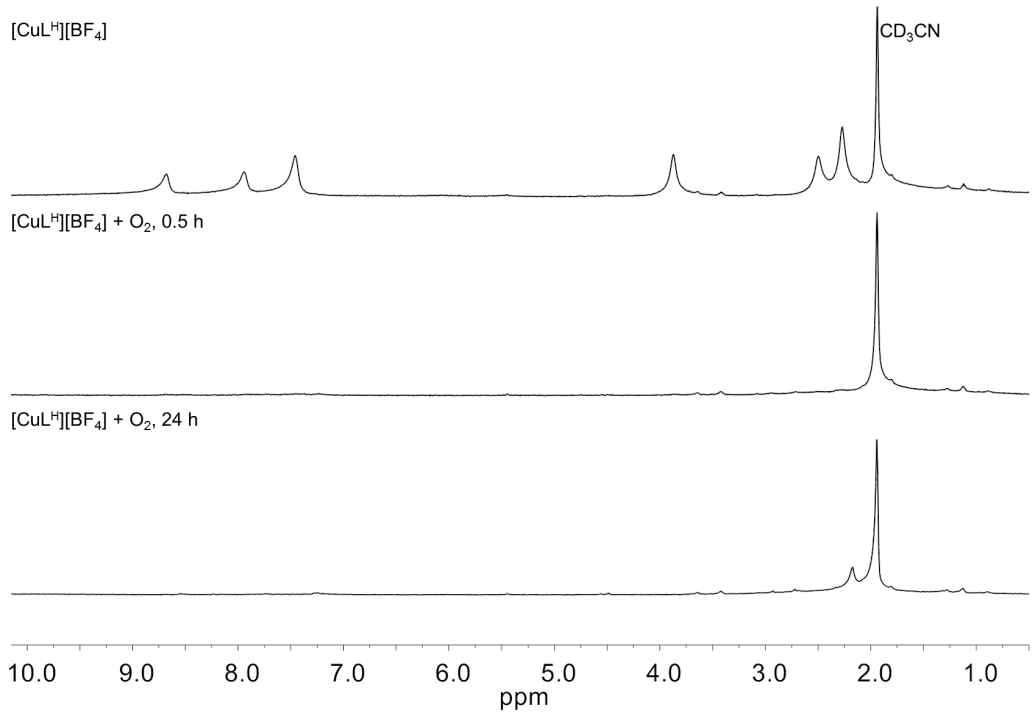

Figure 2.19. ^{1}H NMR spectra of $[CuL^{H}][BF_4]$ upon exposure to 1 atm O_2. Top: complex with no oxygen present. Middle: complex plus oxygen after 30 minutes. Bottom: complex plus oxygen after 24 hours.

The $[CuL^H][BF_4]$ complex becomes entirely paramagnetic 30 minutes after exposure to oxygen and maintains paramagnetism for 24 hours along with a color change from yellow to blue (Figure 2.19). This data suggests the monovalent complex has reacted with oxygen to generate a paramagnetic species. The NMR reaction solution was then analyzed by UV-Vis, IR, EPR, and MS to attempt to determine the presence of newly formed species and will be discussed below.

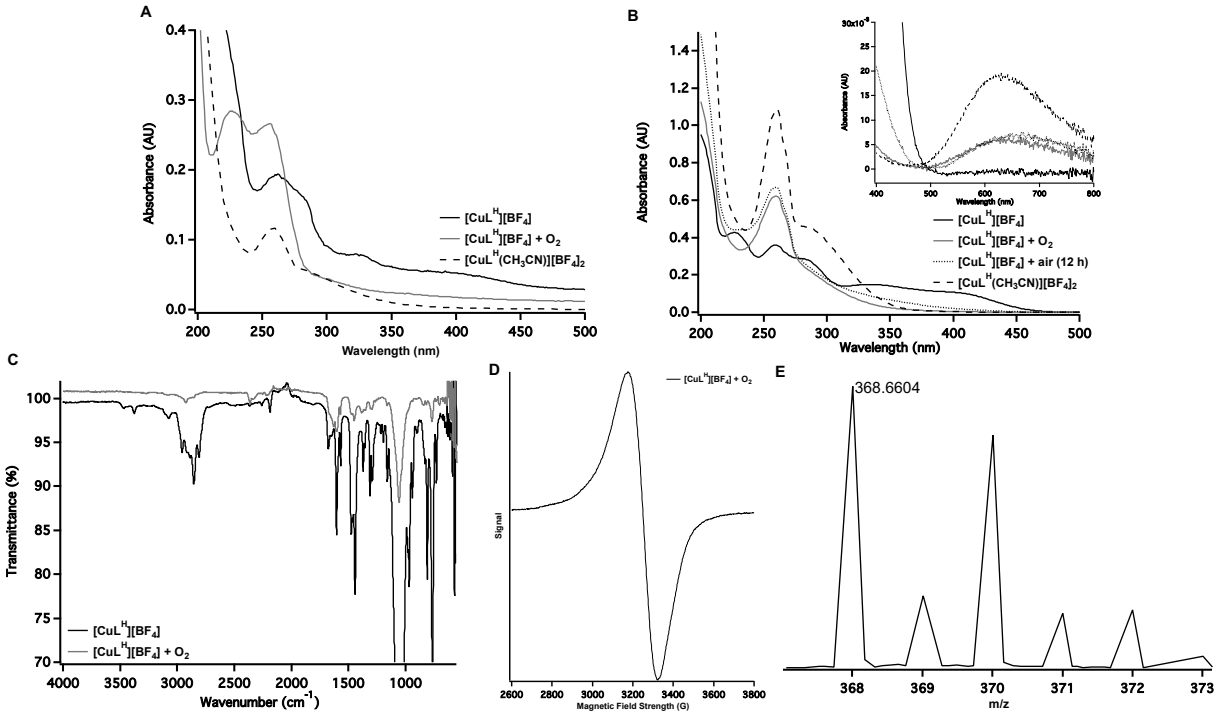

Figure 2.20. Spectra collected of the reaction mixture 24 hours after the addition of 1 atm O_2 to $[CuL^H][BF_4]$: A) UV-Vis spectra of 10 μM CH_3CN solution. B) UV-Vis spectra of 1 mM CH_3CN solution, Inset: Zoomed in *d-d* transition region. $[CuL^H][BF_4]$ (black trace), $[CuL^H][BF_4]$ plus O_2 after 24 h (gray trace), $[CuL^H][BF_4]$ plus O_2 (air) after 12 h (dotted trace), pristine $[CuL^H(CH_3CN)][BF_4]_2$ (dashed trace). C) IR spectra of $[CuL^H][BF_4]$ (black trace) and $[CuL^H][BF_4]$ under O_2 (gray trace). D) EPR spectrum $[CuL^H][BF_4]$ plus O_2 (black trace). Samples taken as 10 mM frozen CH_3CN solutions at 77 K. E) MS spectrum of reaction mixture.

After exposure to oxygen the $[CuL^H][BF_4]$ complex has developed a new absorption band at 226 nm at a concentration of 10 μM (Figure 2.20). Additionally, the spectral profile does not match that of the monovalent or divalent complex. At 1 mM, a *d-d* transition appears and the overall spectrum matches that of the UV-Vis experiment performed with air as the oxygen source.

The EPR spectrum of the reaction indicates a paramagnetic Cu(II) species has been formed with a $g_{\perp}$ value of 2.10 which matches the $[CuL^{H}(CH_3CN)][BF_4]_2$ complex at 77K (Table 2.8). Unfortunately, The IR spectrum does not reveal anything of significance. Resonance Raman spectroscopy is needed to determine charge transfer absorptions and vibrations of Cu-O and O-O events. The mass spectrum for the reaction mixture shows a possible peak relating to a hydrogen peroxide bound species such as $L^{H}Cu\text{-}OOH_2$ (m/z = 368.7) but further studies would be needed. Overall, it is believed dioxygen has reacted with Cu(I) to form a Cu(II) complex, the identity of the product is unknown. The reactivity seen with 1 atm air is similar to that shown here with 1 atm dioxygen.

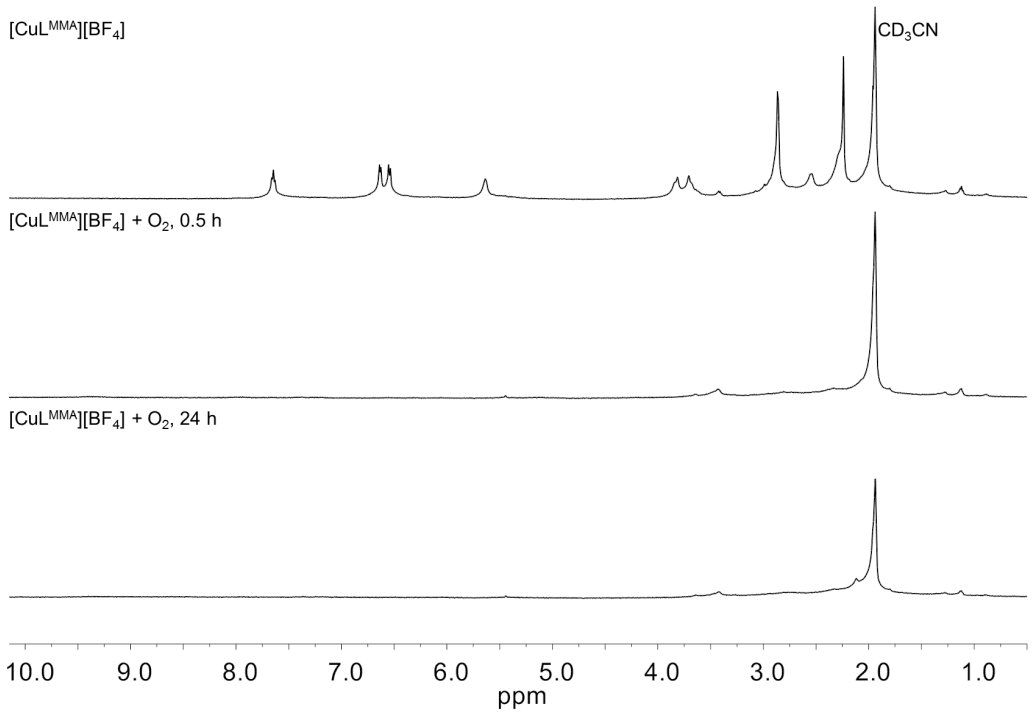

Figure 2.21. ^{1}H NMR spectra of $[CuL^{MMA}][BF_4]$ upon exposure to 1 atm O_2. Top: complex with no oxygen present. Middle: complex plus oxygen after 30 minutes. Bottom: complex plus oxygen after 24 hours.

The $[CuL^{MMA}][BF_4]$ complex becomes entirely paramagnetic 30 minutes after exposure to oxygen and maintains paramagnetism for 24 hours along with a color change from yellow to forest

green (Figure 2.21). This data suggests the monovalent complex has reacted with oxygen to generate a possible divalent paramagnetic species similar to the reactivity with $[CuL^{H}][BF_4]$. The NMR reaction solution was then analyzed by UV-Vis, IR, EPR, and MS in an attempt to determine the presence of newly formed species.

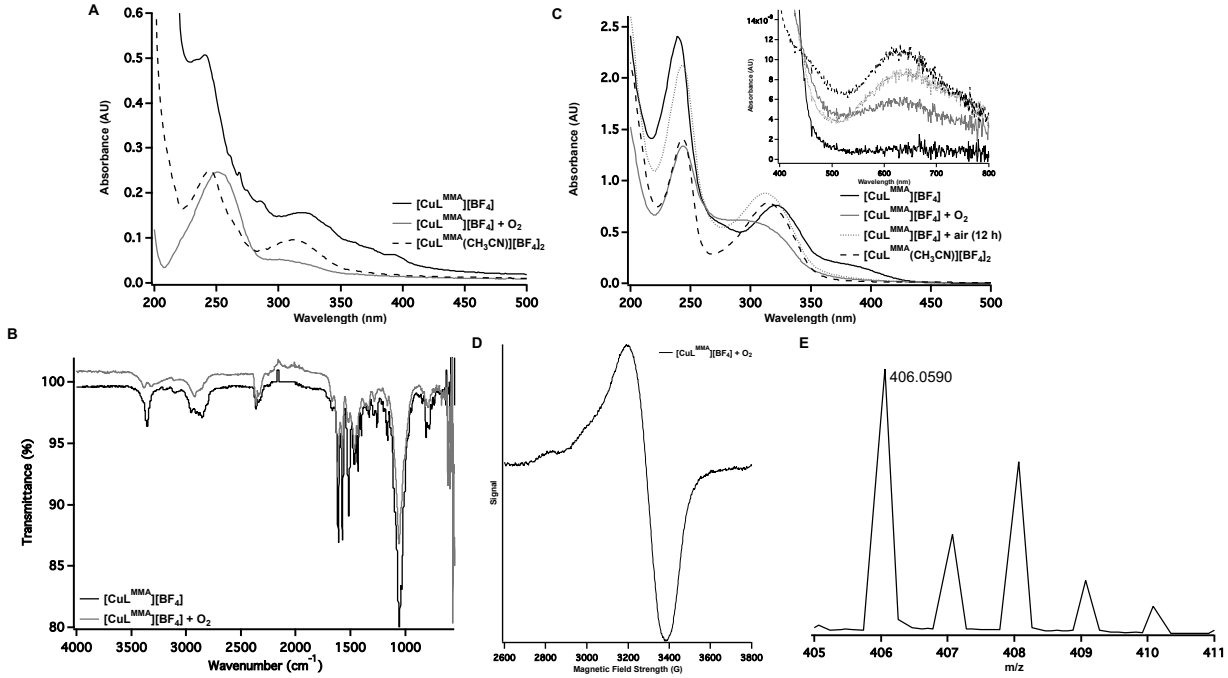

Figure 2.22. Spectra collected of the reaction mixture 24 hours after the addition of 1 atm O_2 to $[CuL^{MMA}][BF_4]$: A) UV-Vis spectra of 10 μM CH_3CN solution. B) UV-Vis spectra of 1 mM CH_3CN solution, Inset: Zoomed in *d-d* transition region. $[CuL^{MMA}][BF_4]$ (black trace), $[CuL^{MMA}][BF_4]$ plus O_2 after 24 h (gray trace), $[CuL^{MMA}][BF_4]$ plus O_2 (air) after 12 h (dotted trace), pristine $[CuL^{MMA}(CH_3CN)][BF_4]_2$ (dashed trace). C) IR spectra of $[CuL^{MMA}][BF_4]$ (black trace) and $[CuL^{MMA}][BF_4]$ under O_2 (gray trace). D) EPR spectrum of $[CuL^{MMA}][BF_4]$ plus O_2 (black trace). Samples taken as 10 mM frozen CH_3CN solutions at 77 K. E) MS spectrum of reaction mixture.

After exposure to oxygen the $[CuL^{MMA}][BF_4]$ complex's spectral profile does not match that of the monovalent or divalent complex with an absorption band at 251 nm at a concentration of 10 μM (Figure 2.22). At 1 mM, the primary absorption is at 244 nm and the secondary absorption band is very broad in comparison to more resolved peak present in the monovalent of divalent complex, and a new *d-d* transition can be seen indicating a new Cu(II) species. The EPR spectrum has a $g_{\perp}$ value of 2.1 which matches the $[CuL^{MMA}(CH_3CN)][BF_4]_2$ complex at 77K but

the $g_{//}$ value of 2.23 and a splitting of 503 MHz that does not match the divalent complex at 77K which is 2.25 with a 528 mHZ splitting (Table 2.8). The IR spectrum does not contain any new information. The mass spectrum for the reaction mixture is similar to that with air as the dioxygen source which shows a possible peak relating to an oxygen bound species such as $L^{MMA}Cu\text{-}O$ (m/z = 406.0) but further studies would be needed for product determination. Dioxygen has oxidized the Cu(I) complex to an unknown Cu(II) species. The reactivity with 1 atm of air is the same as with 1 atm of dioxygen.

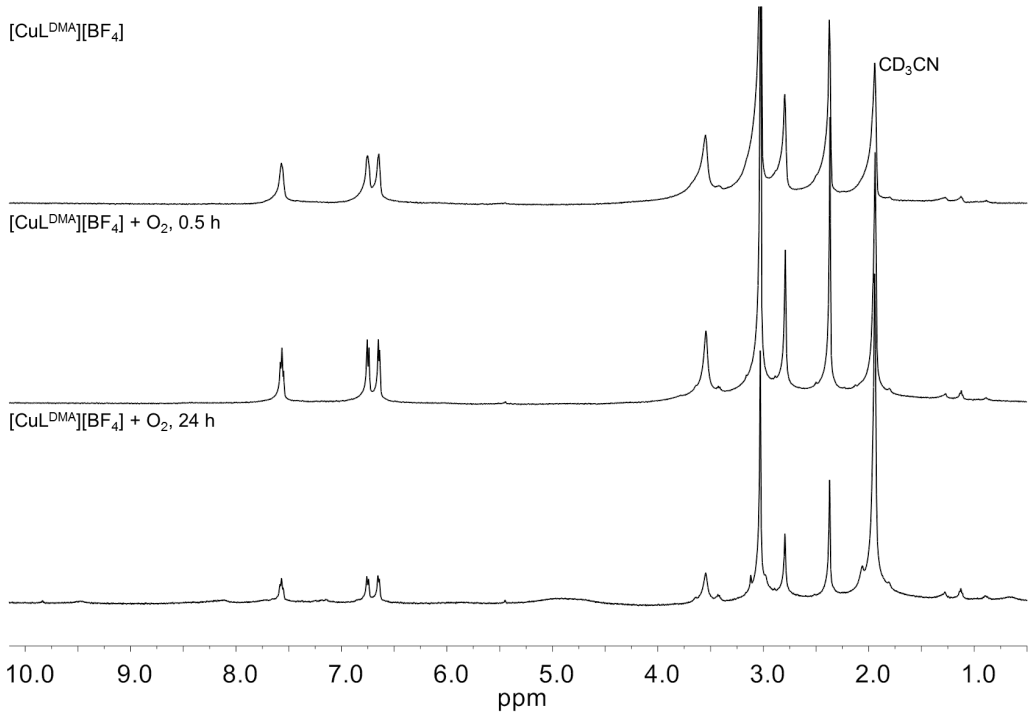

Figure 2.23. ^1H NMR spectra of $[CuL^{DMA}][BF_4]$ upon exposure to 1 atm O_2. Top: complex with no oxygen present. Middle: complex plus oxygen after 30 minutes. Bottom: complex plus oxygen after 24 hours.

Unlike, $[CuL^{H}][BF_4]$ and $[CuL^{MMA}][BF_4]$, the $[CuL^{DMA}][BF_4]$ complex remains diamagnetic for over 24 hours after exposure to oxygen, although there is a slow color change from yellow to olive (Figure 2.23). However, the intensity of the resonances in the ^1H NMR spectra decrease over time which suggests the monovalent complex has reacted with oxygen to generate

a possible divalent paramagnetic species in solution. However, the reactivity appears much slower compared to the ligands that do not include sterically bulky groups. The NMR reaction solution was analyzed by UV-Vis, IR, EPR, and MS in an attempt to determine the identity of the product.

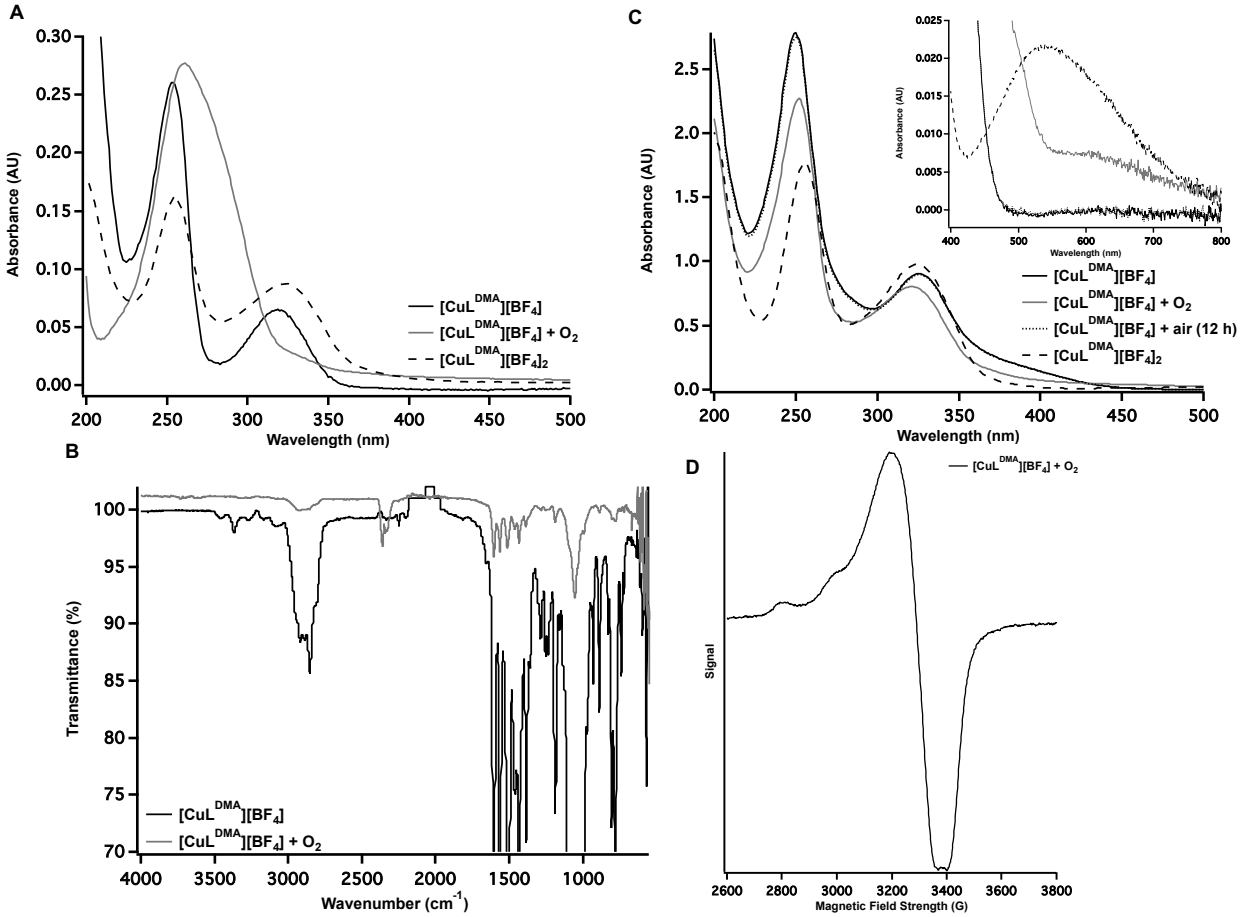

Figure 2.24. Spectra collected of the reaction mixture 24 hours after the addition of 1 atm O_2 to $[CuL^{DMA}][BF_4]$: A) UV-Vis spectra of 10 μM CH_3CN solution. B) UV-Vis spectra of 1 mM CH_3CN solution, Inset: Zoomed in *d-d* transition region. $[CuL^{DMA}][BF_4]$ (black trace), $[CuL^{DMA}][BF_4]$ plus O_2 after 24 h (gray trace), $[CuL^{DMA}][BF_4]$ plus O_2 (air) after 12 h (dotted trace), pristine $[CuL^{DMA}][BF_4]_2$ (dashed trace). C) IR spectra of $[CuL^{DMA}][BF_4]$ (black trace) and $[CuL^{DMA}][BF_4]$ under O_2 (gray trace). D) EPR spectra of $[CuL^{DMA}][BF_4]_2$ (black trace) and $[CuL^{DMA}][BF_4]$ plus O_2 (gray trace). Samples taken as 10 mM frozen CH_3CN solutions at 77 K.

After exposure to oxygen $[CuL^{DMA}][BF_4]$ exhibits a very broad absorption in the UV-Vis profile at 261 nm which does not match that of the monovalent or divalent complex at a concentration of 10 μM (Figure 2.24). At 1 mM there are two bands (252 and 322 nm) which are

similar to that of the divalent complex. However, the *d-d* transition region has a very small absorption band, suggesting a minor amount of a Cu(II) species has been formed. The EPR spectrum indicates the presence of a paramagnetic Cu(II) species with a $g_{\perp}$ value of 2.1 and a hyperfine pattern with a $g_{//}$ value of 2.23 and a splitting of 516 MHz that does not match the $[CuL^{DMA}][BF_4]_2$ complex at 77K, which has a $g_{\perp}$ of 2.08 and $g_{//}$ value of 2.42 (Table 2.8). The IR and MS spectra did not reveal any additional information. A very slow outer sphere oxidation of Cu(I) to a Cu(II) complex has occurred upon exposure to oxygen. The reactivity with 1 atm of air results in no changes to any of the spectral profiles, indicating a higher concentration of dioxygen is needed for $[CuL^{DMA}][BF_4]$. Thus, if the complexes are forming new oxygen bound or reacted species it would appear $[CuL^{DMA}][BF_4]$ is the least reactive.

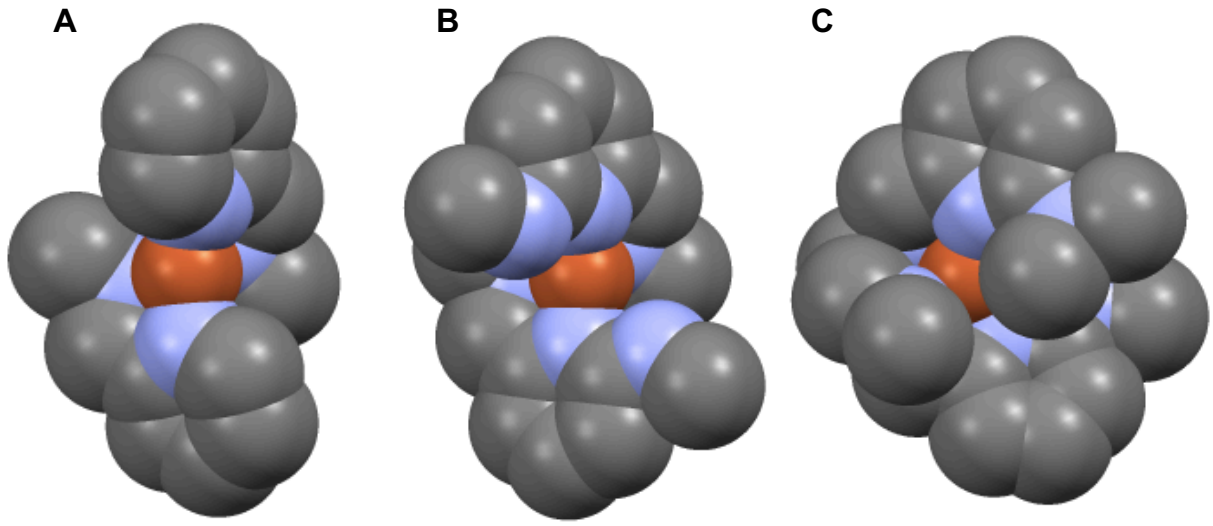

Figure 2.25. Space filling molecular structure of the monovalent copper complexes A) $[CuL^{H}][BF_4]$, B) $[CuL^{MMA}][BF_4]$ and C) $[CuL^{DMA}][BF_4]$ based on solid state crystal structures. The BF_4^- counter anions, solvent molecules and hydrogen atoms have been removed for clarity. Orange = copper, blue = nitrogen, gray = carbon.

The reactivity of the Cu(I) complexes with dioxygen appears to result in a Cu(II) species in all three cases. However, it is possible oxygen is performing an outer sphere oxidization of Cu(I)

and the final product is not an oxygen bound species. The rate of reactivity with oxygen can be ranked in decreasing order as $[CuL^{H}][BF_4] > [CuL^{MMA}][BF_4] > [CuL^{DMA}][BF_4]$. Is likely that faster reactivity with dioxygen for the $[CuL^{H}][BF_4]$ and $[CuL^{MMA}][BF_4]$ complexes is due to the accessible five coordinate structures of the oxidized form. As evident by the space filling models shown in Figure 2.25, oxygen can be accommodated at the monovalent copper complexes supported by the L^{H} and L^{MMA} ligands. $[CuL^{MMA}][BF_4]$ has only one methyl group on the pendant amine, resulting in less steric hindrance around the reactive center compared to $[CuL^{DMA}][BF_4]$. The sterically bulky dimethylamine moieties limit access to the metal center unlike in the $[CuL^{H}][BF_4]$ and $[CuL^{MMA}][BF_4]$ complex, explaining the lack of or slow reactivity with substrates.

2.3.5. Reactivity with Hydrogen Peroxide

Activated oxygen intermediates can reveal mechanistic information about mononuclear catalysts and the effect of pendant bases in the secondary coordination sphere. These activated species are an important step to learning about oxygen bound intermediates in catalysis such as superoxide ($\cdot O_2^{1-}$), peroxide (O_2^{2-}), or hydroperoxide (OOH^{1-}).[59-61]

Scheme 2.4. Reaction of $[CuL^{DMA}][BF_4]_2$ with H_2O_2.

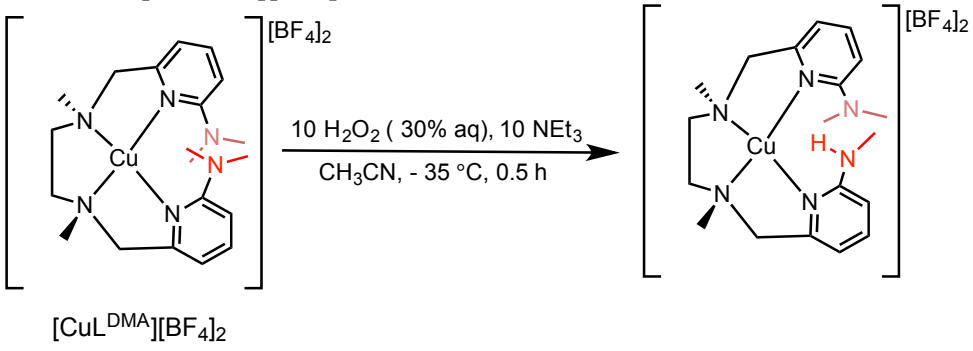

In an attempt to synthesize relevant oxygen reduction intermediates, 10 equivalents of H_2O_2

(30% aq) and 10 equivalents of trimethylamine (TEA) was added to $[CuL^{DMA}][BF_4]_2$ in thawing acetonitrile (Scheme 2.4). There was a significant color change from dark purple to a dark olive green. ^{1}H NMR spectrum indicated no demetallation with no resonances corresponding to free ligand.

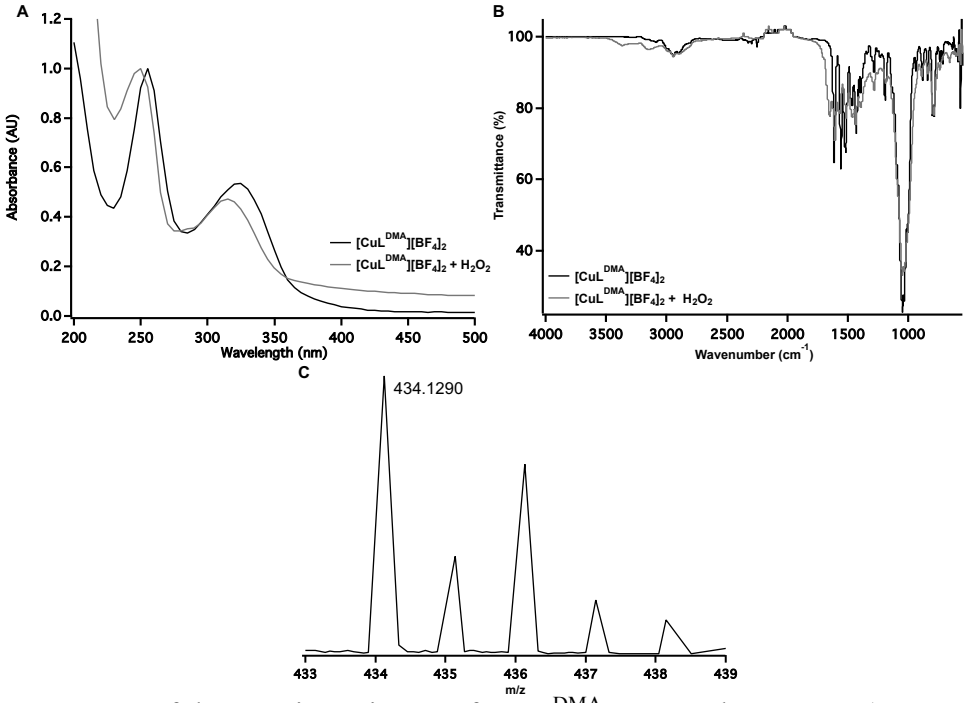

Figure 2.26. Spectra of the reaction mixture of $[CuL^{DMA}][BF_4]_2$ plus H_2O_2: A) UV-Vis spectra of $[CuL^{DMA}][BF_4]_2$ (black trace) and $[CuL^{DMA}][BF_4]_2$ reacted with H_2O_2 (gray trace). All solutions are 10 μM in CH_3CN at 298 K. B) IR spectra of $[CuL^{DMA}][BF_4]_2$ (black trace) and $[CuL^{DMA}][BF_4]_2$ reacted with H_2O_2 (gray trace). C) Mass spectrum of reaction mixture.

The UV-Vis spectra at room temperature show a shift to higher energy absorptions with a primary absorption band at 250 nm and the secondary band at 315 nm (Figure 2.26) although, there is no charge-transfer absorption commonly seen for peroxide based species around 350-400 nm. IR data does not provide evidence that a stable hydroperoxo species has been synthesized based on the lack of an O-H and O-O-H stretching frequency. However, Raman spectroscopy is typically utilized to determine these stretches because they are at lower vibrational energies.[62] Although, there is a newly formed N-H stretching frequency at 3365 cm^{-1} and ESI-MS data suggests

dealkylation of the dimethylamine arm of the ligand. In both the positive and negative ion mode there is a peak corresponding to *m/z* = [ML-15] (a methyl group is equal to 15). The ion peaks corresponding to the dealkylation of the $[CuL^{DMA}][BF_4]_2$ complex are *m/z* = 434.13 [ML + CH_3] and 406.12 [ML-CH_3] in negative ion mode.

Scheme 2.5. Reaction of $[(L^{N(CH_3)_2})Cu(H_2O)]^{2+}$ with H_2O_2 to form dealkylated ligand by Karlin et al.[63]

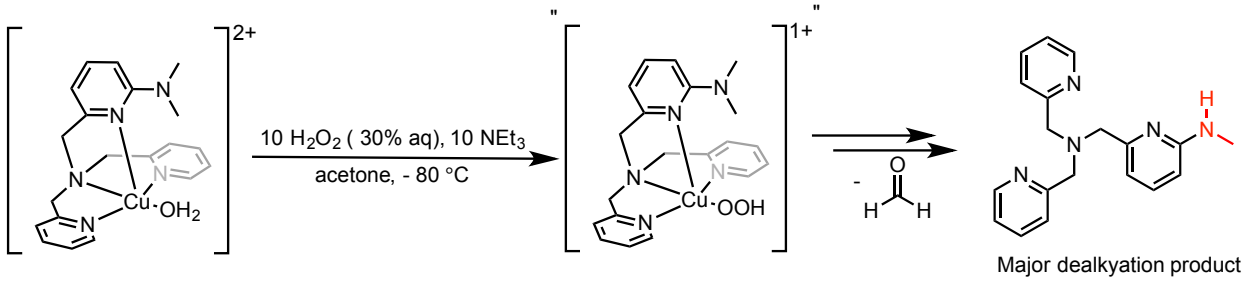

The color change and dealkyation of $[CuL^{DMA}][BF_4]_2$ is consistent with the reaction of hydrogen peroxide and TEA with $(L^{N(CH_3)_2})Cu(H_2O)]^{2+}$, reported by Karlin and coworkers [63] The copper (II) mononuclear complex contains a dimethylamine functionalized tris(2-pyridylmethyl)-amine) (TPA) ligand framework. The reaction of their complex with hydrogen peroxide forms an unstable hydroperoxo copper species that subsequently oxidizes a methyl group from the dimethylamine TPA by formation of formaldehyde, resulting in the major dealkyated product (Scheme 2.5).

The same reaction conditions were performed on the $[CuL^{H}][BF_4]_2$ complex. There was minimal color change from dark blue, and no significant differences in the spectra obtained from the reaction mixture.

2.4. Conclusion

A series of divalent and monovalent copper complexes were synthesized and characterized using L^{H}, L^{MMA}, and L^{DMA} as ligands. The solid state structure of $[CuL^{MMA}(CH_3CN)][BF_4]_2$ revels the L^{MMA} acts as a hydrogen bond donor to another methylamine arm in the complex. The other arm is poised to interact with a substrate bound to the metal center. The L^{DMA} ligand however is too sterically bulky for the copper metal center to act as a hydrogen bond acceptor.

Protonation studies on the diamagnetic Cu(I) complexes of the N_2Py_2 ligands indicate that the amines located on the ligand backbone are more basic than the uncoordinated dimethylamine groups. Protonation at this site is cleanly reversible, indicating that it can serve as a proton reservoir for substrate reactivity at the metal center. This type of protonation study using diamagnetic complexes may prove useful for other systems that incorporate pendant bases in the secondary coordination sphere. Although the pendant bases of L^{DMA} for these complexes are not as basic as anticipated, they are still positioned to serve as hydrogen-bond acceptors to activate polar molecules bound to the metal.

Oxygen reduction activity was tested electrocatalytically and minimal activity is seen for all three complexes. UV-Vis studies of the monovalent complexes under oxygen shows that $[CuL^{DMA}][BF_4]$ has the slowest reactivity with dioxygen. This lack of reactivity is likely due to the steric bulk of the dimethylamine functionalities blocking the metal center, preventing oxygen binding. This hypothesis is supported by the space filling diagrams created using the structural data. Reactivity of the $[CuL^{DMA}][BF_4]$ with hydrogen peroxide may form an unstable hydroperoxo intermediate that subsequently dealkylates the pendant amine.

2.5. Experimental Details

General Experiment Considerations

All reagents were purchased from commercial suppliers and used without further purification. Unless otherwise noted, all organic chemical manipulations were performed in air. Compounds were purified via flash column chromatography using Sorbent Technologies 60 Å, 230–400 mesh silica gel, unless otherwise stated. Unless otherwise noted, inorganic metal complexations were performed in a Vacuum Atmospheres Co. drybox under a nitrogen atmosphere. $[Cu(CH_3CN)_4][BF_4]_2$ was prepared using literature methods.[42] $[Cu(CH_3CN)_4][BF_4]$ was prepared according to literature methods.[43] Anhydrous solvents were sparged with UHP argon (Praxair) and passed through columns containing Q-5 and molecular sieves before use.

Physical Methods

Nuclear Magnetic Resonance (NMR) Spectroscopy: ^{1}H NMR spectra were recorded on 500 MHz on Bruker instruments. ^{1}H NMR spectra chemical shifts are reported as δ values in ppm relative to residual protio solvent: $CDCl_3$ (7.26 ppm), CD_3CN (1.94 ppm). Proton NMR data are reported as follows: chemical shift (δ ppm), multiplicity (s = singlet, d = doublet, t = triplet, q = quartet), coupling constants (J) in Hertz (Hz), and integration. Multiplets (m) are reported over the range (ppm). Data for ^{13}C NMR spectra are decoupled proton spectra and are reported in terms of chemical shift (δ ppm).

Mass Spectrometry (MS): High resolution mass spectra (HR-MS) and electrospray ionization mass spectra (ESI-MS) were obtained on a Micromass LCT and collected at the University of California-Irvine Mass Spectrometry Facility.

Ultraviolet-Visible (UV-Vis) Spectroscopy: Ultraviolet-Visible spectra were collected as 10 μM solutions in 3 mL CH_3CN in a 1 cm quartz cuvette or as 1mM solutions in 0.3 mL CH_3CN in a 1 mm quartz cuvette using an Agilent Technologies Cary 60 UV–vis spectrometer.

Infrared (IR) Spectroscopy: Infrared spectra were collected using a Thermo Scientific Nicolet iS5 spectrometer with an iD5 ATR attachment in a nitrogen filled glovebox. The sample was prepared by evaporating an acetonitrile solution of the compound onto an ATR crystal, unless otherwise noted.

Electron Paramagnetic Resonance (EPR) Spectroscopy: X-band (9.28 GHz) EPR spectra were collected as 10 mM frozen solutions using a Bruker EMX spectrometer equipped with an ER041XG microwave bridge at 77 K or 10 K.

Elemental Analysis (EA): Elemental analyses were performed on a Perkin Elmer 2400 Series II CHNS elemental analyzer.

Cyclic Voltammetry (CV): Electrochemical experiments were performed under an atmosphere of nitrogen in a solution containing 0.1 M Bu_4NBF_4 or Bu_4NPF_6 in acetonitrile. Glassy carbon was used as the working and auxiliary electrode and a silver wire was used as a pseudoreference electrode. Ferrocene was used as an internal standard, and all potentials are referenced to the ferrocenium/ferrocene couple. Cyclic voltammetry experiments were performed with a Pine Wavedriver 10 or 20 potentiostat and Pine Aftermath software version 1.4.7881.

X-Ray Crystallography: A Bruker SMART APEX II diffractometer was used to collect all data. The APEX2 (APEX2 Version 2014.11-0, Bruker AXS, Inc.; Madison, WI 2014) program package was used to determine the unit-cell parameters and for data collection (20 sec/frame scan time for a sphere of diffraction data). The raw frame data was processed using SAINT (SAINT Version 8.34a, Bruker AXS, Inc.; Madison, WI 2013) and SADABS (Sheldrick, G. M. SADABS, Version

2014/5, Bruker AXS, Inc.; Madison, WI 2014) to yield the reflection data file. Subsequent calculations were carried out using the SHELXTL (Sheldrick, G. M. SHELXTL, Version 2014/7, Bruker AXS, Inc.; Madison, WI 2014) program. The structures were solved by direct methods and refined on F^2 (International Tables for Crystallography 1992, Vol. C., Dordrecht: Kluwer Academic Publishers) by full-matrix least-squares techniques. The analytical scattering factors for neutral atoms were used throughout the analysis. Hydrogen atoms H(5) and H(6) of [CuL^{MMA}(CH_3CN)][BF_4]$_2$ and [CuL^{MMA}][BF_4] were located from a difference-Fourier map and refined. The remaining hydrogen atoms were included using a riding model.

Synthesis of Complexes

[CuL^{H}(CH_3CN)][BF_4]$_2$. [$Cu(CH_3CN)_4$][BF_4]$_2$ (74 mg, 0.18 mmol) was added to a solution of $\mathbf{L^H}$ (51 mg, 0.18 mmol) in 5 mL of CH_3CN. The dark blue solution was stirred at 25 °C for 0.5 h. Then 5 mL of Et_2O was added and the supernatant was decanted to reveal a crude blue oil that was triturated with toluene to isolate a dark blue powder. The powder was redissolved in *ca.* 1 mL of CH_3CN and layered with 4 mL of THF. After 1 day at −40 °C, the dark blue microcrystalline solid was isolated by filtration and washed with 2 × 4 mL THF (96 mg, 94% yield). Single dark blue crystals suitable for X-ray crystallographic analysis were obtained by evaporation of a CH_3CN/toluene solution. ESI-MS (CH_3CN) *m*/*z*: 166.55 ([CuL^{H}]$^{2+}$). $\lambda_{max,}$ nm (CH_3CN, ε ($M^{-1} \times cm^{-1}$)) = 260 (11,000), 625 (200). Anal. Calcd (Found) for $C_{16}H_{22}B_2CuF_8N_4$ (%): C, 37.86 (38.25); H, 4.37 (4.48); N, 11.04 (11.83). EPR (CH_3CN, 10 K): $g_{\perp}$ = 2.1.

[CuL^{MMA}(CH_3CN)][BF_4]$_2$. [$Cu(CH_3CN)_4$][BF_4]$_2$ (31 mg, 0.08 mmol) was added to a solution of $\mathbf{L^{MMA}}$ (25 mg, 0.08 mmol) in 5 mL of CH_3CN. The dark teal solution was stirred at 25 °C for

0.5 h. 5 mL of Et_2O was added to precipitate the complex. The supernatant was decanted and resulting teal powder redissolved in *ca.* 1 mL of CH_3CN and layered with 4 mL of Et_2O. After 1 d at −40 °C, the dark teal microcrystalline solid was isolated by filtration and washed with 2 × 4 mL Et_2O. (26 mg, 76% yield). Single dark teal crystals suitable for analysis by X-ray diffraction were obtained by diffusion of Et_2O in a CH_3CN solution. ESI-MS (CH_3CN) *m*/*z*: 195.53 ($[CuL^{MMA}]^{2+}$). $\lambda_{max,}$ nm (CH_3CN, ε ($M^{-1} \times cm^{-1}$)) = 244 (12,000), 312 (6,700), and 630 (21). Anal. Calcd (Found) for $C_{18}H_{28}B_2CuF_8N_6 + 0.5\ CH_3CN$ (%): C, 38.22 (38.93); H, 4.99 (5.07); N, 14.86 (15.53). EPR (CH_3CN, 10 K): $g_\perp = 2.1$, $g_\parallel = 2.3$ (A = 511 MHz)

$[CuL^{DMA}][BF_4]_2$. $[Cu(CH_3CN)_4][BF_4]_2$ (56 mg, 0.14 mmol) was added to a solution of $\mathbf{L^{DMA}}$ (50. mg, 0.14 mmol) in 5 mL of CH_3CN. The dark purple solution was stirred at 25 °C for 0.5 h. 5 mL of Et_2O was added to precipitate the complex. The supernatant was decanted and resulting purple powder redissolved in *ca.* 1 mL of CH_3CN and layered with 4 mL of Et_2O. After 1 d at −40 °C, the dark purple microcrystalline solid was isolated by filtration and washed with 2 × 4 mL Et_2O (68 mg, 82% yield). Single dark purple crystals suitable for X-ray crystallographic analysis were obtained by diffusion of Et_2O in a CH_3CN solution. ESI-MS (CH_3CN) *m*/*z*: 209.6 ($[CuL^{DMA}]^{2+}$). $\lambda_{max,}$ nm (CH_3CN, ε ($M^{-1} \times cm^{-1}$)) = 255 (26,000), 325 (9200), 541 (250). Anal. Calcd (Found) for $C_{20}H_{32}B_2CuF_8N_6$ (%): C, 40.46 (40.04); H, 5.43 (5.38); N, 14.16 (13.92). EPR (CH_3CN, 10 K): $g_\perp = 2.1$.

$[CuL^{H}][BF_4]$. A dark blue solution of $[CuL^{H}(CH_3CN)][BF_4]_2$ (11 mg, 19 μmol) in 3 mL of CH_3CN was cooled to −40 °C in the glovebox freezer for 2 h. The cooled solution was added to a vial containing solid KC_8 (2.7 mg, 19 μmol, 1 equiv), resulting in an immediate color change to light yellow. After stirring at room temperature for 0.5 h, the solution was filtered. Removal of solvent from the filtrate provided the product as a light yellow powder (5.0 mg, 60% yield). Single yellow

crystals suitable for X-ray crystallographic analysis were obtained by diffusion of Et_2O in a CH_3CN solution. ^1H NMR (CD_3CN) δ (ppm): 8.67 (d, $^3J_{HH}$ = 10.0 Hz, 2H, Ar–*H*), 7.93 (t, $^3J_{HH}$ = 10.0 Hz, 2H, Ar–*H*), 7.45 (m, 4H, Ar-*H*), 3.87 (s, 4H, Ar–C*H*$_2$–N–), 2.50 (s, 4H, –C*H*$_2$–C*H*$_2$–), 2.27 (s, 6H, –N–C*H*$_3$). ESI-MS (CH_3CN) *m*/*z*: 333.07 ($[CuL^H]^+$). $\lambda_{max,}$ nm (CH_3CN, ε ($M^{-1} \times cm^{-1}$)) = 260 (11,000). Anal. Calcd (Found) for $C_{16}H_{22}BCuF_4N_4$ + 1.5 CH_3CN (%): C, 47.32 (47.12); H, 5.54 (5.24); N, 15.97 (15.64).

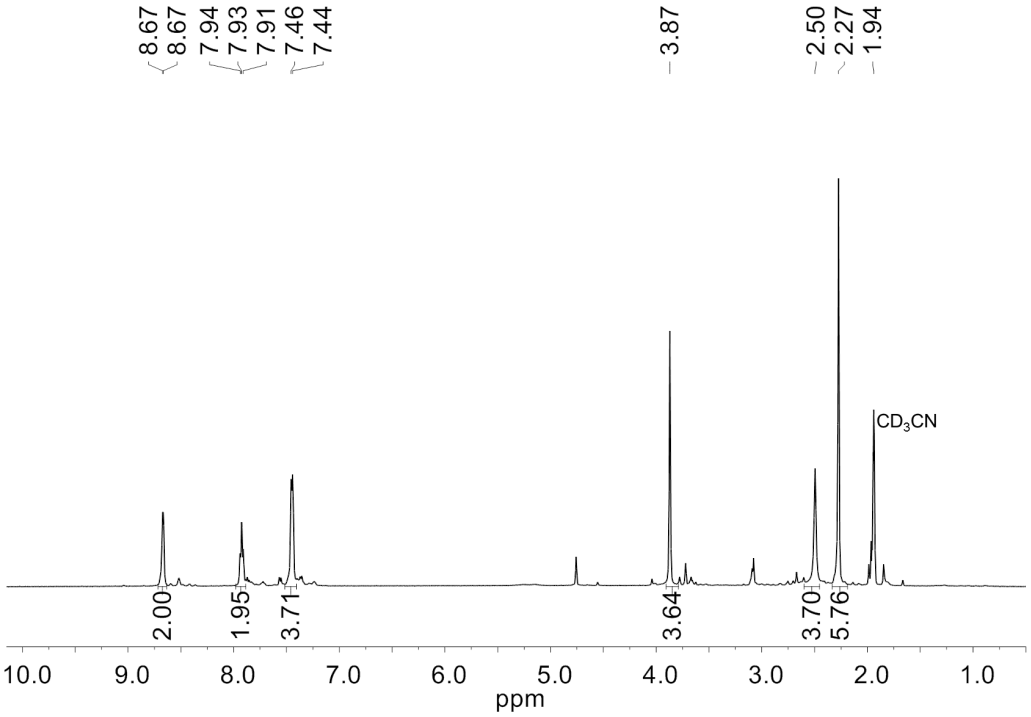

Figure 2.27. ^1H NMR of $[CuL^H][BF_4]$ in CD_3CN.

$[CuL^{MMA}][BF_4]$. Solid $[Cu(CH_3CN)_4][BF_4]$ (46 mg, 0.15 mmol) was added to a solution of $\mathbf{L^{MMA}}$ (48 mg, 0.15 mmol) in 5 mL of CH_3CN. The light yellow solution was stirred at 25 °C for 0.5 h. 5 mL of Et_2O was added to precipitate the complex. The supernatant was decanted and resulting yellow powder redissolved in *ca.* 1 mL of CH_3CN and layered with 4 mL of Et_2O. After 1 d at −40 °C, the yellow microcrystalline solid was isolated by filtration and washed with 2 × 4 mL Et_2O. (26 mg, 76% yield). Single yellow crystals suitable for X-ray crystallographic analysis were

obtained by diffusion of Et_2O in a CH_3CN solution. ESI-MS (CH_3CN) *m*/*z*: 195.53 ($[CuL^{MMA}]^+$). ^1H NMR (CD_3CN) δ (ppm): 7.65 (t, $^3J_{HH}$ = 10.0 Hz, 2H, Ar–*H*), 6.63 (t, $^3J_{HH}$ = 7.2 Hz, 2H, Ar–*H*), 6.55 (d, $^3J_{HH}$ = 8.5 Hz, 2H, Ar-*H*), 5.64 (bs, 2H, –N*H*–CH_3), 3.82 (d, $^3J_{HH}$ = 15.2 Hz, 2H, Ar–CH_2–N–), 3.70 (d, $^3J_{HH}$ = 15.2 Hz, 2H, Ar–CH_2–N–), 2.87 (s, 3H, –NH–CH_3), 2.86 (s, 3H, –NH–CH_3), 2.54 (d, 4H, –CH_2–CH_2–), 2.24 (s, 6H, –N–CH_3). ESI-MS (CH_3CN) *m*/*z*: 391.07 ($[M\text{-}L]^+$). $\lambda_{max,}$ nm (CH_3CN, ε ($M^{-1} \times cm^{-1}$)) = 244 (12,000), 312 (6,000).

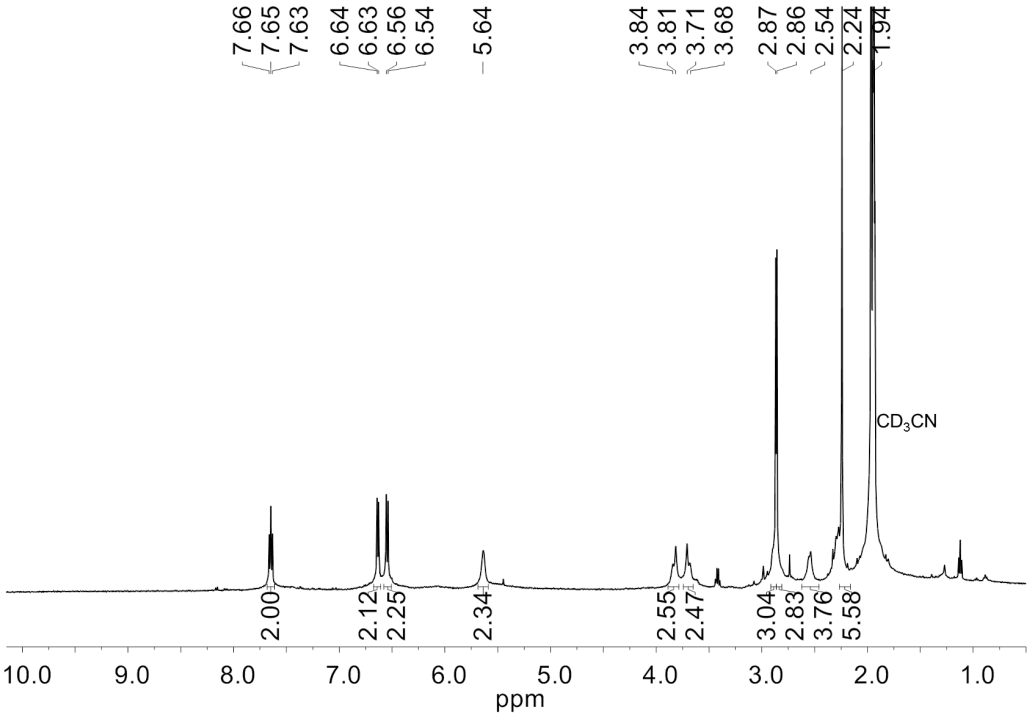

Figure 2.28. ^1H NMR of $[CuL^{MMA}][BF_4]$ in CD_3CN.

$[CuL^{DMA}][BF_4]$. A dark purple solution of $[CuL^{DMA}][BF_4]_2$ (10.0 mg, 17 μmol) in 3 mL of CH_3CN was cooled to -40 °C in the glovebox freezer for 2 h. The cooled solution was added to a vial containing solid KC_8 (2.3 mg, 17 μmol, 1 equiv), resulting in an immediate color change to light yellow. After stirring at room temperature for 0.5 h, the solution was filtered. Removal of solvent from the filtrate provided the pure product as a light yellow microcrystalline solid (8.6 mg, 86% yield). Single yellow crystals suitable for X-ray crystallographic analysis were obtained by

diffusion of Et_2O in a CH_3CN solution. ^1H NMR (CD_3CN) δ (ppm): 7.57 (t, $^3J_{HH}$ = 10.0 Hz, 2H, Ar–*H*), 6.75 (d, $^3J_{HH}$ = 10.0 Hz, 2H, Ar–*H*), 6.64 (d, $^3J_{HH}$ = 10.0 Hz, 2H, Ar–*H*), 3.54 (s, 4H, Ar–C*H*$_2$–N–), 3.03 (s, 12H, –N–(C*H*$_3$)$_2$), 2.79 (s, 4H, –C*H*$_2$–C*H*$_2$–), 2.37 (s, 6H, –N–C*H*$_3$). ESI-MS (CH_3CN) *m*/*z*: 419.15 ([CuL^{DMA}]$^+$). $\lambda_{max,}$ nm (CH_3CN, ε ($M^{-1} \times cm^{-1}$)) = 254 (26,000) and 319 (6500). Anal. Calcd (Found) for $C_{20}H_{32}BCuF_4N_6$ (%): C, 47.39 (47.73); H, 6.36 (6.35); N, 16.58 (16.07).

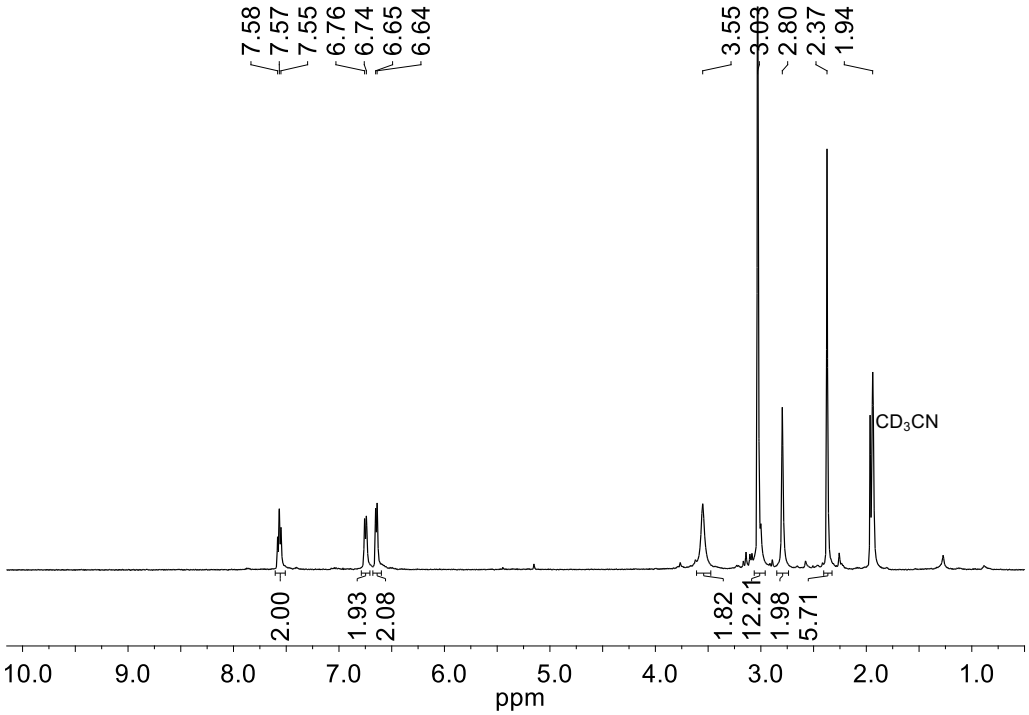

Figure 2.29. ^1H NMR of [CuL^{DMA}][BF_4] in CD_3CN.

2.6. References

(1) Zhang, J. In *PEM Fuel Cell Electrocatalysts and Catalyst Layers*; Springer-Verlang: London, 2008.

(2) Curtin, D. E.; Lousenberg, R. D.; Henry, T. J.; Tangeman, P. C.; Tisack, M. E. *J. Power Sources* **2004**, *131*, 41-48.

(3) Denisov, I. G.; Makris, T. M.; Sligar, S. G.; Schlichting, I. *Chem. Rev.* **2005**, *105*, 2253-2278.

(4) Ferraro, D. J.; Gakhar, L.; Ramaswamy, S. *Biochem. Biophys. Res. Commun.* **2005**, *338*, 175-190.

(5) Solomon, E. I.; Chen, P.; Metz, M.; Lee, S.-K.; Palmer, A. E. *Angew. Chem. Int. Ed.* **2001**, *40*, 4570-4590.

(6) Karlin, K. D. *Science* **1993**, *261*, 701-708.

(7) Holm, R. H.; Kennepohl, P.; Solomon, E. I. *Chem. Rev.* **1996**, *96*, 2239-2314.

(8) Ferguson-Miller, S.; Babcock, G. T. *Chem. Rev.* **1996**, *96*, 2889-2908.

(9) Migliore, A.; Polizzi, N. F.; Therien, M. J.; Beratan, D. N. *Chem. Rev.* **2014**, *114*, 3381-3465.

(10) Reece, S. Y.; Nocera, D. G. *Annu. Rev. Biochem.* **2009**, *78*, 673-699.

(11) Tard, C.; Pickett, C. J. *Chem. Rev.* **2009**, *109*, 2245-2274.

(12) Sigel, A. S., H. ; Sigel, R.K.O *Metal Ions in Life Sciences*; John Wiley & Sons Ltd.: Chichester, 2006.

(13) Schowen, K. B.; Limbach, H. H.; Denisov, G. S.; Schowen, R. L. *Biochim. Biophys. Acta, Bioenerg.* **2000**, *1458*, 43-62.

(14) Shook, R. L.; Borovik, A. S. *Inorg. Chem.* **2010**, *49*, 3646-3660.

(15) Condon, P. J.; Royer, W. E. *J. Biol. Chem.* **1994**, *269*, 25259-25267.

(16) Olson, J. S.; Mathews, A. J.; Rohlfs, R. J.; Springer, B. A.; Egeberg, K. D.; Sligar, S. G.; Tame, J.; Renaud, J.-P.; Nagai, K. *Nature* **1988**, *336*, 265-266.

(17) Schlichting, I.; Berendzen, J.; Chu, K.; Stock, A. M.; Maves, S. A.; Benson, D. E.; Sweet, R. M.; Ringe, D.; Petsko, G. A.; Sligar, S. G. *Science* **2000**, *287*, 1615-1622.

(18) Martinis, S. A.; Atkins, W. M.; Stayton, P. S.; Sligar, S. G. *J. Am. Chem. Soc.* **1989**, *111*, 9252-9253.

(19) Gerber, N. C.; Sligar, S. G. *J. Am. Chem. Soc.* **1992**, *114*, 8742-8743.

(20) Hazes, B.; Kalk, K. H.; Hol, W. G. J.; Magnus, K. A.; Bonaventura, C.; Bonaventura, J.; Dauter, Z. *Protein Science* **1993**, *2*, 597-619.

(21) Solomon, E. I.; Heppner, D. E.; Johnston, E. M.; Ginsbach, J. W.; Cirera, J.; Qayyum, M.; Kieber-Emmons, M. T.; Kjaergaard, C. H.; Hadt, R. G.; Tian, L. *Chem. Rev.* **2014**, *114*, 3659-3853.

(22) Yoshikawa, S.; Shinzawa-Itoh, K.; Nakashima, R.; Yaono, R.; Yamashita, E.; Inoue, N.; Yao, M.; Fei, M. J.; Libeu, C. P.; Mizushima, T.; Yamaguchi, H.; Tomizaki, T.; Tsukihara, T. *Science* **1998**, *280*, 1723-1729.

(23) Collman, J. P.; Ghosh, S. *Inorg. Chem.* **2010**, *49*, 5798-5810.

(24) Ward, A. L.; Elbaz, L.; Kerr, J. B.; Arnold, J. *Inorg. Chem.* **2012**, *51*, 4694-4706.

(25) Kim, E.; Chufán, E. E.; Kamaraj, K.; Karlin, K. D. *Chem. Rev.* **2004**, *104*, 1077-1134.

(26) Collman, J. P.; Devaraj, N. K.; Decréau, R. A.; Yang, Y.; Yan, Y.-L.; Ebina, W.; Eberspacher, T. A.; Chidsey, C. E. D. *Science* **2007**, *315*, 1565-1568.

(27) Shin, H.; Lee, D.-H.; Kang, C.; Karlin, K. D. *Electrochimica Acta* **2003**, *48*, 4077-4082.

(28) Ricard, D.; Didier, A.; L'Her, M.; Boitrel, B. *ChemBioChem* **2001**, *2*, 144-148.

(29) Dogutan, D. K.; Stoian, S. A.; McGuire, R.; Schwalbe, M.; Teets, T. S.; Nocera, D. G. *J. Am. Chem. Soc.* **2011**, *133*, 131-140.

(30) Rosenthal, J.; Nocera, D. G. *Acc. Chem. Res.* **2007**, *40*, 543-553.

(31) Collman, J. P.; Gagne, R. R.; Reed, C.; Halbert, T. R.; Lang, G.; Robinson, W. T. *J. Am. Chem. Soc.* **1975**, *97*, 1427-1439.

(32) Kadish, K. M.; Frémond, L.; Shen, J.; Chen, P.; Ohkubo, K.; Fukuzumi, S.; El Ojaimi, M.; Gros, C. P.; Barbe, J.-M.; Guilard, R. *Inorg. Chem.* **2009**, *48*, 2571-2582.

(33) Chang, C. K.; Liu, H. Y.; Abdalmuhdi, I. *J. Am. Chem. Soc.* **1984**, *106*, 2725-2726.

(34) Thorseth, M. A.; Tornow, C. E.; Tse, E. C. M.; Gewirth, A. A. *Coord. Chem. Rev.* **2013**, *257*, 130-139.

(35) Rokhsana, D.; Shepard, E. M.; Brown, D. E.; Dooley, D. M. In *Copper-Oxygen Chemistry*; John Wiley & Sons, Inc.: 2011, p 53-106.

(36) Karlin, K. D.; Gultneh, Y. In *Progress in Inorganic Chemistry*; John Wiley & Sons, Inc.: 2007, p 219-327.

(37) Fukuzumi, S.; Kotani, H.; Lucas, H. R.; Doi, K.; Suenobu, T.; Peterson, R. L.; Karlin, K. D. *J. Am. Chem. Soc.* **2010**, *132*, 6874-6875.

(38) Carver, C. T.; Matson, B. D.; Mayer, J. M. *J. Am. Chem. Soc.* **2012**, *134*, 5444-5447.

(39) Matson, B. D.; Carver, C. T.; Von Ruden, A.; Yang, J. Y.; Raugei, S.; Mayer, J. M. *Chem. Comm.* **2012**, *48*, 11100-11102.

(40) Yang, J. Y.; Bullock, R. M.; Dougherty, W. G.; Kassel, W. S.; Twamley, B.; DuBois, D. L.; Rakowski DuBois, M. *Dalton Trans.* **2010**, *39*, 3001-3010.

(41) Shook, R. L.; Peterson, S. M.; Greaves, J.; Moore, C.; Rheingold, A. L.; Borovik, A. S. *J. Am. Chem. Soc.* **2011**, *133*, 5810-5817.

(42) Coucouvanis, D. In *Inorganic Syntheses*; John Wiley & Sons, Inc.: 2002, p 75-121.

(43) Kubas, G. J.; Monzyk, B.; Crumbliss, A. L. In *Inorganic Syntheses*; John Wiley & Sons, Inc.: 2007, p 90-92.

(44) Pandiyan, T.; Guadalupe, H. J.; Cruz, J.; Bernès, S.; Ugalde-Salvdivar, V. M.; González, I. *Eur. J. Inorg. Chem.* **2008**, *2008*, 3274-3285.

(45) Addison, A. W.; Rao, T. N.; Reedijk, J.; van Rijn, J.; Verschoor, G. C. *J. Chem. Soc., Dalton Trans.* **1984**, 1349-1356.

(46) Yang, L.; Powell, D. R.; Houser, R. P. *Dalton Trans.* **2007**, 955-964.

(47) Okuniewski, A.; Rosiak, D.; Chojnacki, J.; Becker, B. *Polyhedron* **2015**, *90*, 47-57.

(48) Hirotsu, M.; Kuwamura, N.; Kinoshita, I.; Kojima, M.; Yoshikawa, Y.; Ueno, K. *Dalton Trans.* **2009**, 7678-7683.

(49) Anderson, L. C.; Seeger, N. V. *J. Am. Chem. Soc.* **1949**, *71*, 340-342.

(50) Hathaway, B. J. W., G.; Gillard, R.D.; McCleverty, J.A *Comprehensive Coordination Chemistry*; Pergamon Press: Oxford, England, 1987; Vol. 5.

(51) Massoud, S. S.; Mautner, F. A. *Inorg. Chem. Comm.* **2004**, *7*, 559-562.

(52) Mautner, F. A.; Louka, F. R.; LeGuet, T.; Massoud, S. S. *J. Mol. Struct.* **2009**, *919*, 196-203.

(53) Mautner, F. A.; Soileau, J. B.; Bankole, P. K.; Gallo, A. A.; Massoud, S. S. *J. Mol. Struct.* **2008**, *889*, 271-278.

(54) McLachlan, G. A.; Fallon, G. D.; Martin, R. L.; Spiccia, L. *Inorg. Chem.* **1995**, *34*, 254-261.

(55) Que Jr, L. *Physical Methods in Bioinorganic Chemistry*; University Science Books, 2000.

(56) Kaljurand, I.; Kütt, A.; Sooväli, L.; Rodima, T.; Mäemets, V.; Leito, I.; Koppel, I. A. *J. Org. Chem.* **2005**, *70*, 1019-1028.

(57) Kaljurand, I.; Rodima, T.; Leito, I.; Koppel, I. A.; Schwesinger, R. *J. Org. Chem.* **2000**, *65*, 6202-6208.

(58) Rõõm, E.-I.; Kütt, A.; Kaljurand, I.; Koppel, I.; Leito, I.; Koppel, I. A.; Mishima, M.; Goto, K.; Miyahara, Y. *Chem. Eur. J.* **2007**, *13*, 7631-7643.

(59) Lewis, E. A.; Tolman, W. B. *Chem. Rev.* **2004**, *104*, 1047-1076.

(60) Itoh, S. *Curr. Opin. Chem. Biol.* **2006**, *10*, 115-122.

(61) Mirica, L. M.; Ottenwaelder, X.; Stack, T. D. P. *Chem. Rev.* **2004**, *104*, 1013-1046.

(62) Root, D. E.; Mahroof-Tahir, M.; Karlin, K. D.; Solomon, E. I. *Inorg. Chem.* **1998**, *37*, 4838-4848.

(63) Maiti, D.; Narducci Sarjeant, A. A.; Karlin, K. D. *J. Am. Chem. Soc.* **2007**, *129*, 6720-6721.

CHAPTER 3

Cobalt Tetradentate N_2Py_2 Complexes with Pendant Bases in the Secondary Coordination Sphere: Activity Towards Water Oxidation

3.1. Motivation and Specific Aims

A series of octahedral cobalt complexes bearing neutral tetradentate ligands (N_2Py_2) with pendant bases in the secondary coordination sphere were synthesized to examine their activity towards small molecule activation.

The two N_2Py_2 ligands discussed contain pendant methylamines (L^{MMA}) or dimethylamines (L^{DMA}) that can act as a hydrogen bond donor and hydrogen bond acceptor, respectively. When coordinated to a metal center in octahedral geometry, the pendant bases on these ligands are positioned to facilitate proton transfer to substrates bound in the available coordination sites. The synthesis of the L^{DMA} ligand was previously published but the pendant bases had yet to be utilized in small molecule activation.[1,2] The structure-function relationships of these metal complexes bearing various ligands will help to better understand how to tune the reactivity of a metal complex through the ligand scaffold.

3.2. Background

Growing energy demand and climate change due to fossil fuels are driving interest in the development of renewable energy technology. In particular, there is interest in catalysts that are earth abundant. Molecular catalysts are central to fundamental studies of energy storage reactions because they can be tuned to specific reactivity through chemical design.

Cobalt complexes have been pursued for many small molecule transformations including carbon dioxide reduction[3,4] and water splitting[5-7], to form hydrogen[8-10] and form oxygen[11,12]. Cobalt's many redox states allow access to multi-electron reactivity. The attempt to expand the scope of reactivity and understand the effect of ligand environment on molecular cobalt complexes

is discussed here. The use of ligands in a cobalt system with hydrogen-bonding capabilities will explore reactivity that mimics proton relays found in biology.

3.3. Results and Discussion

3.3.1. Synthesis Divalent Cobalt Complexes

Scheme 3.1. Synthesis of divalent cobalt complexes $[CoL^{H}(CH_3CN)_2][BF_4]_2$, $[Co_2(\mu\text{-}F)_2(L^{MMA})_2][BF_4]_2$ and $[CoL^{DMA}(CH_3CN)_2][BF_4]_2$.

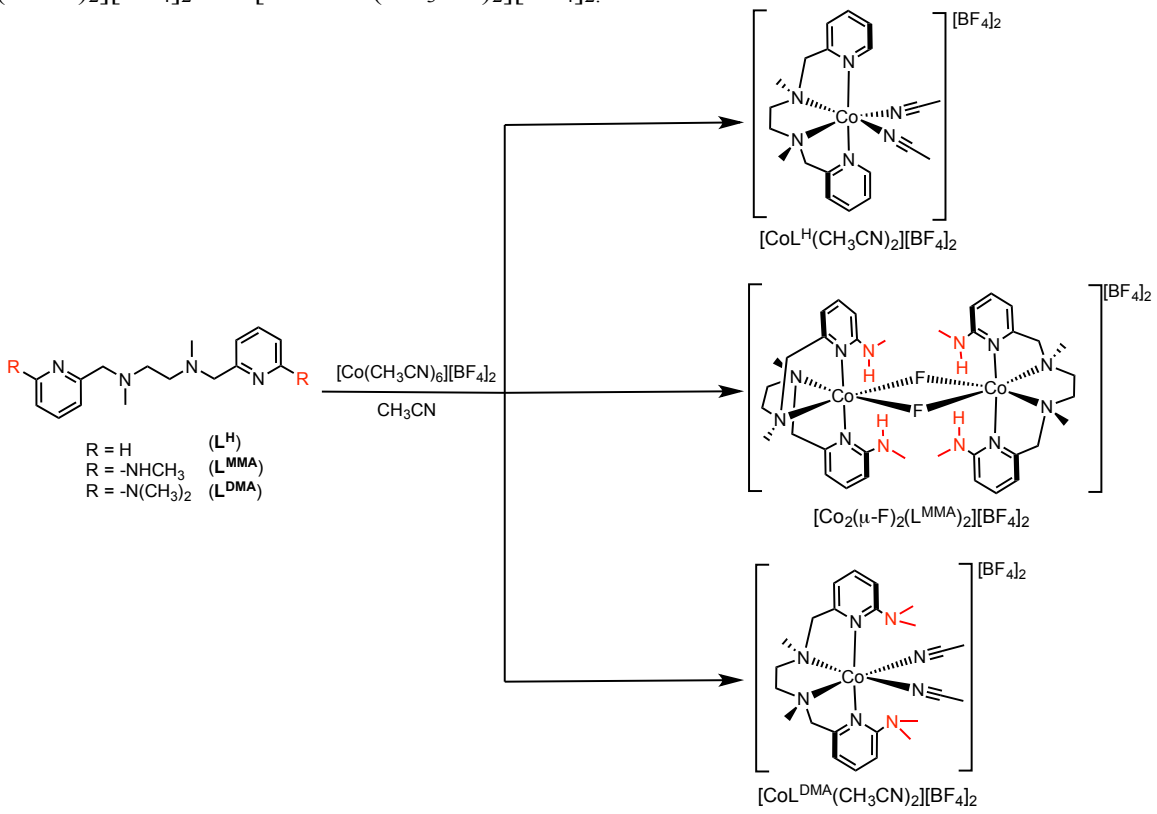

The divalent cobalt complexes $[CoL^{H}(CH_3CN)_2][BF_4]_2$, $[Co_2(\mu\text{-}F)_2(L^{MMA})_2][BF_4]_2$ and $[CoL^{DMA}(CH_3CN)_2][BF_4]_2$ are easily accessible through the metal salt $[Co(CH_3CN)_6][BF_4]_2$[13] in 78-89% yield (Scheme 3.1). All three complexes are orange solids. Formulation and purity, respectively, were confirmed by ESI-MS and elemental analysis. The cobalt complex containing the L^{MMA} ligand forms a bridging bis-μ-F diamond core from fluoride abstraction of the BF_4^-

counter ion. Fluoride abstraction by cobalt complexes is not uncommon[14-17] and bis-fluoride bridged cobalt dimeric structures have also been reported.[18-21]

It should be noted that highly polar solvents such as dimethylformamide (DMF) and dimethylsulfoxide (DMSO) result in demetallation of the complexes. ^{1}H NMR spectra taken in DMF-d_6 or DMSO-d_6 results in free ligand in solution instead of the expected paramagnetic species. In addition, a solid state structure was obtained for the hexakisdimethylformamide cobalt salt from a DMF reaction solution of $[CoL^{DMA}(CH_3CN)_2][BF_4]_2$.

3.3.2. Physical Characterization of Divalent Cobalt Complexes

Solid State Structures of Divalent Co(II) Complexes

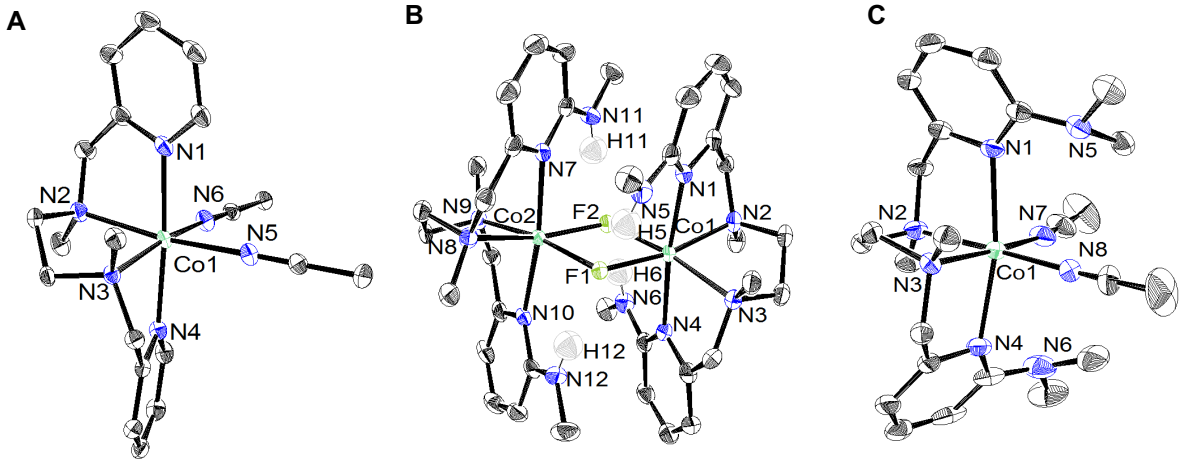

Figure 3.1. ORTEP of the divalent cobalt complexes A) $[CoL^{H}(CH_3CN)_2][BF_4]_2$, B) $[Co_2(\mu\text{-}F)_2(L^{MMA})_2][BF_4]_2$ and C) $[CoL^{DMA}(CH_3CN)_2][BF_4]_2$. Thermal ellipsoids are drawn at the 50% probability level. The BF_4^- counter anions, solvent molecules and hydrogen atoms other than the protons on L^{MMA} have been removed for clarity.

The solid state structures reveal that all three divalent cobalt centers are coordinated by the tetradentate N_2Py_2 ligands (Figure 3.1). Hydrogen atoms shown in $[Co_2(\mu\text{-}F)_2(L^{MMA})_2][BF_4]_2$ structure were found in the difference map. The $[CoL^{H}(CH_3CN)_2][BF_4]_2$ complex is coordinated in an octahedral geometry and has a *cis*-α topological geometry, where the two pyridines in axial

positions are *trans* to each other, and the two labile acetonitrile solvent molecules in the equatorial plane are *cis* to each other. Additionally, the methyl groups on the amine backbone are *trans* to one another.

In the $[Co_2(\mu\text{-}F)_2(L^{MMA})_2][BF_4]_2$ complex, each cobalt center is Co(II) and six-coordinate with a *cis*-α topological geometry, and the methyl groups on each amine backbone are *trans* to one another. It is likely the abstraction occurs and forms a stable crystalline species due to the intramolecular hydrogen-bonding. The hydrogen atoms on the methylamine moieties of the L^{MMA} ligand exhibit hydrogen bonds as designed. Hydrogen atoms, H5 and H12, of one methylamine arm on each cobalt center act as hydrogen bond donors to the fluoride, F1, with a distance of 1.896 Å and 1.924 Å, respectively. Heavy atom distances are N5•••F1 = 2.747 Å and N12•••F1 = 2.757 Å). The hydrogen atoms, H6 and H11, of the other two methylamine arms on each cobalt center hydrogen bond to the other fluoride, F2, with a distance of 1.879 Å and 1.881 Å, respectively. Heavy atom distances are N6•••F2 = 2.729 Å and N11•••F2 = 2.732 Å).

The $[CoL^{DMA}(CH_3CN)_2][BF_4]_2$ complex has an octahedral coordination environment and a *cis*-α topological geometry with the methyl groups on the amine backbone *trans* to one another. The dimethylamine hydrogen bond accepting functionalities are poised over the coordination site so the hydrogen bond acceptor can directly interact with metal-bound substrates, verifying the ligand design allows for secondary interactions with a bound substrate that may aid in activation of small molecules.

Cyclic Voltammetry

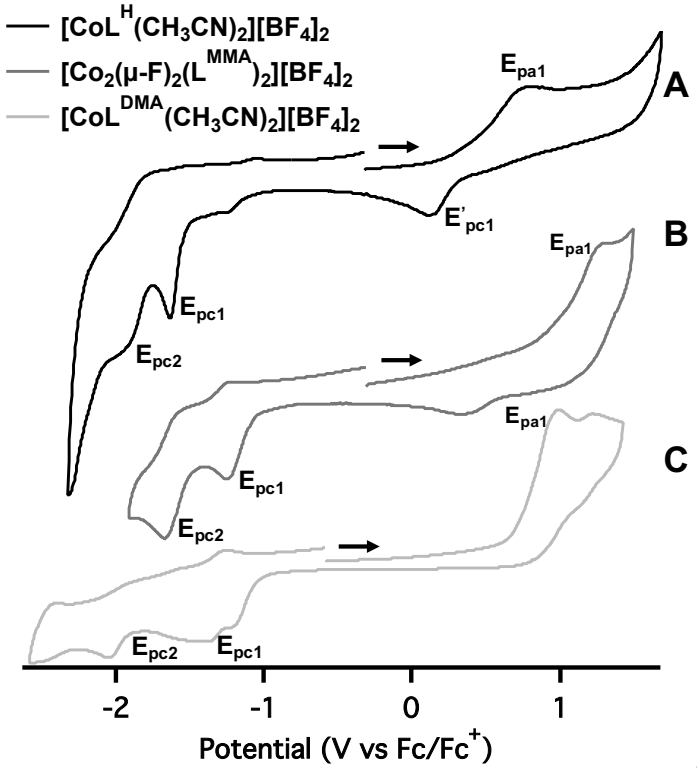

Figure 3.2. Full scan cyclic voltammograms of 1 mM solutions of A) $[CoL^{H}(CH_3CN)_2][BF_4]_2$, B) $[Co_2(\mu\text{-}F)_2(L^{MMA})_2][BF_4]_2$ and C) $[CoL^{DMA}(CH_3CN)_2][BF_4]_2$ in 0.10 M Bu_4NBF_4 in CH_3CN at 100 mV/s.

Table 3.1. Electrochemical values for the Co(II/III) oxidation event (E_{pa}) and Co(II/I) and Co(I/0) reduction events (E_{pc}) of $[CoL^{H}(CH_3CN)_2][BF_4]_2$, $[Co_2(\mu\text{-}F)_2(L^{MMA})_2][BF_4]_2$ and $[CoL^{DMA}(CH_3CN)_2][BF_4]_2$ in CH_3CN at 100 mV/s.

	Potential (V vs Fc)		
	$[CoL^{H}(CH_3CN)_2][BF_4]_2$	**$[Co_2(\mu\text{-}F)_2(L^{MMA})_2][BF_4]_2$**	**$[CoL^{DMA}(CH_3CN)_2][BF_4]_2$**
Co(II/III), E_{pa1}	0.51	1.28	0.96
Co(II/I), E_{pc1}	-1.51	-1.30	-1.39
Co(I/0), E_{pc2}	-2.17	-1.70	-2.08

The full scan cyclic voltammograms of $[CoL^{H}(CH_3CN)_2][BF_4]_2$, $[Co_2(\mu\text{-}F)_2(L^{MMA})_2][BF_4]_2$ and $[CoL^{DMA}(CH_3CN)_2][BF_4]_2$ are shown in Figure 3.2. Tabulated data for E_{pa} of the Co(II/II) oxidation event and E_{pc} for the Co(II/I) and Co(I/0) reduction events are shown in Table 3.1.

The direct comparison of the mononuclear $[CoL^{H}(CH_3CN)_2][BF_4]_2$ and $[CoL^{DMA}(CH_3CN)_2][BF_4]_2$ complexes versus the bridged dinuclear $[Co_2(\mu\text{-}F)_2(L^{MMA})_2][BF_4]_2$ may not be entirely accurate due to the different coordination environments. However, it is apparent that $[Co_2(\mu\text{-}F)_2(L^{MMA})_2][BF_4]_2$ is the most difficult to oxidize to the Co(III) oxidation state (oxidation potential E_{pa} = 1.28 V). Similarly, this complex is also the easiest to reduce with the most positive reduction potentials for the Co(II/I) and Co(I/0) events. This trend is a result of the highly electronegative fluoride atoms which are inductively withdrawing and pull electron density away from the metal center.

When comparing the two mononuclear complexes $[CoL^{H}(CH_3CN)_2][BF_4]_2$ and $[CoL^{DMA}(CH_3CN)_2][BF_4]_2$, the complex containing the more electron rich ligand (L^{DMA}) has a more positive oxidation potential. It would be expected that electron donation would cause the opposite effect in the reduction potentials, where an electron rich metal center would be easier to reduce. Indeed, the $[CoL^{DMA}(CH_3CN)_2][BF_4]_2$ complex has more positive reduction potentials for the events assigned to the Co(II/I) and Co(I/0) events.

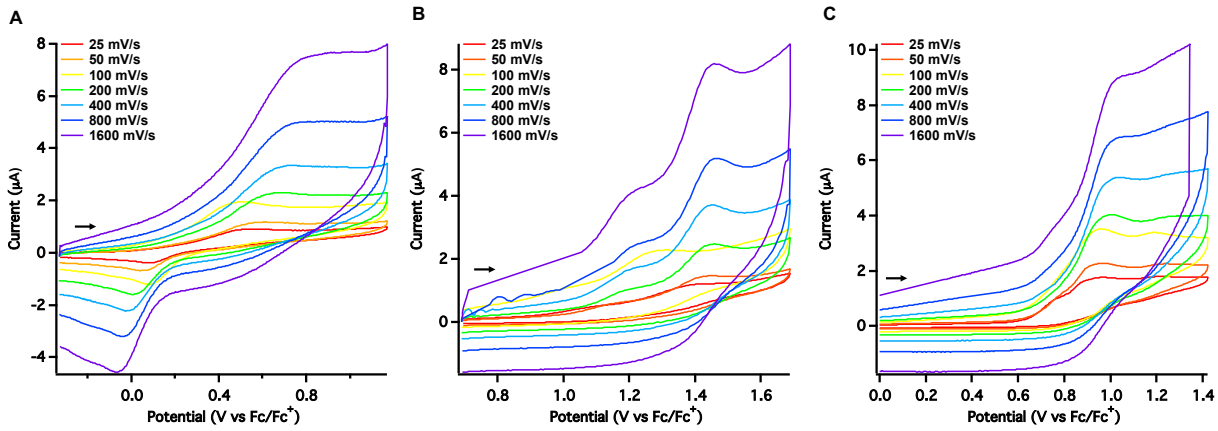

Figure 3.3. Scan rate dependent cyclic voltammograms of the Co(II/III) oxidation events of 1.0 mM solutions of A) $[CoL^{H}(CH_3CN)_2][BF_4]_2$, B) $[Co_2(\mu\text{-}F)_2(L^{MMA})_2][BF_4]_2$ and C) $[CoL^{DMA}(CH_3CN)_2][BF_4]_2$ in 0.10 M Bu_4NBF_4 in CH_3CN at scan rates 25–1600 mV/s.

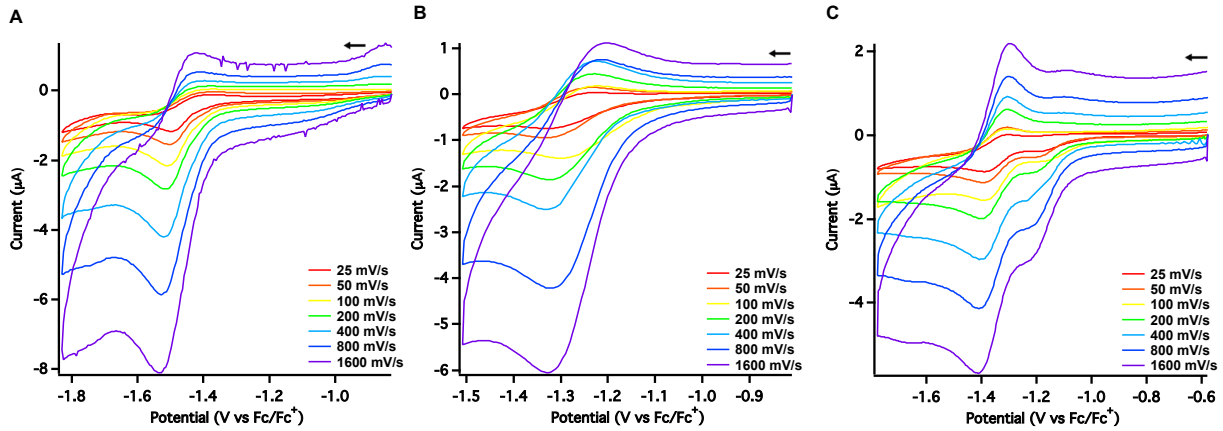

Figure 3.4. Scan rate dependent cyclic voltammograms of the Co(II/I) reduction events of 1.0 mM solutions of A) $[CoL^{H}(CH_3CN)_2][BF_4]_2$, B) $[Co_2(\mu\text{-}F)_2(L^{MMA})_2][BF_4]_2$ and C) $[CoL^{DMA}(CH_3CN)_2][BF_4]_2$ in 0.10 M Bu_4NBF_4 in CH_3CN at scan rates 25–1600 mV/s.

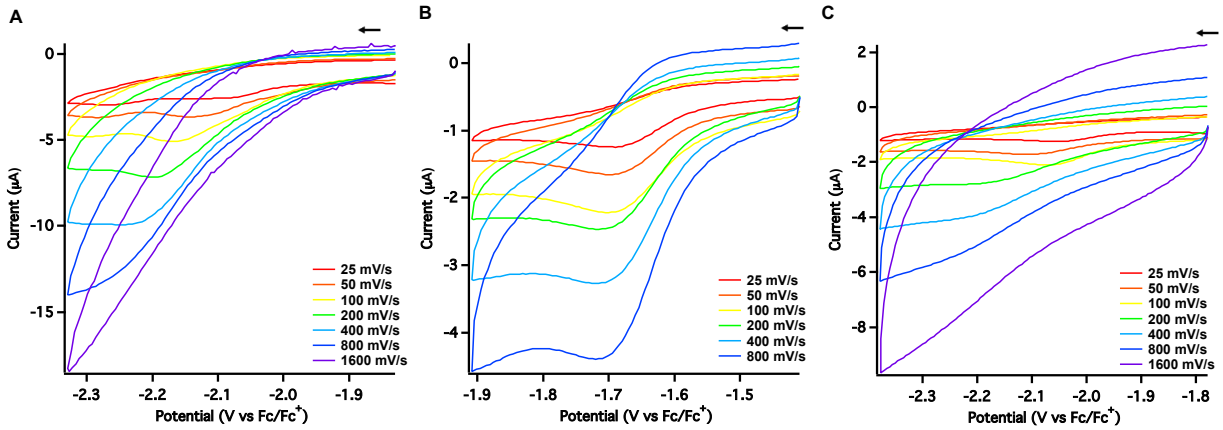

Figure 3.5. Scan rate dependent cyclic voltammograms of the Co(I/0) reduction events of 1.0 mM solutions of A) $[CoL^{H}(CH_3CN)_2][BF_4]_2$, B) $[Co_2(\mu\text{-}F)_2(L^{MMA})_2][BF_4]_2$ and C) $[CoL^{DMA}(CH_3CN)_2][BF_4]_2$ in 0.10 M Bu_4NBF_4 in CH_3CN at scan rates 25–1600 mV/s.

Table 3.2. Electrochemical values for Co(II/I) reduction event of $[CoL^{H}(CH_3CN)_2][BF_4]_2$ at scan rates 25–1600 mV/s.

Scan Rate (mV/s)	i_a (µA)	i_c (µA)	i_a/i_c	E_{pa} (V)	E_{pc} (V)	ΔE_p (mV)
25	0.51	-0.77	0.66	-1.41	-1.50	86.00
50	0.51	-1.11	0.46	-1.41	-1.50	96.20
100	0.64	-1.66	0.38	-1.41	-1.51	95.80
200	0.88	-2.26	0.39	-1.41	-1.51	101.20
400	1.35	-3.47	0.39	-1.42	-1.52	101.30
800	1.87	-4.81	0.39	-1.41	-1.53	116.20
1600	2.94	-6.64	0.44	-1.42	-1.53	117.00

Table 3.3. Electrochemical values for Co(II/I) reduction event of $[Co_2(\mu\text{-}F)_2(L^{MMA})_2][BF_4]_2$ at scan rates 25–1600 mV/s.

Scan Rate (mV/s)	i_a (µA)	i_c (µA)	i_a/i_c	E_{pa} (V)	E_{pc} (V)	ΔE_p (mV)
25	0.43	-0.54	0.79	-1.22	-1.33	108.2
50	0.59	-0.76	0.78	-1.23	-1.33	98.55
100	0.75	-1.11	0.68	-1.22	-1.30	78.64
200	1.30	-1.63	0.80	-1.22	-1.32	98.45
400	1.74	-2.33	0.75	-1.23	-1.33	103.91
800	2.33	-3.84	0.61	-1.21	-1.32	108.46
1600	3.32	-5.64	0.59	-1.20	-1.33	127.91

Table 3.4. Electrochemical values for Co(II/I) reduction event of $[CoL^{DMA}(CH_3CN)_2][BF_4]_2$ at scan rates 25–1600 mV/s.

Scan Rate (mV/s)	i_a (µA)	i_c (µA)	i_a/i_c	E_{pa} (V)	E_{pc} (V)	ΔE_p (mV)
25	0.44	-0.83	0.53	-1.30	-1.39	90.72
50	0.56	-1.07	0.53	-1.31	-1.39	86.18
100	0.63	-1.39	0.45	-1.31	-1.39	86.33
200	1.23	-1.84	0.67	-1.31	-1.40	96.12
400	1.63	-2.72	0.60	-1.31	-1.41	101.44
800	2.66	-3.72	0.71	-1.30	-1.41	111.07
1600	3.40	-4.96	0.69	-1.30	-1.41	115.30

The cyclic voltammograms of $[CoL^{H}(CH_3CN)_2][BF_4]_2$ exhibited an irreversible event attributed oxidation of Co(II) to Co(III) at E_{pa} = 0.51 V (at 100 mV/s). There is a return reduction at E_{pc} = 0.08 V, although the peak to peak separation is ΔE_p = 435 mV, so the event is irreversible. Irreversible events assigned to the Co(II/I) and Co(I/0) reduction events are seen at E_{pc} = −1.51 and −2.17 V, respectively. Both reductions remained completely irreversible at the scan rates examined (25–1600 mV/s). Although, the peak to peak separation of the Co(II/I) event is small (ΔE_p = 95 mV at 100 mV/s) and comparable to the ferrocene/ferrocenium couple in solution (ΔE_p = 110 mV) the i_a/i_c = 0.45 is far from the ideal value of 1.0. The scan rate dependence of all

redox events is shown in Figure 3.3A–3.5A. The tabulated data for the Co(II/I) reduction event is shown in Table 3.2.

Cyclic voltammograms of $[Co_2(\mu\text{-}F)_2(L^{MMA})_2][BF_4]_2$ show an irreversible event assigned to the Co(II/III) oxidation event at E_{pa} = 1.28 V (at 100 mV/s). There is no return reduction upon scanning in the negative direction. There are two irreversible reduction events at E_{pc} = −1.30 and −1.70 V which are attributed to reduction to Co(I) and Co(0), respectively. The Co(II/I) event at 100 mV/s has a i_a/i_c = 0.68, and is therefore not an ideal reversible couple. The tabulated data is shown in Table 3.3. The Co(I/0) event maintained complete irreversibility at all scan rates examined (25–1600 mV/s). The scan rate dependence of all redox events is shown in Figure 3.3B–3.5B.

Cyclic voltammetry of $[CoL^{DMA}(CH_3CN)_2][BF_4]_2$ at 100 mV/s displays three irreversible features. The oxidation event which is assigned to the Co(II/III) oxidation occurs at E_{pa} = 0.96 V and has no return reduction features at any of the scan rates tested (25–1600 mV/s). Additionally, there are two reduction events at E_{pc} = −1.39 and −2.08 V, which remain irreversible at the scan rates examined (25–1600 mV/s). The first reduction is assigned to the Co(II/I) event which has a non-ideal i_a/i_c = 0.45 at 100 mV/s and is not electrochemically reversible. The tabulated data is shown in Table 3.4. The second reduction event is assigned to the Co(I/0). The scan rate dependence of all redox events is shown in Figure 3.3C–3.5C.

Ultraviolet-Visible Spectroscopy

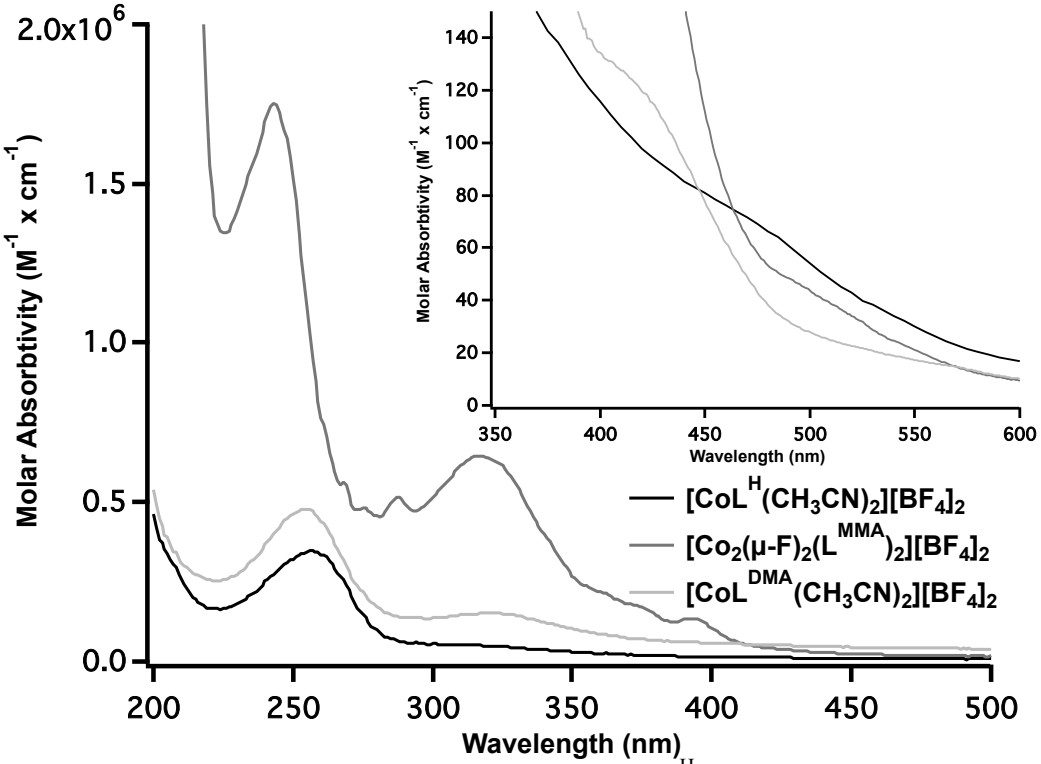

Figure 3.6. UV-Vis spectra of 5 μM CH_3CN solutions of $[CoL^{H}(CH_3CN)_2][BF_4]_2$ (black trace), $[Co_2(\mu\text{-}F)_2(L^{MMA})_2][BF_4]_2$ (dark gray trace), and $[CoL^{DMA}(CH_3CN)_2][BF_4]_2$ (light gray trace). Inset: UV-Vis spectra of 5 mM CH_3CN solutions, *d-d* transitions.

Table 3.5. Maximum wavelength (λ_{max}) and molar absorptivity (ε) values for $[CoL^{H}(CH_3CN)_2][BF_4]_2$, $[Co_2(\mu\text{-}F)_2(L^{MMA})_2][BF_4]_2$ and $[CoL^{DMA}(CH_3CN)_2][BF_4]_2$ determined by UV-Vis.

	π–π*		***π–π****		***d–d***	
	λ_{max}(nm)	**ε ($M^{-1} \times cm^{-1}$)**	**λ_{max}(nm)**	**ε ($M^{-1} \times cm^{-1}$)**	**λ_{max}(nm)**	**ε ($M^{-1} \times cm^{-1}$)**
$[CoL^{H}(CH_3CN)_2][BF_4]_2$	257	4,000	-	-	465	80
$[Co_2(\mu\text{-}F)_2(L^{MMA})_2][BF_4]_2$	243	104,000	317	58,000	491	55
$[CoL^{DMA}(CH_3CN)_2][BF_4]_2$	256	27,000	324	17,000	411	130

UV–Vis spectra of all complexes were taken in CH_3CN and are shown in Figure 3.6. The UV-Vis profile of $[CoL^{H}(CH_3CN)_2][BF_4]_2$ contains an absorption band at 257 nm which is attributed to the pyridyl *π–π** transitions within the ligand. The shoulder at 465 nm is assigned to the *d-d* transition of the metal center which is typical of d^7 octahedral Co(II) complexes.[22] $[Co_2(\mu\text{-}$

F)$_2$(L^{MMA})$_2$][BF_4]$_2$ exhibits two absorption bands at 243 and 317 nm, respectively. The former is the pyridyl π–π* transition while the secondary absorption band is indicative of the tautomeric structure possible for heteroatom substituted pyridines.[23] The *d-d* transition of the octahedral metal center occurs at 491 nm. Evidence of the dimeric structure in solution is noted in the molar absorptivity (ε) value, Table 3.5. The value is an order of magnitude larger than in [CoL^{DMA}(CH_3CN)$_2$][BF_4]$_2$ indicating there may be two ligands present in the structure. [CoL^{DMA}(CH_3CN)$_2$][BF_4]$_2$ also contains two absorption bands due to the two pyridyl π–π* transitions that occur at 256 and 324 nm, respectively. The *d-d* transition for the cobalt complex containing the L^{DMA} ligand occurs that the lowest wavelength, 411 nm.

Infrared Spectroscopy

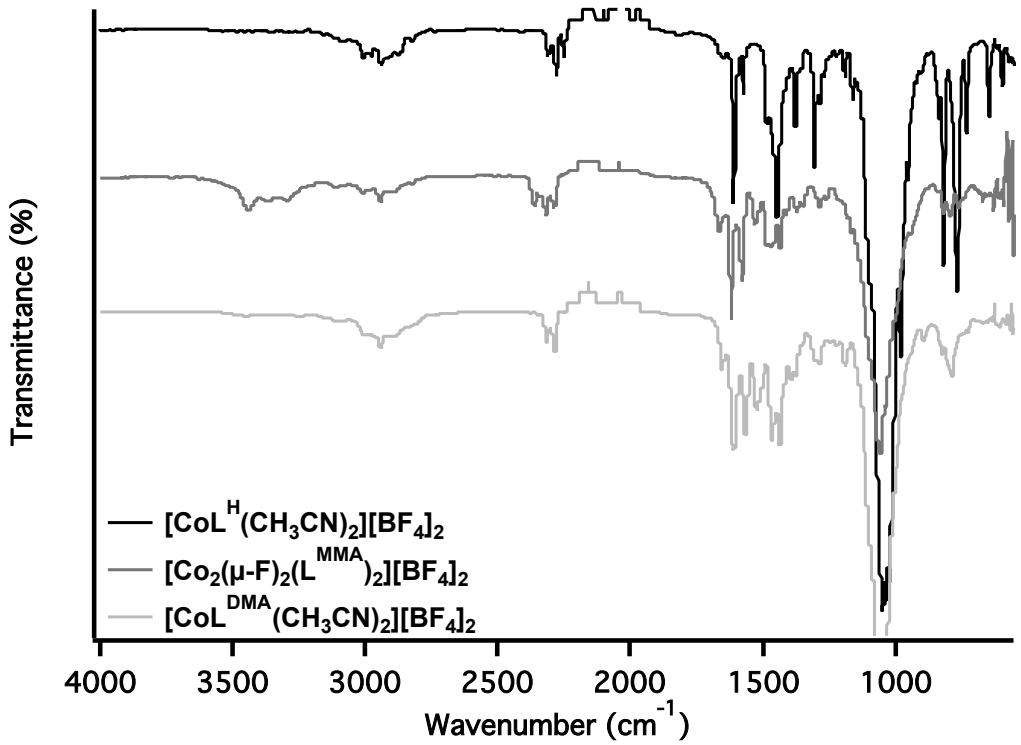

Figure 3.7. IR spectra of [CoL^H(CH_3CN)$_2$][BF_4]$_2$ (black trace), [Co_2(μ-F)$_2$(L^{MMA})$_2$][BF_4]$_2$ (dark gray trace), and [CoL^{DMA}(CH_3CN)$_2$][BF_4]$_2$ (light gray trace).

All three cobalt complexes exhibit a strong absorption band at 1048 cm^{-1} which belongs to the B–F stretching frequency of the BF_4^- anions (Figure 3.7). In the 3000 cm^{-1} region, all complexes contain C-H stretching frequencies of both sp^2 and sp^3 hybridized carbons of the alkane and aromatic functionalities of the ligand. However, a major difference between the ligand structures can be seen in the N–H stretching frequency of the L^{MMA} ligand, which contains a secondary amine. $[Co_2(\mu\text{-}F)_2(L^{MMA})_2][BF_4]_2$ exhibits a stretching frequency at 3440 cm^{-1} which is typical for amines.

Electron Paramagnetic Resonance Spectroscopy

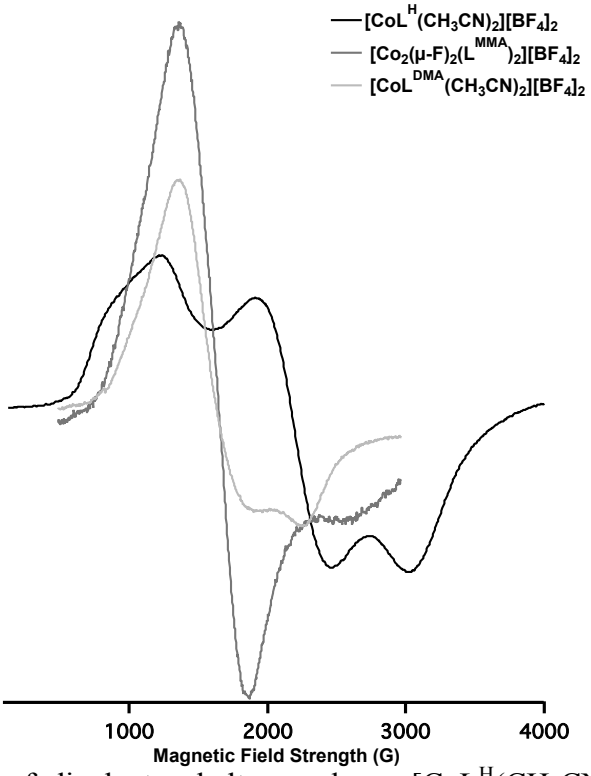

Figure 3.8. EPR spectra of divalent cobalt complexes $[CoL^H(CH_3CN)_2][BF_4]_2$ (black trace), $[Co_2(\mu\text{-}F)_2(L^{MMA})_2][BF_4]_2$ (dark gray trace), and $[CoL^{DMA}(CH_3CN)_2][BF_4]_2$ (light gray trace). All samples taken as 10 mM frozen CH_3CN solutions at 10 K.

Table 3.6. EPR g values of $[CoL^{H}(CH_3CN)_2][BF_4]_2$, $[Co_2(\mu\text{-}F)_2(L^{MMA})_2][BF_4]_2$, and $[CoL^{DMA}(CH_3CN)_2][BF_4]_2$ at 10 K.

	10 K		
	g_1	g_2	g_3
$[CoL^{H}(CH_3CN)_2][BF_4]_2$	5.65	3.19	2.13
$[Co_2(\mu\text{-}F)_2(L^{MMA})_2][BF_4]_2$	-	4.31	-
$[CoL^{DMA}(CH_3CN)_2][BF_4]_2$	-	4.19	2.66

All three cobalt complexes exhibit g values between 3-5 which is typical of Co(II) high spin S=3/2 systems (Figure 3.8 and Table 3.6).[24] Only the mononuclear complexes $[CoL^{H}(CH_3CN)_2][BF_4]_2$ and $[CoL^{DMA}(CH_3CN)_2][BF_4]_2$ show rhombic signals with additional g values. The $[Co_2(\mu\text{-}F)_2(L^{MMA})_2][BF_4]_2$ complex results in a broad signal with a single g value of 4.31.

Table 3.7. Selected bond distances (Å) and angles (°) for the $[Co_2(\mu\text{-}F)_2(L^{MMA})_2][BF_4]_2$ complex.

$[Co_2(\mu\text{-}F)_2(L^{MMA})_2][BF_4]_2$			
Co1-F1	2.078(2)	**Co1-F1-Co2**	100.57
Co2-F1	2.073(2)	**Co1-F2-Co2**	99.87
Co1-F2	2.091(2)		
Co2-F2	2.082(2)		
Co1•••Co2	3.193		
F1-F2	2.669		

Complexes with bridged halides can magnetically couple through the halogen atoms. Typically, the antiferromagnetic coupling is reported by the μ_{eff} value, which are centered around 2.0 for dicobalt fluoride complexes,[21] although coupling can be diminished through a diamond core M_2F_2 framework due to the acute angles and lack of orbital overlap.

In the EPR spectrum of $[Co_2(\mu\text{-}F)_2(L^{MMA})_2][BF_4]_2$, the g value of 4.19 is typical of mononuclear S=3/2 Co(II) complexes, indicating there is no or very little magnetic coupling in

solution. However, it is not surprising based on the bond lengths and angles of the solid state structure in comparison to other dicobalt fluoride complexes.[21] The Co-F and Co•••Co distances are longer than is typically observed in antiferromagnetically coupled $Co_2(\mu\text{-}F)$ complexes (Table 3.7). Additionally, the Co-F-Co angles are more acute than coupled complexes, and is a diamond core M_2F_2 bridged center instead of a linear fluoride bridged complex. These features all may contribute to less orbital overlap and lowered magnetic coupling.

3.3.3. Carbon Dioxide Reduction Reactivity

Carbon Dioxide Reduction Reaction Background

The reduction of carbon dioxide can lead to a variety of products depending on the number of reducing protons and electrons. The two electron reduction leads to carbon monoxide or formic acid and the highly desired six electron reduction gives liquid methanol. Higher order carbon products such as ethylene require formation of a carbon-carbon bond from CO_2, a challenging reaction.[25]

There are many major biological pathways that convert CO_2 to biomass including carbon fixation during photosynthesis; only the simple transformations of carbon dioxide to carbon monooxide and formate will be discussed here.[26] CO dehydrogenase enzymes have heterobimetallic active sites and reversibly convert carbon dioxide to carbon monooxide. [NiFe] CO dehydogenase contains a nickel center that is incorported into a rigid Fe_3S_4 cluster with another distal iron present in close proximity.[27] The heterobimetallic metal active site acts as a cooperative unit for CO_2 activation. Additionally, a secondary coordination sphere histidine has been invoked as a proton transfer agent to aid in the conversion of carbon dioxide.[28] The [MoCu] dehydrogenase contains a molybdenum oxo coordinated by a disulfur molybdopterin cytosine dinucleotide

cofactor as well as a hydroxo ligand.[29] The copper center is bridged to the molybdenum by a sulfur atom. There are various amino acid residues within hydrogen-bonding distance to the oxo and hydroxo ligands which improve substrate activation. Both the [Mo] and [W] formate dehydrogenase are mononuclear metal active sites coordinated by four sulfur atoms through two pyranopterin ligands, a cysteine residue, or a selenium atom from a selenocysteine residue, and either a sulfur or an oxygen atom in the sixth coordination site.[30] There are two distal arginine and histidine residues that contribute to proton movement.

Synthetic inorganic complexes have utilized biomimetic approaches such as cooperative bimetallic centers or distal pendant bases to facilitate CO_2 binding.[28,31,32] A dipalladium complex has been shown to bind CO_2 but has few turnovers before being deactivated by Pd-Pd bond formation.[33] Thus, heterobimetallic systems have been developed to tune the ability of cooperativity. Floriani and coworkers utilized cobalt salen complexes with exogenous alkali metals to reversibly activate CO_2.[34,35]

Protic interactions have also been used to stabilize carboxylate intermediates to enhance CO_2 reduction activity. Iridium complexes with hydroxyl moieties[36,37] or amine protons[38] in the secondary coordination sphere have been used as carbon dioxide reduction catalysts. Savéant and coworkers reported an iron porphyrin with phenol modifications that showed enhanced carbon dioxide reduction activity compared to the unfunctionalized complex.[39] Kubiak and coworkers reported nickel bisdiphosphine complexes with various pendant amines that showed formate oxidation activity to carbon dioxide via coupled proton and electron transfer.[40,41]

Reactivity with Carbon Dioxide

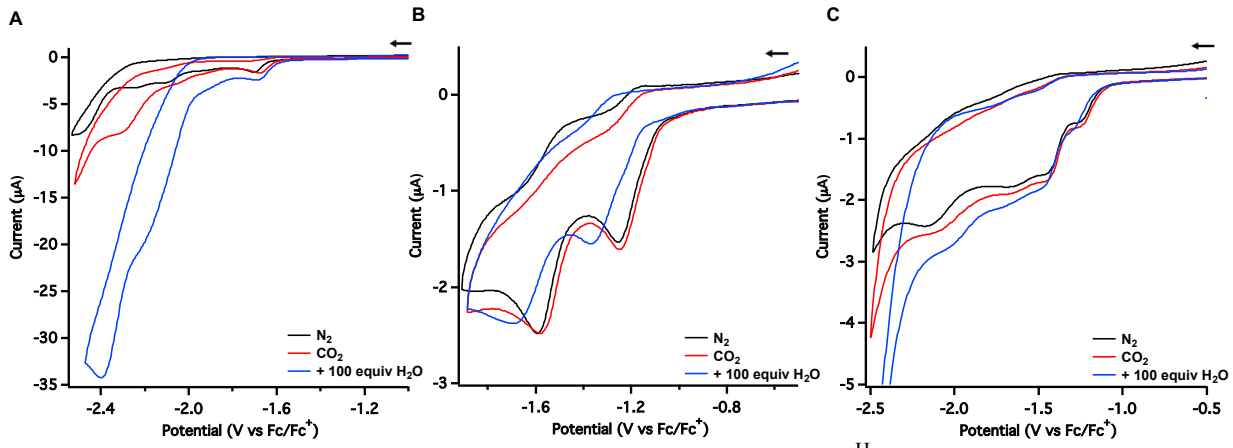

Figure 3.9. Cyclic voltammograms of 1.0 mM solutions of A) $[CoL^{H}(CH_3CN)_2][BF_4]_2$, B) $[Co_2(\mu\text{-}F)_2(L^{MMA})_2][BF_4]_2$ and C) $[CoL^{DMA}(CH_3CN)_2][BF_4]_2$ under N_2 (black trace), CO_2 (red trace), and added water (blue trace) in 0.10 M Bu_4NBF_4 in CH_3CN at 100 mv/s.

The reactivity of the divalent cobalt complexes upon reduction with carbon dioxide present was tested by cyclic voltammetry (Figure 3.9). $[CoL^{H}(CH_3CN)_2][BF_4]_2$ demonstrated a 23 mV positive potential shift at the Co(II/I) event and current enhancement at the Co(I/0) event under CO_2 vs N_2. Upon addition of water as a proton source there was a large current enhancement which may be promising CO_2 reduction reactivity, albeit at a very negative potential. Further studies need to be performed to confirm catalytic activity and product formation. The $[Co_2(\mu\text{-}F)_2(L^{MMA})_2][BF_4]_2$ and $[CoL^{DMA}(CH_3CN)_2][BF_4]_2$ complexes both exhibit minimal current enhancement under CO_2 vs N_2 at both reduction events. After addition of water to $[Co_2(\mu\text{-}F)_2(L^{MMA})_2][BF_4]_2$ there is a shift to more negative potentials. The $[CoL^{DMA}(CH_3CN)_2][BF_4]_2$ complex has a mild current enhancement at both reduction events after addition of water as a proton source.

Floriani and coworkers reported enhanced carbon dioxide activation with cobalt salen complexes when alkali metals were added.[34,35] One equivalent of $LiBF_4$ was added to a solution of $[CoL^{H}(CH_3CN)_2][BF_4]_2$ complex to test for cooperative CO_2 activation by cyclic voltammetry. There was no change in the current enhancement or shift in reduction potential. The lack of

enhancement in activity may be due to the lack of additional ligands to coordinate the alkali metal into close proximity to the cobalt center. This experiment was not performed using the $[Co_2(\mu\text{-}F)_2(L^{MMA})_2][BF_4]_2$ or $[CoL^{DMA}(CH_3CN)_2][BF_4]_2$ complexes.

Cyclic voltammetry studies of $[CoL^{H}(CH_3CN)_2][BF_4]_2$ under CO_2 with water as a proton source demonstrated current enhancement that may be of interest to pursue. The reduction of CO_2 using an external alkali metal did not improve the current enhancement with this ligand. The $[Co_2(\mu\text{-}F)_2(L^{MMA})_2][BF_4]_2$ and $[CoL^{DMA}(CH_3CN)_2][BF_4]_2$ complexes do show minor response to carbon dioxide under reducing conditions that is minimally improved with the addition of a source of protons, water.

3.3.4. Water Splitting Reactivity

$$2\,H_2O \rightleftharpoons O_2 + 4\,H^+ + 4\,e^- \quad \textbf{eq 1}$$

$$4\,H^+ + 4\,e^- \rightleftharpoons 2\,H_2 \quad \textbf{eq 2}$$

$$\boxed{2\,H_2O \rightleftharpoons O_2 + 2\,H_2} \quad \textbf{eq 3}$$

Water splitting (Equation 3) involves two distinct processes requiring a total of four protons and electrons. The first half reaction is water oxidation to dioxygen or the oxygen evolution reaction (OER, Equation 1) and the second reaction is proton reduction to dihydrogen or the hydrogen evolution reaction (HER, Equation 2).

Both half reactions occur in nature with the HER catalyzed by the hydrogenase enzyme and the OER catalyzed by the Oxygen Evolving Complex (OEC) in Photosystem II. These natural systems can serve as models for synthetic systems for energy storage and conversion technology.[42] The proficient conversion of small molecules and energy efficiency of these natural systems is aided by the secondary coordination sphere of the active site. Surrounding amino acid residues

provide controlled movement of protons to and from the active site through proton channels and relays.

3.3.4.1. Proton Reduction Reactivity

Hydrogen Evolution Reaction Background

Hydrogenase enzymes found in bacteria, archaea and eukaryotic cells reversibly convert protons to dihydrogen to generate or metabolize energy.[43,44] The production of dihydrogen is highly inefficient and kinetically slow without a catalyst.[45]

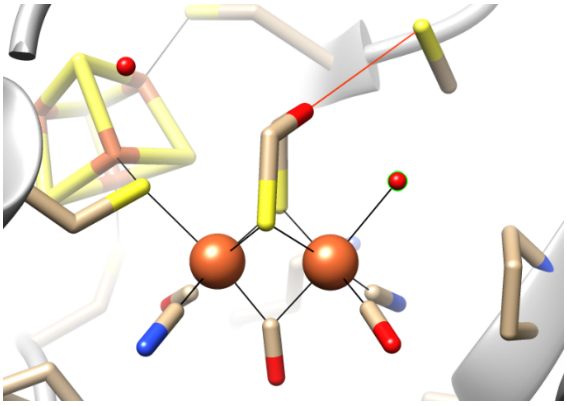

Figure 3.10. Structure of [FeFe]-hydrogenase (PDB 3C8Y). Red = O, orange = Fe, yellow = S, blue = N. Red lines represent H-bonding interactions.

There are three classes of hydrogenases: [NiFe]-hydrogenase, [FeFe]-hydrogenase, and [Fe]-only hydrogenase. The [NiFe]-hydrogenase consists of a heterodimeric unit that contains iron-sulfur clusters and a nickel-iron active site. The iron metal center has cyanide (CN^-) and carbonyl (CO) ligands resulting in an electron deficient iron center. The active site is buried within the enzyme structure and requires multiple secondary networks to shuttle substrates and electrons to and from the site. The substrate channel is formed by hydrophobic residues that connect the outer surface of the enzyme to the active site while the electron transfer chain is a series of iron-sulfur clusters.[44] The [FeFe]-hydrogenase consists of a di-iron cluster with CN^- and CO ligands

bound to the metal centers. A single iron center is bound directly to an iron-sulfur cluster which behaves as an electron transfer unit (Figure 3.10). Additionally, there is a bridging disulfur moiety containing a pendant amine. This unique coordination environment involving covalent attachment of the electron rich iron-sulfur cluster and secondary sphere pendant base lends to the higher H_2 production than the [NiFe].[43,44] The [Fe]-only hydrogenase is a homodimer and differs from the [NiFe] and [FeFe] structurally in that it does not contain any iron-sulfur clusters and does not involve a secondary metal center. The [Fe]-only can activate hydrogen, but only in the presence of an external substrate, methenyltetrahydromethanopterin.

Synthetic systems that have low energetic barriers for hydrogen activation have improved reactivity by increasing the acidity of the bound hydrogen.[44,46,47] Several synthetic complexes have been developed as structural and reactive analogs to the active sites of [NiFe] and [FeFe]-hydrogenase.[48,49] Dubois and coworkers have reported a variety of nickel diphosphine complexes that perform the hydrogen production or oxidation reaction.[50] They have utilized pendant amine bases to increase reactivity and lower activation barriers.[45,51-53] Nocera and coworkers have reported hangman porphyrin complexes that increased rates of proton reduction with proton donating pendant amines or carboxylic acids.[54,55] A ruthenium polypyridyl catalyst had improved proton reduction activity with a proximal naphthalene versus a distal naphthalene.[56]

Proton Reduction Reactivity with Various Acid Sources

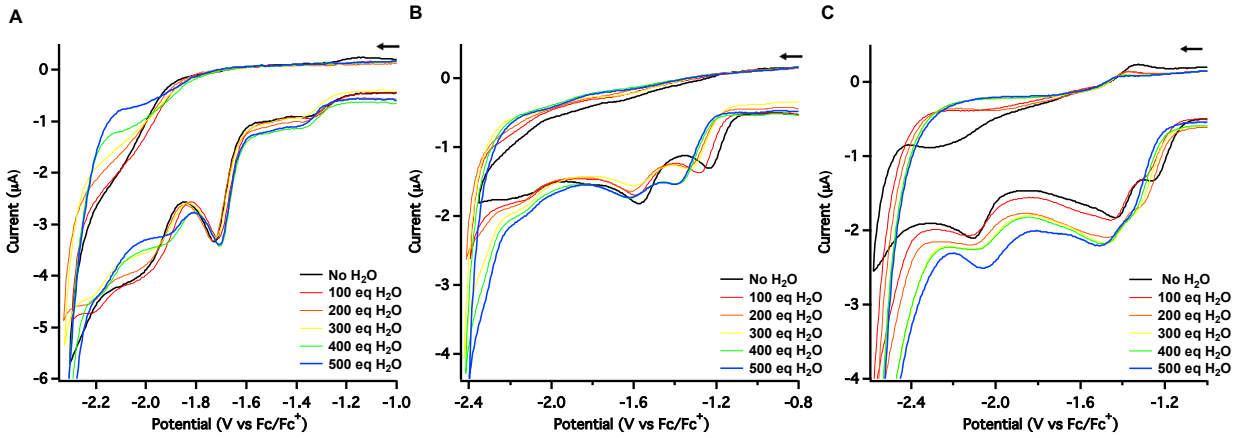

Figure 3.11. Cyclic voltammograms upon addition of water for 1.0 mM solutions of A) $[CoL^{H}(CH_3CN)_2][BF_4]_2$, B) $[Co_2(\mu\text{-}F)_2(L^{MMA})_2][BF_4]_2$ and C) $[CoL^{DMA}(CH_3CN)_2][BF_4]_2$ in 0.10 M Bu_4NBF_4 in CH_3CN at 100 mv/s.

The reactivity of all three cobalt complexes with water as a proton source in CH_3CN is shown in Figure 3.11. $[CoL^{H}(CH_3CN)_2][BF_4]_2$ exhibits no change in the current with added water. The $[Co_2(\mu\text{-}F)_2(L^{MMA})_2][BF_4]_2$ complex has a shift to more negative reduction potentials with water as a proton source. The hydrogen bond accepting complex $[CoL^{DMA}(CH_3CN)_2][BF_4]_2$ displays a mild current enhancement with increasing water concentration. Attempts to use stronger acids such as $[HTEA][BF_4]$ (pK_a = 18.8 in CH_3CN)[57], $[PhNH_3][BF_4]$ (pK_a = 10.6 in CH_3CN)[57], and $[HDMF][BF_4]$ (pK_a = 6.1 in CH_3CN)[58] all resulted in demetallation to the Co^{2+} salt in solution. The current enhancement evident in these solutions was confirmed by independent cyclic voltammograms utilizing $[Co(CH_3CN)_6][BF_4]_2$ and the various acids.

Cyclic voltammetry studies of the cobalt complexes with water as a proton source indicates $[CoL^{DMA}(CH_3CN)_2][BF_4]_2$ shows promising results as a proton reduction catalyst with water as a very weak acid. Use of strong organic acids resulted in decomposition, and other acids with pK_a values > 18.8 were not tested.

3.3.4.2. Oxygen Evolution Reactivity

Oxygen Evolution Reaction Background

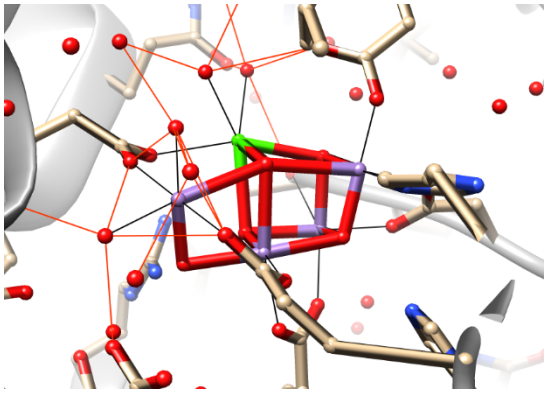

Figure 3.12. Structure of the oxygen evolving complex (PDB 3ARC). Red = O, purple = Mn, green = Ca, blue = N. Red lines represent H-bonding interactions.

Water oxidation occurs in nature as part of the photosynthesis process in plants and algae.[59-62] The active site of the OEC in Photosystem II contains a Mn_4O_5 cluster with a divalent calcium atom (Figure 3.12). The role of the calcium ion is not well understood but it is a structurally important member of the cluster; when removed the enzyme loses oxygen activation reactivity.[63,64] Four water molecules are bound to a dangling manganese atom and the calcium ion as a part of an extensive hydrogen-bonding network. The overall environment is very important to the functionality of catalysis; these proton channels shuttle water or oxygen molecules to and from the active site.

Initial synthetic systems mimicked the cluster structure of the active site,[65-67] or used less abundant metals such as ruthenium and iridium.[65,68-71] Later, single-site catalysts were explored after mononuclear ruthenium catalysts showed they could accommodate the four-electron and four-proton process to directly convert water to dioxygen.[68,72-75] The water oxidation reaction requires a high overpotential, additional potential required by the catalyst beyond the thermodynamic potential of the reaction,[76,77] due to high energy intermediates. The incorporation

of pendant bases aids in effective proton management and improved reactivity by lowering thermodynamic and kinetic barriers.

In synthetic systems, systematic ligand structure and design to facilitate proton-coupled electron transfer (PCET) has been a very effective approach. In particular the role of secondary coordination sphere pendant bases has been utilized in synthetic water oxidation catalysts to circumvent formation of undesired intermediates such as hydrogen peroxide (H_2O_2).[1,68,78,79] Single-site first row homogenous transition metal catalysts for water oxidation are fairly rare, but in the past decade a variety of cobalt catalysts have shown good oxidative stability[11,12,80] and promising activity.[11,12,81,82]

Oxidation Reactivity with Water

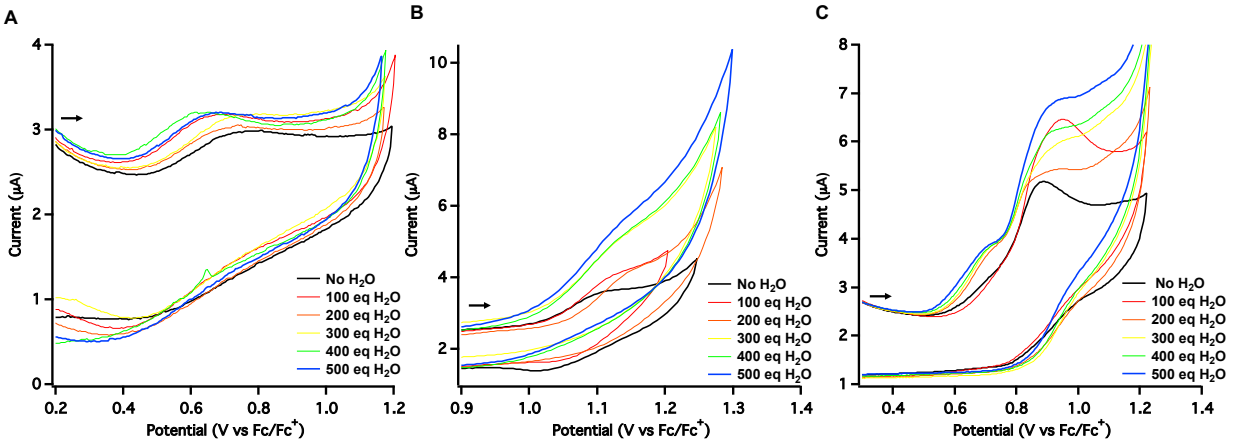

Figure 3.13. Cyclic voltammograms upon addition of water for 1.0 mM solutions of A) $[CoL^{H}(CH_3CN)_2][BF_4]_2$, B) $[Co_2(\mu\text{-}F)_2(L^{MMA})_2][BF_4]_2$ and C) $[CoL^{DMA}(CH_3CN)_2][BF_4]_2$ in 0.10 M Bu_4NBF_4 CH_3CN at 100 mv/s.

Due to the sparing solubility of the cobalt complexes in water, water oxidation activity was tested in solutions of acetonitrile with added aliquots of water (Figure 3.13). The complex with no hydrogen-bonding functionality, $[CoL^{H}(CH_3CN)_2][BF_4]_2$, displays minimal changes in the cyclic voltammogram profile upon addition of water, indicating minimal or no electrocatalytic reactivity.

The complexes containing a hydrogen-bonding donor and acceptor, $[Co_2(\mu\text{-}F)_2(L^{MMA})_2][BF_4]_2$ and $[CoL^{DMA}(CH_3CN)_2][BF_4]_2$ respectively, both exhibit an enhanced current response with increasing water content. Unsurprisingly, the dimer has a smaller response, likely due to the strongly coordinating fluoride anions which limit access to open coordination sites.

Cyclic voltammetry of $[CoL^{DMA}(CH_3CN)_2][BF_4]_2$ has the most promising features for water oxidation activity. The initial current enhancement occurs at 0.95 V but after 200 equivalents of water a new feature develops at 0.70 V which is not catalytically active. The new feature is proposed to be the monoaquo bound species (*vide infra)*. Another feature develops at 0.91 V, replacing the original 0.95 V feature of the bulk $[CoL^{DMA}(CH_3CN)_2][BF_4]_2$ species, and becomes the prominent feature exhibiting current enhancement; it is proposed to be the bisaquo bound species (*vide infra)*.

Preparation and Structure of Aquo Adducts

Scheme 3.2. Synthesis of aquo bound complexes $[CoL^{DMA}(CH_3CN)(H_2O)][BF_4]_2$ and $[CoL^{DMA}(H_2O)_2][BF_4]_2$.

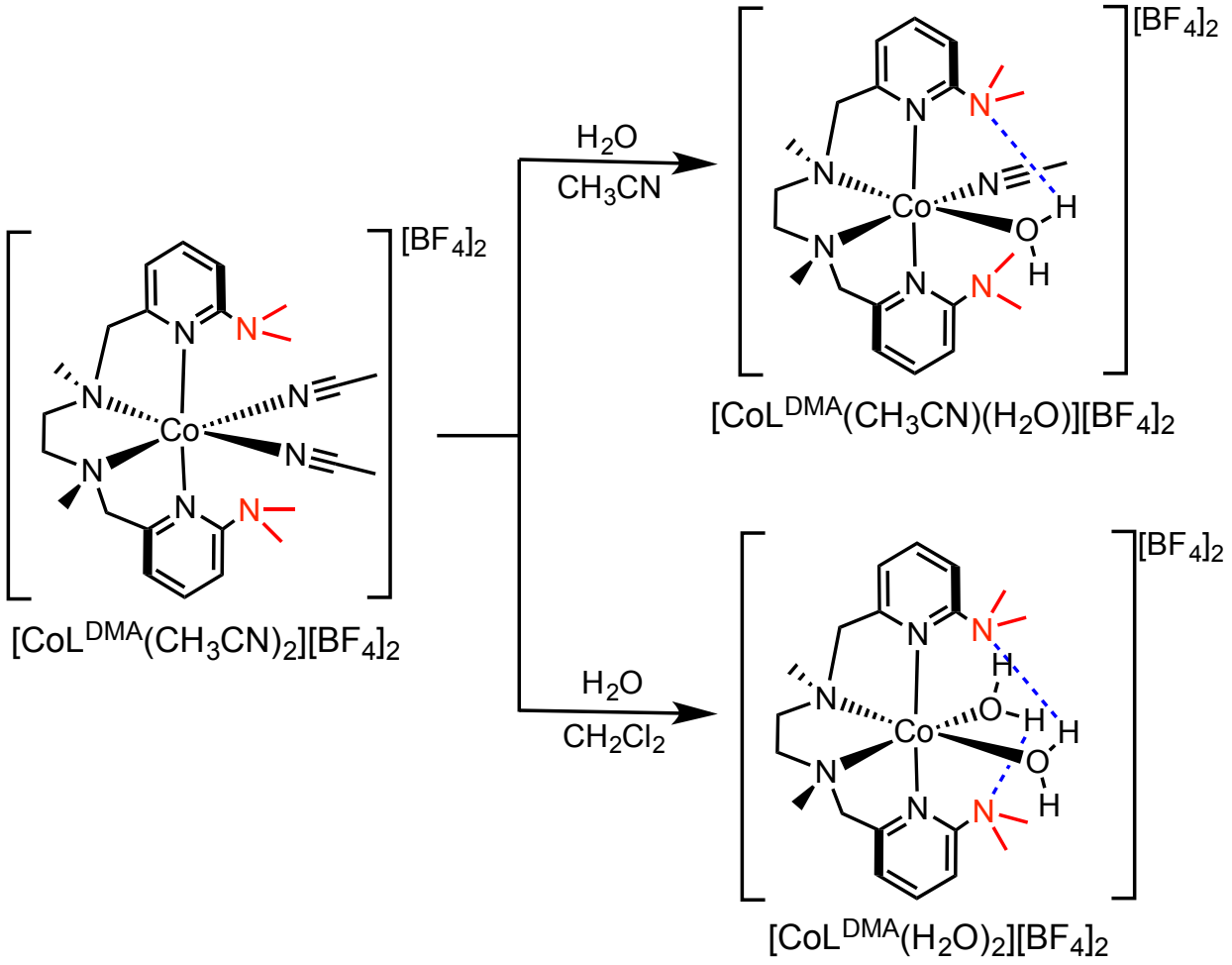

Synthesis of the monoaquo and bisaquo bound structures was pursued as the possible catalytic resting state and to determine if the L^{DMA} ligand behaves as a hydrogen bond acceptor, Scheme 3.2. Synthesis of the monoaquo complex, $[CoL^{DMA}(CH_3CN)(H_2O)][BF_4]_2$, was achieved with ligand displacement by addition of two equivalents of H_2O to an CH_3CN solution of $[CoL^{DMA}(CH_3CN)_2][BF_4]_2$. The bisaquo bound structure $[CoL^{DMA}(H_2O)_2][BF_4]_2$ required a less coordinating solvent, DCM, for both water molecules to coordinate to the metal center. The $[CoL^{DMA}(H_2O)_2][BF_4]_2$ complex is a pink solid which is typical for aquo bound cobalt species. It

should be noted that the aquo ligand is labile and an unknown blue solid results when it is placed under reduced pressure.[83]

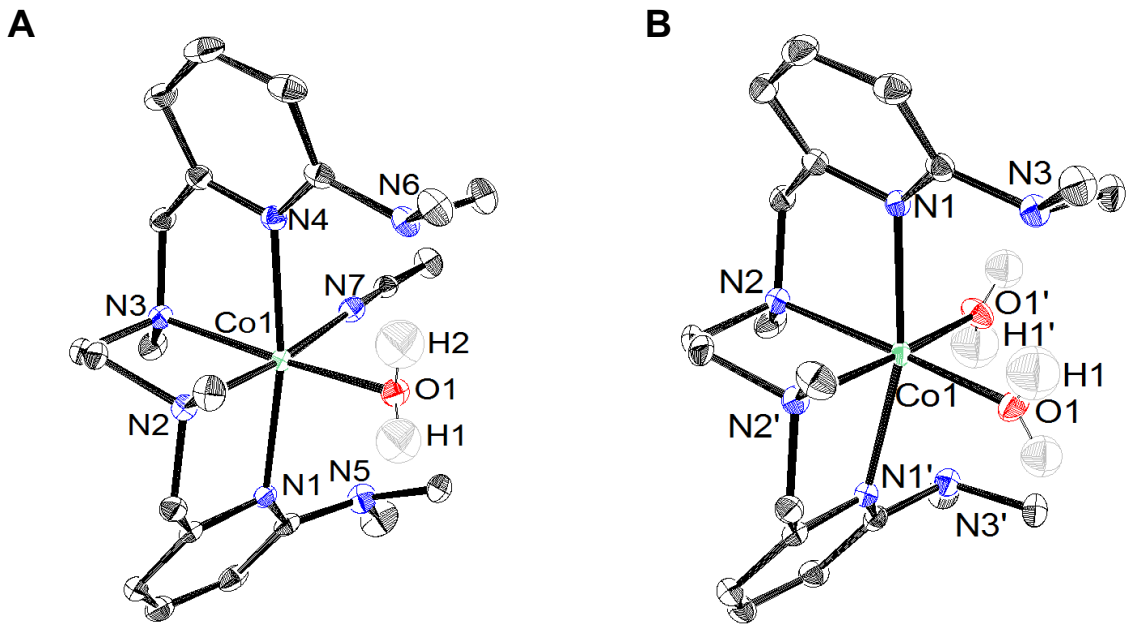

Figure 3.14. ORTEP of the aquo complexes A) $[CoL^{DMA}(CH_3CN)(H_2O)][BF_4]_2$ and B) $[CoL^{DMA}(H_2O)_2][BF_4]_2$. Thermal ellipsoids are drawn at the 50% probability level. The BF_4^- counter anions, solvent molecules and hydrogen atoms other than those on the aquo ligands have been removed for clarity.

The solid state structures of both $[CoL^{DMA}(CH_3CN)(H_2O)][BF_4]_2$ and $[CoL^{DMA}(H_2O)_2][BF_4]_2$ exhibit octahedral coordination geometries and are shown in Figure 3.14. Hydrogen atoms shown in $[CoL^{DMA}(CH_3CN)(H_2O)][BF_4]_2$ and $[CoL^{DMA}(H_2O)_2][BF_4]_2$ structures were found in the difference map. The dimethylamine moiety behaves as designed with hydrogen bonds to the aquo ligands. The $[CoL^{DMA}(CH_3CN)(H_2O)][BF_4]_2$ complex has a hydrogen-bonding interaction between the dimethylamine nitrogen, N6, and H2 of the water ligand with a distance of 1.798 Å (N6•••O1 = 2.653 Å). The $[CoL^{DMA}(H_2O)_2][BF_4]_2$ solid state structure exhibits two bound water molecules and two hydrogen-bonding interactions although only one is unique because the structure was generated from a two-fold C_2 axis. The dimethylamine nitrogen, N3,

acts as a hydrogen bond acceptor for H1 on water with a distance of 2.225 Å (N3•••O1 = 2.869 Å).

Table 3.8. Selected bond angles (°) for the $[CoL^{DMA}(CH_3CN)_2][BF_4]_2$, $[CoL^{DMA}(CH_3CN)(H_2O)][BF_4]_2$, and $[CoL^{DMA}(H_2O)_2][BF_4]_2$ complexes.

$[CoL^{DMA}(CH_3CN)_2][BF_4]_2$		$[CoL^{DMA}(CH_3CN)(H_2O)][BF_4]_2$		$[CoL^{DMA}(H_2O)_2][BF_4]_2$	
C1-N5-C17	118.03°	C1-N5-C17	119.67	C1-N3-C9	113.56
C1-N5-C18	118.37	C1-N5-C18	120.65	C1-N3-C10	115.43
C14-N6-C19	119.56	C14-N6-C19	114.75		
C14-N6-C20	119.17	C14-N6-C20	110.71		

The aquo bound complexes exhibit an interesting distortion in the dimethylamine angles compared to one that has no exogenous interactions (Table 3.8). The angles for the C(pyridine)-N(dimethylamine)-CH_3 in $[CoL^{DMA}(CH_3CN)_2][BF_4]_2$ are 118.03° and 118.37° for N5 and 119.56° and 119.17° for N6. The dimethylamine arm, N5, that does not participate in hydrogen-bonding in the $[CoL^{DMA}(CH_3CN)(H_2O)][BF_4]_2$ complex, has similar angles at 119.67° and 120.65°. However, N6 has more acute angles, 114.75° and 110.70°, indicating a contraction to accommodate the hydrogen-bonding interaction with a proton from water. The bisaquo bound structure $[CoL^{DMA}(H_2O)_2][BF_4]_2$ also demonstrates angular distortion with the acute N3 angles of 113.56° and 115.43°.

Controlled Potential Electrolysis

To measure the catalytic oxygen reduction activity of $[CoL^{DMA}(CH_3CN)_2][BF_4]_2$, controlled potential electrolysis (CPE) was performed. The electrolyses were performed in a sealed glass reaction vessel containing 1 mM compound in a 5% v/v solution of H_2O in CH_3CN. Carbon foam cylinders were used for the working and counter electrodes and a non-aqueous Ag/Ag^+ electrode was used as the reference. The counter electrode was separated from the bulk solution

by a fine fritted glass disc.[84] The potential values in the CPE were adjusted to be referenced to ferrocene by using E_{pa2} for a 1.0 mM solution $[CoL^{DMA}(CH_3CN)_2][BF_4]_2$ in 0.10 M Bu_4NBF_4 CH_3CN at 100 mV/s.

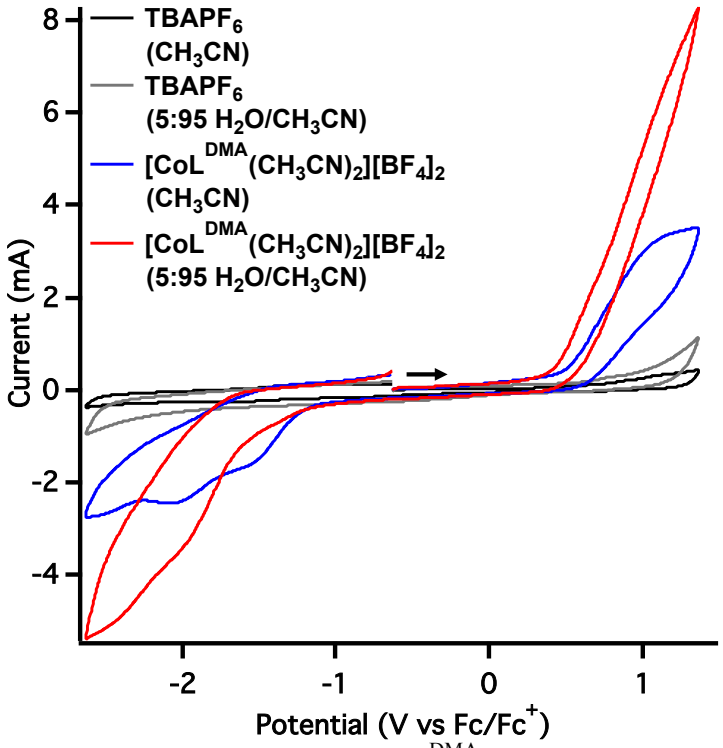

Figure 3.15. Cyclic voltammograms in CPE cell. $[CoL^{DMA}(CH_3CN)_2][BF_4]_2$ in 5:95 H_2O/CH_3CN (red), $[CoL^{DMA}(CH_3CN)_2][BF_4]_2$ in 0:100 H_2O/CH_3CN (blue), and no catalyst present under the same conditions (gray and black).

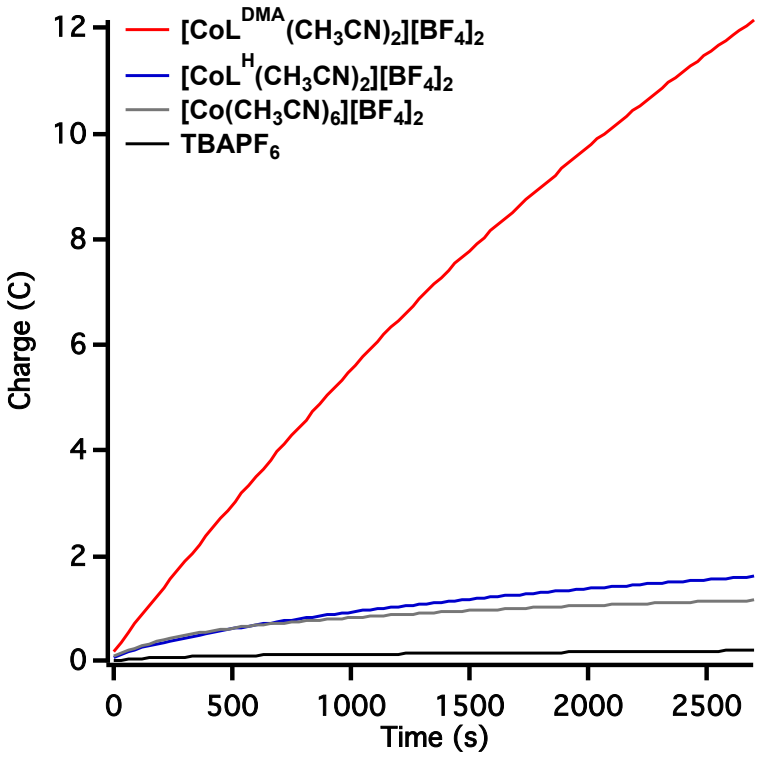

Figure 3.16. Charge passed vs time in the controlled potential electrolysis of a 1 mM solution of $[CoL^{DMA}(CH_3CN)_2][BF_4]_2$ in 5:95 H_2O/CH_3CN at 1.07 V vs Fc/Fc^+ (red trace). Equivalent electrolyses under the same conditions; $[CoL^{H}(CH_3CN)_2][BF_4]_2$ (blue trace), $[Co(CH_3CN)_6][BF_4]_2$ (gray trace), and $TBAPF_6$ (black trace).

The total charge passed over a 45 minute electrolysis at 1.07 V vs Fc/Fc^+ is shown in Figure 3.16. Evidence of OER was obtained from detection of O_2 using gas chromatography (calibration curve shown in Figure 3.17). The Faradaic yield is 98.6% indicating the catalysis is selective for the four electron process towards dioxygen. It should be noted that the minimal oxygen generation at the working electrode with no complex present is below detectable limit with the calibration curve used to calculate the percent oxygen (Figure 3.15, gray trace and Figure 3.16, black trace).

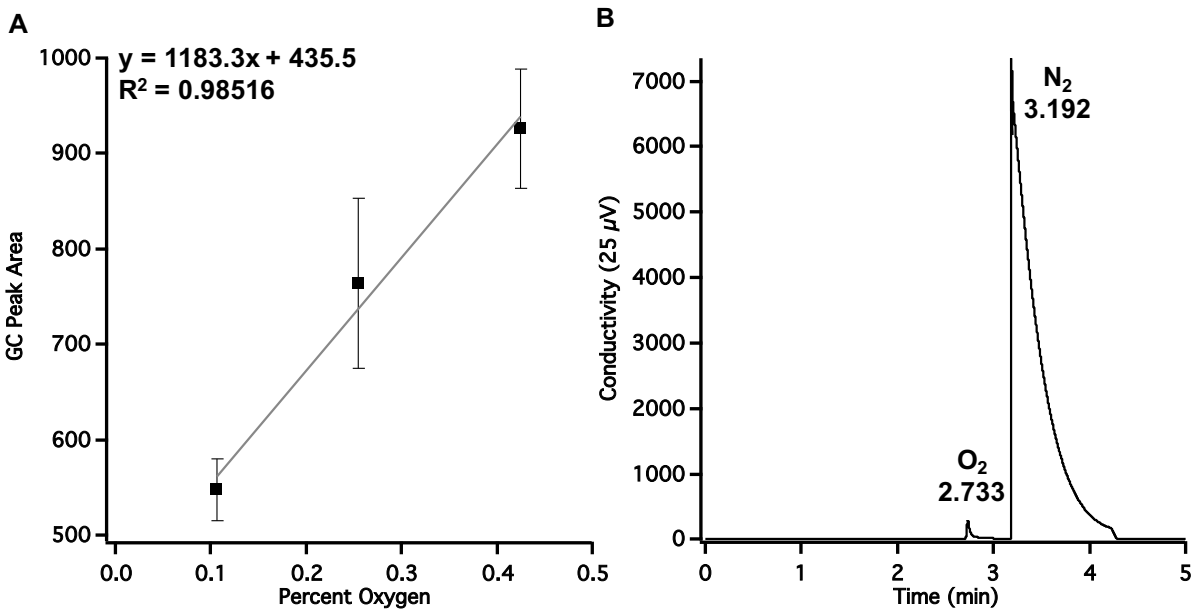

Figure 3.17. A) GC calibration curve for O_2. Points show the average peak area and error bars show the standard deviation across five measurements. Linear fit equation is shown on graph. B) Representative GC trace for headspace of $[CoL^{DMA}(CH_3CN)_2][BF_4]_2$ electrolysis.

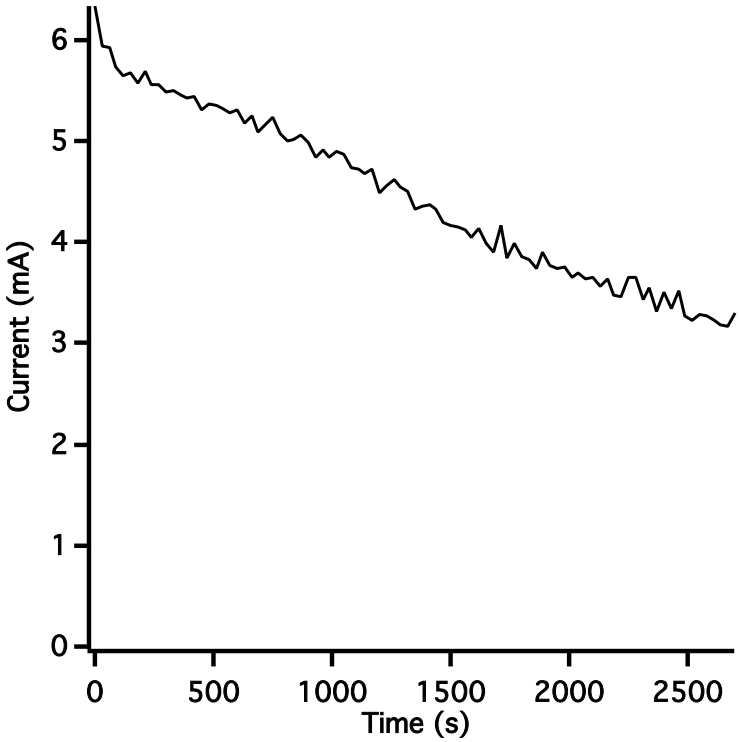

Figure 3.18. Current vs time plot of 45 minutes electrolysis of 1 mM solution of $[CoL^{DMA}(CH_3CN)_2][BF_4]_2$ in 5:95 H_2O/CH_3CN at 1.07 V vs Fc/Fc^+.

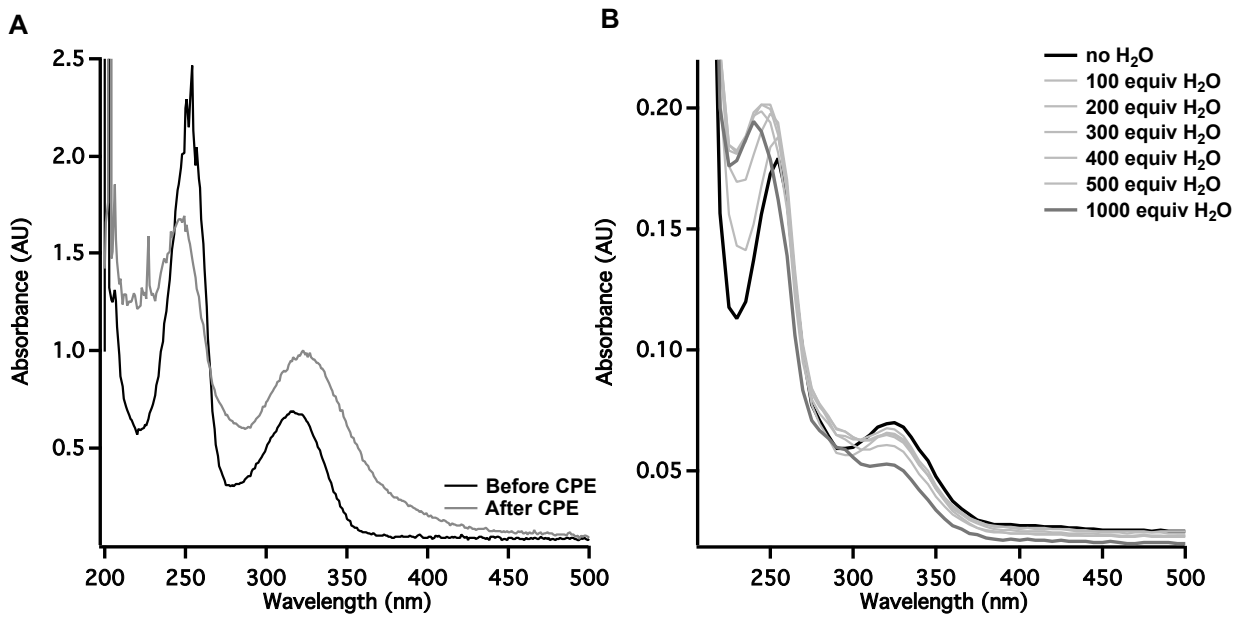

Figure 3.19. UV-Vis spectra A) before (black trace) and after (dark gray trace) CPE. B) Titration of water into a 10 μM CH_3CN solution of $[CoL^{DMA}(CH_3CN)_2][BF_4]_2$.

The total amount of dioxygen generated is just under one equivalent with respect to $[CoL^{DMA}(CH_3CN)_2][BF_4]_2$. The lack of turnover might be as a result of the short electrolysis time. Additionally, it is unclear if the bisacetonitrile bound complex, $[CoL^{DMA}(CH_3CN)_2][BF_4]_2$, is the active species due to a decrease in current over time, Figure 3.18, and the post CPE analysis, Figure 3.19.

During the electrolysis the charge decreased over the 45 minute time period, Figure 3.18. More than one equivalent of dioxygen could have been generated with a longer electrolysis time as significant current was still being passed when the experiment was ended. The decrease in current may also be an indication of instability of the $[CoL^{DMA}(CH_3CN)_2][BF_4]_2$ complex.

To determine the stability of $[CoL^{DMA}(CH_3CN)_2][BF_4]_2$, a post electrolysis analysis using UV-Vis was performed. The post electrolysis analysis shows a change in the UV-Vis profile before and after electrolysis with a shift in the absorption bands from 254 to 247 nm and 317 to 322 nm (Figure 3.19A). A similar hypsochromic shift occurs when water is titrated into a CH_3CN solution

of $[CoL^{DMA}(CH_3CN)_2][BF_4]_2$ which may suggest the active WOC species is an aquo adduct (Figure 3.19B).

Control experiments were performed to confirm water oxidation activity is from the homogenous $[CoL^{DMA}(CH_3CN)_2][BF_4]_2$ species. Identical electrolyses were performed with a 1 mM solution of $[Co(CH_3CN)_6][BF_4]_2$ which passed minimal current, demonstrating that oxidation of Co^{2+} salt species are not generating significant amounts of oxygen (Figure 3.16, gray trace). Secondly, the working electrode was rinsed with water and acetonitrile and reused in a fresh solution of 5% v/v solution of H_2O in CH_3CN to confirm no heterogeneous cobalt had deposited onto the electrode surface (Figure 3.16, black trace). Lastly, a mercury pool was included at the bottom of the electrolysis cell during the electrolysis of $[CoL^{DMA}(CH_3CN)_2][BF_4]_2$ to form an amalgam with possible cobalt oxide heterogeneous particles.[85,86]

The role of the dimethylamine functionalities of L^{DMA} in the oxidation of water to dioxygen can be shown by the identical electrolysis performed with 1 mM $[CoL^{H}(CH_3CN)_2][BF_4]_2$ in a 5% v/v solution of H_2O in CH_3CN that passes minimal charge and generates trivial amounts of dioxygen (Figure 3.16, blue trace). This data suggests the efficiency of oxygen generation is aided by the presence of pendant bases in the secondary sphere of the cobalt metal center.

Secondary interactions have been previously shown to stabilize aquo, hydroxide or hydroperoxo bound intermediates in the OER.[87,88] The solid state structures of the metal bound aquo ligands for $[CoL^{DMA}]^{2+}$ indicate that the dimethylamine unit likely behaves as a pendant base to accept a proton upon oxidation of the aquo species. The pK_a values for the bound aquo ligands, Co(II)-OH_2, are likely between 6-8 based on other amine-based Co(II) aquo complexes.[89] The pK_a value is expected to greatly decrease upon metal oxidation to Co(III), therefore increasing the acidity of the bound water ligand.[90,91]

The presence of a pendant base may invoke a PCET mechanistic pathway to synchronize proton and electron transfer steps that otherwise would be stepwise. The total charge buildup of the species due to multiple oxidations would be compensated by proton removal to lower the oxidation potential.[92-96] This redox-leveling process significantly affects the stability of highly energetic intermediates.

Although further studies are necessary to determine the exact PCET mechanism, the pendant base may avoid the acidic Co(III)-OH_2, a high energy intermediate. The coupling of a proton transfer step to the oxidation of the cobalt center would result in an Co(III)-OH intermediate to lower the energetic barrier to other reactive intermediates for O-O bond formation.[11,82,97,98]

3.4. Conclusion

A series of cobalt compounds have been synthesized with ligands capable of hydrogen-bonding. The L^{MMA} ligand resulted in a cobalt dimer from fluoride abstraction from the BF_4^- counter anion. The ligand exhibited the design properties of a hydrogen bond donor to the bridged fluoride unit. The hydrogen bond acceptor ligand L^{DMA} promoted the isolation of stable cobalt aquo species which form hydrogen bond(s) with aquo ligand(s) in the solid state.

Cyclic voltammetry reactivity studies of the cobalt complexes with CO_2 showed minor current enhancement with all three complexes. The most promising complex for CO_2 reduction was $[CoL^{H}(CH_3CN)_2][BF_4]_2$ with the addition of water as a proton source. Reactivity of the cobalt complexes toward proton reduction with water as an added proton source indicate $[CoL^{DMA}(CH_3CN)_2][BF_4]_2$ had the largest current enhancement and is a potential proton reduction catalyst.

The water oxidation activity of $[CoL^{DMA}(CH_3CN)_2][BF_4]_2$ reveals it is a single site first row transition metal homogenous catalyst toward the OER. Controlled potential electrolysis data indicate that oxygen gas, detected by gas chromatography, is being formed at moderate potentials with high faradaic yield. The presence of a pendant base greatly increases the water oxidation activity compared to the non-functionalized L^H ligand containing cobalt complex, suggesting PCET plays a role in facilitating catalysis.

3.5. Experimental Details

General Experiment Considerations

All reagents were purchased from commercial suppliers and used without purification. Unless otherwise noted, all organic chemical manipulations were performed in air. Compounds were purified via flash column chromatography using Sorbent Technologies 60 Å, 230–400 mesh silica gel, unless otherwise stated. Unless otherwise noted, inorganic metal syntheses were performed in a Vacuum Atmospheres Co. drybox under a nitrogen atmosphere. $[Co(CH_3CN)_6][BF_4]_2$ was prepared using literature methods.[13] Anhydrous solvents were sparged with UHP argon (Praxair) and passed through columns containing Q-5 and molecular sieves before use.

Physical Methods

Nuclear Magnetic Resonance (NMR) Spectroscopy: ^{1}H NMR spectra were recorded on 500 MHz on Bruker instruments. ^{1}H NMR spectra chemical shifts are reported as δ values in ppm relative to residual protio solvent: $CDCl_3$ (7.26 ppm), CD_3CN (1.94 ppm). Proton NMR data are reported as follows: chemical shift (δ ppm), multiplicity (s = singlet, d = doublet, t = triplet, q = quartet), coupling constants (J) in Hertz (Hz), and integration. Multiplets (m) are reported over

the range (ppm). Data for ^{13}C NMR spectra are decoupled proton spectra and are reported in terms of chemical shift (δ ppm).

Mass Spectrometry (MS): High resolution mass spectra (HR-MS) and electrospray ionization mass spectra (ESI-MS) were obtained on a Micromass LCT and collected at the University of California-Irvine Mass Spectrometry Facility.

Ultraviolet-Visible (UV-Vis) Spectroscopy: Ultraviolet-Visible spectra were collected as 10 μM solutions in 3 mL CH_3CN in a 1 cm quartz cuvette or as 1mM solutions in 0.3 mL CH_3CN in a 1 mm quartz cuvette using an Agilent Technologies Cary 60 UV–vis spectrometer. A Bruker SMART APEX II diffractometer was used to collect all the data.

Infrared (IR) Spectroscopy: Infrared spectra were collected using a Thermo Scientific Nicolet iS5 spectrometer with an iD5 ATR attachment in a nitrogen filled glovebox. The sample was prepared by evaporating an acetonitrile solution of the compound onto an ATR crystal.

Electron Paramagnetic Resonance (EPR) Spectroscopy: X-band (9.28 GHz) EPR spectra were collected as 10 mM frozen solutions using a Bruker EMX spectrometer equipped with an ER041XG microwave bridge at 77 K or 10 K.

Elemental Analysis (EA): Elemental analyses were performed on a Perkin Elmer 2400 Series II CHNS elemental analyzer.

Cyclic Voltammetry (CV): Electrochemical experiments were performed under an atmosphere of nitrogen in a solution containing 0.1 M Bu_4NBF_4 or Bu_4NPF_6 in acetonitrile. Glassy carbon was used as the working and auxiliary electrode and a silver wire was used as a pseudoreference electrode. Ferrocene was used as an internal standard, and all potentials are referenced to the ferrocenium/ferrocene couple. Cyclic voltammetry experiments were performed with a Pine Wavedriver 10 or 20 potentiostat and Pine Aftermath software version 1.4.7881.

Controlled Potential Electrolysis[84]: Controlled potential electrolyses were performed in a Pine 150 mL cell for rotating electrodes with water jacket and five ground-glass ports (one 24/40, four 14/20). All cell ports were sealed with greased ground-glass joints with the exception of one 14/20 port, which was sealed with a SubaSeal rubber septum used for headspace sampling. Vitreous carbon foam rods were used for the working and counter electrodes, while an acetonitrile Ag/Ag^+ wire electrode was used as the reference. The carbon foam rods were attached to copper wire leads using conductive silver epoxy (AI Technology Prima-Solder EG8050) under Loctite epoxy. The counter electrode was separated from the bulk solution by a 10 mm glass tube with an extra-fine (Ace glass porosity E) fritted glass bottom; the tube was inserted through the 24/40 cell port and sealed with a ground-glass joint. The working and reference electrodes were connected to the exterior of the cell via nickel sleeves joining the electrode leads to a tungsten wire that was sealed through a 14/20 ground-glass stopper. A mercury pool, contained in a shallow glass cup, was placed at the S3 bottom of each electrolysis sample. Cell headspace was sampled with a Restek A-2 Luer lock gas-tight syringe.

Gas Chromatography (GC): Headspace oxygen was quantified by gas chromatography on an Agilent 7890B instrument with a Molsieve column. GC method details are as follows: helium carrier gas, 40 °C column temperature, TCD detector at 200 °C. Calibration curves were generated by injecting known percentages of O_2 into a nitrogen filled roundbottom flask (235.4 mL) and stirring for 10 mins. Background oxygen formation by the carbon foam electrode was estimated by running a controlled potential electrolysis of equal duration (45 min) on a blank electrolyte solution with no catalyst.

X-Ray Crystallography: A Bruker SMART APEX II diffractometer was used to collect all data. The APEX2 (APEX2 Version 2014.11-0, Bruker AXS, Inc.; Madison, WI 2014) program package

was used to determine the unit-cell parameters and for data collection (20 sec/frame scan time for a sphere of diffraction data). The raw frame data was processed using SAINT (SAINT Version 8.34a, Bruker AXS, Inc.; Madison, WI 2013) and SADABS (Sheldrick, G. M. SADABS, Version 2014/5, Bruker AXS, Inc.; Madison, WI 2014) to yield the reflection data file. Subsequent calculations were carried out using the SHELXTL (Sheldrick, G. M. SHELXTL, Version 2014/7, Bruker AXS, Inc.; Madison, WI 2014) program. The structures were solved by direct methods and refined on F^2 by full-matrix least-squares techniques. The analytical scattering factors for neutral atoms were used throughout the analysis (International Tables for Crystallography 1992, Vol. C., Dordrecht: Kluwer Academic Publishers). The N-H hydrogen atoms of $[Co_2(\mu\text{-}F)_2(L^{MMA})_2][BF_4]_2$ were located from a difference-Fourier map and refined (x,y,z, fixed U_{iso}) with d(N-H) = 0.90Å. The O-H hydrogen atoms on water of $[CoL^{DMA}(CH_3CN)(H_2O)][BF_4]_2$ and $[CoL^{DMA}(H_2O)_2][BF_4]_2$ were located from a difference-Fourier map and refined. The molecule $[CoL^{DMA}(H_2O)_2][BF_4]_2$ was located on a two-fold rotation axis. The remaining hydrogen atoms were included using a riding model.

Synthesis of Complexes

$[CoL^{H}(CH_3CN)_2][BF_4]_2$. $[Co(CH_3CN)_6][BF_4]_2$ (180 mg, 0.40 mmol) was added to a solution of $\mathbf{L^H}$ (109 mg, 0.40 mmol) in 5 mL of CH_3CN. The dark orange solution was stirred at 25 °C for 0.5 h upon which 5 mL of Et_2O was added and the precipitate isolated by filtration. The crude product, isolated as a brown precipitate, was redissolved in *ca.* 1 mL of CH_3CN and layered with 4 mL of Et_2O. After 1 day at −40 °C, the pure orange product was isolated by filtration and washed with 2 × 4 mL Et_2O. (170 mg, 78% yield). Single dark orange crystals suitable for X-ray crystallographic analysis were obtained by diffusion of Et_2O in a CH_3CN solution. ESI-MS

(CH_3CN) *m*/*z*: 164.4 ($[CoL^H]^{2+}$). $\lambda_{max,}$ nm (CH_3CN, ε ($M^{-1} \times cm^{-1}$)) = 257 (4,000) and 465 (80). Anal. Calcd (Found) for $C_{16}H_{22}B_2CoF_8N_4$ (%): C, 38.21 (38.25); H, 4.41 (4.79); N, 11.14 (11.30).

$[Co_2(\mu\text{-}F)_2(L^{MMA})_2][BF_4]_2$. $[Co(CH_3CN)_6][BF_4]_2$ (140 mg, 0.29 mmol) was added to a solution of $\mathbf{L^{MMA}}$ (97 mg, 0.29 mmol) in 5 mL of CH_3CN. The dark orange solution was stirred at 25 °C for 0.5 h then 5 mL of Et_2O was added to precipitate the complex. The supernatant was decanted and resulting orange powder redissolved in *ca.* 1 mL of CH_3CN and layered with 4 mL of Et_2O. After 1 d at −40 °C, an orange microcrystalline solid was isolated by filtration and washed with 2 × 4 mL Et_2O (120 mg, 87% yield). Single light pink crystals suitable for X-ray crystallographic analysis were obtained by diffusion of Et_2O in a CH_3CN solution. ESI-MS (CH_3CN) *m*/*z*: 406.1 ($[Co_2(L^{MMA})_2F_2]^{2+}$). $\lambda_{max,}$ nm (CH_3CN, ε ($M^{-1} \times cm^{-1}$)) = 243 (104,000), 317 (58,000) and 491 (55). Anal. Calcd (Found) for $C_{18}H_{28}B_2CoF_8N_6$ (%): C, 38.54 (38.48); H, 5.03 (5.04); N, 14.38 (14.53).

$[CoL^{DMA}(CH_3CN)_2][BF_4]_2$. $[Co(CH_3CN)_6][BF_4]_2$ (134 mg, 0.28 mmol) was added to a solution of $\mathbf{L^{DMA}}$ (103 mg, 0.128 mmol) in 5 mL of CH_3CN. The dark orange solution was stirred at 25 °C for 0.5 h and then 5 mL of Et_2O was added to precipitate the complex. The supernatant was decanted and resulting tan powder redissolved in *ca.* 1 mL of CH_3CN and layered with 4 mL of Et_2O. After 1 d at −40 °C, the dark orange product was isolated by filtration and washed with 2 × 4 mL Et_2O (170 mg, 89% yield). Single light orange crystals suitable for X-ray crystallographic analysis were obtained by diffusion of Et_2O in a CH_3CN solution. ESI-MS (CH_3CN) *m*/*z*: 207.7 ($[CoL^{DMA}]^{2+}$). $\lambda_{max,}$ nm (CH_3CN, ε ($M^{-1} \times cm^{-1}$)) = 256 (27,000), 324 (17,000) and 411 (130). Anal. Calcd (Found) for $C_{20}H_{32}B_2CoF_8N_6$ (%): C, 40.78 (40.40); H, 5.48 (5.43); N, 14.27 (14.39).

$[CoL^{DMA}(CH_3CN)(H_2O)][BF_4]_2$. H_2O (1.1 μL, 2.0 equiv) was added to a solution of $[CoL^{DMA}(CH_3CN)_2][BF_4]_2$ (20.0 mg, 0.03 mmol) in 5 mL of CH_3CN. The orange solution was stirred at 25 °C for 0.5 h and then 5 mL of Et_2O was added to precipitate the complex and was left

overnight at −40 °C. The supernatant was decanted and resulting orange powder was isolated (8 mg, 40% yield). Removal of solvent resulted in an insoluble blue solid attributed to the loss of the aquo ligand. Single orange crystals suitable for X-ray crystallographic analysis were obtained by diffusion of Et_2O in a CH_3CN solution. APCI-MS (CH_3CN) *m*/*z*: 433.3 ($[CoL^{DMA} + H_2O]^+$).

$[CoL^{DMA}(H_2O)_2][BF_4]_2$. H_2O (1.1 μL, 2.0 equiv) was added to a solution of $[CoL^{DMA}(CH_3CN)_2][BF_4]_2$ (20.0 mg, 0.03 mmol) in 5 mL of DCM. The peach solution was stirred at 25 °C for 0.5 h. Removal of solvent resulted in an insoluble pink solid. Single dark pink crystals were obtained by diffusion of Et_2O in a DCM solution.

3.6. References

(1) Hoffert, W. A.; Mock, M. T.; Appel, A. M.; Yang, J. Y. *Eur. J. Inorg. Chem.* **2013**, *2013*, 3846-3857.

(2) Khosrowabadi Kotyk, J. F.; Ziller, J. W.; Yang, J. Y. *J. Coord. Chem.* **2016**, *69*, 1990-2002.

(3) Fisher, B. J.; Eisenberg, R. *J. Am. Chem. Soc.* **1980**, *102*, 7361-7363.

(4) Lehn, J.-M.; Ziessel, R. *Proc. Natl. Acad. Sci.* **1982**, *79*, 701-704.

(5) Artero, V.; Chavarot-Kerlidou, M.; Fontecave, M. *Angew. Chem. Int. Ed.* **2011**, *50*, 7238-7266.

(6) Du, P.; Eisenberg, R. *Energy Environ. Sci.* **2012**, *5*, 6012-6021.

(7) Eckenhoff, W. T.; McNamara, W. R.; Du, P.; Eisenberg, R. *Biochim. Biophys. Acta, Bioenerg.* **2013**, *1827*, 958-973.

(8) Kellett, R. M.; Spiro, T. G. *Inorg. Chem.* **1985**, *24*, 2373-2377.

(9) Sun, Y.; Bigi, J. P.; Piro, N. A.; Tang, M. L.; Long, J. R.; Chang, C. J. *J. Am. Chem. Soc.* **2011**, *133*, 9212-9215.

(10) Hu, X.; Brunschwig, B. S.; Peters, J. C. *J. Am. Chem. Soc.* **2007**, *129*, 8988-8998.

(11) Dogutan, D. K.; McGuire, R.; Nocera, D. G. *J. Am. Chem. Soc.* **2011**, *133*, 9178-9180.

(12) Wasylenko, D. J.; Ganesamoorthy, C.; Borau-Garcia, J.; Berlinguette, C. P. *Chem. Comm.* **2011**, *47*, 4249-4251.

(13) Coucouvanis, D. In *Inorganic Syntheses*; John Wiley & Sons, Inc.: 2002, p 75-121.

(14) Rietmeijer, F. J.; Van Albada, G. A.; De Graaff, R. A. G.; Haasnoot, J. G.; Reedijk, J. *Inorg. Chem.* **1985**, *24*, 3597-3601.

(15) Rietmeijer, F. J.; Haasnoot, J. G.; Den Hartog, A. J.; Reedijk, J. *Inorg. Chim. Acta* **1986**, *113*, 147-155.

(16) Reger, D. L.; Pascui, A. E.; Smith, M. D.; Jezierska, J.; Ozarowski, A. *Inorg. Chem.* **2012**, *51*, 11820-11836.

(17) Meyer, F.; Heinze, K.; Nuber, B.; Zsolnai, L. *J. Chem. Soc., Dalton Trans.* **1998**, 207-214.

(18) Reedijk, J.; Jansen, J. C.; Van Koningsveld, H.; Van Kralingen, C. G. *Inorg. Chem.* **1978**, *17*, 1990-1994.

(19) Gobeze, W. A.; Milway, V. A.; Chilton, N. F.; Moubaraki, B.; Murray, K. S.; Brooker, S. *Eur. J. Inorg. Chem.* **2013**, *2013*, 4485-4498.

(20) Gobeze, W. A.; Milway, V. A.; Moubaraki, B.; Murray, K. S.; Brooker, S. *Dalton Trans.* **2012**, *41*, 9708-9721.

(21) Cho, Y. I.; Ward, M. L.; Rose, M. J. *Dalton Trans.* **2016**.

(22) Lever, A. B. P. *Inorganic Electronic Spectroscopy*; Elsevier, 1984.

(23) Anderson, L. C.; Seeger, N. V. *J. Am. Chem. Soc.* **1949**, *71*, 340-342.

(24) Que Jr, L. *Physical Methods in Bioinorganic Chemistry*; University Science Books, 2000.

(25) Hori, Y. In *Modern Aspects of Electrochemistry*; Springer New York: 2008; Vol. 42, p 89-189.

(26) Fuchs, G. *Annu. Rev. Microbio.* **2011**, *65*, 631-658.

(27) Jeoung, J.-H.; Dobbek, H. *Science* **2007**, *318*, 1461-1464.

(28) Appel, A. M.; Bercaw, J. E.; Bocarsly, A. B.; Dobbek, H.; DuBois, D. L.; Dupuis, M.; Ferry, J. G.; Fujita, E.; Hille, R.; Kenis, P. J. A.; Kerfeld, C. A.; Morris, R. H.; Peden, C. H. F.; Portis, A. R.; Ragsdale, S. W.; Rauchfuss, T. B.; Reek, J. N. H.; Seefeldt, L. C.; Thauer, R. K.; Waldrop, G. L. *Chem. Rev.* **2013**, *113*, 6621-6658.

(29) Dobbek, H.; Gremer, L.; Kiefersauer, R.; Huber, R.; Meyer, O. *Proc. Natl. Acad. Sci.* **2002**, *99*, 15971-15976.

(30) Dobbek, H. *Coord. Chem. Rev.* **2011**, *255*, 1104-1116.

(31) Finn, C.; Schnittger, S.; Yellowlees, L. J.; Love, J. B. *Chem. Comm.* **2012**, *48*, 1392-1399.

(32) Benson, E. E.; Kubiak, C. P.; Sathrum, A. J.; Smieja, J. M. *Chem. Soc. Rev.* **2009**, *38*, 89-99.

(33) Steffey, B. D.; Curtis, C. J.; DuBois, D. L. *Organometallics* **1995**, *14*, 4937-4943.

(34) Fachinetti, G.; Floriani, C.; Zanazzi, P. F. *J. Am. Chem. Soc.* **1978**, *100*, 7405-7407.

(35) Gambarotta, S.; Arena, F.; Floriani, C.; Zanazzi, P. F. *J. Am. Chem. Soc.* **1982**, *104*, 5082-5092.

(36) Hull, J. F.; Himeda, Y.; Wang, W.-H.; Hashiguchi, B.; Periana, R.; Szalda, D. J.; Muckerman, J. T.; Fujita, E. *Nat Chem* **2012**, *4*, 383-388.

(37) Wang, W.-H.; Hull, J. F.; Muckerman, J. T.; Fujita, E.; Himeda, Y. *Energy Environ. Sci.* **2012**, *5*, 7923-7926.

(38) Schmeier, T. J.; Dobereiner, G. E.; Crabtree, R. H.; Hazari, N. *J. Am. Chem. Soc.* **2011**, *133*, 9274-9277.

(39) Costentin, C.; Drouet, S.; Robert, M.; Savéant, J.-M. *Science* **2012**, *338*, 90-94.

(40) Galan, B. R.; Schöffel, J.; Linehan, J. C.; Seu, C.; Appel, A. M.; Roberts, J. A. S.; Helm, M. L.; Kilgore, U. J.; Yang, J. Y.; DuBois, D. L.; Kubiak, C. P. *J. Am. Chem. Soc.* **2011**, *133*, 12767-12779.

(41) Seu, C. S.; Appel, A. M.; Doud, M. D.; DuBois, D. L.; Kubiak, C. P. *Energy Eviron. Sci.* **2012**, *5*, 6480-6490.

(42) Lubitz, W.; Reijerse, E. J.; Messinger, J. *Energy Environ. Sci.* **2008**, *1*, 15-31.

(43) Fontecilla-Camps, J. C.; Volbeda, A.; Cavazza, C.; Nicolet, Y. *Chem. Rev.* **2007**, *107*, 4273-4303.

(44) Lubitz, W.; Ogata, H.; Rüdiger, O.; Reijerse, E. *Chem. Rev.* **2014**, *114*, 4081-4148.

(45) DuBois, D. L.; Bullock, R. M. *Eur. J. Inorg. Chem.* **2011**, *2011*, 1017-1027.

(46) Vincent, K. A.; Parkin, A.; Armstrong, F. A. *Chem. Rev.* **2007**, *107*, 4366-4413.

(47) Rakowski DuBois, M.; DuBois, D. L. *Chem. Soc. Rev.* **2009**, *38*, 62-72.

(48) Tard, C.; Pickett, C. J. *Chem. Rev.* **2009**, *109*, 2245-2274.

(49) Gloaguen, F.; Rauchfuss, T. B. *Chem. Soc. Rev.* **2009**, *38*, 100-108.

(50) Rakowski Dubois, M.; Dubois, D. L. *Acc. Chem. Res.* **2009**, *42*, 1974-1982.

(51) O'Hagan, M.; Shaw, W. J.; Raugei, S.; Chen, S.; Yang, J. Y.; Kilgore, U. J.; DuBois, D. L.; Bullock, R. M. *J. Am. Chem. Soc.* **2011**, *133*, 14301-14312.

(52) Helm, M. L.; Stewart, M. P.; Bullock, R. M.; DuBois, M. R.; DuBois, D. L. *Science* **2011**, *333*, 863-866.

(53) Yang, J. Y.; Smith, S. E.; Liu, T.; Dougherty, W. G.; Hoffert, W. A.; Kassel, W. S.; DuBois, M. R.; DuBois, D. L.; Bullock, R. M. *J. Am. Chem. Soc.* **2013**, *135*, 9700-9712.

(54) Graham, D. J.; Nocera, D. G. *Organometallics* **2014**, *33*, 4994-5001.

(55) Lee, C. H.; Dogutan, D. K.; Nocera, D. G. *J. Am. Chem. Soc.* **2011**, *133*, 8775-8777.

(56) Boyer, J. L.; Polyansky, D. E.; Szalda, D. J.; Zong, R.; Thummel, R. P.; Fujita, E. *Angew. Chem. Int. Ed.* **2011**, *50*, 12600-12604.

(57) Kaljurand, I.; Kütt, A.; Sooväli, L.; Rodima, T.; Mäemets, V.; Leito, I.; Koppel, I. A. *J. Org. Chem.* **2005**, *70*, 1019-1028.

(58) Izutsu, K. *Acid-Base Dissociation Constants in Dipolar Aprotic Solvents*; Blackwell Scientific: Oxford, U.K., 1990.

(59) Yano, J.; Kern, J.; Sauer, K.; Latimer, M. J.; Pushkar, Y.; Biesiadka, J.; Loll, B.; Saenger, W.; Messinger, J.; Zouni, A.; Yachandra, V. K. *Science* **2006**, *314*, 821.

(60) Ago, H.; Adachi, H.; Umena, Y.; Tashiro, T.; Kawakami, K.; Kamiya, N.; Tian, L.; Han, G.; Kuang, T.; Liu, Z.; Wang, F.; Zou, H.; Enami, I.; Miyano, M.; Shen, J.-R. *J. Biol. Chem.* **2016**, *291*, 5676-5687.

(61) Umena, Y.; Kawakami, K.; Shen, J.-R.; Kamiya, N. *Nature* **2011**, *473*, 55-60.

(62) Loll, B.; Kern, J.; Saenger, W.; Zouni, A.; Biesiadka, J. *Nature* **2005**, *438*, 1040-1044.

(63) Cady, C. W.; Crabtree, R. H.; Brudvig, G. W. *Coord. Chem. Rev.* **2008**, *252*, 444-455.

(64) Yocum, C. F. *Coord. Chem. Rev.* **2008**, *252*, 296-305.

(65) Gersten, S. W.; Samuels, G. J.; Meyer, T. J. *J. Am. Chem. Soc.* **1982**, *104*, 4029-4030.

(66) Yagi, M.; Kaneko, M. *Chem. Rev.* **2001**, *101*, 21-36.

(67) Brimblecombe, R.; Swiegers, G. F.; Dismukes, G. C.; Spiccia, L. *Angew. Chem.* **2008**, *120*, 7445-7448.

(68) Zong, R.; Thummel, R. P. *J. Am. Chem. Soc.* **2005**, *127*, 12802-12803.

(69) Blakemore, J. D.; Crabtree, R. H.; Brudvig, G. W. *Chem. Rev.* **2015**, *115*, 12974-13005.

(70) Hetterscheid, D. G. H.; Reek, J. N. H. *Angew. Chem. Int. Ed.* **2012**, *51*, 9740-9747.

(71) McDaniel, N. D.; Coughlin, F. J.; Tinker, L. L.; Bernhard, S. *J. Am. Chem. Soc.* **2008**, *130*, 210-217.

(72) Masaoka, S.; Sakai, K. *Chem. Lett.* **2009**, *38*, 182-183.

(73) Concepcion, J. J.; Tsai, M.-K.; Muckerman, J. T.; Meyer, T. J. *J. Am. Chem. Soc.* **2010**, *132*, 1545-1557.

(74) Duan, L.; Bozoglian, F.; Mandal, S.; Stewart, B.; Privalov, T.; Llobet, A.; Sun, L. *Nat Chem* **2012**, *4*, 418-423.

(75) Wasylenko, D. J.; Palmer, R. D.; Berlinguette, C. P. *Chem. Comm.* **2013**, *49*, 218-227.

(76) Savéant, J.-M. *Chem. Rev.* **2008**, *108*, 2348-2378.

(77) Appel, A. M.; Helm, M. L. *ACS Catal.* **2014**, *4*, 630-633.

(78) Zeng, Q.; Lewis, F. W.; Harwood, L. M.; Hartl, F. *Coord. Chem. Rev.* **2015**, *304–305*, 88-101.

(79) Gagliardi, C. J.; Vannucci, A. K.; Concepcion, J. J.; Chen, Z.; Meyer, T. J. *Energy Environ. Sci.* **2012**, *5*, 7704-7717.

(80) Nakazono, T.; Parent, A. R.; Sakai, K. *Chem. Comm.* **2013**, *49*, 6325-6327.

(81) Wasylenko, D. J.; Palmer, R. D.; Schott, E.; Berlinguette, C. P. *Chem. Comm.* **2012**, *48*, 2107-2109.

(82) Wasylenko, D. J.; Tatlock, H. M.; Bhandari, L. S.; Gardinier, J. R.; Berlinguette, C. P. *Chem. Sci.* **2013**, *4*, 734-738.

(83) Lacy, D. C.; Park, Y. J.; Ziller, J. W.; Yano, J.; Borovik, A. S. *J. Am. Chem. Soc.* **2012**, *134*, 17526-17535.

(84) Tsay, C.; Yang, J. Y. *J. Am. Chem. Soc.* **2016**.

(85) Artero, V.; Fontecave, M. *Chem. Soc. Rev.* **2013**, *42*, 2338-2356.

(86) Stracke, J. J.; Finke, R. G. *J. Am. Chem. Soc.* **2011**, *133*, 14872-14875.

(87) Borovik, A. S. *Acc. Chem. Res.* **2005**, *38*, 54-61.

(88) Wallen, C. M.; Palatinus, L.; Bacsa, J.; Scarborough, C. C. *Angew. Chem. Int. Ed.* **2016**, *55*, 11902-11906.

(89) Hawkins, C. J. S., A. M.; Searle, G. H. *Aust. J. Chem.* **1964**, *17*, 598-600

(90) Gilson, R.; Durrant, M. C. *Dalton Trans.* **2009**, 10223-10230.

(91) Schilling, M.; Patzke, G. R.; Hutter, J.; Luber, S. *J. Phys. Chem. C* **2016**, *120*, 7966-7975.

(92) Rüttinger, W.; Dismukes, G. C. *Chem. Rev.* **1997**, *97*, 1-24.

(93) Yachandra, V. K.; Sauer, K.; Klein, M. P. *Chem. Rev.* **1996**, *96*, 2927-2950.

(94) Berardi, S.; Drouet, S.; Francas, L.; Gimbert-Surinach, C.; Guttentag, M.; Richmond, C.; Stoll, T.; Llobet, A. *Chem. Soc. Rev.* **2014**, *43*, 7501-7519.

(95) Kärkäs, M. D.; Verho, O.; Johnston, E. V.; Åkermark, B. *Chem. Rev.* **2014**, *114*, 11863-12001.

(96) Sala, X.; Maji, S.; Bofill, R.; García-Antón, J.; Escriche, L.; Llobet, A. *Acc. Chem. Res.* **2014**, *47*, 504-516.

(97) Lai, W.; Cao, R.; Dong, G.; Shaik, S.; Yao, J.; Chen, H. *J. Phys. Chem. Lett.* **2012**, *3*, 2315-2319.

(98) Wang, D.; Groves, J. T. *Proc. Natl. Acad. Sci.* **2013**, *110*, 15579-15584.

APPENDIX A

Copper and Cobalt N_2Py_2 Complexes with Chloride Ligands

A.1. Motivation and Specific Aims

The use of chloride salts to synthesize copper and cobalt compounds of the tetradentate N_2Py_2 ligands often did not result in the desired product. In most cases, the N_2Py_2 ligands did not coordinate through all four nitrogens. Ligands containing bulky substituents had vastly different coordination modes than were intended, such as dangling units or dinuclear complexes. Additionally, the Cu(I) complexes were prone to chloride abstraction from residual dichloromethane (DCM), resulting in Cu(II) chloride complexes. This appendix is to emphasize the necessity of utilizing non-coordinating tetraflouroborate (BF_4^-) anions. As a result of these studies, the complexes presented in Chapter 2 and 3 were prepared using metal BF_4^- starting materials. The use of non-coordinating anions results in tetradentate ligand coordination and eliminates the possibility of competitive binding of chloride in place of substrates during catalysis.

A.2. Background

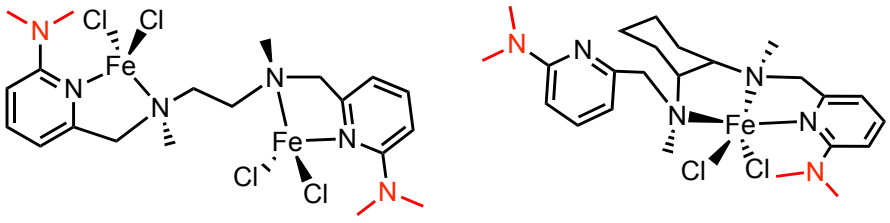

$[Fe_2L^{DMA}Cl_4]$ $[Fe(\kappa\text{-}3)L^{cyDMA}Cl_2]$

Figure A.1. Undesired coordination modes of ligands L^{DMA} and L^{cyDMA} on previously reported Fe(II) complexes.[1]

Previously published results of tetradentate N_2Py_2 ligands with bound halogens did not generally result in the desired product.[1] Iron complexes with sterically bulky groups in the 2 and 2' positions of the N_2Py_2 ligands, such as L^{DMA}, resulted in an uncoordinated pyridine arm or

dinuclear products (Figure A.1). This appendix exhibits other examples of undesired coordination modes of metal centers utilizing chloride ligands.

A.3. Results and Discussion

Copper Complexes with Chloride Ligands

Synthesis and characterization of the Cu(I) complexes $[CuL^{H}][BF_4]$ and $[CuL^{DMA}][BF_4]$ are described in Chapter 2.

Scheme A.1. Synthesis of chloride bound Cu(II) complexes $[CuL^{H}Cl][BF_4]$ and $[Cu(\kappa\text{-}3)L^{DMA}Cl][BF_4]$ from chloride abstraction from dichloromethane.

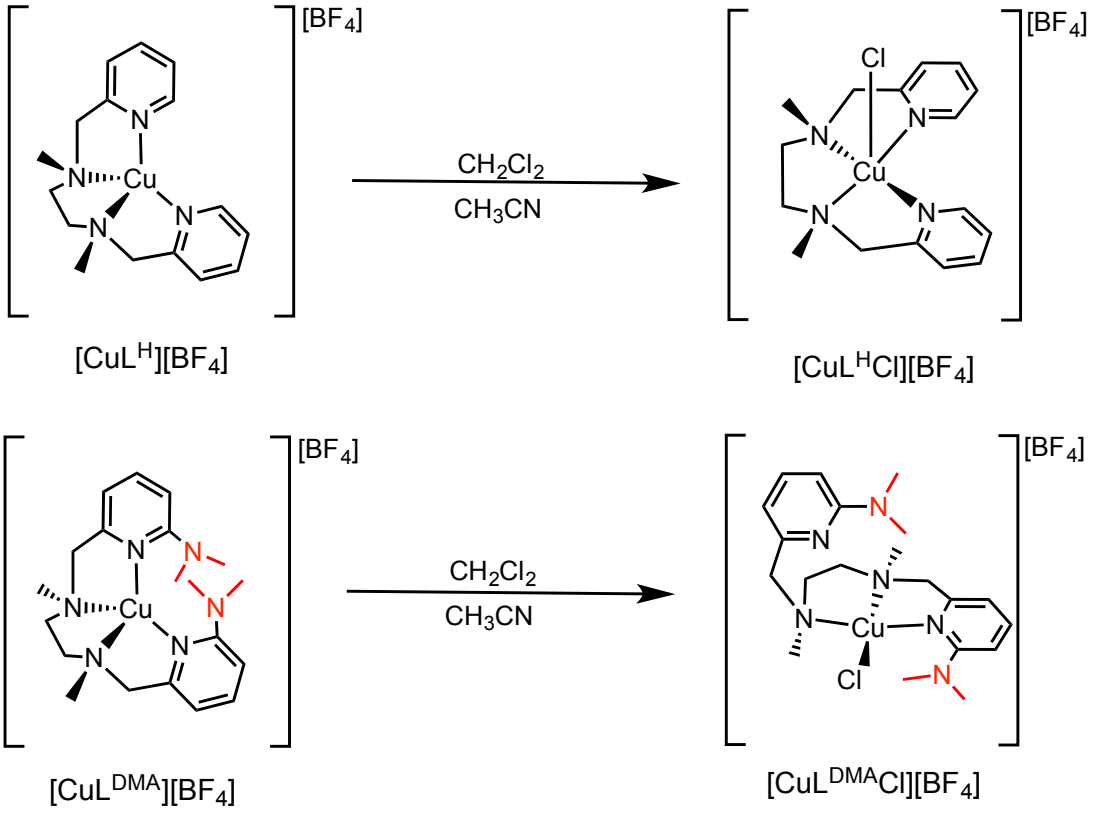

Cu(I) complexes can react with alkylhalogens via a reductive dechlorination process to form halide bound Cu(II) products.[2-4] When residual dicholoromethane was present in solution with the $[CuL^{H}][BF_4]$ or $[CuL^{DMA}][BF_4]$ compounds, the Cu(I) complexes would spontaneously form the chloride bound Cu(II) complexes, all of which were green solids (Scheme A.1). The solid

state crystal structures are shown in Figure A.2. Stirring the diamagnetic Cu(I) complexes in DCM overnight and analyzing the resulting product by ^{1}H NMR spectroscopy gave no proton signals. This result is indicative of a paramagnetic species, likely the new chloride bound Cu(II). These complexes could also be independently synthesized by metalation of the ligand with the divalent $CuCl_2$ starting material. The resulting complex has one Cl^- bound to the copper metal center and one outer sphere chloride.

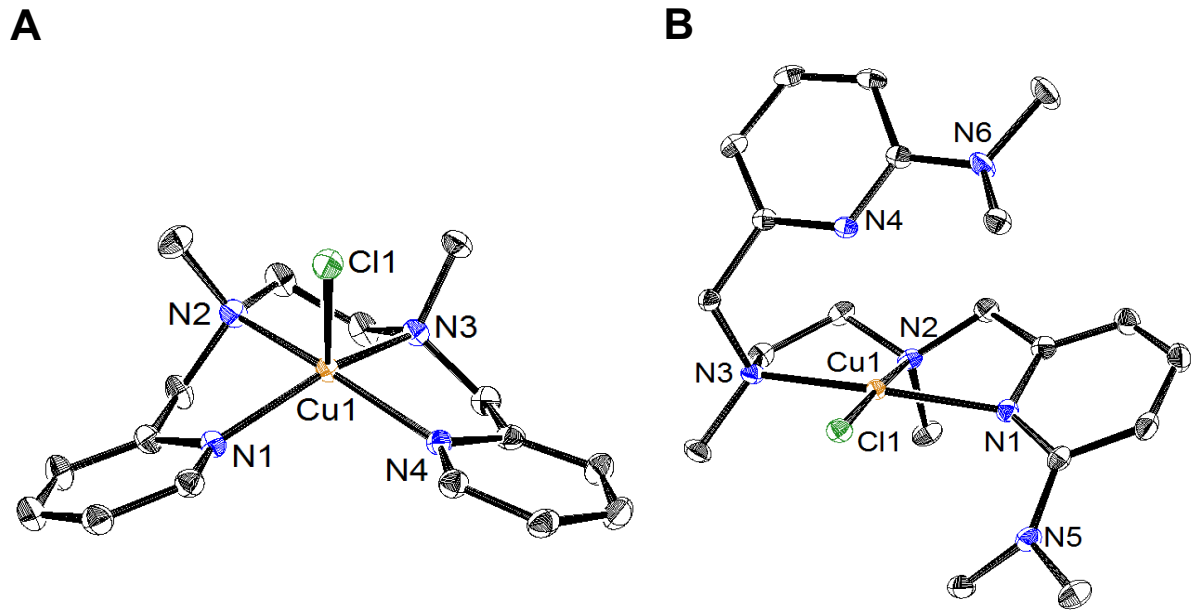

Figure A.2. ORTEP of the divalent copper complexes A) $[CuL^{H}Cl][BF_4]$ and B) $[Cu(\kappa\text{-}3)L^{DMA}Cl][BF_4]$. Thermal ellipsoids are drawn at the 50% probability level. BF_4^- counter anions, solvent molecules, and hydrogen atoms have been removed for clarity.

The $[CuL^{H}Cl][BF_4]$ complex has a five-coordinate coordination environment similar to that of $[CuL^{H}(CH_3CN)][BF_4]_2$ in Chapter 2. Additionally, the methyl groups on the amine backbone of are *cis* to one another (Figure A.2).

However, when the bulkier ligand L^{DMA} is utilized, the copper center cannot accommodate a five-coordinate geometry (Figure A.2). A chloride anion is coordinated leaving an uncoordinated

pyridyl nitrogen. The result is a κ-3 coordination mode of the remaining nitrogen ligands of the L^{DMA} ligand. Additionally, the methyl groups on the amine backbone are *cis* to one another and on the opposite face as the uncoordinated pyridyl arm. The *cis* conformation does not occur when all four nitrogens are coordinated to the metal center, as they are in $[CuL^{DMA}][BF_4]_2$. These observations can be explained by steric crowding resulting from the dimethylamine groups, which do not allow a fifth ligand to coordinate.

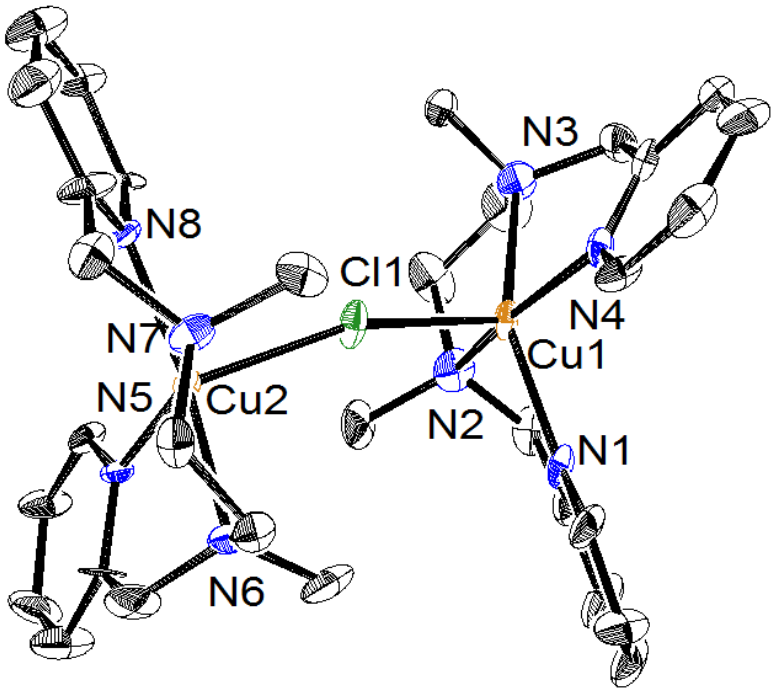

Figure A.3. ORTEP of the dimer copper $[Cu_2(\mu\text{-}Cl)(L^H)_2][BF_4]_3$. Thermal ellipsoids are drawn at the 30% probability level. BF_4^- counter anions, solvent molecules and hydrogen atoms have been removed for clarity.

When the Cu(I) complex $[CuL^H][BF_4]$ is exposed to dichloromethane in a basic environment it forms a rare bridging chloride dimer as shown in Figure A.3. To date, very few crystallographically characterized chloride bridged Cu(II) dimers with nitrogen supported ligands have been reported [5-7] and they are typically grown in extreme pH conditions and/or formed using polyoxometalate oxide clusters. The $[Cu_2(\mu\text{-}Cl)(L^H)_2][BF_4]_3$ structure has two Cu(II) metal centers bridged by a chloride. The single crystals were of poor quality and only connectivity can be gained

from the solid state structure shown. The ligands are in an *anti*-like conformation relative to each and appear to have aromatic π-π stacking interaction via the pyridyl units. Additionally, the methyl groups on the amine backbone of are *cis* to one another.

Cobalt Complexes with Chloride Ligands

Scheme A.2. Synthesis of dinuclear Co(II) chloride bound complex $[Co_2L^{DMA}Cl_4]$ with $CoCl_2$.

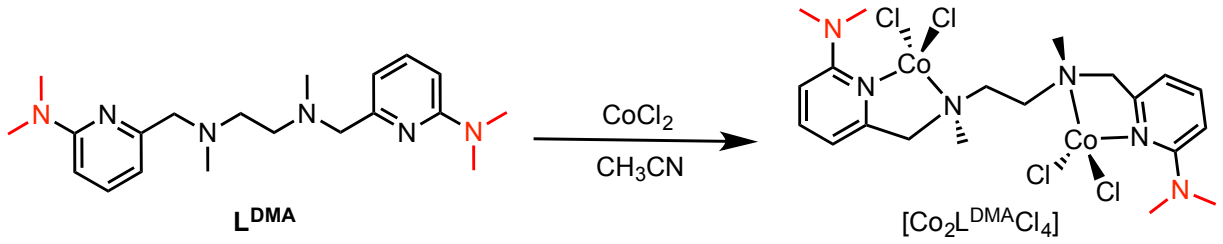

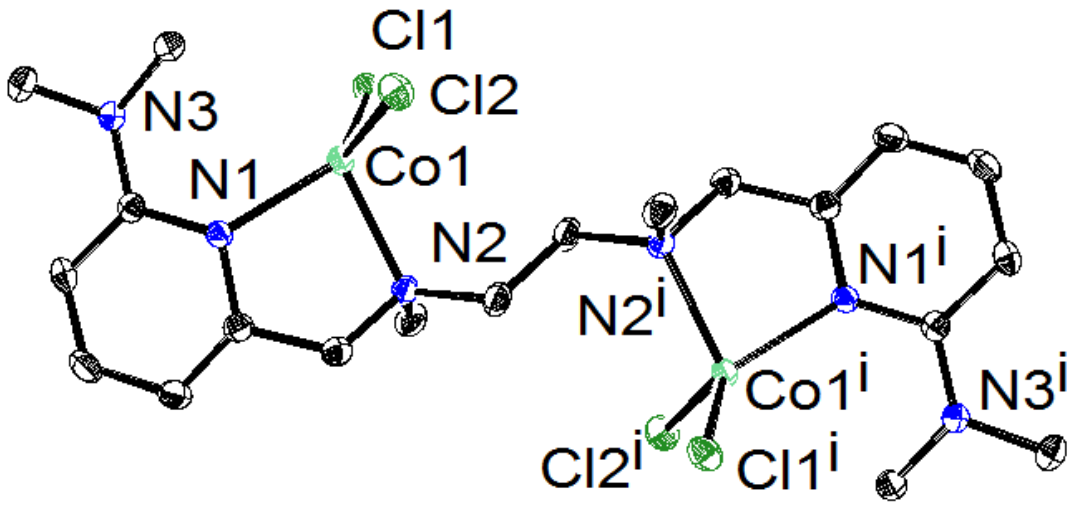

Figure A.4. ORTEP of the dinuclear Co(II) chloride bound complex $[Co_2L^{DMA}Cl_4]$. Thermal ellipsoids are drawn at the 50% probability level. Solvent molecules and hydrogen atoms have been removed for clarity.

Metalation of the ligand L^{DMA} with cobalt (II) dichloride results in an similar structure to that shown for iron (Scheme A.2 and Figure A.4).[1] Each cobalt metal center is Co(II), with two nitrogens of the N_2Py_2 ligand bound and two chloride anions.

A.4. Conclusion

The use of strongly coordinating anions such as chloride ions provided undesired geometric arrangements and coordination modes. In particular, the ligands with a large steric footprint typically resulted in dinuclear products or dangling units. This non-ideal coordination may lower the functionally of the ligand design or the chloride anions may compete with other substrates during reactivity studies. As a result of these early synthetic attempts, the metal chloride starting materials were replaced with metal tetraflouroborate (BF_4^-) salts. The results of these syntheses are discussed in Chapter 2 and 3.

A.5. Experimental Details

General Experiment Considerations

All reagents were purchased from commercial suppliers and used without further purification. Unless otherwise noted, all chemical manipulations were performed in a Vacuum Atmospheres Co. drybox under a nitrogen atmosphere. Anhydrous solvents were sparged with UHP argon (Praxair) and passed through columns containing Q-5 and molecular sieves before use.

Physical Methods

X-Ray Crystallography: A Bruker SMART APEX II diffractometer was used to collect all data. The APEX2 (APEX2 Version 2014.11-0, Bruker AXS, Inc.; Madison, WI 2014) program package was used to determine the unit-cell parameters and for data collection (20 sec/frame scan time for a sphere of diffraction data). The raw frame data was processed using SAINT (SAINT Version 8.34a, Bruker AXS, Inc.; Madison, WI 2013) and SADABS (Sheldrick, G. M. SADABS, Version 2014/5, Bruker AXS, Inc.; Madison, WI 2014) to yield the reflection data file. Subsequent

calculations were carried out using the SHELXTL (Sheldrick, G. M. SHELXTL, Version 2014/7, Bruker AXS, Inc.; Madison, WI 2014) program. The structures were solved by direct methods and refined on F^2 by full-matrix least-squares techniques. The analytical scattering factors for neutral atoms were used throughout the analysis (International Tables for Crystallography 1992, Vol. C., Dordrecht: Kluwer Academic Publishers).

A.6. References

(1) Hoffert, W. A.; Mock, M. T.; Appel, A. M.; Yang, J. Y. *Eur. J. Inorg. Chem.* **2013**, *2013*, 3846-3857.

(2) Lucchese, B.; Humphreys, K. J.; Lee, D.-H.; Incarvito, C. D.; Sommer, R. D.; Rheingold, A. L.; Karlin, K. D. *Inorg. Chem.* **2004**, *43*, 5987-5998.

(3) Jacobson, R. R.; Tyeklár, Z.; Karlin, K. D. *Inorg. Chim. Acta* **1991**, *181*, 111-118.

(4) Karlin, K. D. *Science* **1993**, *261*, 701-708.

(5) Bauer, R. A.; Robinson, W. R.; Margerum, D. W. *J. Chem. Soc., Chem. Comm.* **1973**, 289-290.

(6) Lu, X.; Shi, X.; Bi, Y.; Yu, C.; Chen, Y.; Chi, Z. *Eur. J. Inorg. Chem.* **2009**, *2009*, 5267-5276.

(7) Zhang, C.-D.; Liu, S.-X.; Sun, C.-Y.; Ma, F.-J.; Su, Z.-M. *Cryst. Growth Des.* **2009**, *9*, 3655-3660.

APPENDIX B

pH Dependent Luminescence of Copper (I) Complexes

B.1. Motivation and Specific Aims

Most luminescent metal complexes are composed of expensive metals such as iridium and ruthenium.[1] Luminescence modulation based on external stimuli such as proton concentration has been studied primarily using Ir complexes for pH sensors.[2,3] Cu(I) complexes however also have shown desirable optical properties and is much more abundant and lower in cost.[4] An attempt to develop a pH dependent luminescent Cu(I) complex is shown here. The $[CuL^{DMA}][BF_4]$ complex incorporates bulky substituents in an effort to increase the quantum lifetime by minimizing geometric rearrangement upon excitation. The complexes studied include $[CuL^{H}][BF_4]$, which contains no uncoordinated basic sites, and $[CuL^{DMA}][BF_4]$, which contains two pendant dimethylamine base functionalities, to compare pH dependence.

B.2. Background

An interesting application of luminescent metal-based complexes is organic light-emitting diodes (OLED) and fluorescent pH sensors.[5] Low cost transition metals exhibiting room temperature light emission have gained recognition as an alternative to the current use of expensive and rare materials.[6-8] Copper (I) coordination complexes have been extensively studied due to their wide range of luminescence intensity, quantum yield, and application in devices.[9-11] Bulky substituents on bis-phenanthroline complexes have been shown to exhibit longer quantum lifetimes.[12] Longer lifetimes result from low overall structural reorganization between the ground and emissive excited states. The Cu(I) d^{10} electronic configuration generally results in tetrahedral coordination geometry while the excited Cu(II) d^9 state is a flattened pseudo square planar structure. Steric bulk may slow the geometric rearrangement, which is a source of emission quenching, and increase efficiency and quantum lifetimes. Here, two copper complexes are

discussed in an attempt to develop pH dependent luminescent complex that may exhibit longer lifetimes due to incorporated steric bulk.

B.3. Results and Discussion

Synthesis and characterization of the Cu(I) complexes $[CuL^{H}][BF_4]$ and $[CuL^{DMA}][BF_4]$ are described in Chapter 2.

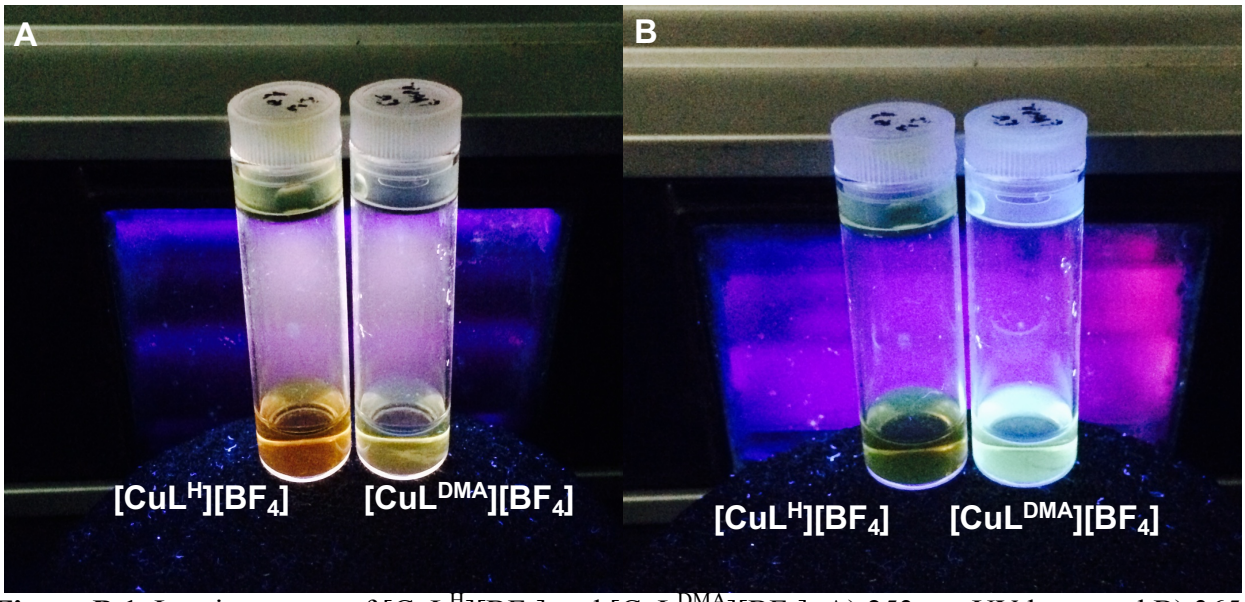

Figure B.1. Luminescence of $[CuL^{H}][BF_4]$ and $[CuL^{DMA}][BF_4]$. A) 253 nm UV lamp and B) 365 nm UV lamp.

The qualitative luminescence of $[CuL^{H}][BF_4]$ and $[CuL^{DMA}][BF_4]$ is shown in Figure B.1. $[CuL^{DMA}][BF_4]$ appeared to exhibit more fluorescence. As a result, the UV-Vis and fluorescence emission spectra for $[CuL^{DMA}][BF_4]$ were taken to understand the pH-responsive photochemical properties of these Cu(I) complexes.

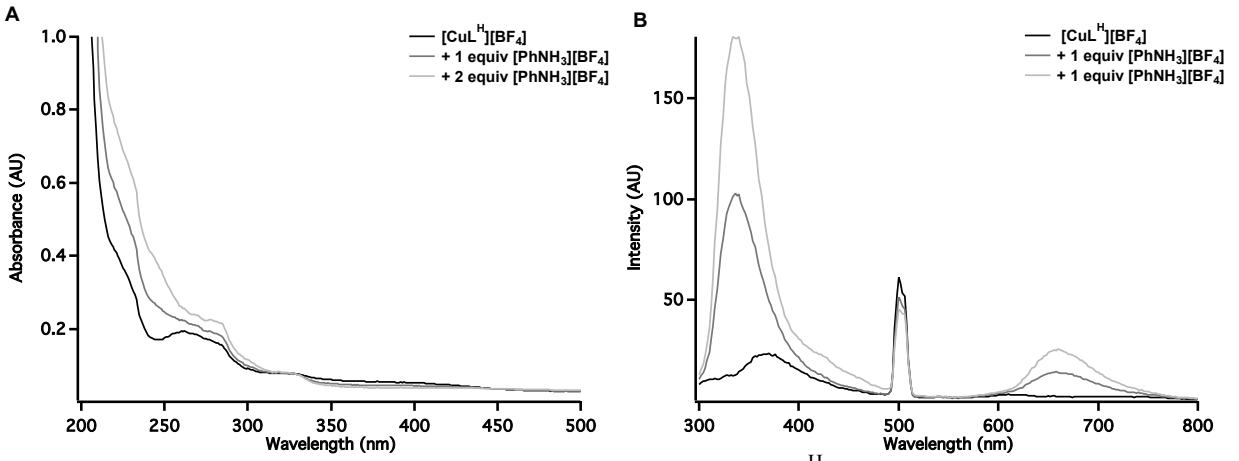

Figure B.2. Electronic absorption and emission spectra of $[CuL^{H}][BF_4]$ with added equivalents of $[PhNH_3][BF_4]$. A) UV-Vis spectra and B) Emission fluorescence spectra. (excitation at 250 nm). $[CuL^{H}][BF_4]$ (black trace), 1 equiv. $[PhNH_3][BF_4]$ (dark gray trace), and 2 equiv. $[PhNH_3][BF_4]$ (light gray trace). All spectra collected at 10 μM in CH_3CN.

The absorbance of $[CuL^{H}][BF_4]$ increases with added equivalents of the weak acid anilinium ($[PhNH_3][BF_4]$, pK_a = 10.62 in CH_3CN),[13] however this increase may be due to the UV absorbance of free aniline which occurs at 235 and 285 nm (Figure B.2A).[14] The initial emission spectra shows only one peak at 366 nm and after acid is added there is the appearance of a peak at 336 nm and 660 nm which is attributed to aniline (Figure B.2B).[15]

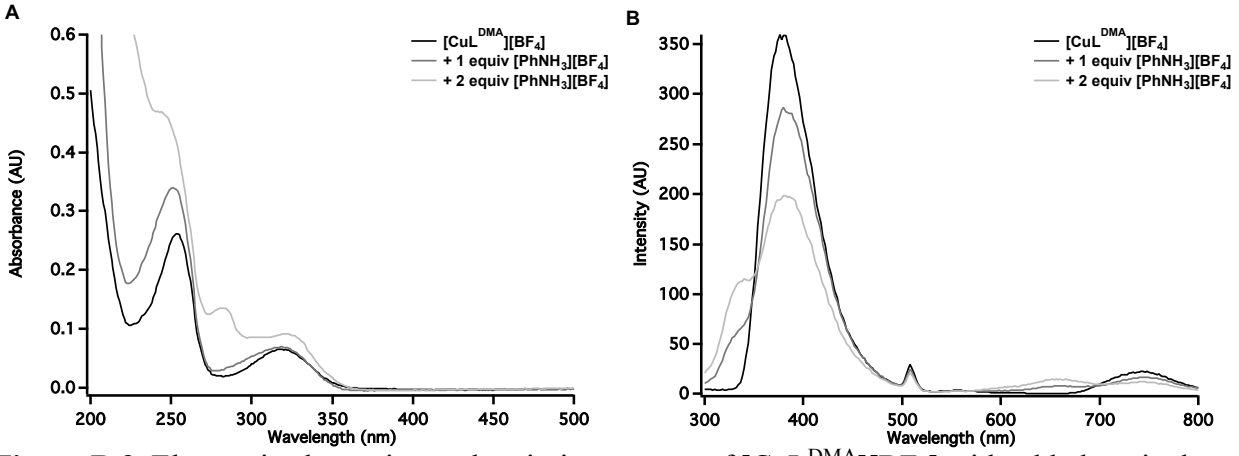

Figure B.3. Electronic absorption and emission spectra of $[CuL^{DMA}][BF_4]$ with added equivalents of $[PhNH_3][BF_4]$. A) UV-Vis spectra and B) Emission fluorescence spectra. (excitation at 250 nm). $[CuL^{DMA}][BF_4]$ (black trace), 1 equiv. $[PhNH_3][BF_4]$ (dark gray trace), and 2 equiv. $[PhNH_3][BF_4]$ (light gray trace). All spectra collected at 10 μM in CH_3CN.

The increase in absorbance of $[CuL^{DMA}][BF_4]$ after the addition of anilinium and the small peak at 285 nm can be attributed to the UV absorbance of free aniline (Figure B.3A).[14] After acidification a decrease in intensity of the emission at 382 nm and 744 nm occurs with increasing equivalents (Figure B.3B). Additionally, the appearance of two peaks at 336 nm and 660 nm are both attributed to aniline.[14] The quenching of the emission intensities from $[CuL^{DMA}][BF_4]$ with increasing acidity occurs due to lability of the protonated of nitrogen atoms.

It is known from previous studies shown in Chapter 2 that the site of protonation is the ethylenediamine tertiary nitrogens in the Cu(I) complexes. Upon protonation and subsequent dissociation, there is decreased σ-donation to the metal center lowering the HOMO−LUMO energy gap.[2] However, if protonation were to occur at the pyridine arms it could also disrupt the π-electron conjugated double-bond system and result in significant fluorescence quenching.[3,16]

Electronic properties are usually obtained from Density Functional Theory (DFT) calculations but the frontier orbital energy gap and corresponding energy separations can also be determined with cyclic voltammetry using the oxidation potential for the HOMO and the reduction potential for the LUMO.[17] The Cu(II/I) couples for these complexes are not reversible, so the HOMO and LUMO energy levels calculated are approximations from the quasi-reversible couples. A summary of the three Cu(I) complexes is shown in Figure B.4. The HOMO−LUMO gap for $[CuL^{DMA}][BF_4]$ is smaller than that of $[CuL^{H}][BF_4]$, explaining the increased emission intensity without acid. As discussed in Chapter 2, the oxidized Cu(II) complexes require geometric rearrangement, but $[CuL^{DMA}][BF_4]$ does not necessitate a ligand dissociation beforehand and thus the HOMO−LUMO gap is likely smaller.

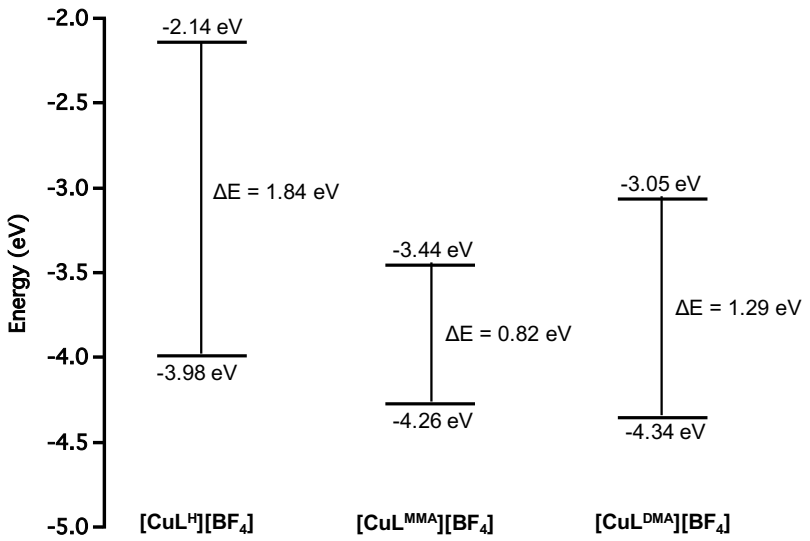

Figure B.4. HOMO and LUMO energies of Cu(I) complexes based on cyclic voltammetry values.

B.4. Conclusion

The fluorescence spectroscopy for $[CuL^{H}][BF_4]$ shows no major emission features and it is not responsive to addition of acid. The $[CuL^{DMA}][BF_4]$ complex has a large intensity at 382 nm that decreases after the addition of anilinium resulting from the quenching of the protonated ligand.

B.5. Experimental Details

General Experiment Considerations

All reagents were purchased from commercial suppliers and used without further purification. Unless otherwise noted, all chemical manipulations were performed in a Vacuum Atmospheres Co. drybox under a nitrogen atmosphere. Anhydrous solvents were sparged with UHP argon (Praxair) and passed through columns containing Q-5 and molecular sieves before use.

Physical Methods

Ultraviolet-Visible (UV-Vis) Spectroscopy: Ultraviolet-Visible spectra were collected as 10 μM solutions in 3 mL CH_3CN in a 1 cm quartz cuvette or as 1mM solutions in 0.3 mL CH_3CN in a 1 mm quartz cuvette using an Agilent Technologies Cary 60 UV–Vis spectrometer.

Emission Fluorescence Spectroscopy: Emission spectra were collected as 10 μM solutions in 3 mL CH_3CN in a 1 cm quartz cuvette equipped with red rubber septa using a Cary Eclipse Spectrofluorometer at 298 K.

B.6. References

(1) Keefe, M. H.; Benkstein, K. D.; Hupp, J. T. *Coord. Chem. Rev.* **2000**, *205*, 201-228.

(2) Werrett, M. V.; Muzzioli, S.; Wright, P. J.; Palazzi, A.; Raiteri, P.; Zacchini, S.; Massi, M.; Stagni, S. *Inorg. Chem.* **2014**, *53*, 229-243.

(3) Nakagawa, A.; Hisamatsu, Y.; Moromizato, S.; Kohno, M.; Aoki, S. *Inorg. Chem.* **2014**, *53*, 409-422.

(4) Wallesch, M.; Volz, D.; Zink, D. M.; Schepers, U.; Nieger, M.; Baumann, T.; Bräse, S. *Chem. Eur. J.* **2014**, *20*, 6578-6590.

(5) Evans, R. C.; Douglas, P.; Winscom, C. J. *Coord. Chem. Rev.* **2006**, *250*, 2093-2126.

(6) Yersin, H. *Highly Efficient OLEDs with Phosphorescent Materials*; Wiley-VCH Verlag GmbH & Co. KGaA, 2008.

(7) Liu, Z.; Qayyum, M. F.; Wu, C.; Whited, M. T.; Djurovich, P. I.; Hodgson, K. O.; Hedman, B.; Solomon, E. I.; Thompson, M. E. *J. Am. Chem. Soc.* **2011**, *133*, 3700-3703.

(8) Deaton, J. C.; Switalski, S. C.; Kondakov, D. Y.; Young, R. H.; Pawlik, T. D.; Giesen, D. J.; Harkins, S. B.; Miller, A. J. M.; Mickenberg, S. F.; Peters, J. C. *J. Am. Chem. Soc.* **2010**, *132*, 9499-9508.

(9) Armaroli, N.; Accorsi, G.; Cardinali, F.; Listorti, A. In *Photochemistry and Photophysics of Coordination Compounds I*; Balzani, V., Campagna, S., Eds.; Springer: Berlin, Heidelberg, 2007, p 69-115.

(10) Chia, Y. Y.; Tay, M. G. *Dalton Trans.* **2014**, *43*, 13159-13168.

(11) Igawa, S.; Hashimoto, M.; Kawata, I.; Yashima, M.; Hoshino, M.; Osawa, M. *J. Mat. Chem. C* **2013**, *1*, 542-551.

(12) Ruthkosky, M.; Kelly, C. A.; Castellano, F. N.; Meyer, G. J. *Coord. Chem. Rev.* **1998**, *171*, 309-322.

(13) Kaljurand, I.; Kütt, A.; Sooväli, L.; Rodima, T.; Mäemets, V.; Leito, I.; Koppel, I. A. *J. Org. Chem.* **2005**, *70*, 1019-1028.

(14) Cumper, C. W. N.; Singleton, A. *J. Chem. Soc. B: Phys. Org.* **1968**, 649-651.

(15) Köhler, G. *J. Photochem.* **1987**, *38*, 217-238.

(16) Jiang, H.-L.; Feng, D.; Wang, K.; Gu, Z.-Y.; Wei, Z.; Chen, Y.-P.; Zhou, H.-C. *J. Am. Chem. Soc.* **2013**, *135*, 13934-13938.

(17) Leonat, L.; Sbârcea, G.; Branzoi, I. V. *UPB Sci. Bull. Ser. B* **2013**, *75*, 111-118.

APPENDIX C

Intramolecular C–H Bond Activation in a Rhodium Complex

C.1. Motivation and Specific Aims

Due to the sensitivity of $[CoL^{DMA}(CH_3CN)_2][BF_4]_2$ to ligand loss in the presence of strong nucleophiles and acids described in Chapter 3, the L^{DMA} ligand was complexed with a kinetically inert second row transition metal. A functional group tolerant metal such as rhodium may allow for the isolation of reactivate intermediates and fundamental pK_a studies required for proton-coupled electron transfer (PCET) studies. However, an unexpected intramolecular C–H activation of the methyl group on the dimethylamine moiety of L^{DMA} occurred upon metalation with $RhCl_3$, possibly through intramolecular deprotonation by a secondary pyridine on the ligand. An asymmetric ligand (L^{Asym}) that contains only one pyridine was synthesized and complexed with $RhCl_3$ in an attempt to determine the participation of the additional pyridine in the C–H activation.

C.2. Background

Controlled transformation of molecules from C–H bonds to C–C bonds is important for organic natural product synthesis as well as inorganic small molecule activation.[1,2] Rhodium(III) is well known for sp^2 C–H activation[3-6] and has shown promising sp^3 C–H activation of acidic protons adjacent to heteroatoms or allylic moieties.[7-9] Reactivity of rhodium complexes with unactivated C–H bonds is much more difficult and very rare.[10-12] However, density functional theory (DFT) studies has shown that Rh(III) may be capable of highly desired methane oxidation through base assisted C–H activation.[13]

Scheme C.1. Pyridine directed chelation assistance in C–H activation.

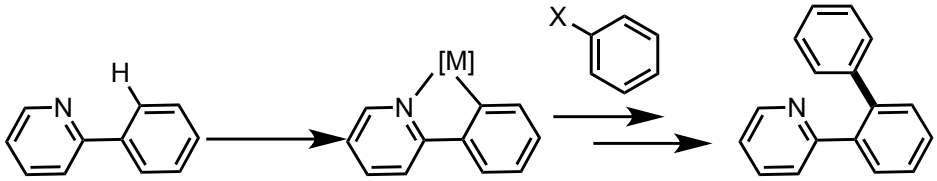

Scheme C.2. Role of acetate concerted metalation-deprotonation (CMD) mechanism.

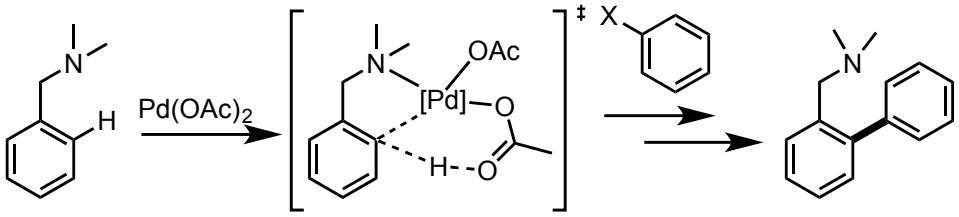

Chelation assistance through directing groups that coordinate and bring the desired C–H bond into close proximity to the metal center has been used to provide selective and more facile C–H bond cleavage (Scheme C.1). Nitrogen-based heterocycles are especially common due to reversible metal coordination for faster rate during the catalytic cycle.[4] Additionally, anions such as acetate and carboxylate from the metal starting material have been shown to behave as bases in a concerted metalation-deprotonation (CMD) mechanism where the carbon-metal bond formation of the metallocycle intermediate is assisted by the deprotonation of the C–H functionality by a Lewis base (Scheme C.2).[14]

Here a rhodium(III) complex ([$RhL^{DMA}Cl_2$][Cl]) that exhibits intramolecular C–H bond activation possibly through a CMD mechanism is presented. An additional rhodium(III) complex with a ligand not capable of intramolecular deprotonation is also described.

C.3. Results and Discussion

C.3.1. Synthesis and Solid State Structures of Rhodium Complexes

Synthesis of [RhL^{DMA}Cl$_2$][Cl]

Scheme C.3. Complexation of L^{DMA} with $RhCl_3$.

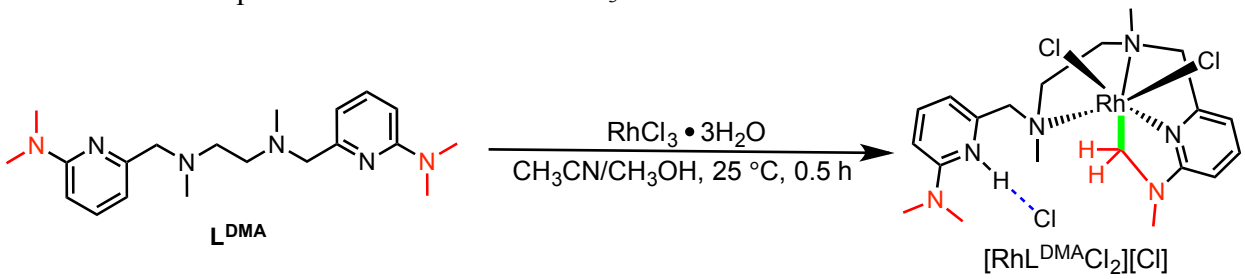

Complexation of L^{DMA} with $RhCl_3$ in 1:1 CH_3CN/CH_3OH gave [RhL^{DMA}Cl$_2$][Cl] as the product. The solid state structure revealed an unexpected sp^3 C–H activated product, Scheme C.3. This activation is through heterolytic bond cleavage; the oxidation state of the Rh(III) remains unchanged. The secondary pyridine is protonated, likely from deprotonation of the activated carbon. Formulation and purity of the product, were confirmed by ESI-MS and elemental analysis, respectively.

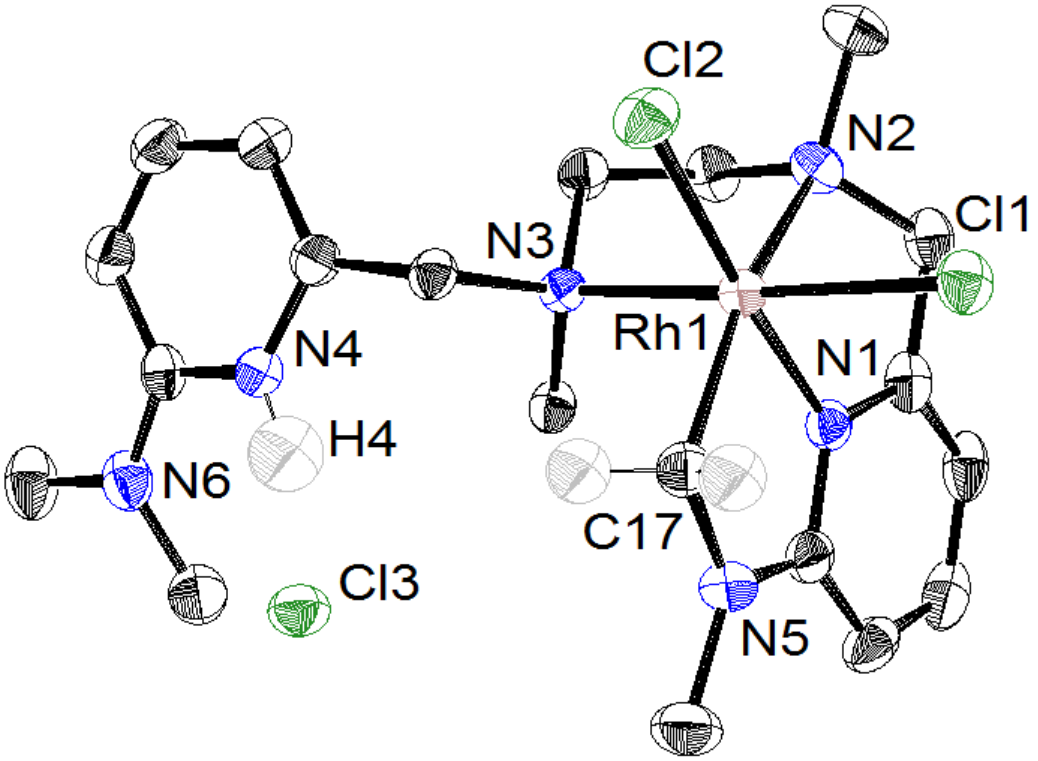

Figure C.1. ORTEP of [RhL^{DMA}Cl$_2$][Cl]. Thermal ellipsoids are drawn at the 50% probability level. The solvent molecules and hydrogen atoms other than H4 and those on the activated methyl group have been removed for clarity.

The solid state structure of [RhL^{DMA}Cl$_2$][Cl] is shown in Figure C.1. The rhodium metal center is six-coordinate with the L^{DMA} ligand in an κ-3 coordination mode with respect to nitrogen atoms N1, N2 and N3. Two equatorial positions are chloride anions while the remaining axial position is the activated carbon (C17) belonging to the methyl group of the dimethylamine moiety forming a five-membered rhodium metallocycle. The pyridine that is not coordinated to the metal center is protonated (H4) and is hydrogen bound to an outer sphere chloride Cl3 with a distance of 2.225 Å. Hydrogen atom (H4) shown in [RhL^{DMA}Cl$_2$][Cl] structure was found in the difference map.

Rhodacycles are common intermediates in C–H activation mechanisms and [RhL^{DMA}Cl$_2$][Cl] may be an example of a CMD mechanism where the second pyridine arm acts

as the base to deprotonate the activated methyl group. This particular C–H bond activation occurs at room temperature and incorporates three principles known to facilitate reactivity. Firstly, chelation assistance directed reactivity to the methyl group of dimethylamine (N5) because it is positioned proximal to the metal center for selective cleavage due to the pyridine coordination (N1). Secondly, the C–H bond may be highly acidic due to its position α to N5. Thirdly, intramolecular deprotonation likely enabled C–H bond activation. The involvement of the second uncoordinated pyridine of the ligand scaffold suggests an intramolecular base assisted mechanism. To test this hypothesis an asymmetric ligand lacking the secondary pyridine was synthesized.

Synthesis of L^{Asym} Ligand

Scheme C.4. Synthesis of L^{Asym} ligand using 6-bromo-2-pyridinecarboxaldehyde.

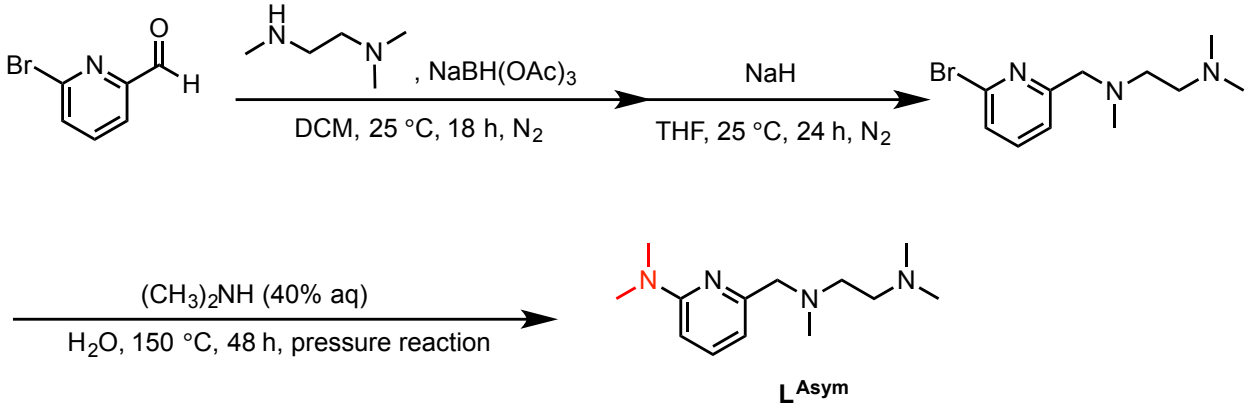

One-pot reductive amination using *N*,*N*,*N*′-trimethylethylenediamine and 6-bromo-2-formylpyridine followed by deprotonation yields L^{AysmBr} containing a bromo- functionality in the 6-position of the pyridine ring. Nucleophilic aromatic substitution using aqueous dimethylamine under pressure affords L^{Asym} in 74% yield, Scheme C.4. This ligand scaffold contains only one pyridine arm and therefore lacks the intramolecular base present in $[RhL^{DMA}Cl_2][Cl]$.

Synthesis of [RhL^{Asym}(CH$_3$CN)Cl$_2$][Cl]

Scheme C.5. Complexation of L^{Asym} with RhCl$_3$.

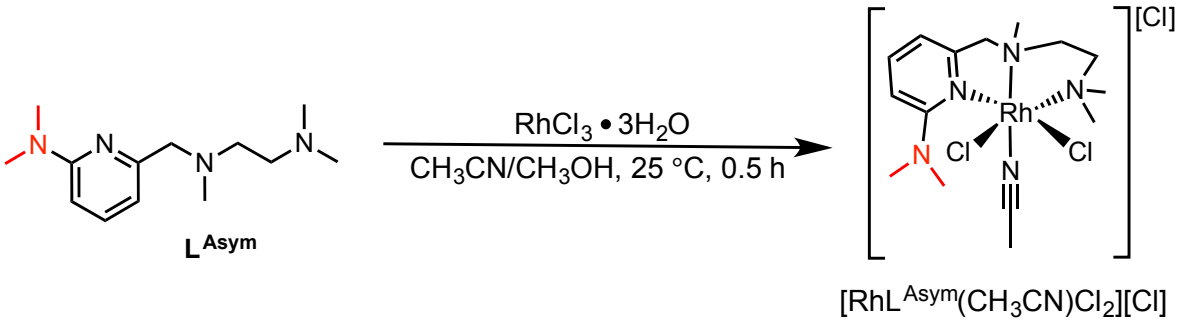

Complexation of L^{Asym} with RhCl$_3$ (Scheme C.5) under the same conditions as [RhL^{DMA}Cl$_2$][Cl] reveals no evidence of C–H activation or cyclometalation product, which may indicate that this process requires a base. Formulation and purity of the complex were confirmed by ESI-MS and elemental analysis, respectively.

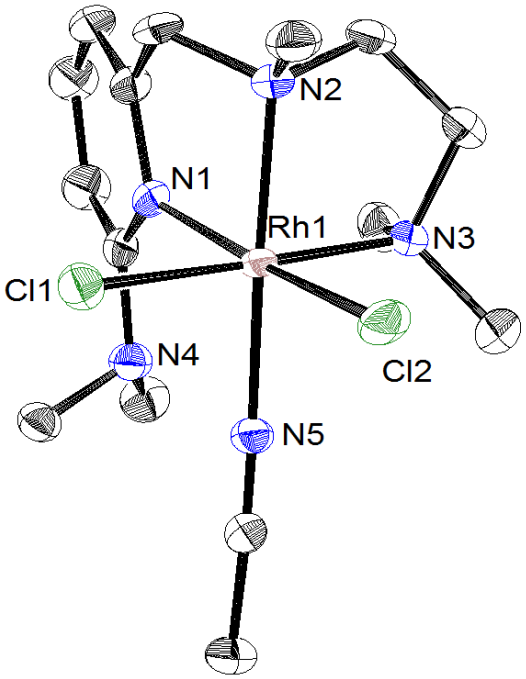

Figure C.2. ORTEP of [RhL^{Asym}(CH$_3$CN)Cl$_2$][Cl]. Thermal ellipsoids are drawn at the 50% probability level. The Cl$^-$ counter anion, solvent molecules and hydrogen atoms have been removed for clarity.

The solid state structure of $[RhL^{Asym}(CH_3CN)Cl_2][Cl]$ is shown in Figure C.2. The rhodium metal center has an octahedral structure with L^{Asym} coordinated in a κ-3 coordination mode. Two equatorial positions are chloride anions with the sixth position taken by an acetonitrile solvent molecule. The methyl group of the dimethylamine moiety remains intact. Given the similar coordination and electronic environment as $[RhL^{DMA}Cl_2][Cl]$, the lack of C–H activation suggests the intramolecular pyridine of may be necessary for activation and isolation of a stable rhodacyle through a CMD mechanism.

C.3.2. Physical Characterization of Rhodium Complexes

^{1}H NMR Spectroscopy

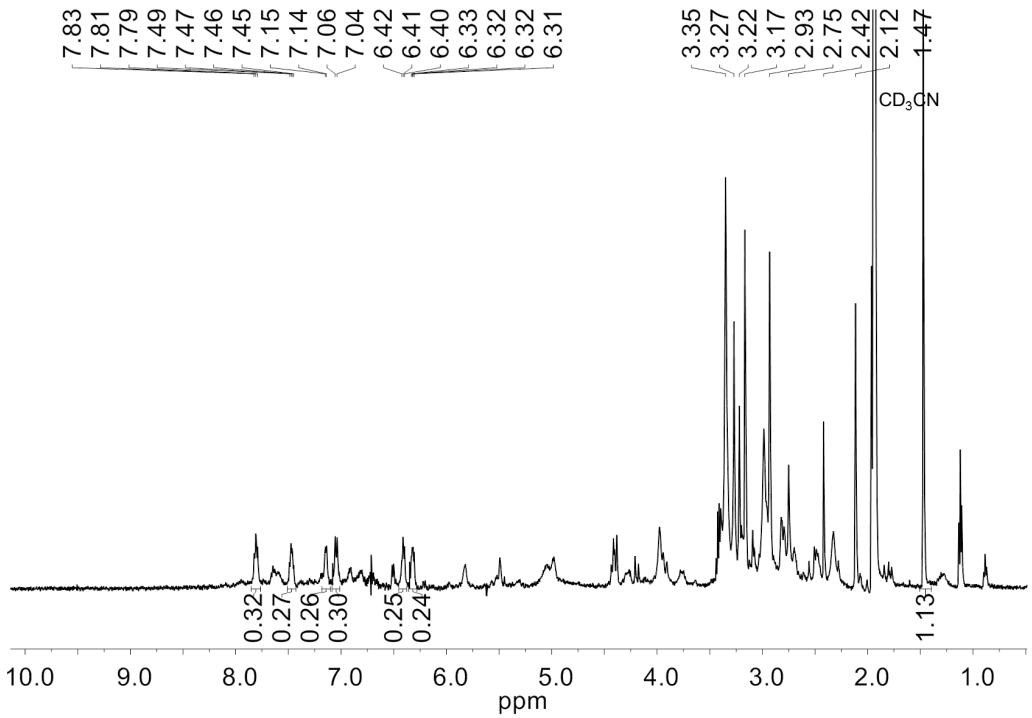

Figure C.3. ^{1}H NMR spectra of $[RhL^{DMA}Cl_2][Cl]$ in CD_3CN.

The ^{1}H NMR spectra of single crystals of $[RhL^{DMA}Cl_2][Cl]$ reveals six inequivalent aromatic proton resonances which suggests the symmetry of the ligand has been broken (Figure

C.3). A non-activated complex should have only three aromatic proton resonances for both equivalent pyridine rings. The C–H activation is presumably responsible for the asymmetry of the aromatic protons and is consistent with the solid state structure.

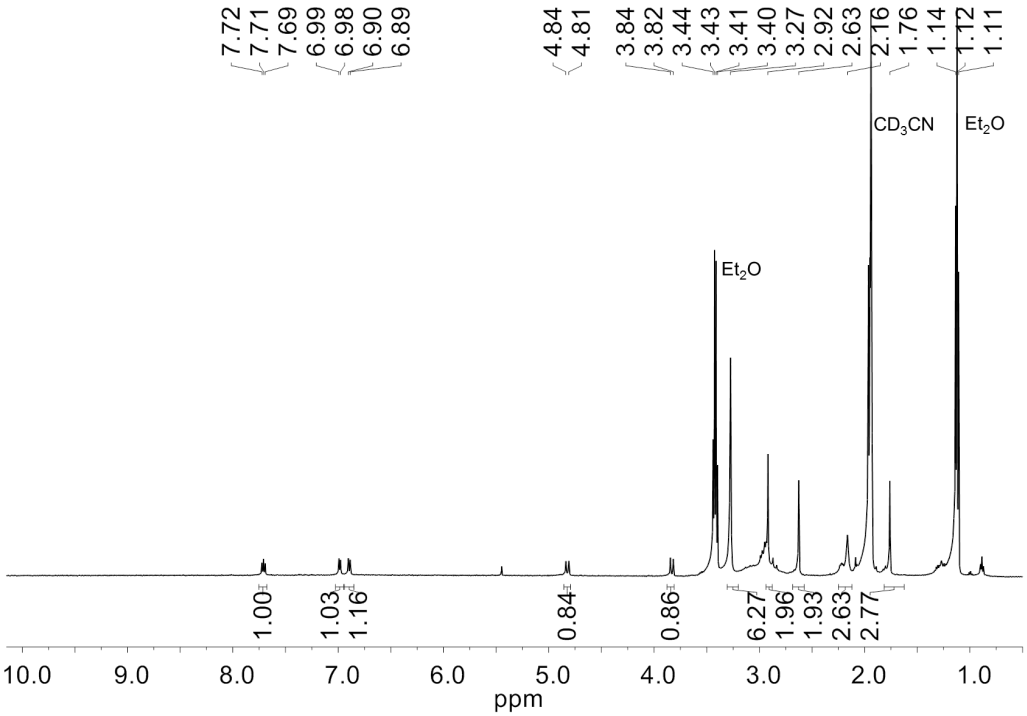

Figure C.4. ^{1}H NMR spectra of [RhL^{Asym}(CH$_3$CN)Cl$_2$][Cl] in CD$_3$CN.

The ^{1}H NMR spectra of [RhL^{Asym}(CH$_3$CN)Cl$_2$][Cl] contains only three aromatic proton resonances for the one pyridine ring present and is consistent with the solid state structure, indicating there has been no C–H activation (Figure C.4). This complex has only one pyridine ring and may not be capable of C–H at room temperature without an external base.

Infrared Spectroscopy

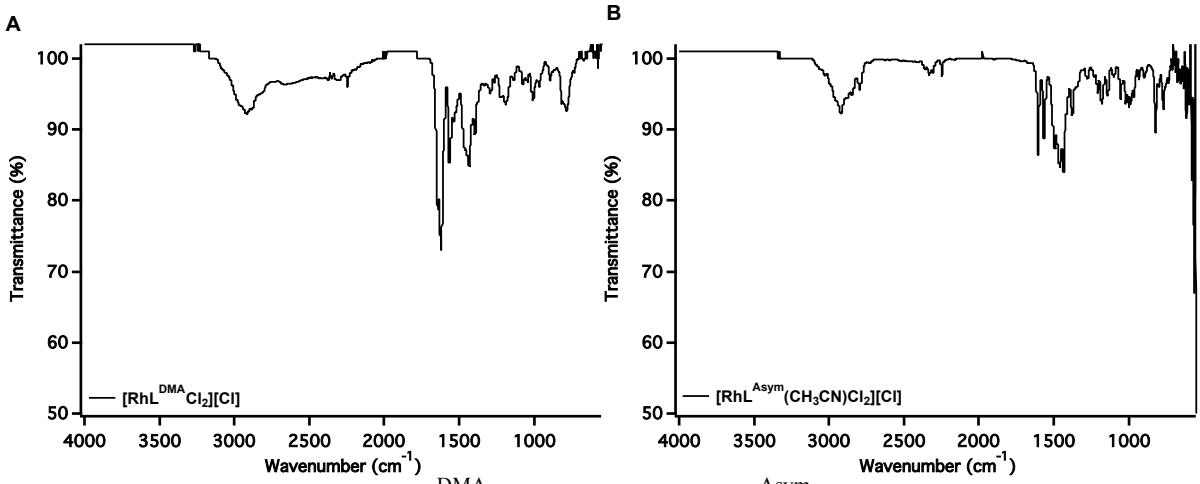

Figure C.5. IR spectra of A) $[RhL^{DMA}Cl_2][Cl]$ and B) $[RhL^{Asym}(CH_3CN)Cl_2][Cl]$.

The solid state IR spectra of $[RhL^{DMA}Cl_2][Cl]$ and $[RhL^{Asym}(CH_3CN)Cl_2][Cl]$ are shown in Figure C.5. $[RhL^{DMA}Cl_2][Cl]$ has a protonated pyridine salt in the solid state structure which is corroborated by the IR spectra which exhibits a broad N–H stretch from 3000–2000 cm^{-1} indicative of amine salts.[15] This broad N–H stretch is not present in the IR spectra of $[RhL^{Asym}(CH_3CN)Cl_2][Cl]$. Additionally, $[RhL^{DMA}Cl_2][Cl]$ has an N–H bend at 1620 cm^{-1} which is also not present in the IR spectra of $[RhL^{Asym}(CH_3CN)Cl_2][Cl]$.

C.3.3. Reactivity of $[RhL^{Asym}(CH_3CN)Cl_2][Cl]$ with External Base

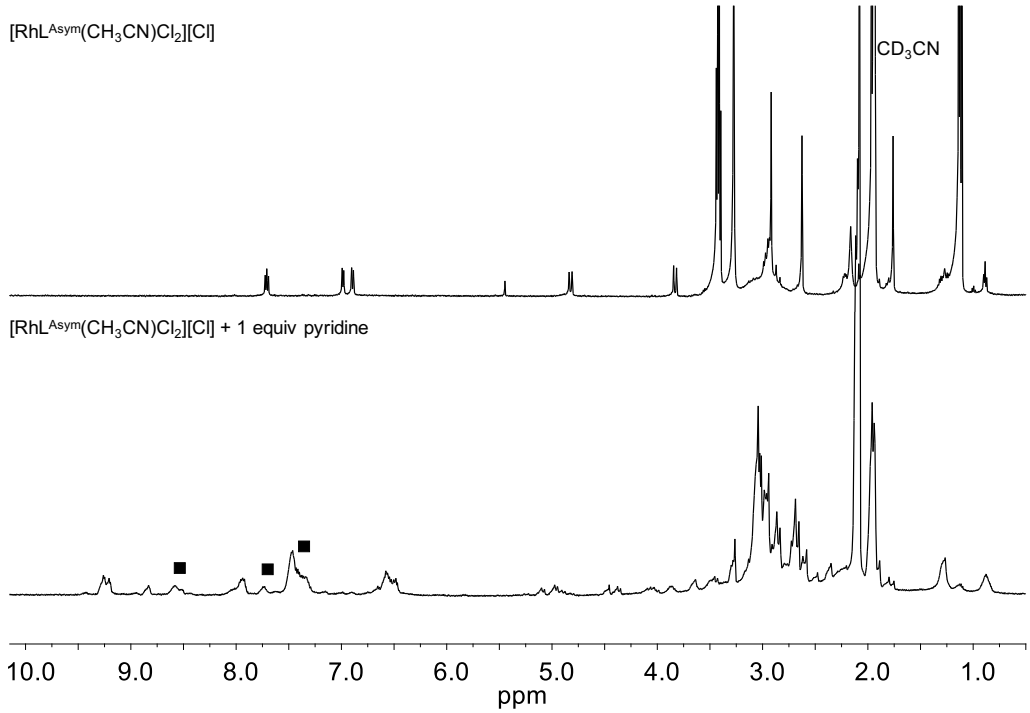

Figure C.6. ^{1}H NMR spectra of $[RhL^{Asym}(CH_3CN)Cl_2][Cl]$ in CD_3CN in the presence of base. Top: complex with no base present. Bottom: 1 equiv pyridine added, square symbol (■) indicates $[HPy][BF_4]$ resonances.

The solid state structural and physical characterization of $[RhL^{DMA}Cl_2][Cl]$ and $[RhL^{Asym}(CH_3CN)Cl_2][Cl]$ suggests that a base is needed for room temperature C–H activation of the methyl group. $[RhL^{DMA}Cl_2][Cl]$ has the secondary pyridine as an intramolecular base while $[RhL^{Asym}(CH_3CN)Cl_2][Cl]$ has no base present.

In an effort to determine if an intermolecular base could perform C–H activation of the methyl group of the dimethylamine unit, deprotonation studies of $[RhL^{Asym}(CH_3CN)Cl_2][Cl]$ were performed using ^{1}H NMR spectroscopy, shown in Figure C.6. Addition of one equivalent of pyridine ($[HPy][BF_4]$, pK_a = 10.62 in CH_3CN)[16] reveals pyridinium resonances and none for free pyridine indicating full proton transfer. In the presence of an external base the aromatic proton resonances have shifted from the chemical shift of $[RhL^{Asym}(CH_3CN)Cl_2][Cl]$ complex with no

base present. Additionally, after base is added the methyl group of the dimethylamine unit resonance at 3.42 ppm is no longer present. This data suggests $[RhL^{Asym}(CH_3CN)Cl_2][Cl]$ may be capable of C–H activation with addition of an external base. Conversely, $[RhL^{DMA}Cl_2][Cl]$ which contains an intramolecular base does not require an external substrate which is suggestive of a CMD mechanism.

C.4. Conclusion

A stable rhodacyle of $[RhL^{DMA}Cl_2][Cl]$ was isolated and studied to reveal intramolecular C–H activation via protonation of a pyridine arm on the ligand in neutral and mild reaction conditions. The features of this complex may be an important intermediate in C–H activation catalytic cycles. This particular C–H activation was likely aided by chelation assistance and a more acidic proton adjacent to a heteroatom.

An asymmetric ligand containing no intramolecular base has been synthesized and coordinated with trivalent rhodium to study the necessity of an intramolecular base for C–H activation. Analysis of the $[RhL^{Asymm}(CH_3CN)Cl_2][Cl]$ complex indicates it does not undergo C–H activation under that same conditions as $[RhL^{DMA}Cl_2][Cl]$. However, addition of an external base suggests a structural change by ^1H NMR spectroscopy.

There appears to be an important correlation between the presence of an intramolecular base for C–H activation. $[RhL^{Asymm}(CH_3CN)Cl_2][Cl]$ does not undergo reactivity until an external base is present while $[RhL^{DMA}Cl_2][Cl]$ exhibits reactivity without external stimuli suggestive of an intramolecular CMD mechanism.

C.5. Experimental Details

General Experiment Considerations

All reagents were purchased from commercial suppliers and used without further purification. Unless otherwise noted, all chemical manipulations were performed in a Vacuum Atmospheres Co. drybox under a nitrogen atmosphere. Anhydrous solvents were sparged with UHP argon (Praxair) and passed through columns containing Q-5 and molecular sieves before use.

Physical Methods

Nuclear Magnetic Resonance (NMR) Spectroscopy: ^{1}H NMR spectra were recorded on 500 MHz on Bruker instruments. ^{1}H NMR spectra chemical shifts are reported as δ values in ppm relative to residual protio solvent: $CDCl_3$ (7.26 ppm), CD_3CN (1.94 ppm). Proton NMR data are reported as follows: chemical shift (δ ppm), multiplicity (s = singlet, d = doublet, t = triplet, q = quartet), coupling constants (J) in Hertz (Hz), and integration. Multiplets (m) are reported over the range (ppm). Data for ^{13}C NMR spectra are decoupled proton spectra and are reported in terms of chemical shift (δ ppm).

Mass Spectrometry (MS): High resolution mass spectra (HR-MS) and electrospray ionization mass spectra (ESI-MS) were obtained on a Micromass LCT and collected at the University of California-Irvine Mass Spectrometry Facility.

Ultraviolet-Visible (UV-Vis) Spectroscopy: Ultraviolet-Visible spectra were collected as 10 μM solutions in 3 mL CH_3CN in a 1 cm quartz cuvette or as 1mM solutions in 0.3 mL CH_3CN in a 1 mm quartz cuvette using an Agilent Technologies Cary 60 UV–vis spectrometer. A Bruker SMART APEX II diffractometer was used to collect all the data.

Infrared (IR) Spectroscopy: Infrared spectra were collected using a Thermo Scientific Nicolet iS5 spectrometer with an iD5 ATR attachment in a nitrogen filled glovebox. The sample was prepared by evaporating an acetonitrile solution of the compound onto an ATR crystal, unless otherwise noted.

Electron Paramagnetic Resonance (EPR) Spectroscopy: X-band (9.28 GHz) EPR spectra were collected as 10 mM frozen solutions using a Bruker EMX spectrometer equipped with an ER041XG microwave bridge at 77 K or 10 K.

Elemental Analysis (EA): Elemental analyses were performed on a Perkin Elmer 2400 Series II CHNS elemental analyzer.

X-Ray Crystallography: A Bruker SMART APEX II diffractometer was used to collect all data. The APEX2 (APEX2 Version 2014.11-0, Bruker AXS, Inc.; Madison, WI 2014) program package was used to determine the unit-cell parameters and for data collection (20 sec/frame scan time for a sphere of diffraction data). The raw frame data was processed using SAINT (SAINT Version 8.34a, Bruker AXS, Inc.; Madison, WI 2013) and SADABS (Sheldrick, G. M. SADABS, Version 2014/5, Bruker AXS, Inc.; Madison, WI 2014) to yield the reflection data file. Subsequent calculations were carried out using the SHELXTL (Sheldrick, G. M. SHELXTL, Version 2014/7, Bruker AXS, Inc.; Madison, WI 2014) program. The structures were solved by direct methods and refined on F^2 by full-matrix least-squares techniques. The analytical scattering factors for neutral atoms were used throughout the analysis (International Tables for Crystallography 1992, Vol. C., Dordrecht: Kluwer Academic Publishers). Hydrogen atom H4 of $[RhL^{DMA}Cl_2][Cl]$ was located from a difference-Fourier map and refined (x,y,z and U iso). The remaining hydrogen atoms were included using a riding model.

Synthesis of Ligands

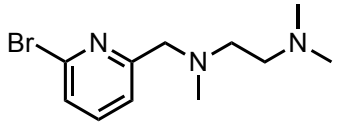

N^1-((6-bromopyridin-2-yl)methyl)-N^1,N^2,N^2-trimethylethane-1,2-diamine (L^{AsymBr}). A solution of sodium triacetoxyborohydride (1.9 g, 8.9 mmol) and 6-bromo-2-formylpyridine (2.0 g, 5.4 mmol) in dry dichloromethane (20 mL) was treated with *N,N,N′*-trimethylethylenediamine (0.58 mL, 0.46 g, 4.5 mmol) and the mixture was stirred at 25 °C under nitrogen for 18 h. The resulting mixture was quenched with 20 mL sat. aqueous sodium bicarbonate. The organic layer was removed and the aqueous layer was extracted 3 × 20 mL portions of ethyl acetate. The organic layers were combined, dried over $MgSO_4$, filtered and concentrated to afford a tan solid (2.2 g, 5.3 mmol). The protonated N^1-((6-bromopyridin-2-yl)methyl)-N^1,N^2,N^2-trimethylethane-1,2-diamine obtained above was dissolved in 20 mL dry tetrahydrofuran. Sodium hydride (60% dispersion in mineral oil, 0.23 g, 5.7 mmol) was added and the resulting solution was stirred at 25 °C under nitrogen for 24 h. The solution was concentrated to give a brown oil that was dissolved in large portions of hexane and filtered three times. The resulting filtrate was concentrated to give a light yellow oil (1.0 g, 84% yield). ^{1}H NMR ($CDCl_3$): δ = 7.52 (t, $^3J_{HH}$ = 10.0 Hz, 1H, Ar–*H*), 7.45 (d, $^3J_{HH}$ = 10.0 Hz, 1H, Ar–*H*), 7.35 (d, $^3J_{HH}$ = 10.0 Hz, 1H, Ar–*H*), 3.68 (s, 2H, Ar–C*H*$_2$–N–), 2.60 (t, 2H, –CH$_2$–C*H*$_2$–), 2.53 (t, 2H, –C*H*$_2$–CH$_2$–), 2.30 (s, 7H, –N–C*H*$_3$ and –N(C*H*$_3$)$_2$); ^{13}C NMR ($CDCl_3$): δ = 161.29, 138.94, 126.41, 121.90, 63.63, 57.14, 55.16, 45.68, 42.87; HR-MS (ESI) *m/z* calcd for $C_{11}H_{19}BrN_3$ ([M+H]$^+$) 272.0762, found 272.0756.

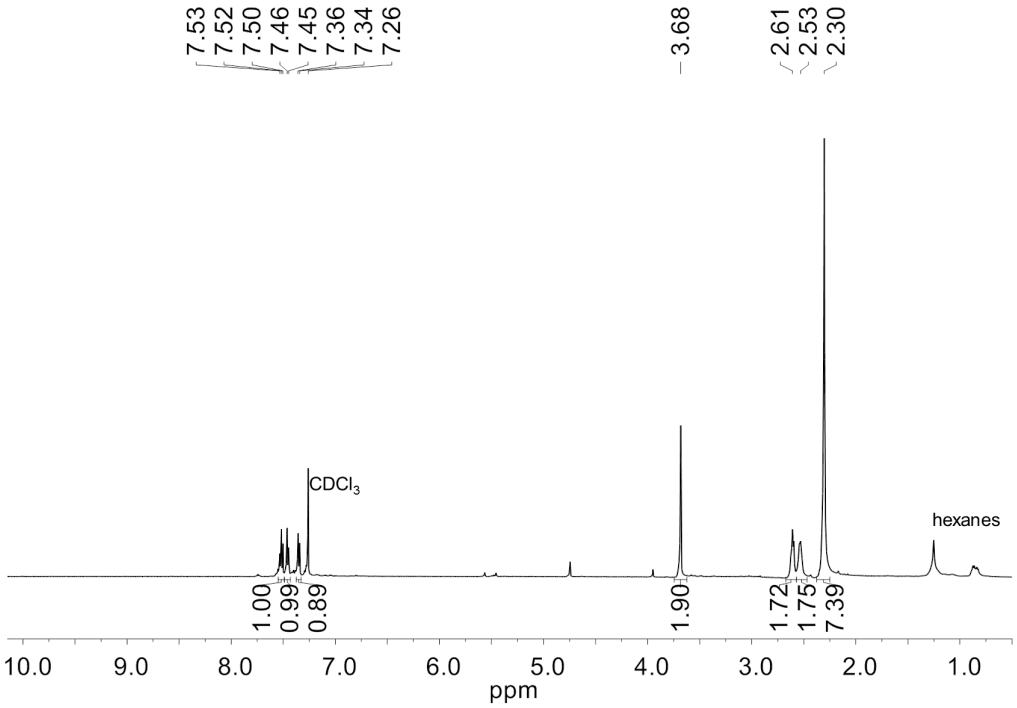

Figure C.7. ^{1}H NMR of L^{AsymBr} in $CDCl_3$.

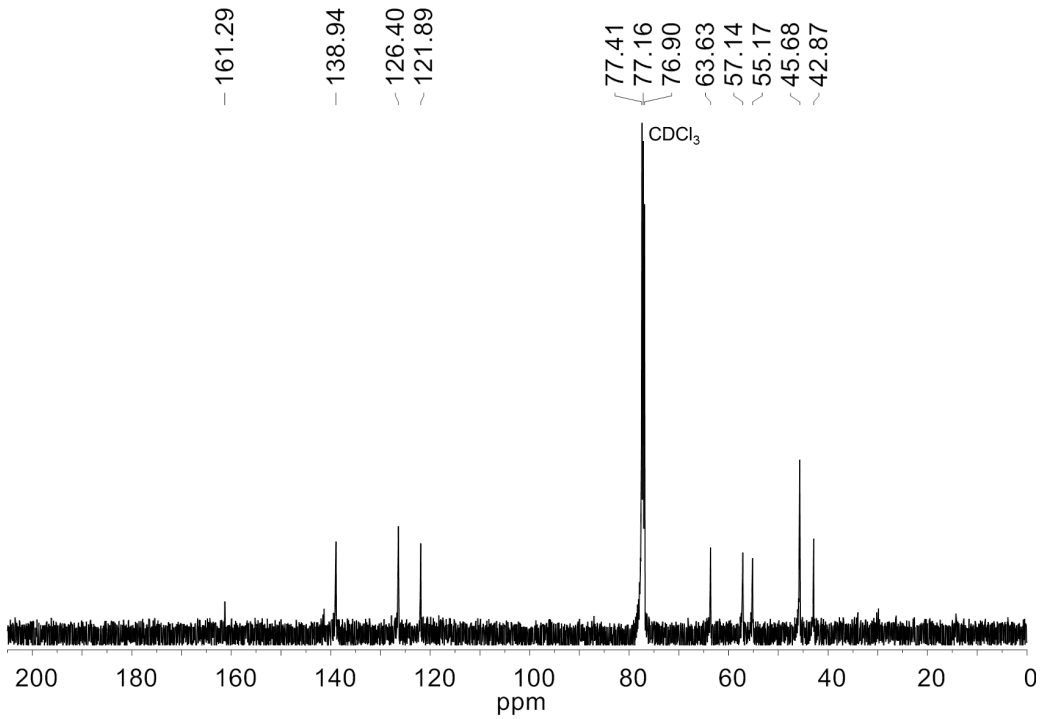

Figure C.8. $^{13}C\{^{1}H\}$ NMR of L^{AsymBr} in $CDCl_3$.

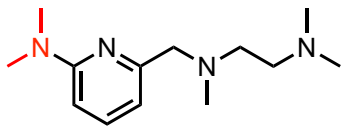

N^1-((6-(dimethylamino)pyridin-2-yl)methyl)-N^1,N^2,N^2-trimethylethane-1,2-diamine (L^{Asym}). In a Schlenk flask, aqueous DMA (40% w/w, 2.4 mL, 2.1 g, 19 mmol) was added to a solution of L^{AsymBr} (1.0 g, 3.8 mmol) in water (5 mL). The resulting mixture was sealed under pressure, stirred and heated to 50 °C for 48 h then cooled to room temperature. The resulting mixture was extracted with dichloromethane several times and the organic layers were combined, dried over $MgSO_4$, filtered and concentrated to give a dark brown oil (0.90 g, 88% yield). ^{1}H NMR ($CDCl_3$): δ = 7.40 (t, $^3J_{HH}$ = 10.0 Hz, 1H, Ar-*H*), 6.64 (d, $^3J_{HH}$ = 10.0 Hz, 1H, Ar–*H*), 6.37 (d, $^3J_{HH}$ = 10.0 Hz, 1H, Ar–*H*), 3.57 (s, 2H, Ar-C*H*$_2$–N–), 3.06 (s, 6H, Ar–N–(C*H*$_3$)$_2$), 2.61 (t, $^3J_{HH}$ = 10.0 Hz, 2H, –CH$_2$–C*H*$_2$–), 2.50 (t, $^3J_{HH}$ = 10.0 Hz, 2H, –C*H*$_2$–CH$_2$–), 2.34 (s, 3H, –N–C*H*$_3$), 2.26 (s, 6H, –N–(C*H*$_3$)$_2$); ^{13}C{^{1}H} NMR ($CDCl_3$): δ = 137.52, 110.76, 103.88, 64.24, 57.43, 55.21, 45.87, 43.01, 38.07; HR-MS (ESI) *m/z* calcd for $C_{13}H_{25}N_4$ ([M+H]$^+$) 237.2079, found 237.2087.

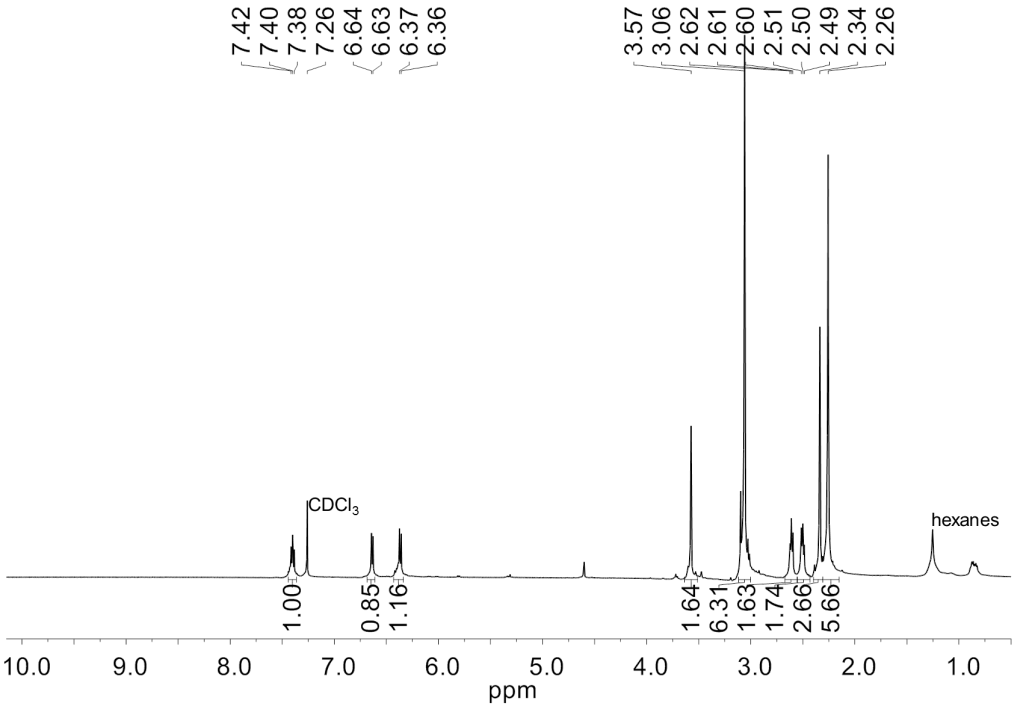

Figure C.9. ^{1}H NMR of L^{Asym} in $CDCl_3$.

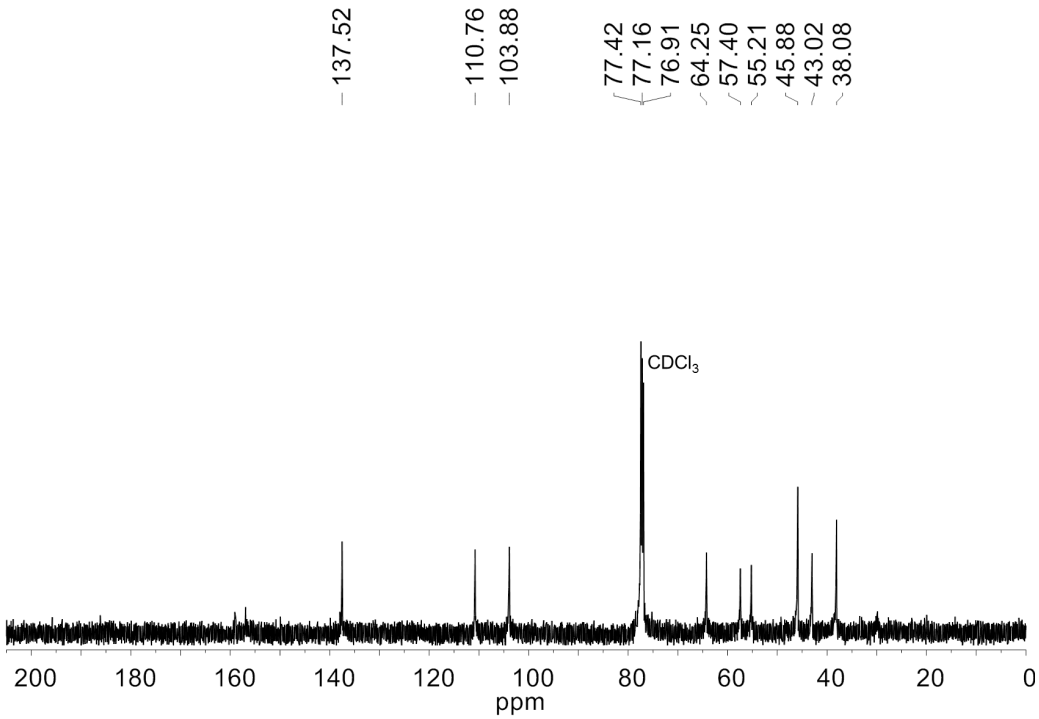

Figure C.10. $^{13}C\{^{1}H\}$ NMR of L^{Asym} in $CDCl_3$.

Synthesis of Complexes

[RhL^{DMA}Cl$_2$][Cl]. A solution of $RhCl_3(H_2O)_3$ (12 mg, 0.06 mmol) in 1 mL CH_3OH was added to a solution of **L^{DMA}** (20 mg, 0.06 mmol) in 2 mL of CH_3CN. The orange solution was stirred at 25 °C for 0.5 h and then 5 mL of Et_2O was added to precipitate the complex. After standing overnight at −40 °C, a yellow solid precipitated. (20 mg, 63% yield). Single yellow crystals were obtained by diffusion of Et_2O in a CH_3CN/CH_3OH solution. ESI-MS (CH_3CN) *m*/*z*: 529.1 ([RhL^{DMA}Cl$_2$]$^+$). $\lambda_{max,}$ nm (CH_3CN, ε ($M^{-1} \times cm^{-1}$)) = 253 (16,000) and 332 (4400). Calcd (Found) for $C_{20}H_{32}Cl_3N_6Rh$ (%): C, 42.46 (42.40); H, 5.70 (5.45); N, 14.85 (14.52).

[RhL^{Asym}(CH$_3$CN)Cl$_2$][Cl]. A solution of $RhCl_3(H_2O)_3$ (22 mg, 0.10 mmol) in 1 mL CH_3OH was added to a solution of **L^{Asym}** (29 mg, 0.10 mmol) in 2 mL of CH_3CN. The orange solution was stirred at 25 °C for 0.5 h and then 5 mL of Et_2O was added to precipitate the complex. After standing overnight at −40 °C, a yellow solid precipitated. (32 mg, 63% yield). Single yellow crystals were obtained by diffusion of Et_2O in a CH_3CN/CH_3OH solution. ESI-MS (CH_3CN) *m*/*z*: 371.1 ([RhL^{Asymm} + CH_3OH]$^+$). $\lambda_{max,}$ nm (CH_3CN, ε ($M^{-1} \times cm^{-1}$)) = 214 (68,000) and 321 (6700). Calcd (Found) for $C_{13}H_{24}Cl_3N_4Rh$ + CH_3CN (%): C, 37.02 (36.91); H, 5.59 (5.23); N, 14.39 (14.31).

C.6. References

(1) Davies, H. M. L.; Morton, D. *J. Org. Chem.* **2016**, *81*, 343-350.

(2) Labinger, J. A.; Bercaw, J. E. *Nature* **2002**, *417*, 507-514.

(3) Colby, D. A.; Bergman, R. G.; Ellman, J. A. *Chem. Rev.* **2010**, *110*, 624-655.

(4) Colby, D. A.; Tsai, A. S.; Bergman, R. G.; Ellman, J. A. *Acc. Chem. Res.* **2012**, *45*, 814-825.

(5) Song, G.; Wang, F.; Li, X. *Chem. Soc. Rev.* **2012**, *41*, 3651-3678.

(6) Satoh, T.; Miura, M. *Chem. Eur. J.* **2010**, *16*, 11212-11222.

(7) Cochet, T.; Bellosta, V.; Roche, D.; Ortholand, J.-Y.; Greiner, A.; Cossy, J. *Chem. Comm.* **2012**, *48*, 10745-10747.

(8) Kawamorita, S.; Miyazaki, T.; Iwai, T.; Ohmiya, H.; Sawamura, M. *J. Am. Chem. Soc.* **2012**, *134*, 12924-12927.

(9) Tan, X.; Liu, B.; Li, X.; Li, B.; Xu, S.; Song, H.; Wang, B. *J. Am. Chem. Soc.* **2012**, *134*, 16163-16166.

(10) Bernskoetter, W. H.; Schauer, C. K.; Goldberg, K. I.; Brookhart, M. *Science* **2009**, *326*, 553.

(11) Liu, B.; Zhou, T.; Li, B.; Xu, S.; Song, H.; Wang, B. *Angew. Chem. Int. Ed.* **2014**, *53*, 4191-4195.

(12) Wayland, B. B.; Ba, S.; Sherry, A. E. *J. Am. Chem. Soc.* **1991**, *113*, 5305-5311.

(13) Fu, R.; Nielsen, R. J.; Goddard, W. A.; Fortman, G. C.; Gunnoe, T. B. *ACS Catal.* **2014**, *4*, 4455-4465.

(14) Kapdi, A. R. *Dalton Trans.* **2014**, *43*, 3021-3034.

(15) Pavia, D. L. L., G. M.; Kriz, G. S.; Vyvyan, J. R. *Introduction to Spectroscopy*; Brooks/Cole, 2009.

(16) Kaljurand, I.; Kütt, A.; Sooväli, L.; Rodima, T.; Mäemets, V.; Leito, I.; Koppel, I. A. *J. Org. Chem.* **2005**, *70*, 1019-1028.

APPENDIX D

Single-Molecule Force Spectroscopy Studies of Electronically Modified Intramolecular Hydrogen Bonds in Titin Mimic Oligomers

This work was performed in the Guan Lab from 2011-2013 prior to joining the Yang Lab.

D.1. Motivation and Specific Aims

The muscle protein titin possesses a highly desirable combination of strength, toughness and elasticity which are useful properties for incorporation into multifunctional polymers.[1] Synthetic polymers containing strong hydrogen-bonding motifs have been designed as biomimetic materials based on the modular structure of natural titin. Here, an electronic series of 2nd generation stack-blocked UPy titin mimic monomers have been synthesized to examine the correlation between electronically perturbed hydrogen bond lengths and single molecule force rupture within the corresponding biomimetic oligomers. Single-molecule force spectroscopy (SMFS) studies of the different electronic oligomer derivatives have successfully replicated the diagnostic saw-tooth pattern of natural titin and comparatively have a statistically different population of rupture force at a single loading rate.

D.2. Background

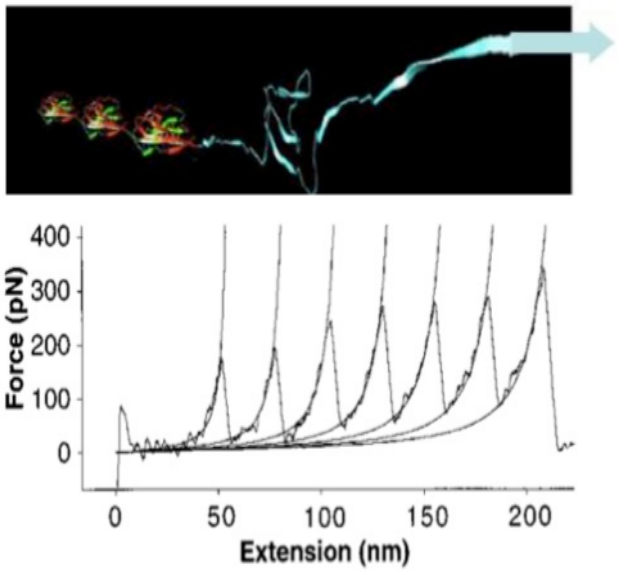

Figure D.1. Top: The natural polymer titin. Bottom: Characteristic saw-tooth pattern in the single molecule force versus extension curve in SMFS studies.[2-6]

Drawing inspiration from natural materials with high strength, stimuli response, and elasticity, synthetic biomimetic polymers have been designed that exhibit similar mechanical properties as natural systems while affording a higher degree of structural control.[7-10]

Titin, the largest known protein and a popular biomimetic target, exploits reversible hydrogen-bonding modules to create strength and extensibility within the sarcomere of muscle cells.[3,11,12] The immunoglobulin (Ig) domain of titin employs a linear array of over 200 covalently linked modular units that unfold sequentially upon extension and automatically refold with the release of tension.[5,13-15] Each module is supported by six cooperative hydrogen bonds, between β-strands A' and G, and have been shown by steered molecular dynamics simulations to be the first intermolecular force to rupture upon elongation due to their weak non-covalent nature.[2]

An atomic force microscopy (AFM) force-extension curve for the titin Ig domain I27 reveals sequential unfolding of individual modular domains where the maximum force required to rupture a single domain is represented by each peak of the curve (Figure D.1).[4] While the cumulative effects of the hydrogen-bonding interactions establish the load bearing strength, the sequential unfolding provides the elastic character of the muscle sarcomere.[6,16] This extensibility can be evaluated using the worm-like chain (WLC) mathematical model, which describes the force dependent behavior of polymer-like elasticity.[17-19] The Ig domain's load bearing strength and elasticity, otherwise unobservable properties, directly connect macroscopic function to their causal molecular interactions and conformational changes.

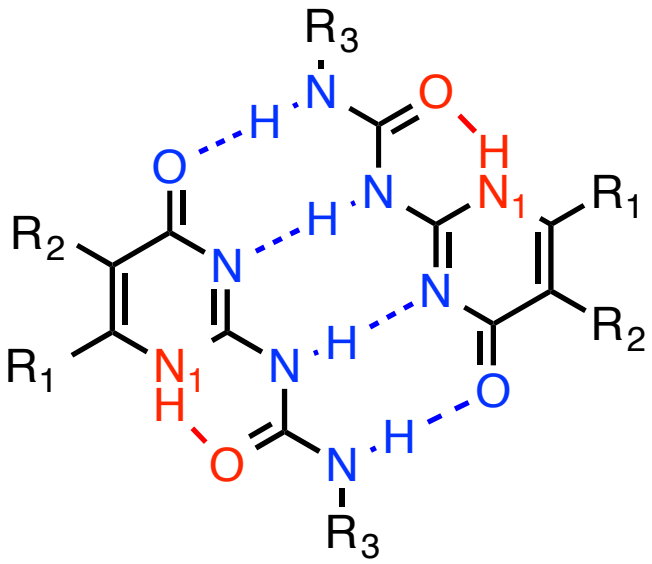

Figure D.2. The DDAA dimer of the UPy, structure designed by Meijer.[20]

Originally designed and synthesized by Meijer, the 2–ureido–4[1*H*]–pyrimidinone (UPy) dimer motif contains a donor-donor-acceptor-acceptor pattern (DDAA) of hydrogen bonds (Figure D.2).[20] The preorganized DDAA arrangement of N(1)–H donation to the urea carbonyl locks each monomer in the conformation shown and allows dimer assembly through four intermolecular hydrogen bonds. The large dimerization constants of the synthetic UPy dimer in nonpolar solvents, 10^7 M^{-1} (−10.6 kcal/mol) in chloroform and 10^8 M^{-1} (−12 kcal/mol) in toluene, indicate remarkable strength and are comparable to constants observed for the energy required for protein stability.[21]

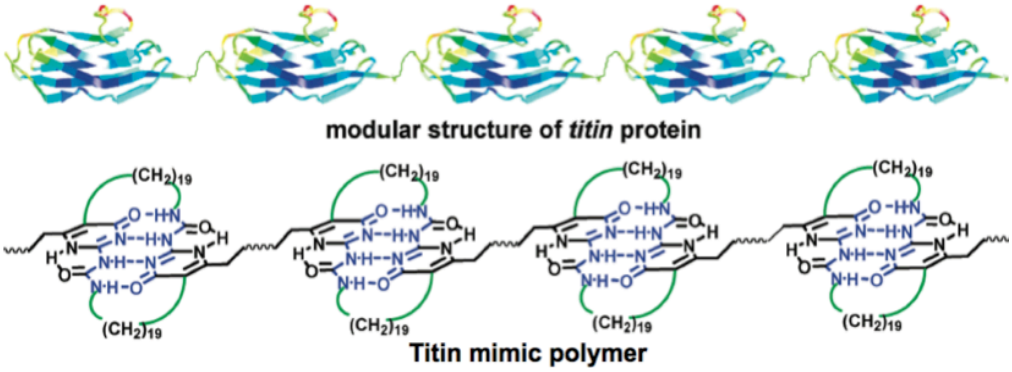

Figure D.3. Top: Linear modular structure of titin. Bottom: Linear titin mimic UPy DCL modular polymer. The green curve indicates a polymethylene linker.[22]

The hydrogen-bonding strength of UPy has been exploited in several linear polymers and 3D-networks that attempt to emulate the strength and reversibility of biological titin.[22-25] In order to enhance the binding reversibility during AFM studies, long chain linkers are implemented to tether the dimer. The double closed loop (DCL) linear system was designed with two alkyl chain linkers that join the UPy dimer to form a modular titin mimic (Figure D.3). This polymer shows a saw-tooth curve in single molecule studies as well as a combination of high modulus, toughness, and shape memory in bulk.[22] However, the reversible binding was disturbed by π-π stacking within the UPy system upon elongation.[22,23] Furthermore, polymer processing was complicated by aggregation and low solubility due to the π-π stacking. In order to prevent these problematic interactions, isopropyl alkyl groups were incorporated into the DCL system using 2,6-diisopropyl aniline to form the urea of UPy in the first generation stack-blocked DCL system.[24] This first generation stack-blocked DCL system showed direct correlation between single molecule properties and bulk polymer mechanical preformance.[26]

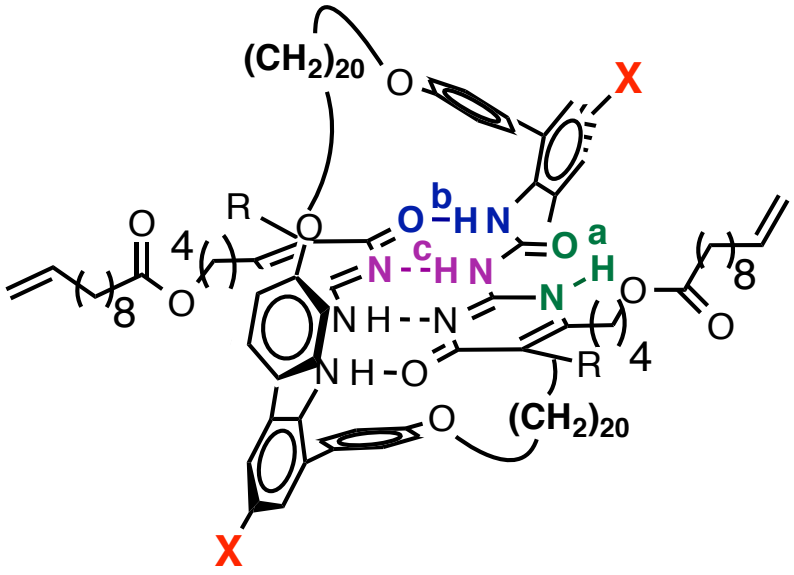

Figure D.4. Modular design of 2nd generation stack-blocked UPy DCL monomer. X represents the adjustable position for electronic perturbation.

Table D.1. DFT calculations of UPy hydrogen bond length (Å) from structure in Figure D.4 according to electronic perturbation where X = OMe, H and CF_3.[24]

	Bond Length (Å)		
	OMe	**H**	**CF_3**
A	1.654	1.659	1.667
B	1.674	1.667	1.654
C	1.844	1.841	1.837

Here, a second generation DCL monomer module is described in which a sterically bulky terphenyl unit is incorporated in order to disrupt π-π stacking through intercalation of the UPy dimer (Figure D.4).[24] Moreover, electronic variations on the para position of the aniline terphenyl unit have been investigated to understand the electronic perturbation of hydrogen bond length and strength within the UPy dimer. Previous density functional theory (DFT) calculations show that the incorporation of electron donating and withdrawing groups in the para (X) position can affect the internal hydrogen-bonding lengths by a total of 0.02 Å and 0.007 Å for internal hydrogen bonds B and C, respectively (Table D.1).[24] These alterations are predicted to change the linear rupture force across the series during AFM-based single molecule force experiments.

D.3. Results and Discussion

D.3.1. Synthesis of Titin Mimic Oligomers

Scheme D.1. Synthesis of guanidine pyrimidinone **1.1** from benzyl protected β-Ketoester **A**.[20,24,27]

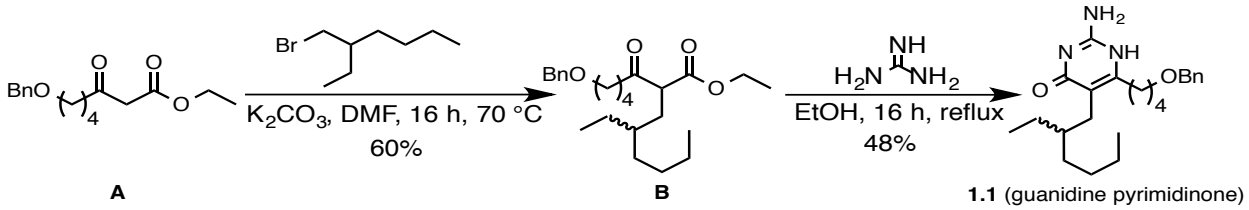

Guanidine pyrimidinone **1.1** was synthesized through the alkylation of β-Ketoester **A**, as prepared by Stille,[27] using 2-ethylhexyl bromide followed by a condensation with guanidine carbonate (Scheme D.1).[24] The starting material, 2-ethylhexyl bromide was obtained as a mixture of *R* and *S* enantiomers resulting in the racemic mixture of compound **1.1**. Compound **1.1** was used in the synthesis of the dimer modules producing a mixture of diastereomers, but stereochemically pure materials were not critical for the SMFS studies and therefore the isomers were not separated.

Synthesis of Ring Closed Diol 3a-d

Scheme D.2. Synthesis of electronic variants of ring closed diol **3** using previously synthesized benzyl protected terphenyl aniline **1.2**.[24]

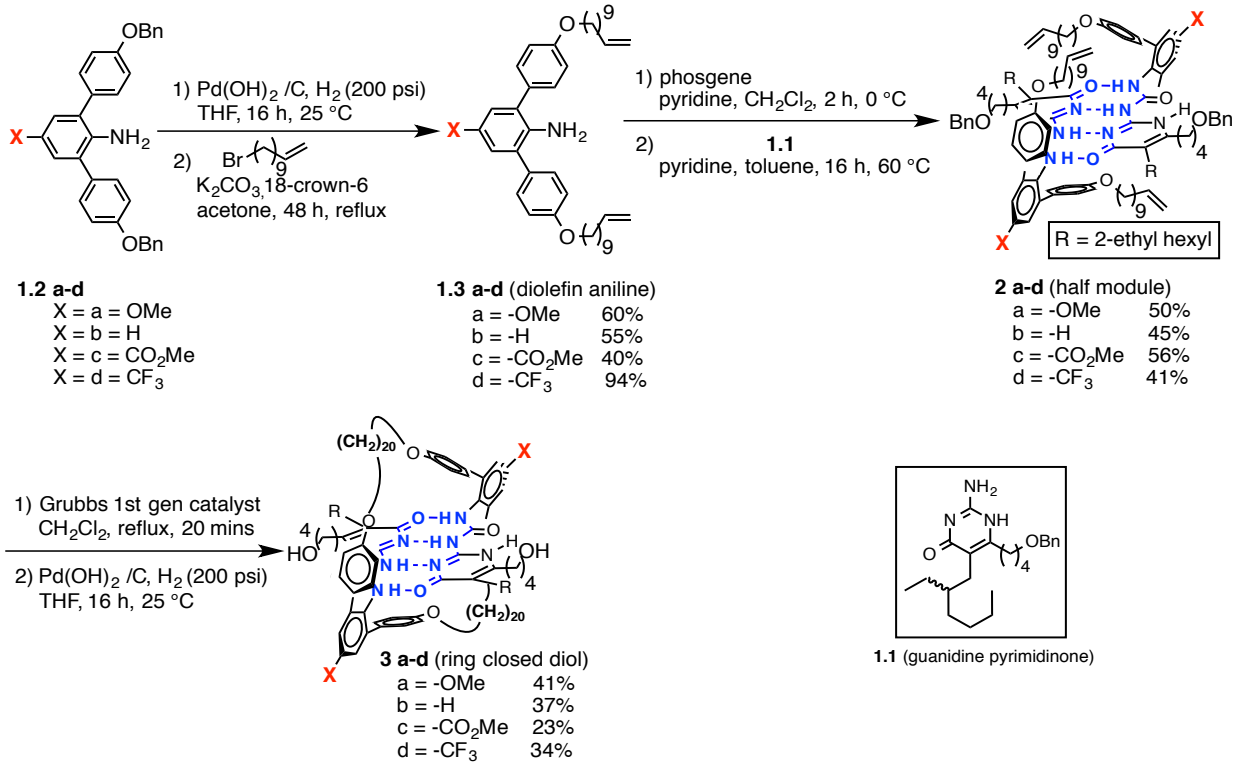

1.2 a-d
X = a = OMe
X = b = H
X = c = CO_2Me
X = d = CF_3

1.3 a-d (diolefin aniline)
a = -OMe 60%
b = -H 55%
c = -CO_2Me 40%
d = -CF_3 94%

2 a-d (half module)
a = -OMe 50%
b = -H 45%
c = -CO_2Me 56%
d = -CF_3 41%

3 a-d (ring closed diol)
a = -OMe 41%
b = -H 37%
c = -CO_2Me 23%
d = -CF_3 34%

1.1 (guanidine pyrimidinone)

The synthesis of compounds **3a-d** (Scheme D.2) was accomplished from compounds **1.2a-d**, previously synthesized by electrophilic aromatic bromination of a para substituted aniline derivative followed by a Suzuki cross coupling reaction with a benzyl protected phenol.[24] Deprotection of compounds **1.2a-d** and alkylation with 11-bromo-undecene afforded diolefin aniline compounds **1.3a-d**. The aniline was converted to the isocyanate derivative by treatment with phosgene. After nucleophilic addition of guanidine pyrimidinone **1.1**, the UPy dimer half module **2a-d** was formed.[24] Grubbs' first generation catalyst was used for ring closing metathesis (RCM) between the terminal olefins in compounds **2a-d** to form the double closed loop. Deprotection of the benzyl alcohol under hydrogen atmosphere yielded the hydrogenated ring closed diols **3a-d**.

Synthesis of ADMET Monomer 4a-d

Scheme D.3. Synthesis of monomer **4** from diol **3**.

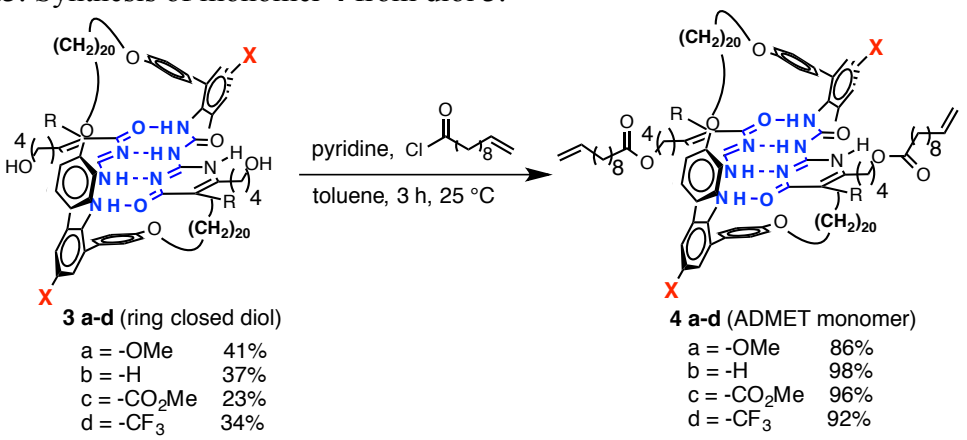

3 a-d (ring closed diol)

a = -OMe	41%
b = -H	37%
c = -CO_2Me	23%
d = -CF_3	34%

4 a-d (ADMET monomer)

a = -OMe	86%
b = -H	98%
c = -CO_2Me	96%
d = -CF_3	92%

Compounds **3a-d** were acylated using 10-undecenoyl chloride to obtain the acyclic diene metathesis (ADMET) monomers **4a-d** (Scheme D.3). Previously, the acylation of compounds **3a-d** conducted in dichloromethane (DCM) had been unsuccessful. However, when the acylation was performed in toluene, the resulting pyridinium chloride salt precipitated from solution, driving the reaction forward by Le Chatlier's principle.

Table D.2. Hydrogen bond chemicals shifts (ppm) in ^{1}H NMR spectra across the electronic series of monomer **4**.

	ppm			
	OMe	**H**	**CO_2Me**	**CF_3**
a	12.607	12.565	12.448	12.442
b	11.927	12.102	12.271	12.338
c	11.927	11.989	12.053	12.068

Additional evidence, beyond DFT calculations, of the affect of electronic perturbation on hydrogen-bonding is shown by the chemical shifts of the hydrogen-bonding hydrogen atoms in the ^{1}H NMR spectra (Table D.2). There is a downfield chemical shift across the series from electron donating to electron withdrawing for the internal hydrogen-bonded hydrogen atoms

within the UPy dimer, B and C. There is an upfield chemical shift for the external hydrogen bond A due to less available electron density for the urea carbonyl to accept the N(1) amine hydrogen bond donation in an electron withdrawing environment.

Synthesis of Oligomer 6a-d

Scheme D.4. ADMET polymerization of monomers **4** to afford thiol endcapped oligomer **6**.

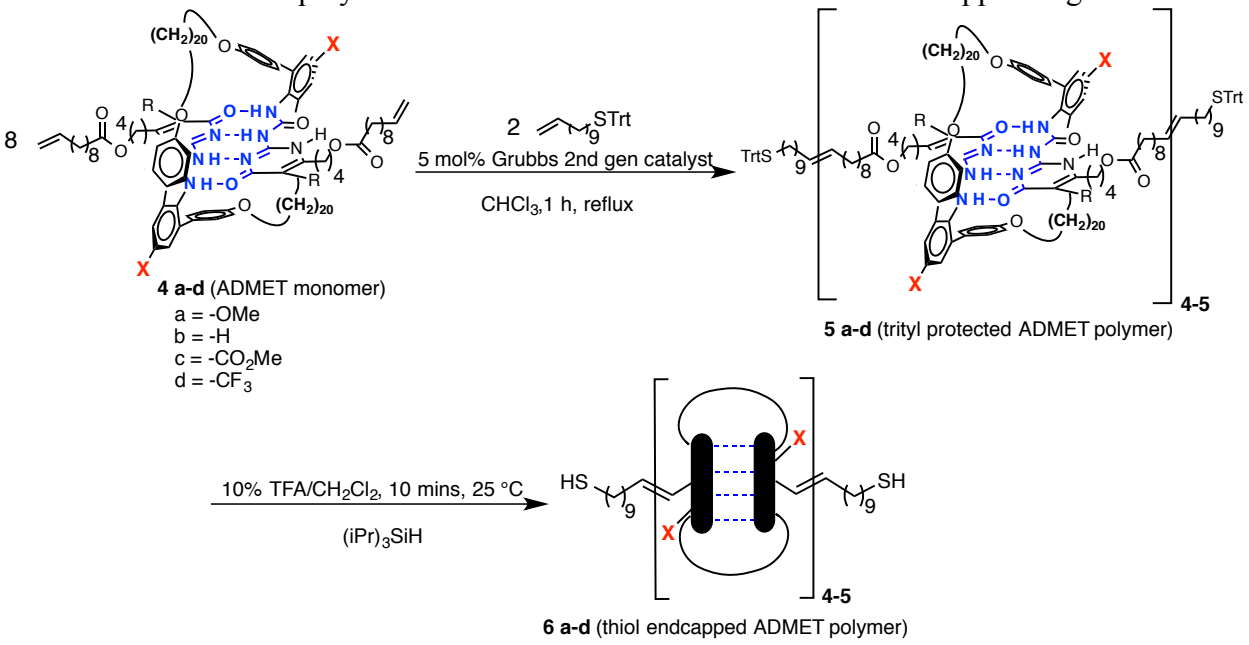

After ADMET monomer syntheses, polymerization of **4a**, **4c** and **4d** were conducted to generate the modular oligomers **5a**, **5c**, and **5d** (Scheme D.4). A trityl protected thiol was used to cap the oligomer. Protected thiols were used for their processibility and solubility after polymerization. Thiol endcapped oligomers were used for improvement over the usual technique of physioadsorption to promote anchoring with the gold plated cantilever tip and surface via a gold-sulfur bond during AFM studies. Both ^{1}H NMR spectroscopy and gel permeation chromatography (GPC) confirm that oligomers **5a**, **5c**, and **5d** are capped on both ends and have an average of five repeat units. It is likely longer polymer chains could not be obtained due to the

very large monomer molecular weight (2 KDa). The trityl unit was subsequently deprotected using trifluoroacetic acid to yield the bisendcapped thiol oligomer **6a**, **6c**, and **6d**. Full deprotection of the trityl unit was demonstrated by the upfield shift of trityl proton signals and the subsequent formation of the free triphenylmethane in the ^{1}H NMR spectrum.

Polymerization of the non-electronically perturbed monomer derivative **4b**=X=H was performed following Scheme D.4. However, only dimers were obtained and could not be compared to the five repeat unit oligomers obtained for **6a**, **6c**, and **6d**. Considering the undesired reactivity of the unperturbed monomer, SMFS data was obtained for the available OMe and CF_3 oligomers to determine the range of rupture forces for the series.

D.3.2. Single-Molecule Force Studies of Oligomers 6a and 6d

AFM-based single-molecule force spectroscopy (SFMS) studies were conducted on oligomers **6a** and **6d** to compare the behavior of the synthesized oligomer to that of the natural titin protein. The methoxy oligomer **6a**, according to DFT calculations, is the most electron donating and contains the longest hydrogen bonds which should correlate to the lowest force rupture value while trifluoromethyl oligomer **6d** is the most electron withdrawing and has the shortest hydrogen bonds which corresponds to the highest rupture force value.[24]

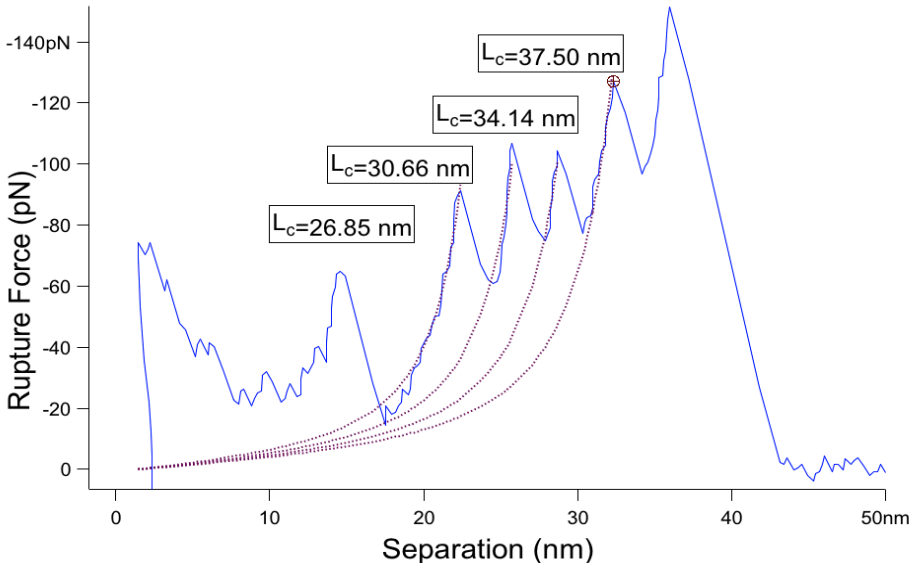

Figure D.5. Representative AFM force-extension curve (blue) of oligomer **6a** (0.1 mg/mL) in dry toluene at 1 μm/s loading rate. WLC model fit shown in red with contour lengths in boxes.

As shown in the force-extension curve for oligomer **6a** (Figure D.5), the modular oligomers show a distinct saw-tooth pattern similar to titin. Sequential unfolding and rupture of individual UPy dimer modules is proposed based on this pattern. The WLC mathematical model fits the force curve, indicating the oligomers have force dependent stretching behavior which corresponds to elasticity, analogous to that of titin.[11,28] The difference in contour length (ΔL_c), calculated with the WLC model as the distance between each saw-tooth peak, represents the increase in length from the hydrogen bound state to the ruptured state of a module unit. As shown in Figure D.5, the five saw tooth peaks from 20 nm to 40 nm illustrate five individual rupture events with ΔL_c equal to 3–4 nm for each event. This value confirms the rupture of individual modules of oligomer **6a** and is consistent with previous modeling and SMFS studies of similar DCL systems.[22,24]

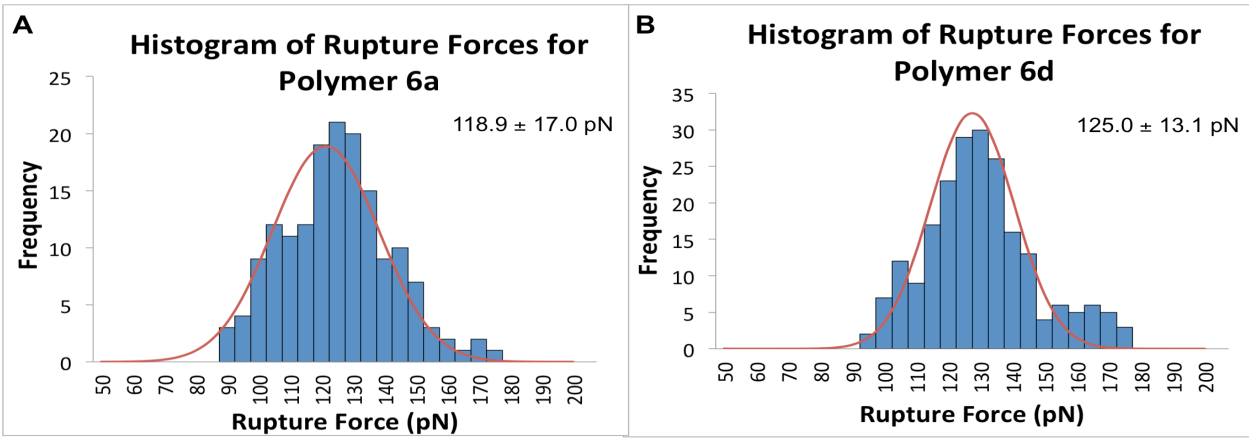

Figure D.6. Histogram of rupture force data from WLC model fit curves for oligomer **6a** (A) centered at 118.9 pN and oligomer **6d** (B) centered at 125.0 pN. SMFS studies were performed on 0.1 mg/mL in dry toluene at 1 µm/s loading rate.

Histogram data of the WLC model best-fit curves corroborates the hypothesis that the increase in electron withdrawing ability and thus a shorter hydrogen bond relates to increased rupture force (Figure D.6). The most electron donating methoxy oligomer, **6a**, has a rupture force value centered at 118.9 ± 17.0 pN while the most electron withdrawing trifluoromethyl oligomer, **6d**, has a rupture force value centered at 125.0 ± 13.1 pN. With a p-value less than 0.05, this data can be said to be statistically different populations from one another. This data illustrates that a 0.02 Å difference in bond length, a thermodynamic parameter, can have a discernable effect on the kinetic rupture force of those bonds. Due to the small variance in bond length between the other derivatives within this series (<0.005 Å), it may be difficult to achieve consequential force rupture values between these intermediate derivatives. However, rupture force is dependent on loading rate thus rupture force data at multiple loading rates must be collected and undergo statistical analysis to determine the relative strength differentiation of each module derivative.

D.4. Conclusion

All four electronic derivatives of the second generation UPy stack-blocked DCL ADMET monomer have been synthesized. Successful polymerization of three monomers has been performed for the first time and SMFS experiments consistent with the titin saw-tooth pattern have been observed. The electron donating oligomer **6a** demonstrates a lower rupture force value than that of the electron withdrawing trifluoromethyl oligomer **6d** by 6 pN. This data may support the hypothesis, calculated by DFT that a change in hydrogen bond length by electronic perturbation can affect the kinetic rupture force of those bonds but is not discernable until rupture forces are measured at various velocities and statistical analysis is performed. This experiment has the potential to relate the thermodynamic stability of hydrogen bonds to the force required to break the bonds, a property typically described in regards to kinetics.[29] Using the Bell-Evans model it is it is possible to extract kinetic parameters using SMFS in a two-state model of mechanical unfolding from a closed state to generate a potential energy landscape.[30] Two parameters that can be determined are the free energy barrier (ΔG) to unfolding from the hydrogen bound closed state, which depends on the unfolding rate constant or rate of dissociation (k_0), and the distance to the transition state (x_u). Determination of these values requires the generation of a force versus loading rate curve at various loading rate values to demonstrate the dependence of force on the loading rate, which allows for the rate of dissociation and distance to the transition state to be obtained mathematically and late coorelated to bulk polymer materials.[26]

D.5. Experimental Details

General Experiment Considerations

All reagents were purchased from commercial suppliers and used without further purification. Unless otherwise noted, all organic chemical manipulations were performed in air. Compounds were purified via flash column chromatography using Sorbent Technologies 60 Å, 230–400 mesh silica gel, unless otherwise stated. Anhydrous solvents were sparged with UHP argon (Praxair) and passed through columns containing Q-5 and molecular sieves before use.

Physical Methods

Nuclear Magnetic Resonance (NMR) Spectroscopy: ^{1}H NMR spectra were recorded on 500 MHz on Bruker instruments. ^{1}H NMR spectra chemical shifts are reported as δ values in ppm relative to residual protio solvent: $CDCl_3$ (7.26 ppm), CD_3CN (1.94 ppm). Proton NMR data are reported as follows: chemical shift (δ ppm), multiplicity (s = singlet, d = doublet, t = triplet, q = quartet), coupling constants (J) in Hertz (Hz), and integration. Multiplets (m) are reported over the range (ppm). Data for ^{13}C NMR spectra are decoupled proton spectra and are reported in terms of chemical shift (δ ppm).

Mass Spectrometry (MS): High resolution mass spectra (HR-MS) and electrospray ionization mass spectra (ESI-MS) were obtained on a Micromass LCT and collected at the University of California-Irvine Mass Spectrometry Facility.

Gel Permeation Chromatography (GPC): GPC was performed on an Agilent 1100 SEC system using a Polymer Laboratories PLgel Mixed-C column (Amherst, MA) with THF or DMF + 0.1% LiBr as the elutant to determine molecular weights and molecular weight distributions,

Mw/Mn, of polymer samples with respect to polystyrene standards purchased from Aldrich (Milwaukee, WI).

Single-Chain Force−Extension Measurements by Atomic Force Microscopy: Atomic force microscopy (AFM) was performed on a MFP-3D-SA AFM instrument (Asylum Research, Santa Barbara, CA) using gold coated silicon wafers (1.2 cm × 1.2 cm). A solution of oligomer (0.1 mg/mL) in toluene was loaded in a Closed Fluid Cell (Model CCELL). The sample was tested using a Biolever cantilever tip, which has a force constant in the range of 20-30 pN/nm as calibrated by Asylum Research, to collect the force−extension data. Force versus separation curves were acquired using a spectroscopy mode (ML06C cantilever) with a frequency of 0.3−0.5 Hz and a distance of 0.2−0.7 μm, and a pulling speed of 1μm/s.

Synthesis of Guanidine Pyrimidinone

2-amino-6-(4-(benzyloxy)butyl)-5-(2-ethylhexyl)pyrimidin-4(1*H*)-one (1.1). To a solution of previously synthesized ethyl 7-(benzyloxy)-3-oxoheptanoate[26] (8.7 g, 31 mmol) in 156 mL of DMF was added 2-ethylhexyl bromide (7.3 g, 38 mmol) and potassium carbonate (6.5 g, 47 mmol). The reaction mixture was allowed to stir at 70°C over 16 h then concentrated *in vacuo.* The residue was extracted with 1 x 100 mL Et_2O, washed with 1 x 200 mL water, washed with 1 x 200 mL brine, dried over anhydrous $MgSO_4$, filtered, and concentrated *in vacuo* resulting in a yellow oil (5.9 g). To a solution of the previous yellow oil (5.9 g, 15 mmol) in 100.0 mL of ethanol was added guanidine carbonate (2.7 g, 15 mmol), the reaction mixture was allowed to reflux for 24 hours then concentrated *in vacuo*. The residue was purified by flash column chromatography (0:100 – 5:95, MeOH:CH_2Cl_2) to afford **1.1** as a yellow oil (1.1 g, 18%). ^{1}H NMR ($(CD_3)_2SO$) δ 7.31 (m, 5H), 6.35 (s, 1H), 4.43 (s, 2H), 3.42 (t, J = 5.5, 2H and s, 2H), 2.32

(d, J = 7.5, 2H), 2.20 (t, J = 7.5, 2H), 1.57 (m, 4H), 1.41 (m, 1H), 1.18 (m, 8H), 0.81 (m, 6H); ^{13}C NMR (125 MHz, $(CD_3)_2SO$) δ 174.9, 153.1, 139.1, 128.7, 127.8, 127.7, 111.2, 72.3, 69.9, 69.7, 33.8, 32.5, 29.7, 29.1, 29.0, 25.7, 25.3, 23.0, 21.8, 14.4, 11.3; HRMS m / z calcd for $C_{23}H_{35}N_3O_2Na$ $(M + Na)^+$ 408.2627, found 408.2624.

Synthesis of ADMET Monomers

5'-methoxy-4,4''-bis(undec-10-en-1-yloxy)-[1,1':3',1''-terphenyl]-2'-amine (1.3a). To a solution of **1.2a** (0.81 g, 1.7 mmol) dissolved in degassed 10.0 mL THF was added $Pd(OH)_2/C$ (20 wt. percent, 0.012 g). The mixture was placed in a steel bomb and pressurized to 200 psi with hydrogen. After 48 hours, the pressure was released, nitrogen was bubbled through the solution for 15 minutes and the $Pd(OH)_2/C$ catalyst was removed by filtration through Celite. The filtrate was concentrated *in vacuo* and purified by flash column chromatography (0:100 – 3:97, MeOH: CH_2Cl_2) to afford an off-white oil (0.43 g, 84%). To a solution of the off white oil (0.43 g, 1.4 mmol) dissolved in 7.0 mL acetone was added 11-bromo-undecene (0.70 mL, 3.1 mmol), 18-crown-6 (0.018 g, 0.07 mmol), and K_2CO_3 (0.59 g, 4.2 mmol). The reaction mixture was heated to reflux for 48 hours, then cooled. The reaction mixture was diluted with 25 mL $CHCl_3$, filtered, washed with 1 x 25 mL water, 1 x 25 mL brine, dried over anhydrous $MgSO_4$, and concentrated *in vacuo*. The residue was purified by flash column chromatography (CH_2Cl_2) to afford **1.3a** as an white oil (0.83 g, 60%). ^{1}H NMR ($CDCl_3$) δ 7.44 (d, J = 6.5, 4H), 6.99 (d, J = 6.5, 4H), 6.71 (s, 2H), 5.85 (ddt, J = 17.0, 10.5, 6.0, 2H), 5.02 (dd, J = 17.0, 3.5, 2H), 4.95 (dd, J = 10.5, 3.5, 2H), 4.01 (t, J = 6.0, 4H), 3.80 (s, 3H), 3.54 (s, 2H), 2.06 (q, J = 6.0, 4H), 1.81 (quin, J = 6.0, 4H), 1.49 – 1.26 (m, 24H); ^{13}C NMR (125 MHz, $CDCl_3$) δ 158.9, 152.2, 139.3, 134.5, 130.4,

128.9, 127.6, 115.4, 114.9, 114.2, 66.1, 65.6, 30.0, 29.8-29.0, 26.1; HRMS *m* / *z* calcd for $C_{41}H_{57}NO_3Na$ $(M + Na)^+$ 634.4236, found 634.4248.

Methoxy Half Module (2a). To a cooled (0 °C) solution of **1.3a** (3.9 g, 6.5 mmol) dissolved in 26 mL anhydrous CH_2Cl_2 was added phosgene (20 wt. percent in toluene, 4.5 mL) and anhydrous pyridine (2.1 mL, 11 mmol) dropwise. The reaction solution was allowed to stir at 0 °C for 2 hours, filtered, concentrated *in vacuo* and subjected to benzene azeotrope to remove residual pyridine. The solution was filtered and concentrated *in vacuo* to afford a white residue. To the aforementioned residue was added **1.1** (2.5 g, 6.5 mmol) dissolved in 30.0 mL anhydrous pyridine, the mixture was allowed to stir for 24 hours at 25 °C. The solution was concentrated *in vacuo* and the final residue was purified by flash column chromatography (0:100 – 4:96, EtOAc: CH_2Cl_2) to afford **2a** as a white gel (3.8 g, 50%). ^{1}H NMR ($CDCl_3$) δ 12.54 (s, 1H), 11.93 (s, 1H), 11.90 (s, 1H), 7.46 (d, *J* = 8.5, 4H), 7.35 – 7.30 (m, 5H), 6.83 (d, *J* = 8.5, 4H), 6.71 (s, 2H),), 5.82 (ddt, *J* = 17.0, 10.0, 6.0, 2H), 5.00 (dd, *J* = 17.0, 3.5, 2H), 4.92 (dd, *J* = 10.0, 3.5, 2H), 4.49 (s, 2H), 4.11 (t, *J* = 6.5, 4H), 3.97 (s, 3H), 3.44 (t, *J* = 6.0, 2H), 2.38 (t, *J* = 7.5, 2H), 2.28 (d, *J* = 7.5, 2H), 2.04 (q, *J* = 6.0, 4H), 1.78 – 1.10 (m, 42H), 0.81 (t, *J* = 7.0, 3H), 0.76 (t, *J* = 7.0, 3H); ^{13}C NMR (125 MHz, $CDCl_3$) δ 172.5, 158.3, 158.2, 155.7, 153.0, 146.8, 143.1, 139.3, 139.2, 138.4, 132.4, 130.4, 128.5, 127.6, 123.9, 117.2, 114.9, 114.8, 114.7, 114.6, 114.2, 113.9, 73.0, 69.7, 67.8, 55.5, 39.0, 33.8, 32.6-23.1, 14.2, 11.1; HRMS *m* / *z* calcd for $C_{65}H_{90}N_4O_6Na$ $(M + Na)^+$ 1045.6758, found 1045.6742.

Methoxy Ring Closed Diol (3a). To a solution of **2a** (1.5 g, 1.5 mmol) dissolved in 74 mL degassed CH_2Cl_2 heated to reflux was added first-*generation Grubbs metathesis* catalyst (0.12 g, 0.15 mmol), the mixture was placed under nitrogen atmosphere and allowed to stir for 0.5 hours heated at reflux. The solution was cooled to room temperature, concentrated *in vacuo*, and

purified by flash column chromatography (0:100 – 10:90 EtOAc: CH_2Cl_2) to afford a white residue (1.2 g, 35%). To a solution of the residue dissolved in 5.0 mL degassed THF was added $Pd(OH)_2/C$ (20 wt. percent, 0.004 g). The mixture was placed in a steel bomb and pressurized to 200 psi with hydrogen. After 48 hours, the pressure was released, nitrogen was bubbled through the solution for 15 minutes and the $Pd(OH)_2/C$ catalyst was removed by filtration through Celite. The filtrate was concentrated *in vacuo* and purified by flash column chromatography (0:100 – 10:90 EtOAc: CH_2Cl_2) to afford **3a** as a white foam (0.57 g, 41%). ^{1}H NMR ($CDCl_3$) δ 12.44 (s, 2H), 11.82 (s, 2H), 11.76 (s, 2H), 7.32 (d, *J* = 8.5, 8H), 6.77 (s, 4H), 6.74 (d, *J* = 8.5, 8H), 3.82 (t, *J* = 7.0, 8H), 3.74 (s, 6H), 3.48 (t, *J* = 7.0, 4H), 2.39 (t, *J* = 7.0, 4H), 2.21 (d, *J* = 7.0, 4H), 1.67 – 1.20 (m, 96H), 0.76 (t, *J* = 7.5 Hz, 6H), 0.73 (t, *J* = 7.5 Hz, 6H); ^{13}C NMR (125 MHz, $CDCl_3$) δ 172.5, 158.3, 158.2,155.6, 153.0, 146.6, 142.9, 132.4, 130.4, 123.9, 117.3, 114.9, 113.9, 68.0, 62.3, 55.5, 38.9, 32.6, 32.0, 30.0, 29.7, 29.5, 29.4, 29.2, 29.0, 28.9, 28.5, 28.1, 27.9, 27.7, 26.1, 25.6, 24.0, 23.1, 14.1, 11.1; ES-MS *m* / *z* calcd for $C_{112}H_{165}N_8O_{12}$ $(M + H)^+$ 1814.25, found 1814.50.

Methoxy ADMET Monomer (4a). To a solution of **3a** (0.098 g, 0.040 mmol) in 1.2 mL toluene was added dry pyridine (0.013 g, 0.21 mmol) and 10-undecenoyl chloride (0.022 g, 0.11 mmol) sequentially. The reaction mixture was allowed to stir at 25 °C for 3 hours. The solution was diluted with 5 mL toluene, washed with 2 x 5 mL H_2O, dried over anhydrous $MgSO_4$, concentrated *in vacuo*, and purified by flash column chromatography (1:99 – 20:80 EtOAc/hexanes). The pure fractions were combined and evaporated to afford **4a** as a white foam (0.11 g, 86%). ^{1}H NMR ($CDCl_3$) δ 12.61 (s, 2H), 11.93 (s, 4H), 7.48 (d, *J* = 7.5, 8H), 6.90 (s, 4H), 6.86 (d, *J* = 7.5, 8H), 5.82 (ddt, *J* = 17.5, 10.0, 7.0, 2H), 5.01 (dd, *J* = 17.5, 3.5, 2H), 4.94 (dd, *J* = 10.0, 3.5, 2H), 4.07 (t, *J* = 6.0, 4H), 3.95 (t, *J* = 5.5, 8H), 3.86 (s, 6H), 2.41 (t, *J* = 7.0,

4H), 2.34 – 2.31 (m, 8H), 2.05 (q, J = 7.0, 4H), 1.79 – 1.28 (m, 124H), 0.91 (t, J = 7.0, 6H), 0.88 (t, J = 7.0, 6H); ^{13}C NMR (125 MHz, $CDCl_3$) δ 173.9, 172.5, 158.4, 158.3, 155.7, 153.1, 148.4, 143.0, 139.2, 132.3, 130.4, 123.8, 117.3, 114.9, 114.2, 113.9, 67.9, 63.5, 55.5, 39.0, 34.3, 24.4, 14.2, 11.1; ES-MS, APCI-MS, MALDI m / z calcd for $C_{134}H_{200}N_8O_{14}$ (M^+) not detected.

4,4''-bis(undec-10-en-1-yloxy)-[1,1':3',1''-terphenyl]-2'-amine (**1.3b**)**.** To a solution of **1.2b** (4.0 g, 8.7 mmol) dissolved in degassed 10.0 mL THF was added $Pd(OH)_2$/C (20 wt. percent, 0.061 g). The mixture was placed in a steel bomb and pressurized to 200 psi with hydrogen. After 48 hours, the pressure was released, nitrogen was bubbled through the solution for 15 minutes and the $Pd(OH)_2$/C catalyst was removed by filtration through Celite. The filtrate was concentrated *in vacuo* and purified by flash column chromatography (0:100 – 3:97, MeOH: CH_2Cl_2) to afford an off-white oil (1.5 g, 64%). To a solution of the off white oil (1.5 g, 5.4 mmol) dissolved in 25 mL acetone was added 11-bromo-undecene (2.6 mL, 12 mmol), 18-crown-6 (0.025 g, 0.10 mmol), and K_2CO_3 (2.2 g, 16 mmol). The reaction mixture was heated to reflux for 48 hours, then cooled. The reaction mixture was diluted with 100 mL $CHCl_3$, filtered, washed with 1 x 50 mL water, 1 x 50 mL brine, dried over anhydrous $MgSO_4$, and concentrated *in vacuo*. The residue was purified by flash column chromatography (CH_2Cl_2) to afford **1.3b** as an white oil (1.9 g, 55%). ^{1}H NMR ($CDCl_3$) δ 7.41 (d, J = 8.5, 4H), 7.08 (d, J = 7.5, 2H), 6.97 (d, J = 8.5, 4H), 6.85 (t, J = 7.5, 1H), 5.82 (ddt, J = 17.0, 10.5, 6.5, 2H), 4.99 (dd, J = 17.0, 3.5, 2H), 4.93 (dd, J = 10.5, 3.5, 2H), 3.99 (t, J = 6.5, 4H), 3.81 (s, 2H), 2.04 (q, J = 6.5, 4H), 1.80 (quin, J = 6.5, 4H), 1.56 – 1.26 (m, 24H); ^{13}C NMR (125 MHz, $CDCl_3$) δ 158.4, 141.2, 139.3, 131.8, 130.4, 129.5, 127.7, 116.1, 114.8, 114.2, 68.0, 33.9, 29.6, 29.5, 29.4, 29.3, 29.2, 29.0, 26.1; HRMS m / z calcd for $C_{40}H_{56}NO_2$ $(M + H)^+$ 582.4311, found 582.4318.

Hydrogen Half Module (2b). To a cooled (0 °C) solution of **1.3b** (1.8 g, 3.0 mmol) dissolved in 12 mL anhydrous CH_2Cl_2 was added phosgene (20 wt. percent in toluene, 2.1 mL) and anhydrous pyridine (0.98 mL, 6.0 mmol) dropwise. The reaction solution was allowed to stir at 0 °C for 2 hours, filtered, concentrated *in vacuo* and subjected to benzene azeotrope to remove residual pyridine. The solution was filtered and concentrated *in vacuo* to afford a white residue. To the aforementioned residue was added **1.1** (1.2 g, 3.0 mmol) dissolved in 15 mL anhydrous pyridine, the mixture was allowed to stir for 24 hours at 25 °C. The solution was concentrated *in vacuo* and the final residue was purified by flash column chromatography (0:100 – 2:98, MeOH:CH_2Cl_2) to afford **2b** as a white oil (1.4 g, 45%). ^{1}H NMR ($CDCl_3$) δ 12.49 (s, 1H), 12.07 (s, 1H), 11.96 (s, 1H), 7.44 (d, *J* = 8.0, 4H), 7.38 – 7.22 (m, 8H), 6.82 (d, *J* = 8.0, 4H), 5.80 (ddt, *J* = 17.0, 10.0, 7.0, 2H), 4.98 (dd, *J* = 17.0, 3.5, 2H), 4.92 (dd, *J* = 10.0, 3.5, 2H), 4.49 (s, 2H), 3.90 (t, *J* = 6.5, 4H), 3.45 (t, *J* = 6.5, 2H), 2.37 (t, *J* = 6.5, 2H), 2.26 (d, *J* = 6.5, 2H), 2.03 (q, *J* = 7.0, 4H), 1.73 – 1.10 (m, 42H), 0.83 (t, *J* = 7.0, 3H), 0.77 (t, *J* = 7.0, 3H); ^{13}C NMR (125 MHz, $CDCl_3$) δ 172.5, 158.2, 158.1, 155.4, 153.0, 146.8, 141.9, 139.2, 138.4, 132.4, 131.0, 130.5, 129.6, 128.4, 127.8, 127.6, 117.2, 114.2, 113.9, 73.1, 69.7, 67.9, 38.9, 33.8-23.1, 14.2, 11.1; HRMS *m* / *z* calcd for $C_{64}H_{89}N_4O_5$ $(M + H)^+$ 993.6833, found 993.6826.

Hydrogen Ring Closed Diol (3b). To a solution of **2b** (1.5 g, 1.5 mmol) dissolved in 120 mL degassed CH_2Cl_2 heated to reflux was added first-*generation Grubbs metathesis* catalyst (0.12 g, 0.15 mmol), the mixture was placed under nitrogen atmosphere and allowed to stir for 0.5 hours heated at reflux. The solution was cooled to room temperature, concentrated *in vacuo*, and purified by flash column chromatography (CH_2Cl_2) to afford a white residue (0.60 g, 35%). To a solution of the residue dissolved in 8.0 mL degassed THF was added $Pd(OH)_2$/C (20 wt. percent, 0.003 g).The mixture was placed in a steel bomb and pressurized to 200 psi with hydrogen. After

48 hours, the pressure was released, nitrogen was bubbled through the solution for 15 minutes and the $Pd(OH)_2/C$ catalyst was removed by filtration through Celite. The filtrate was concentrated *in vacuo* and purified by flash column chromatography (0:100 – 2:98 EtOAc: CH_2Cl_2) to afford **3b** as a orange gel (0.21 g, 37%). ^{1}H NMR ($CDCl_3$) δ 12.45 (s, 2H), 12.04 (s, 2H), 12.01 (s, 2H), 7.45 (d, *J* = 7.5, 8H), 7.37 (t, *J* = 7.0, 2H), 7.34 (d, *J* = 7.0, 4H), 6.86 (d, *J* = 7.5, 8H), 3.94 (t, *J* = 7.0, 8H), 3.61 (t, *J* = 6.5, 4H), 2.42 (t, *J* = 6.5, 4H), 2.27 (d, *J* = 6.5, 4H), 1.77 – 1.25 (m, 96H), 0.84 (t, *J* = 6.5 Hz, 6H), 0.79 (t, *J* = 6.5 Hz, 6H); ^{13}C NMR (125 MHz, $CDCl_3$) δ 172.4, 166.8, 158.2, 158.1, 155.2, 152.9, 146.7, 141.7, 132.5, 132.4, 130.9, 130.5, 130.4, 129.6, 127.8, 117.3, 113.9, 68.0, 62.3, 38.9, 32.6, 32.0, 30.0, 29.5, 29.4, 29.2, 29.0, 28.9, 28.5, 28.4, 28.3, 28.2, 28.0, 27.9, 27.8, 27.7, 27.6, 27.5, 26.1, 25.7, 24.0, 23.1, 14.1, 11.1; ES-MS *m* / *z* calcd for $C_{110}H_{161}N_8O_{10}$ $(M + Na)^+$ 1777.50, found 1777.59.

Hydrogen ADMET Monomer (4b). To a solution of **3b** (0.10 g, 0.060 mmol) in 1.4 mL dry toluene was added dry pyridine (0.021 g, 0.25 mmol) and 10-undecenoyl chloride (0.032 g, 0.17 mmol) sequentially. The reaction mixture was allowed to stir at 25 °C for 3 hours. The solution was diluted with 5 mL toluene, washed with 2 x 5 mL H_2O, dried over anhydrous $MgSO_4$, concentrated *in vacuo*, and purified by flash column chromatography (1:99 – 30:70 EtOAc/hexanes). The pure fractions were combined and evaporated to afford **4b** as a white foam (0.12 g, 98%). ^{1}H NMR ($CDCl_3$) δ 12.57 (s, 2H), 12.10 (s, 2H), 11.99 (s, 2H), 7.47 (d, *J* = 8.0, 8H), 7.41 (t, *J* = 7.5, 2H), 7.35 (d, *J* = 7.5, 4H), 6.87 (d, *J* = 8.0, 8H), 5.81 (ddt, *J* = 17.0, 10.0, 7.0, 2H), 5.00 (dd, *J* = 17.0, 3.5, 2H), 4.94 (dd, *J* = 10.0, 3.5, 2H), 4.07 (t, *J* = 6.0, 4H), 3.95 (t, *J* = 6.0, 8H), 2.40 (t, *J* = 6.0, 4H), 2.34 – 2.31 (m, 8H), 2.04 (q, *J* = 7.0, 4H), 1.79 – 1.13 (m, 124H), 0.90 (t, *J* = 7.0, 6H), 0.88 (t, *J* = 7.0, 6H); ^{13}C NMR (125 MHz, $CDCl_3$) δ 173.8, 172.4, 158.1, 155.3, 153.0, 146.4, 141.9, 139.2, 132.3, 130.9, 130.4, 129.7, 127.8, 117.3, 114.2, 113.9,

67.9, 63.4, 38.9, 34.3-22.7, 14.2, 11.1; ES-MS, APCI-MS, MALDI *m* / *z* calcd for $C_{132}H_{196}N_8O_{12}$ (M^+) not detected.

Methyl 2'-amino-4,4''-bis(undec-10-en-1-yloxy)-[1,1':3',1''-terphenyl]-5'-carboxylate (1.3c). To a solution of **1.2c** (6.7 g, 13 mmol) dissolved in degassed 100 mL THF was added $Pd(OH)_2/C$ (20 wt. percent, 0.078 g). The mixture was placed in a steel bomb and pressurized to 200 psi with hydrogen. After 48 hours, the pressure was released, nitrogen was bubbled through the solution for 15 minutes and the $Pd(OH)_2/C$ catalyst was removed by filtration through Celite. The filtrate was concentrated *in vacuo* and purified by flash column chromatography (0:100 – 3:97, MeOH: CH_2Cl_2) to afford an off-white oil (3.5 g, 81%). To a solution of the off white oil (3.4 g, 15 mmol) dissolved in 75 mL acetone was added 11-bromo-undecene (7.4 mL, 33 mmol), 18-crown-6 (0.025 g, 0.10 mmol), and K_2CO_3 (5.3 g, 38 mmol). The reaction mixture was heated to reflux for 48 hours, then cooled. The reaction mixture was diluted with 100 mL $CHCl_3$, filtered, washed with 1 x 50 mL water, 1 x 50 mL brine, dried over anhydrous $MgSO_4$, and concentrated *in vacuo*. The residue was purified by flash column chromatography (CH_2Cl_2) to afford **1.3c** as an white oil (3.8 g, 40%). ^{1}H NMR ($CDCl_3$) δ: 7.79 (s, 2H), 7.39 (d, *J* = 8.5, 4H), 6.98 (d, *J* = 8.5, 4H), 5.82 (ddt, *J* = 10.3, 2.0, 1.3, 2H), 4.96 (ddt, *J* = 17.5, 1.9, 1.7, 4H), 4.25 (s, 2H), 3.99 (t, *J* = 6.8, 4H), 3.85 (s, 3H), 2.04 (q, *J* = 7.2, 4H), 1.80 (quin, *J* = 7.1, 4H), 1.47 (quin, *J* = 7.4, 4H), 1.43 – 1.26 (m, 26H); ^{13}C NMR (125 MHz, ($CDCl_3$) δ 167.4, 158.7, 145.9, 139.2, 131.3, 131.0, 130.7, 126.7, 119.2, 115.0, 114.2, 68.1, 51.7, 38.8, 33.9-29.2, 29.0; ES-MS *m* / *z* calcd for C42H58NO4Na (M+Na)+: 662.42, found 662.42.

Methyl Ester Half Module (2c). To a cooled (0 °C) solution of **1.3c** (3.0 g, 4.7 mmol) dissolved in 20.0 mL anhydrous CH_2Cl_2 was added phosgene (20 wt. percent in toluene, 3.3 mL) and anhydrous pyridine (1.5 mL, 7.0 mmol) dropwise. The reaction solution was allowed to stir at 0

°C for 2 hours, filtered, concentrated *in vacuo* and subjected to benzene azeotrope to remove residual pyridine. The solution was filtered and concentrated *in vacuo* to afford a white residue. To the aforementioned residue was added **1.1** (1.0 g, 2.6 mmol) dissolved in 8.0 mL anhydrous pyridine, the mixture was allowed to stir for 24 hours at 25 °C. The solution was concentrated *in vacuo* and purified by flash column chromatography (0:100 – 2:98, MeOH: CH_2Cl_2) to afford **2c** as a white gel (2.8 g, 56%). ^{1}H NMR ($CDCl_3$) δ 12.38 (s, 1H), 12.27 (s, 1H), 12.02 (s, 1H), 8.01 (s, 2H), 7.45 (d, *J* = 8.5, 4H), 7.34 – 7.26 (m, 5H), 6.84 (d, *J* = 8.5, 4H), 5.79 (ddt, *J* = 17.0, 10.0, 6.5, 2H), 4.98 (dd, *J* = 17.0, 3.5, 2H), 4.92 (dd, *J* = 10.0, 3.5, 2H), 4.48 (s, 2H), 3.92 (s, 3H), 3.90 (t, *J* = 6.5, 4H), 3.44 (t, *J* = 5.5, 2H), 2.38 (t, *J* = 7.0, 2H), 2.05 (d, *J* = 7.0, 2H), 2.03 (q, *J* = 6.5, 4H), 1.74 – 1.09 (m, 42H), 0.84 (t, *J* = 7.0, 3H), 0.78 (t, *J* = 7.0, 3H); ^{13}C NMR (125 MHz, $CDCl_3$) δ 172.4, 166.8, 158.4, 155.0, 152.9, 146.9, 142.2, 139.2, 138.4, 135.5, 131.5, 130.7, 130.5, 130.4, 129.3, 128.4, 127.7, 117.4, 114.2, 114.1, 73.1, 69.6, 67.9, 52.3, 38.9, 33.8, 32.7-23.0, 14.2, 11.1; HRMS *m* / *z* calcd for $C_{66}H_{90}N_4O_7Na$ $(M + Na)^+$ 1073.6708, found 1073.6705.

Methyl Ester Ring Closed Diol (3c). To a solution of **2c** (1.5 g, 1.6 mmol) dissolved in 80.0 mL degassed CH_2Cl_2 heated to reflux was added first-*generation Grubbs metathesis* catalyst (0.13 g, 0.16 mmol), the mixture was placed under nitrogen atmosphere and allowed to stir for 0.5 hours heated at reflux. The solution was cooled to room temperature, concentrated *in vacuo*, and purified by flash column chromatography (0:100 – 16:84, EtOAc:hexanes) to afford a white residue (0.70 g, 41%). To a solution of the residue dissolved in 10.0 mL degassed THF was added $Pd(OH)_2/C$ (20 wt. percent, 0.012 g).The mixture was placed in a steel bomb and pressurized to 200 psi with hydrogen. After 48 hours, the pressure was released, nitrogen was bubbled through the solution for 15 minutes and the $Pd(OH)_2/C$ catalyst was removed by filtration through Celite. The filtrate was concentrated *in vacuo* and purified by flash column

chromatography (0:100 – 4:96 EtOAc: CH_2Cl_2) to afford **3c** as a white foam (0.68 g, 23%). ^{1}H NMR ($CDCl_3$) δ 12.34 (s, 2H), 12.23 (s, 2H), 12.07 (s, 2H), 8.01 (s, 4H), 7.45 (d, *J* = 8.0, 8H), 6.86 (d, *J* = 8.0, 8H), 3.92 (t, *J* = 7.0, 8H), 3.91 (s, 6H), 3.62 (t, *J* = 5.5, 4H), 2.41 (t, *J* = 7.0, 4H), 2.25 (d, *J* = 7.0, 4H), 1.78 – 1.16 (m, 96H), 0.84 (t, *J* = 6.5 Hz, 6H), 0.78 (t, *J* = 6.5 Hz, 6H); ^{13}C NMR (125 MHz, $CDCl_3$) δ 172.4, 166.8, 158.5, 158.4,154.9, 152.7, 146.8, 141.9, 135.5, 131.6, 130.8, 130.4, 129.2, 117.4, 114.1, 68.1, 62.3, 52.3, 38.8, 32.6, 32.0, 31.9, 29.9, 29.7, 29.5, 29.4, 29.2, 29.0, 28.8, 28.6, 28.2, 28.1, 28.0, 27.9, 27.8, 27.2, 27.6, 26.2, 26.1, 25.7, 24.0, 23.1, 14.1, 11.1; ES-MS *m* / *z* calcd for $C_{114}H_{165}N_8O_{14}$ $(M + H)^+$ 1871.59, found 1871.42.

Methyl Ester ADMET Monomer (4c). To a solution of **3c** (0.10 g, 0.050 mmol) in 1.3 mL dry toluene was added dry pyridine (0.019 g, 0.24 mmol) and 10-undecenoyl chloride (0.025 g, 0.12 mmol) sequentially. The reaction mixture was allowed to stir at 25 °C for 3 hours. The solution was diluted with 5 mL toluene, washed with 2 x 5 mL H_2O, dried over anhydrous $MgSO_4$, concentrated *in vacuo*, and purified by flash column chromatography (1:99 – 20:80 EtOAc/hexanes). The pure fractions were combined and evaporated to afford **4c** as a white foam (0.11 g, 93%). ^{1}H NMR ($CDCl_3$) δ 12.45 (s, 2H), 12.27 (s, 2H), 12.05 (s, 2H), 8.03 (s, 4H), 7.49 (d, *J* = 8.0, 8H), 6.87 (d, *J* = 8.0, 8H), 5.80 (ddt, *J* = 17.0, 10.0, 6.5, 2H), 4.99 (dd, *J* = 17.0, 3.5, 2H), 4.92 (dd, *J* = 10.0, 3.5, 2H), 4.06 (t, *J* = 6.0, 4H), 3.94 (t, *J* = 7.0, 8H), 3.92 (s, 6H), 2.41 (t, *J* = 7.5, 4H), 2.34 – 2.29 (m, 8H), 2.03 (q, *J* = 6.5, 4H), 1.80 – 1.21 (m, 124H), 0.91 (t, *J* = 7.0, 6H), 0.88 (t, *J* = 7.0, 6H); ^{13}C NMR (125 MHz, $CDCl_3$) δ 173.9, 172.4, 168.7, 158.5, 155.0, 152.9, 148.6, 142.1, 139.1, 135.4, 131.5, 130.8, 130.5, 129.3, 117.5, 114.2, 114.1, 68.0, 63.4, 52.2, 38.8, 34.3-24.3, 14.2, 11.1; ES-MS, APCI-MS, MALDI for *m* / *z* calcd $C_{136}H_{201}N_8O_{16}$ (M^+) not detected.

5'-(trifluoromethyl)-4,4''-bis(undec-10-en-1-yloxy)-[1,1':3',1''-terphenyl]-2'-amine (1.3d). To a solution of **1.2d** (8.0 g, 15 mmol) dissolved in degassed 100.0 mL THF was added $Pd(OH)_2/C$ (20 wt. percent, 0.20 g). The mixture was placed in a steel bomb and pressurized to 200 psi with hydrogen. After 48 hours, the pressure was released, nitrogen was bubbled through the solution for 15 minutes and the $Pd(OH)_2/C$ catalyst was removed by filtration through Celite. The filtrate was concentrated *in vacuo* and purified by flash column chromatography (0:100 – 3:97, MeOH: CH_2Cl_2) to afford a white oil (3.6 g, 73%). To a solution of the white oil (3.6 g, 11 mmol) dissolved in 55 mL acetone was added 11-bromo-undecene (6.1 mL, 27 mmol), 18-crown-6 (0.15 g, 0.56 mmol), and K_2CO_3 (4.6 g, 33 mmol). The reaction mixture was heated to reflux for 48 hours, then cooled. The reaction mixture was diluted with 100.0 mL $CHCl_3$, filtered, washed with 1 x 50 mL water, 1 x 50 mL brine, dried over anhydrous $MgSO_4$, and concentrated *in vacuo*. The residue was purified by flash column chromatography (CH_2Cl_2) to afford **1.3d** as an white oil (6.7 g, 94%). ^{1}H NMR ($CDCl_3$) δ 7.39 (d, J = 8.5, 4H), 7.31 (s, 2H), 6.99 (d, J = 8.5, 4H), 5.82 (ddt, J = 16.5, 10.0, 6.5, 2H), 4.99 (dd, J = 16.5, 3.5, 2H), 4.95 (dd, J = 10.0, 3.5, 2H), 4.12 (s, 2H), 4.00 (t, J = 6.5, 4H), 2.04 (q, J = 7.0, 4H), 1.81 (quin, J = 6.5, 4H), 1.57 – 1.26 (m, 24H); ^{13}C NMR (125 MHz, $CDCl_3$) δ 158.9, 144.4, 139.3, 130.9, 130.5, 126.4, 126.3, 126.0, 119.5, 115.0, 114.2, 68.1, 33.8, 30.4, 29.8, 29.6, 29.6, 29.1, 28.9, 23.0; HRMS m / z calcd for $C_{41}H_{55}F_3NO_2$ $(M + H)^+$ 650.4185, found 650.4204.

Trifluoromethyl Half Module (2d). To a cooled (0 °C) solution of **1.3d** (2.0 g, 3.1 mmol) dissolved in 12 mL anhydrous CH_2Cl_2 was added phosgene (20 wt. percent in toluene, 2.3 mL) and anhydrous pyridine (1.0 mL, 6.0 mmol) dropwise. The reaction solution was allowed to stir at 0 °C for 2 hours, filtered, concentrated *in vacuo* and subjected to benzene azeotrope to remove residual pyridine. The solution was filtered and concentrated *in vacuo* to afford a white residue.

To the aforementioned residue was added **1.1** (1.2 g, 3.1 mmol) dissolved in 16 mL anhydrous pyridine, the mixture was allowed to stir for 24 hours at 25 °C. The solution was concentrated *in vacuo* and purified by flash column chromatography (CH_2Cl_2) to afford **2d** as a white gel (1.3 g, 41%). ^{1}H NMR ($CDCl_3$) δ 12.36 (s, 1H), 12.32 (s, 1H), 12.03 (s, 1H), 7.58 (s, 2H), 7.42 (d, *J* = 8.5, 4H), 7.31 - 7.24 (m, 5H), 6.84 (d, *J* = 8.5, 4H), 5.80 (ddt, *J* = 17.5, 10.0, 7.0, 2H), 4.98 (dd, *J* = 17.5, 3.5, 2H), 4.92 (dd, *J* = 10.0, 3.5, 2H), 4.49 (s, 2H), 3.91 (t, *J* = 6.5, 4H), 3.45 (t, *J* = 6.5, 2H), 2.38 (t, *J* = 6.5, 2H), 2.26 (d, *J* = 6.5, 2H), 2.03 (q, *J* = 7.0, 4H), 1.74 – 1.10 (m, 42H), 0.82 (t, *J* = 7.5, 3H), 0.78 (t, *J* = 7.5, 3H); ^{13}C NMR (125 MHz, $CDCl_3$) δ 172.5, 158.6, 155.1,152.8, 147.0, 142.7, 139.2, 138.4, 134.4, 131.0, 129.6, 128.5, 127.6, 126.4, 125.2, 123.0, 117.4, 114.2, 73.1, 69.6, 67.9, 38.9, 33.8, 32.6-23.0, 14.1, 11.2; HRMS *m* / *z* calcd for $C_{65}H_{87}F_3N_4O_5Na$ $(M + Na)^+$ 1083.6526, found 1083.6553.

Trifluoromethyl Ring Closed Diol (3d). To a solution of **2d** (3.0 g, 1.4 mmol) dissolved in 80.0 mL degassed CH_2Cl_2 heated to reflux was added first-*generation Grubbs metathesis* catalyst (0.12 g, 0.14 mmol), the mixture was placed under nitrogen atmosphere and allowed to stir for 0.5 hours heated at reflux. The solution was cooled to room temperature, concentrated *in vacuo*, and purified by flash column chromatography (CH_2Cl_2) to afford a white residue (0.90 g, 41%). To a solution of the residue dissolved in 15 mL degassed THF was added $Pd(OH)_2$/C (20 wt. percent, 0.014 g).The mixture was placed in a steel bomb and pressurized to 200 psi with hydrogen. After 48 hours, the pressure was released, nitrogen was bubbled through the solution for 15 minutes and the $Pd(OH)_2$/C catalyst was removed by filtration through Celite. The filtrate was concentrated *in vacuo* and purified by flash column chromatography (0:100 – 4:96 EtOAc: CH_2Cl_2) to afford **3d** as a white foam (0.11 g, 33%). ^{1}H NMR ($CDCl_3$) δ 12.32 (s, 2H), 12.28 (s, 2H), 12.06 (s, 2H), 7.58 (s, 4H), 7.45 (d, *J* = 8.0, 8H), 6.87 (d, *J* = 8.0, 8H), 3.93 (t, *J* = 6.0, 8H),

3.63 (t, J = 6.0, 4H), 2.42 (t, J = 6.0, 4H), 2.25 (d, J = 6.0, 4H), 1.78 – 1.23 (m, 96H), 0.83 (t, J = 7.0 Hz, 6H), 0.76 (t, J = 7.0 Hz, 6H); ^{13}C NMR (125 MHz, $CDCl_3$) δ 172.4, 158.6, 158.5, 155.0, 152.7, 146.9, 142.5, 134.4, 131.2, 131.1, 130.4 130.3, 129.8, 129.5, 126.4, 125.1, 122.9, 117.5, 114.5, 114.2, 68.1, 62.3, 38.8, 32.6, 31.9, 30.0, 29.4, 29.2, 29.0, 28.9, 28.6, 28.2, 28.1, 28.0, 27.9, 27.8, 27.7, 26.1, 25.7, 24.0, 23.1, 14.1, 11.1; ES-MS m / z calcd for $C_{112}H_{159}F_6N_8O_{10}$ $(M + H)^+$ 1891.49, found 1891.43.

Trifluoromethyl ADMET Monomer (4d). To a solution of **3d** (0.10 g, 0.050 mmol) in 1.3 mL dry toluene was added dry pyridine (0.018 g, 0.23 mmol) and 10-undecenoyl chloride (0.025 g, 0.12 mmol) sequentially. The reaction mixture was allowed to stir at 25 °C for 3 hours. The solution was diluted with 5 mL toluene, washed with 2 x 5 mL H_2O, dried over anhydrous $MgSO_4$, concentrated *in vacuo*, and purified by flash column chromatography (1:99 – 20:80 EtOAc/hexanes). The pure fractions were combined and evaporated to afford **4c** as a white foam (0.10 g, 82%). ^{1}H NMR ($CDCl_3$) δ 12.44 (s, 2H), 12.34 (s, 2H), 12.07 (s, 2H), 7.60 (s, 4H), 7.47 (d, J = 7.5, 8H), 6.89 (d, J = 7.5, 8H), 5.81 (ddt, J = 17.5, 10.0, 6.5, 2H), 4.99 (dd, J = 17.5, 3.5, 2H), 4.92 (dd, J = 10.0, 3.5, 2H), 4.07 (t, J = 6.0, 4H), 3.96 (t, J = 6.0, 8H), 2.42 (t, J = 6.5, 4H), 2.32 – 2.28 (m, 8H), 2.04 (q, J = 6.5, 4H), 1.79 – 1.28 (m, 124H), 0.88 (t, J = 7.5, 6H), 0.86 (t, J = 7.5, 6H); ^{13}C NMR (125 MHz, $CDCl_3$) δ 173.8, 172.4, 158.7, 155.1, 152.9, 146.6, 142.7, 139.2, 134.3, 131.0, 130.4, 129.9, 128.4, 125.2, 117.6, 114.2, 68.0, 63.4, 38.9, 34.4-23.1, 14.2, 11.1; ES-MS, APCI-MS, MALDI m / z calcd for $C_{134}H_{194}N_8O_{12}$ (M^+) not detected.

Synthesis of the Thiol Endcapped Oligomers

Methoxy Trityl Protected ADMET Oligomer (5a). To a solution of **4a** (0.07 g, 0.033 mmol) and trityl(undec-10-en-1-yl)sulfane (0.003 g, 0.008 mmol) in 1.0 mL $CHCl_3$ heated to reflux was added second-*generation Grubbs metathesis* catalyst (5 mol %, 0.002 g,). The reaction mixture was allowed to stir for 1 h. The solution was precipitated out of MeOH to afford **5a** as a cream gel (0.037 g). ^{1}H NMR (CD_2Cl_2) δ: 12.47 (s, 2H), 12.21 (s, 2H), 12.05 (s, 2H), 7.98 (s, 4H), 7.41 (d, *J* = 8.0, 8H), 7.27 (d, *J* = 6.5, 1H), 7.23 (d, *J* = 6.5, 2H), 7.21 (t, *J* = 6.5, 1H), 6.85 (s, 2H; d, *J* = 8.0, 8H), 5.38 (s, 2H), 4.02 (t, *J* = 6.5, 4H), 3.92 (t, *J* = 7.0, 8H), 3.84 (s, 5H), 2.45 (t, *J* = 7.0, 4H), 2.36 (m, 9H), 2.10 – 1.21 (m, 147H), 0.88 (t, *J* = 7.0, 6H; t, *J* = 7.0, 6H); GPC (THF) *Mn*: 13,121 g/mol, *Mw*: 16,138 g/mol; *Mw*/*Mn:* 1.23.

Methoxy Thiol endcapped ADMET Oligomer (6a). To a solution of **5a** (0.037 g) in 0.9 mL CH_2Cl_2 was added 0.1 mL) TFA dropwise. The solution was allowed to stir at 25 °C for 10 min. Triisopropyl silane (200 μL) was added dropwise until the yellow solution turned brown. The reaction solution was washed with 2 x 1 mL $NaHCO_3$, dried over anhydrous $MgSO_4$, and concentrated *in vacuo* to afford a cream gel (0.025 g). ^{1}H NMR (CD_2Cl_2) δ: 12.47 (s, 2H), 12.21 (s, 2H), 12.05 (s, 2H), 7.98 (s, 4H), 7.41 (d, *J* = 8.0, 8H), 7.20 (d, *J* = 6.5, 1H), 7.16 (d, *J* = 6.5, 2H), 7.00 (t, *J* = 6.5, 1H), 6.85 (s, 2H; d, *J* = 8.0, 8H), 5.55 (s, 1H), 5.38 (s, 2H), 4.02 (t, *J* = 6.5, 4H), 3.92 (t, *J* = 7.0, 8H), 3.84 (s, 5H), 2.45 (t, *J* = 7.0, 4H), 2.36 (m, 9H), 2.10 – 1.21 (m, 147H), 0.88 (t, *J* = 7.0, 6H; t, *J* = 7.0, 6H) ; GPC (THF) *Mn*: 14.833 g/mol, *Mw*: 18,986 g/mol; *Mw*/ *Mn:* 1.28.

Methyl Ester Trityl Protected ADMET Oligomer (5c). To a solution of **4c** (0.15 g, 0.050 mmol) and trityl(undec-10-en-1-yl)sulfane (0.012 g, 0.020 mmol) in 1.0 mL $CHCl_3$ heated to reflux was added second-*generation Grubbs metathesis* catalyst (5 mol %, 0.002 g,). The

reaction mixture was allowed to stir for 1 h. The solution was precipitated out of MeOH to afford **5c** as a cream gel (0.062 g). ^{1}H NMR (CD_2Cl_2) δ: 12.47 (s, 2H), 12.21 (s, 2H), 12.05 (s, 2H), 7.98 (s, 4H), 7.48 (d, *J* = 8.0, 8H), 7.47 (d, *J* = 6.5, 2H), 7.27 (t, *J* = 6.5, 2H), 7.21 (t, *J* = 6.5, 1H), 6.85 (d, *J* = 8.0, 8H), 5.89 (s, 2H), 4.03 (t, *J* = 6.5, 4H), 3.91 (t, *J* = 7.0, 8H), 3.90 (s, 6H), 2.46 (t, *J* = 7.0, 4H), 2.34 – 2.29 (m, 8H), 2.03 (q, *J* = 6.5, 4H), 2.10 – 1.21 (m, 150H), 0.91 (t, *J* = 7.0, 6H), 0.88 (t, *J* = 7.0, 6H); GPC (THF) *Mn*: 12,655 g/mol, *Mw*: 15,431 g/mol; *Mw*/*Mn:* 1.22.

Methyl Ester Thiol endcapped ADMET Oligomer (6c). To a solution of **5c** (0.062 g) in 0.9 mL CH_2Cl_2 was added 0.1 mL) TFA dropwise. The solution was allowed to stir at 25 °C for 10 min. Triisopropyl silane (200 μL) was added dropwise until the yellow solution turned brown. The reaction solution was washed with 2 x 1 mL $NaHCO_3$, dried over anhydrous $MgSO_4$, and concentrated *in vacuo* to afford a cream gel (0.042 g). ^{1}H NMR (CD_2Cl_2) δ: 12.47 (s, 2H), 12.21 (s, 2H), 12.05 (s, 2H), 7.98 (s, 4H), 7.42 (d, *J* = 8.0, 8H), 7.30 (d, *J* = 6.5, 2H), 7.23 (t, *J* = 6.5, 2H), 7.12 (t, *J* = 6.5, 1H), 6.85 (d, *J* = 8.0, 8H), 5.89 (s, 2H), 4.03 (t, *J* = 6.5, 4H), 3.91 (t, *J* = 7.0, 8H), 3.90 (s, 6H), 2.46 (t, *J* = 7.0, 4H), 2.34 – 2.29 (m, 8H), 2.03 (q, *J* = 6.5, 4H), 2.10 – 1.21 (m, 150H), 0.91 (t, *J* = 7.0, 6H), 0.88 (t, *J* = 7.0, 6H); GPC (THF) *Mn*: 11,623 g/mol, *Mw*: 15,710 g/mol; *Mw*/ *Mn:* 1.35.

Trifluoromethyl Trityl Protected ADMET Oligomer (5d). To a solution of **4d** (0.007 g, 0.033 mmol) and trityl(undec-10-en-1-yl)sulfane (0.0003 g, 0.008 mmol) in 1.0 mL $CHCl_3$ heated to reflux was added second-*generation Grubbs metathesis* catalyst (5 mol %, 0.002 g,). The reaction mixture was allowed to stir for 1 h. The solution was precipitated out of MeOH to afford **5c** as a cream gel (0.018 g). ^{1}H NMR (CD_2Cl_2) δ: 12.45 (s, 2H), 12.27 (s, 2H), 12.05 (s, 2H), 7.59 (s, 4H), 7.41 (d, *J* = 8.0, 8H), 7.28 (d, *J* = 6.5, 2H), 7.26 (t, *J* = 6.5, 1H), 6.85 (d, *J* = 8.0,

8H), 5.37 (s, 2H), 4.03 (t, *J* = 6.5, 4H), 3.91 (t, *J* = 7.0, 8H), 2.46 (t, *J* = 7.0, 4H), 2.25 (m, 11H), 2.03 (q, *J* = 6.5, 4H), 2.10 – 1.21 (m, 170H), 0.89 (t, *J* = 7.0, 6H; t, *J* = 7.0, 6H); GPC (THF) *Mn*: 12,252 g/mol, *Mw*: 14,334 g/mol; *Mw*/*Mn:* 1.17.

Trifluromethyl Thiol endcapped ADMET Oligomer (6d). To a solution of **5d** (0.018 g) in 0.9 mL CH_2Cl_2 was added 0.1 mL) TFA dropwise. The solution was allowed to stir at 25 °C for 10 min. Triisopropyl silane (200 μL) was added dropwise until the yellow solution turned brown. The reaction solution was washed with 2 x 1 mL $NaHCO_3$, dried over anhydrous $MgSO_4$, and concentrated *in vacuo* to afford a cream gel (0.010 g). ^{1}H NMR (CD_2Cl_2) δ: 12.45 (s, 2H), 12.27 (s, 2H), 12.05 (s, 2H), 7.59 (s, 4H), 7.41 (d, *J* = 8.0, 8H), 7.20 (d, *J* = 6.5, 2H), 7.17 (t, *J* = 6.5, 1H), 6.72 (d, *J* = 8.0, 8H), 5.56 (s, 1H), 5.37 (s, 2H), 4.03 (t, *J* = 6.5, 4H), 3.91 (t, *J* = 7.0, 8H), 2.46 (t, *J* = 7.0, 4H), 2.25 (m, 11H), 2.03 (q, *J* = 6.5, 4H), 2.10 – 1.21 (m, 170H), 0.89 (t, *J* = 7.0, 6H; t, *J* = 7.0, 6H); GPC (THF) *Mn*: 14,407 g/mol, *Mw*: 18,008 g/mol; *Mw*/ *Mn:* 1.25.

D.6. References

(1) Smith, B. L.; Schaffer, T. E.; Viani, M.; Thompson, J. B.; Frederick, N. A.; Kindt, J.; Belcher, A.; Stucky, G. D.; Morse, D. E.; Hansma, P. K. *Nature* **1999**, *399*, 761-763.

(2) Lu, H.; Schulten, K. *Biophys. J.* **2000**, *79*, 51-65.

(3) Marszalek, P. E.; Lu, H.; Li, H.; Carrion-Vazquez, M.; Oberhauser, A. F.; Schulten, K.; Fernandez, J. M. *Nature* **1999**, *402*, 100-103.

(4) Rief, M.; Gautel, M.; Oesterhelt, F.; Fernandez, J. M.; Gaub, H. E. *Science* **1997**, *276*, 1109.

(5) Trombitás, K.; Greaser, M.; Labeit, S.; Jin, J.-P.; Kellermayer, M.; Helmes, M.; Granzier, H. *The Journal of Cell Biology* **1998**, *140*, 853.

(6) Tskhovrebova, L.; Trinick, J.; Sleep, J. A.; Simmons, R. M. *Nature* **1997**, *387*, 308-312.

(7) Guan, Z. *Polym. Int.* **2007**, *56*, 467-473.

(8) Kushner, A. M.; Guan, Z. *Angew. Chem. Int. Ed.* **2011**, *50*, 9026-9057.

(9) Li, H. *Adv. Funct. Mater.* **2008**, *18*, 2643-2657.

(10) Rowan, S. J. *Nat Chem* **2009**, *1*, 347-348.

(11) Linke, W. G., H.; Kellermayer, M. *Mechanics of Elastic Biomolecules*; 2nd ed.; Springer: Dordrecht, 2003.

(12) Maruyama, K. *The FASEB Journal* **1997**, *11*, 341-345.

(13) Labeit, S.; Kolmerer, B. *Science* **1995**, *270*, 293.

(14) Linke, W. A.; Stockmeier, M. R.; Ivemeyer, M.; Hosser, H.; Mundel, P. *J. Cell Sci.* **1998**, *111*, 1567.

(15) Opitz, C. A.; Kulke, M.; Leake, M. C.; Neagoe, C.; Hinssen, H.; Hajjar, R. J.; Linke, W. A. *Proc. Natl. Acad. Sci.* **2003**, *100*, 12688-12693.

(16) Kellermayer, M. S. Z.; Smith, S. B.; Granzier, H. L.; Bustamante, C. *Science* **1997**, *276*, 1112.

(17) Baumann, C. G.; Smith, S. B.; Bloomfield, V. A.; Bustamante, C. *Proc. Natl. Acad. Sci.* **1997**, *94*, 6185-6190.

(18) Bouchiat, C.; Wang, M. D.; Allemand, J.; Strick, T.; Block, S. M.; Croquette, V. *Biophys. J.* **1999**, *76*, 409-413.

(19) Bustamante, C.; Marko, J. F.; Siggia, E. D.; Smith, S. *Science* **1994**, *265*, 1599.

(20) Beijer, F. H.; Sijbesma, R. P.; Kooijman, H.; Spek, A. L.; Meijer, E. W. *J. Am. Chem. Soc.* **1998**, *120*, 6761-6769.

(21) Myers, J. K.; Pace, C. N. *Biophys. J.* **1996**, *71*, 2033-2039.

(22) Kushner, A. M.; Vossler, J. D.; Williams, G. A.; Guan, Z. *J. Am. Chem. Soc.* **2009**, *131*, 8766-8768.

(23) Guan, Z.; Roland, J. T.; Bai, J. Z.; Ma, S. X.; McIntire, T. M.; Nguyen, M. *J. Am. Chem. Soc.* **2004**, *126*, 2058-2065.

(24) Kushner, A. M., University of California Irvine, 2010.

(25) Kushner, A. M.; Gabuchian, V.; Johnson, E. G.; Guan, Z. *J. Am. Chem. Soc.* **2007**, *129*, 14110-14111.

(26) Chung, J.; Kushner, A. M.; Weisman, A. C.; Guan, Z. *Nat Mater* **2014**, *13*, 1055-1062.

(27) Paulvannan, K.; Schwarz, J. B.; Stille, J. R. *Tetrahedron Lett.* **1993**, *34*, 215-218.

(28) Zou, S.; Schönherr, H.; Vancso, G. J. *Angew. Chem. Int. Ed.* **2005**, *44*, 956-959.

(29) Tinoco Jr, I.; Bustamante, C. *Biophys. Chem.* **2002**, *101–102*, 513-533.

(30) Merkel, R.; Nassoy, P.; Leung, A.; Ritchie, K.; Evans, E. *Nature* **1999**, *397*, 50-53.